Oscar Camara Mihaela Pop
Kawal Rhode Maxime Sermesant
Nic Smith Alistair Young (Eds.)

LNCS 6364

Statistical Atlases and Computational Models of the Heart

First International Workshop, STACOM 2010
and Cardiac Electrophysiological Simulation Challenge, CESC 2010
Held in Conjunction with MICCAI 2010
Beijing, China, September 2010, Proceedings

Springer

Lecture Notes in Computer Science 6364

Commenced Publication in 1973
Founding and Former Series Editors:
Gerhard Goos, Juris Hartmanis, and Jan van Leeuwen

Editorial Board

Oscar Camara Mihaela Pop Kawal Rhode
Maxime Sermesant Nic Smith Alistair Young
(Eds.)

Statistical Atlases and Computational Models of the Heart

First International Workshop, STACOM 2010 and
Cardiac Electrophysiological Simulation Challenge, CESC 2010
Held in Conjunction with MICCAI 2010
Beijing, China, September 20, 2010
Proceedings

Springer

Volume Editors

Oscar Camara
Universitat Pompeu Fabra, Barcelona, Spain
E-mail: oscar.camara@upf.edu

Mihaela Pop
University of Toronto, Canada
E-mail: mihaela.pop@utoronto.ca

Kawal Rhode
King's College London, UK
E-mail: kawal.rhode@kcl.ac.uk

Maxime Sermesant
INRIA, Sophia Antipolis, France
E-mail: maxime.sermesant@sophia.inria.fr

Nic Smith
University of Oxford, UK
E-mail: nic.smith@comlab.ox.ac.uk

Alistair Young
The University of Auckland, New Zealand
E-mail: a.young@auckland.ac.nz

Library of Congress Control Number: 2010934136

CR Subject Classification (1998): J.3, H.4, H.5.2, H.1.2, H.5.1

LNCS Sublibrary: SL 6 – Image Processing, Computer Vision, Pattern Recognition, and Graphics

ISSN 0302-9743
ISBN-10 3-642-15834-X Springer Berlin Heidelberg New York
ISBN-13 978-3-642-15834-6 Springer Berlin Heidelberg New York

Typesetting: Camera-ready by author, data conversion by Scientific Publishing Services, Chennai, India
Printed on acid-free paper 06/3180

Preface

Recently, there has been considerable progress in the construction and application of cardiac atlases and computational models which integrate heart shape, function, and physiology. Several major initiatives have identified computational and morphological atlases as a major infrastructural platform, for instance the Physiome project and the European Virtual Physiological Human project. Non-invasive cardiovascular imaging plays an important role in defining the computational domain, the boundary/initial conditions, and tissue function and properties. Hence, one of the most important current challenges in the field is the development of robust and effective methods for the parameterization and personalization of these computational models using only minimally-invasive clinical imaging. However, in order to evaluate the model output and achieve clinical impact, such personalized models have to be both augmented with and compared to generic knowledge on the healthy and pathological heart. This knowledge can be acquired through the building of statistical models of the heart. Several efforts are now established to provide web-accessible structural and functional atlases of the normal and pathological heart for clinical, research, and educational purposes. We believe all these approaches will only be effectively developed through collaboration across the full research scope of the imaging and modeling communities.

Integrative models of cardiac function are important for understanding disease, evaluating treatment, and planning intervention. To provide a focus for the developing array of techniques which underpin the application of these models in the clinic a simulation challenge was included in the workshop. The goal of this challenge was to compare strategies for the personaliszation of different cardiac computational models with experimental data. A complete dataset was provided in advance, containing the cardiac geometry and fibre orientations from MRI as well as epicardial transmembrane potentials from optical mapping. Participants submitted personalized models and resulting isochrones, in order to allow a discussion on the different personalization strategies and results.

This workshop provides a forum for the discussion of the latest developments in the areas of heart mapping, including atlas construction, statistical modeling of cardiac function across patient groups, cardiac computational physiology, model personalization, ontological schemata for data and results, atlas-based functional analysis, and integrated functional/structural analyses. It also brings together experts in cardiology, radiology, biology, and physiology. Through this workshop we would also particularly like to engage a new generation of early-career researchers in working at this interface.

September 2010

Oscar Camara, Mihaela Pop
Kawal Rhode, Maxime Sermesant
Nic Smith, Alistair Young

Organization

We would like to thank the Program Committee, the additional reviewers, and all the participants who made this first workshop of its type a great success. We would especially like to thank the industrial sponsors Siemens AG, Siemens Corporate Research, and Scimedia/Brainvision.

Chairs

Oscar Camara	Universitat Pompeu Fabra, Spain
Mihaela Pop	University of Toronto, Canada
Kawal Rhode	King's College London, UK
Maxime Sermesant	INRIA, France
Nic Smith	University of Oxford, UK
Alistair Young	University of Auckland, New Zealand

Program Committee

Hervé Delingette	INRIA, France
Alejandro Frangi	Universitat Pompeu Fabra, Spain
Peter Hunter	University of Auckland, New Zealand
Reza Razavi	King's College London, UK
Graham Wright	University of Toronto, Canada

Challenge Organizing Team

Oscar Camara
Mihaela Pop
Jatin Relan
Maxime Sermesant

Additional Referees

Ruben Cárdenes	Corné Hoogendoorn	Stéphanie Marchesseau
Brett Cowan	Hoi-Leng Lam	Jatin Relan
Mathieu De Craene	Pedro Omedas	Vicky Wang
Carissa Grace Fonseca	Ali Pashaei	

Sponsoring Institutions

The workshop was sponsored by Siemens AG, Siemens Corporate Research, and Scimedia/Brainvision. The challenge was endorsed by the euHeart FP7 European Project.

Table of Contents

Keynote Presentations

Methods and Infrastructure for Atlas Construction

Structure and Flow

Mechanics and Motion

Electrophysiology and Electrical Activation

Computational Electrophysiological Simulation Challenge (CESC 2010)

Atlas Construction and Image Analysis Using Statistical Cardiac Models

Mathieu De Craene[1,2], Federico M. Sukno[2,1], Catalina Tobon-Gomez[1,2], Constantine Butakoff[1,2], Rosa M. Figueras i Ventura[1,2], Corné Hoogendoorn[1,2], Gemma Piella[1,2], Nicolas Duchateau[1,2], Emma Muñoz-Moreno[1,2], Rafael Sebastian[3], Oscar Camara[1,2], and Alejandro F. Frangi[1,2,4]

[1] Center for Computational Imaging & Simulation Technologies in Biomedicine; Department of Information and Communication Technologies, Universitat Pompeu Fabra, Barcelona, Spain
[2] Biomedical Research Networking Center in Bioengineering, Biomaterials and Nanomedicine (CIBER-BBN), Barcelona, Spain
[3] Department of Computer Science, Universitat de Valencia, Valencia, Spain
[4] Institució Catalana de Recerca i Estudis Avançats (ICREA), Spain

Abstract. This paper presents a brief overview of current trends in the construction of population and multi-modal heart atlases in our group and their application to atlas-based cardiac image analysis. The technical challenges around the construction of these atlases are organized around two main axes: groupwise image registration of anatomical, motion and fiber images and construction of statistical shape models. Application-wise, this paper focuses on the extraction of atlas-based biomarkers for the detection of local shape or motion abnormalities, addressing several cardiac applications where the extracted information is used to study and grade different pathologies. The paper is concluded with a discussion about the role of statistical atlases in the integration of multiple information sources and the potential this can bring to *in-silico* simulations.

1 Introduction

Four dimensional medical images become ubiquitous as routine diagnostic tool. They also are very important research instruments that allow understanding normal and diseased conditions, and grading the severity or stages of a disease. The variety of clinically available image modalities base their acquisition on wide physical phenomena. Hence, each modality offers the possibility to observe the object of interest from a distinct perspective, sometimes unique, sometimes complementary to other related imaging examinations. Clinicians extract and complement information from different studies to form a mental model, in three or four dimensions, which may allow them to classify each patient's pathology. Nonetheless, parameter values can not be regarded as comparable since each of them is measured under distinct principles. Ideally, information should be extracted from the various sources through the application of methodologies that minimize the bias towards the specific processing chain and, instead, enhance the

O. Camara et al. (Eds.): STACOM-CESC 2010, LNCS 6364, pp. 1–13, 2010.

fact that there is a physical or physiological complementarity of the underlying information sources. Statistical atlases and models are a recognized paradigm to integrate observations into quantitative, self-consistent and comprehensive descriptions [52]. This is particularly challenging in the context of cardiac imaging, since both shape and motion variability must be taken into account.

1.1 Atlas Challenges and Evolution

Historically, anatomical atlases aimed at providing a standard reference frame for comparing patients in a common space. They were obtained through the detailed segmentation of a single subject, considering this subject to be representative of the standard anatomy. Over the years, atlases have evolved to encode, on top of the template anatomy, the variability within a population. In this context, groupwise alignment of a population generated considerable research interest [6,14,50]. Several challenges were tackled to extend atlas construction algorithms to large populations, such as the automatic detection of cases with incorrectly parameterized anatomy (outliers) [8,4], the design of flexible registration techniques that can solve for small and large transformations and produce smooth and invertible transformations without compromising registration accuracy [42,51] and the appropriate selection of the reference instance(s) [6]. Recent advances on this latter issue are presented together with some of our recent work on this matter in Section 2.1.

In parallel to extending traditional atlases towards population atlases, an additional challenge is to integrate multi-scale and heterogeneous information. In cardiac studies, this information can consist of myocardial motion and deformation, perfusion, and fiber orientation, to name just a few. Issues related to the construction of motion and fiber atlases are discussed in Sections 2.2 and 2.3.

After bringing into correspondence multi-modal data from all subjects, the anatomical variability captured in the population needs to be projected on a set of basis functions, giving a more compact representation of this variability. A widespread option is to construct a statistical shape model [10,9] based on Principal Component Analysis (PCA). Statistical shape models have been applied to all major cardiac imaging modalities, with encouraging results for the quantification of cardiac function [21,47,36] (Section 3).

Alternatives to the PCA representation focus on localized components such as Independent Component Analysis (ICA) [45], sparse component analysis [44], or physiologically inspired modes like thickening or twisting [41].

1.2 Some Applications of Cardiac Atlases

The application of atlases to cardiac studies can be articulated around three main axes: (1) the automatic extraction of patient-specific biomarkers, (2) the integration of multi-modal data into a unified space for visualization purposes and (3) the generation of patient-specific models for personalized simulation of alternative treatment scenarios.

Section 4 presents three possible strategies for extracting *probabilistic* biomarkers detecting and quantifying pathological shape or motion abnormalities. By probabilistic biomarkers, we mean indexes that compare the value of a given parameter representing local anatomy and function towards a population atlas and output a statistical significance test of observing this same value within the population. The first example of biomarker we describe in this paper focus on local myocardial thickness for differentiating hypertrophic myopathy and hypertensive diseases (Section 4.1). Another example of biomarker concerns the local quantification of abnormality in myocardial velocities, and their application to the quantification of cardiac dyssynchrony in the context of cardiac resynchronization therapy (Section 4.2). The last example of biomarker presented in this paper integrates local shape and motion information using bilinear models for the integrated detection of shape and motion abnormalities (Section 4.3). Perspectives in the second and third axes are briefly given in Section 5.

2 Image Registration for Automated Construction of Cardiac Atlases

Image-based inter-subject registration has established itself as a corner stone for populational atlas construction. Its main function is to bring into correspondence the anatomy of large databases of 3D or 3D+t acquisitions. This is a prerequisite for further statistical modeling of the variability included in the population under study.

From the group-wise alignment procedure, the entire population can be encoded in the form of an average exemplar of the anatomy, and a representation of the anatomical variability obtained by analysis of the deformation fields that warp the atlas image to all the sample images in the population [31].

Obtaining the atlas anatomy from large populations has been a central question for ensuring reproducibility and robustness of the atlas construction pipeline. Incorporating the computation of the atlas within the groupwise registration guarantees that the same reference will be obtained by different operators, if there exists a unique solution to the problem (Section 2.1).

The obtained atlas anatomy defines a basic structural layer on which all patients from the population can be mapped and compared. This layer can be seen as a skeleton on which relevant pathological descriptors will be projected. Possible descriptors include, but are not limited to, motion (Section 2.2), strain, perfusion, fibers (Section 2.3) etc.

2.1 Atlases of Cardiac Anatomy

The construction of a statistical atlas of the heart first requires the joint alignment of a population into a Normalized Coordinate System (NCS). In our previous work [19,31], a registration pipeline was proposed to efficiently register large populations and compute the NCS simultaneously.

The complete procedure iterates between registering each subject to the current estimate of the NCS, averaging the set of obtained non-rigid transformations and applying the inverse of this average transformation to the current NCS estimate, as originally proposed by Guimond [20]. The reason for updating iteratively the reference is to remove a potential bias towards an atypical choice of reference within the input population.

Indeed, if the constructed atlas is biased and depicts peculiar anatomical features for the population being studied, there is a risk that when normalizing an individual sample to this space, systematic shape difference to the template anatomy could arise. This, in turn, could further influence statistical analysis [14]. Alternatives for choosing an initial reference include ranking based on groupwise mutual information, where the histograms used are those of the candidate image and the aggregate histogram of the remainder of the population [23]; minimizing the mean square TPS bending energy [32]; and manual selection [33].

2.2 Atlas of Myocardial Motion

The construction of statistical atlases of motion requires to generalize the concepts of aligning large populations of 3D data to handle the temporal dimensionality of this data, so that motion within each sequence can be integrated in the registration and statistical analysis pipeline. This process can be divided in two steps.

The first step consists in extracting motion from cardiac sequences. Traditionally, this has been estimated by decomposing the problem as a sequential set of pairwise registrations [7], which can be made diffeomorphic (continuous, differentiable and with continuous inverse [49]) in space so that the topology and the orientation of anatomical structures are preserved. However, such a strategy does not enforce temporal consistency, particularly critical when handling spatiotemporal sequences. This constraint was partially addressed by the introduction of a time-continuous transformation [27], although the temporal causality of motion is not completely represented by such a scheme. This can be achieved by extending pairwise diffeomorphic registration approaches as proposed in [11,12,17]. In such cases, the total motion field is obtained as the composition of smooth and continuous velocity fields over time, which ensures that motion depends on all previous time points, and is diffeomorphic in both time and space.

The second step addresses normalization of the different sequences to a reference anatomy. A first pipeline adapted to cardiac image sequences was proposed by [35]. The use of diffeomorphic paths was recently proposed for the alignment and the comparison of longitudinal datasets, using parallel transport techniques [28,39], but has not been applied to cardiac images yet. The accuracy of the computed paths can be increased by coupling the inter- and intra-subject registration, as described in [38]. In any of these normalization methods, the transport of the locally computed motion fields to a reference anatomy requires their local reorientation. This operation is generally achieved using a push-forward action on vector fields [40], based on the Jacobian of the mapping to the reference.

2.3 Atlas of Myocardial Fibers

The use of Diffusion Tensor Imaging (DTI) opens the possibility to extend anatomical atlases to model the myocardial fiber structure, which is essential for building realistic models of the electro-mechanical contraction of the heart. Traditionally, models of the muscle tissue have been based on histological studies, but in recent years, DTI has been used to analyze fiber orientation [2]. This image modality measures the molecular diffusion in tissues, by the estimation of a diffusion tensor (DT) at each voxel, that describes direction, magnitude and anisotropy of the diffusion [5]. Since molecular diffusion is constrained by the cell membranes, the principal direction of diffusion provides an estimation of the fiber orientation. From the eigen analysis of the DT, the principal direction can be computed (Fig. 1a) and tractography algorithms [29] can be applied to DTI data sets to visualize fibers in 3D, as shown in Fig. 1.

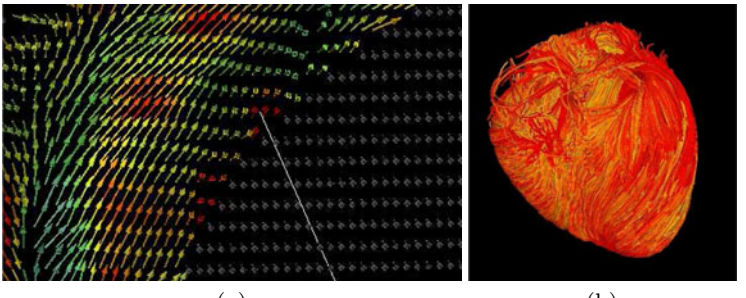

(a) (b)

Fig. 1. a) Detail of the fiber orientation in the septal wall of the left ventricle; b) 3D reconstruction of fibers in the myocardium computed from DTI

To remove individual variation and to build models of the fiber distribution, images are aligned to a reference and then averaged. This spatial normalization must be performed with DTI-specific registration methods, as the use of algorithms proposed for other modalities require their adaptation to deal with the tensorial nature of the data. The main issues are the definition of the similarity metric that is optimized along the registration procedure, and the need for warping tensors coherently with the geometrical transformation of the image. In Muoz-Moreno & Frangi [30], we propose a similarity metric related to different features of the diffusion as orientation, shape and magnitude to perform the registration. Initial results point out the advantages of these specific metrics. Since tensors are related to the fiber orientation, if this orientation changes due to a rotation of the registered volume, tensors should be reoriented to remain aligned with the fiber structures [1].

On the other hand, since atlas construction involves averaging and statistical analysis over the aligned data, the definition of tensor calculus frameworks for averaging the DT is another challenging topic. In [30], a framework to compute the average between tensors is also described to obtain more accurate fiber models.

3 Automatic Construction of Statistical Shape Models

A very extended strategy to represent objects in medical imaging and other fields, where there is a necessity to extract the geometry of objects from an image, is to employ several keypoints or *landmarks* distributed along the object's boundary [15]. Among techniques using such representation we are especially interested in Active Shape Models (ASMs) [10], as they allow for a highly automated processing. They constitute a generative model-based approach in which a priori information of the class of objects of interest is encoded into a Point Distribution Model (PDM), which is constructed by applying Principal Component Analysis (PCA) to the set of aligned training shapes. As it can be identified from the name of PDM, it characterizes the distribution of landmarks, therefore it is imperative that the shapes in the training set have a consistent landmarking strategy so that every landmark is placed in the same spot in all the instances of the object. This is often obtained through manual annotation. While this task is possible in 2D, where a hundred landmarks are usually more than enough, its extension to volumetric 3D data is nearly unfeasible. The possibility to construct large population atlases (Section 2), which relate every image to the template through invertible deformation fields can drastically simplify the task: it is enough to annotate the template image and *propagate* the annotations to the remaining dataset using the inverse transform [19,31]. As a result, this framework can provide highly consistent annotations for large sets of images with minimal amount of manual labor.

To extract the geometry from an image, the PDM has to be fit to it. This is taken care of by the other component of the ASM – local intensity models. As opposed to the cardiac geometry, that is the same independently of the image modality, the intensity models do depend on the imaging technique. Extracting the geometry from these modalities would require creating a training set for each of them. To overcome this difficulty in an automatic manner, we investigated the possibility of using synthetic datasets training intensity models [47].

A number of medical image acquisition simulation tools have been developed for virtually all major medical image modalities [24,25,43]. They usually require as input a 3D labeled image, which provides the anatomy and the tissue properties. The labeled image can be generated from the PDM itself, or from computer phantoms like 4D-XCAT [43], with the enormous advantage of an accurate knowledge of the geometry that will be embedded in the generated images. This approach to train the intensity model, eliminates the costly and expert dependent process of manual delineation, and allows constructing arbitrarily large training sets, wherefrom the intensity models can be learned in a completely automatic manner.

4 Identification and Analysis of Abnormal Patterns

4.1 Morphological Analysis of the Left Ventricle

Although most of the contemporary cardiac imaging modalities provide high resolution 3D images, cardiac morphological analysis at clinical level is performed

with a few 2D distance measurements. These distance measurements are used to categorize the pathology of the patient. For instance, an infarcted patient presents a localized thin wall; a dilated patient presents increased left ventricular diameter and overall thin walls; a hypertrophic patient presents either localized or overall thick walls. Recent studies have explored the use of novel geometric indices for diagnosis [3, 26]. Ardekani *et al.* [3] used PCA to analyze shape differences between a test subject and an average heart to classify ischemic versus non-ischemic dilated cardiomyopathy. Kown *et al.* [26] analyzed the relationship between the aortic root angle and the degree of left ventricular outflow tract obstruction in hypertrophic patients.

An atlas based segmentation approach allows for this sort of 3D morphological analysis. However, the optimal descriptor that characterizes a pathology (or a phenotype) must be identified. For instance, for left ventricular hypertrophy the expected optimal descriptor is wall thickness (WT). Unfortunately, WT values may vary greatly from normal (WT $\leq$ 12mm), to mild hypertrophy (WT $\leq$ 16mm), to severe hypertrophy (WT $\leq$ 30mm). This creates a phenotypic overlap, which clearly complicates the characterization of each condition [37].

A proper analysis of the spatial distribution of the hypertrophy can shed some light on this issue. Such an analysis can be performed thanks to the 3D atlas-based segmentation, which assures topology consistency among all datasets. Therefore, we can compute wall thickness measurements per vertex and patient and analyze the thickness variability in our population. In a recent study, we investigated this possibility [48]. The methodology was tested in fifty three subjects: 18 patients with hypertrophic cardiomyopathy, 13 patients with hypertensive heart disease and 22 sedentary subjects. Control subjects were successfully classified in 96% of the cases. The classification of each hypertrophic phenotype was correct in 90% of the cases.

4.2 Atlas-Based Motion Indexes for the Characterization of Septal Flash in CRT Patients

In Duchateau *et al.* [16], we proposed an atlas-based pipeline for the analysis of abnormal septal motion patterns in cardiac resynchronization therapy (CRT) patients from 2D echocardiographic images. A motion atlas was built from a population of 21 volunteers and locally represents the average septal velocity in the atlas space of coordinates. The variability around this average is encoded by the covariance matrix of the local velocity distribution. This gives a compact representation of healthy motion and allows for the computation of a local index of abnormality based on a statistical distance from the atlas (Mahalanobis distance and associated p-value). This index encodes the probability of locally observing a motion pattern on an individual, given the variability expected from a healthy population. Low p-values indicate high degree of abnormality.

These p-values are available at any point in time and space, which allows convenient representation for clinical studies: an abnormality map can be plotted on top of the gray level image at each time point for accurately relating the localization of motion abnormalities with the cardiac anatomy. A second alternative

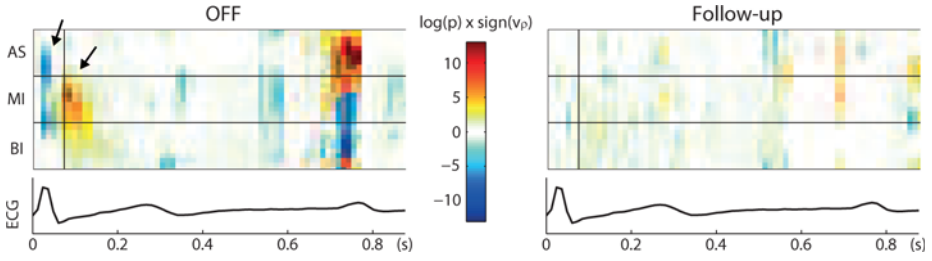

Fig. 2. Abnormality maps for septal motion, before CRT and at 12 months follow-up. The correction of the septal flash pattern (black arrows) is accurately located and quantified through this mode of representation.

consists in representing a spatiotemporal map of abnormality, as illustrated in Fig. 2. The horizontal axis represents time and the position in the septum (basal inferoseptal [BI], mid inferoseptal [MI], and apical septal [AS]) is used as vertical axis. In this figure, the p-value is displayed in logarithmic scale and multiplied by the sign of the radial velocity to enlighten abnormal inward and outward motion patterns.

The potential of this new index is directly visible in this figure for quantifying changes in myocardial motion induced by CRT. Before the therapy, a fast inward-outward motion pattern known in the literature as *septal flash* (SF) [34] is observed during the isovolumic contraction period, as indicated by the two arrows. At 12 months follow-up, the spatiotemporal map shows that the abnormality has been totally corrected, which correlates with the clinical response of this patient to therapy. It was demonstrated in [34] that the correction of the SF mechanism was highly predictive of a positive clinical response to CRT.

4.3 Dimensionality Reduction in Spatio-Temporal Cardiac Morphological Analysis

Motion analysis is a key element to deal with certain moving organs (such as heart or arterial flow) since many pathologies cannot be identified with static anatomical analysis. This has caused a growing interest in moving sequences of 4D medical data (3D+time), and the need to develop proper tools to analyze these sequences. While traditional shape modeling methods may still be used in these settings (e.g. by processing every temporal frame), they are not designed to handle (nor to take advantage of) the temporal component.

The ideal model should result from one single modeling step, where the two different sources of variation (patient anatomy and motion) are recognized and incorporated in a compact, meaningful way. In a recent work [22], we used bilinear models to establish an anatomy/motion factorization on cardiac shapes.

Bilinear and multilinear models [46,13] are multi-dimensional generalizations of singular value decomposition, where two different types of information can be represented in a bilinear basis through two sets of coefficients. These models

allow to create one set of coefficients for changes due to motion and one set of coefficients for changes due to patient anatomy, but where all the coefficients are related to the same basis and obtained simultaneously. They have been effectively used to separate anatomical information of a patient from its motion behavior, giving very compact representation of both anatomy and motion [18, 22]. This kind of models can be applied to the template mesh, obtained with an automated segmentation approach based on atlases or using a statistical method. Its direct use in image segmentation has also been demonstrated [53].

The compact and independent representation of anatomical and motion variations in bilinear models can be used to efficiently apply movement of a given patient, obtained through a dynamic modality such as magnetic resonance (MRI) or ultrasound (US), to still images, as shown in the experiments performed in [18, 22], where motion is extrapolated from only the first images of the sequence. This can be used as interventional aid, giving the possibility of moving the reference image used to implant devices in the heart according to specific patient motion coefficients, and thus improving their precision in localizing the implant zone.

5 Other Applications of Statistical Cardiac Models: Multimodal Integration of Structural, Sub-structural and Functional Information

Multimodal imaging can help clinicians by providing integrated information, beyond the limitations of single modalities. On the other hand, multimodal data provides different (and often incomplete) information layers from the same organ. Hence, the data fusion is often complicated and many times is performed implicitly in the clinician's mind, with evident shortcomings. In this context, methods based on statistical atlases provide a natural way of integration. The presence of a reference anatomy serves as a template where information can be mapped. As explained in the previous sections, multimodal information can include geometric measurements, deformation/motion patterns, myocardial fiber structure, tissue elastic and activation properties, etc.

Fig. 3 illustrates this concept: a four chamber model of the heart in which multimodal information has been reconstructed and integrated from the most appropriate modality (CT for atrial geometry; structural MRI for ventricular geometry; DT-MRI for fiber orientation; and electroanatomical mapping, EPM for electrical activation). The integration of multiple sources of information into the same anatomical reference will allow the investigation of the interplay among various parameters associated with a disease condition. Key elements for data integration are the accuracy of the correspondences, identified either by registration (Section 2) or by model-to-image adaptation (Section 3), the repeatability of the measurements and the degree of automation. However, none of this can be considered solved problems, except for very specific situations.

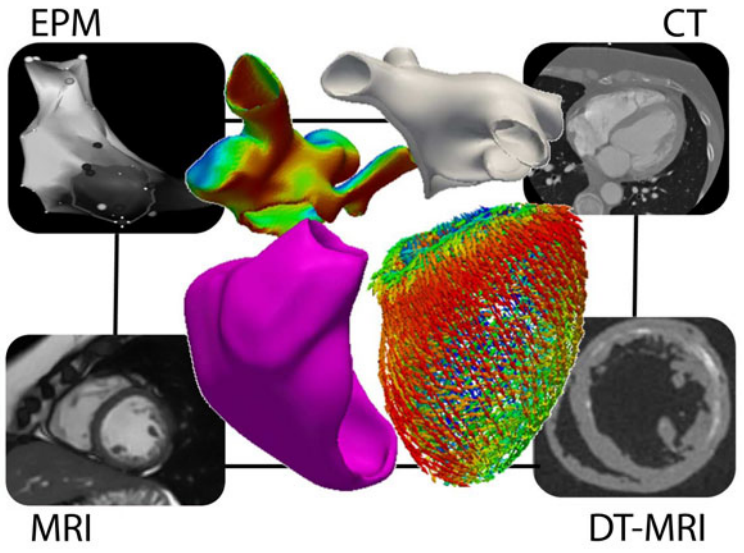

Fig. 3. A four chamber model of the heart in which multimodal information has been reconstructed and integrated from the most appropriate modality

Besides its value for image analysis and image-based diagnosis, the integration of multimodal information is required for the personalization and validation of computational physiology models. The use of simulations to model the multi-physics (mechanics, electrophysiology, fluid) mechanisms that govern the heart behaviour can help to better understand pathological processes affecting the heart function as well as providing additional information to the clinician for improved diagnosis and optimized interventional planning. Hence, the resulting *in silico* simulations are more realistic when considering multi-scale data that could be available in a statistical atlas, including information extracted from images or models of substructural information such as myocardial fibres or the semi-automatic generation of Purkinje networks generated semi-automatically as proposed by Zimmerman *et al.* [54]. Finally, simulation results can also be incorporated into the statistical atlas as a new layer of information since computational models can provide insights about non-observable parameters such as contractility or apparent conductivity maps.

6 Conclusions

Computer-aided diagnosis can be thought of as finding measurements or patterns that significantly deviate from *normality* and exhibit good correlation with pathological states. Statistical atlases build upon this paradigm and aim at establishing a common coordinate frame to facilitate comparison and statistical analysis across populations. The key element is that atlas construction allows to establish dense

correspondences between the reference and all datasets involved in the process. Therefore, it is possible to perform measurements that are consistent for a population of individuals, or even fuse the information provided by different image modalities to obtain an augmented representation. This augmented representation is expected to aid the diagnosis, by providing a holistic vision of the patient's condition and ease the prediction of the likely treatment outcome.

Acknowledgements

This work has been funded by the Integrated Project euHeart (FP7/ICT-2007-224495) in the European Commissions 7th Framework Programme, and by the Spanish Ministry of Innovation and Science through grant TIN2009-14536-C02-01, Plan E and FEDER, and through the cvREMOD project (CEN-20091044) under the CENIT programme of the Industrial and Technological Development Center (CDTI).

References

[1] Alexander, D., et al.: Spatial transformations of diffusion tensor magnetic resonance images. IEEE Trans. Med. Imag. 20(11), 1131–1139 (2001)
[2] Anderson, R.H., et al.: The three-dimensional arrangement of the myocytes in the ventricular walls. Clin. Anat. 22, 64–76 (2009)
[3] Ardekani, S., et al.: Computational method for identifying and quantifying shape features of human left ventricular remodeling. Ann. Biomed. Eng. 37(6), 1043–1054 (2009)
[4] Ashburner, J., Friston, K.J.: Voxel-based morphometry – the methods. NeuroImage 11(6), 805–821 (2000)
[5] Basser, P.J., et al.: Estimation of the effective self-diffusion tensor from the NMR spin echo. J. Magn. Reson. Ser. B 103(3), 247–254 (1994)
[6] Blezek, D.J., Miller, J.V.: Atlas stratification. Med. Image Anal. 11(5), 443–457 (2007)
[7] Chandrashekara, R., et al.: Analysis of 3-D myocardial motion in tagged MR images using nonrigid image registration. IEEE Trans. Med. Imag. 23(10), 1245–1250 (2004)
[8] Commowick, O., et al.: Detection of DTI white matter abnormalities in multiple sclerosis patients. In: Metaxas, D., Axel, L., Fichtinger, G., Székely, G. (eds.) MICCAI 2008, Part I. LNCS, vol. 5241, pp. 975–982. Springer, Heidelberg (2008)
[9] Cootes, T.F., Taylor, C.J.: Anatomical statistical models and their role infeature extraction. Brit. J. Radiol. 77, S133–S139 (2004)
[10] Cootes, T.F., Taylor, C.J.: Statistical models of appearance for computer vision. Tech. Rep., University of Manchester, UK (2004)
[11] De Craene, M., et al.: Temporal diffeomorphic free-form deformation for strain quantification in 3D-US images. In: MICCAI 2010 (2010) (in press)
[12] De Craene, M., et al.: Large diffeomorphic FFD registration for motion and strain quantification from 3D-US sequences. In: Ayache, N., Delingette, H., Sermesant, M. (eds.) FIMH 2009. LNCS, vol. 5528, pp. 437–446. Springer, Heidelberg (2009)
[13] De Lathauwer, L., et al.: A multilinear singular value decomposition. SIAM J. Matrix Anal. A. 21(4), 1253–1278 (2000)
[14] Diedrichsen, J.: A spatially unbiased atlas template of the human cerebellum. NeuroImage 33(1), 127–138 (2006)

[15] Dryden, I.L., Mardia, K.V.: Statistical Shape Analysis. Wiley, Chichester (1998)
[16] Duchateau, N., et al.: Septal flash assessment on CRT candidates based on statistical atlases of motion. In: Yang, G.-Z., Hawkes, D., Rueckert, D., Noble, A., Taylor, C. (eds.) MICCAI 2009. LNCS, vol. 5762, pp. 759–766. Springer, Heidelberg (2009)
[17] Durrleman, S., et al.: Spatiotemporal atlas estimation for developmental delay detection in longitudinal datasets. In: Yang, G.-Z., Hawkes, D., Rueckert, D., Noble, A., Taylor, C. (eds.) MICCAI 2009. LNCS, vol. 5761, pp. 297–304. Springer, Heidelberg (2009)
[18] Figueras i Ventura, R.M., et al.: Bilinear point distribution models for heart motion analysis. In: ISBI 2010, pp. 476–479 (2010)
[19] Frangi, A.F., et al.: Automatic construction of multiple-object three-dimensional statistical shape models: Application to cardiac modeling. IEEE Trans. Med. Imag. 21(9), 1151–1166 (2002)
[20] Guimond, A., et al.: Average brain models: A convergence study. Comput. Vision and Image Understanding 77(2), 192–210 (1999)
[21] Hansegård, J., et al.: Constrained active appearance models for segmentation of triplane echocardiograms. IEEE Trans. Med. Imag. 26(10), 1391–1400 (2007)
[22] Hoogendoorn, C., et al.: Bilinear models for spatio-temporal point distribution analysis: Application to extrapolation of left ventricular, biventricular and whole heart cardiac dynamics. Int. J. Comput. Vision (2009) (in Press)
[23] Hoogendoorn, C., et al.: A groupwise mutual information metric for cost efficient selection of a suitable reference in cardiac computational atlas construction. In: SPIE Med. Im., vol. 7623, pp. 76231R–76231R-9 (2010)
[24] Jensen, J.A., Svendsen, N.B.: Calculation of pressure fields from arbitrarily shaped, apodized, and excited ultrasound transducers. IEEE T. Ultrason. Ferr. 39(2), 262–267 (1992)
[25] Kwan, R.K., et al.: MRI simulation-based evaluation of image-processing and classification methods. IEEE Trans. Med. Imag. 18(11), 1085–1097 (1999)
[26] Kwon, D.H., et al.: Steep left ventricle to aortic root angle and hypertrophic obstructive cardiomyopathy: study of a novel association using three-dimensional multimodality imaging. Heart 95(21), 1784–1791 (2009)
[27] Ledesma-Carbayo, M.J., et al.: Spatio-temporal nonrigid registration for ultrasound cardiac motion estimation. IEEE Trans. Med. Imag. 24(9), 1113–1126 (2005)
[28] Miller, M.I., Qiu, A.: The emerging discipline of computational functional anatomy. NeuroImage 45(1), suppl. 1, 16–39 (2009)
[29] Mori, S., van Zijl, P.C.M.: Fiber tracking: principles and strategies - a technical review. NMR Biomed. 15, 468–480 (2002)
[30] Muñoz Moreno, E., Frangi, A.F.: Spatial normalization of cardiac diffusion tensor imaging for modeling the muscular structure of the myocardium. In: ICIP 2010 (2010) (in press)
[31] Ordás, S., et al.: A statistical shape model of the heart and its application to model-based segmentation. In: SPIE Med. Im., vol. 6511, p. 6511K (2007)
[32] Park, H., et al.: Least biased target selection in probabilistic atlas construction. In: Duncan, J.S., Gerig, G. (eds.) MICCAI 2005. LNCS, vol. 3750, pp. 419–426. Springer, Heidelberg (2005)
[33] Park, H., et al.: Construction of an abdominal probabilistic atlas and its application in segmentation. IEEE Trans. Med. Imag. 22(4), 483–492 (2003)

[34] Parsai, C., et al.: Toward understanding response to cardiac resynchronization therapy: left ventricular dyssynchrony is only one of multiple mechanisms. Eur. Heart J. 30(8), 940–949 (2009)
[35] Perperidis, D., et al.: Spatio-temporal free-form registration of cardiac MR image sequences. Med. Image Anal. 9(5), 441–456 (2005)
[36] Peters, J., et al.: Optimizing boundary detection via simulated search with applications to multi-modal heart segmentation. Med. Image Anal. 14, 70–84 (2010)
[37] Petersen, S.E., et al.: Differentiation of athlete's heart from pathological forms of cardiac hypertrophy by means of geometric indices derived from cardiovascular magnetic resonance. J. Cardiovasc. Magn. Reson. 7(3), 551–558 (2005)
[38] Peyrat, J.-M., et al.: Registration of 4D cardiac CT sequences under trajectory constraints with multichannel diffeomorphic demons. IEEE Trans. Med. Imag. 29(7), 1351–1368 (2010)
[39] Qiu, A., et al.: Time sequence diffeomorphic metric mapping and parallel transport track time-dependent shape changes. NeuroImage 45(1), supp. 1, 51–60 (2009)
[40] Rao, A., et al.: Spatial transformation of motion and deformation fields using nonrigid registration. IEEE Trans. Med. Imag. 23(9), 1065–1076 (2004)
[41] Remme, E.W., et al.: Extraction and quantification of left ventricular deformation modes. IEEE Trans. Biomed. Eng. 51(11), 1923–1931 (2004)
[42] Rueckert, D., et al.: Diffeomorphic registration using B-splines. In: Larsen, R., Nielsen, M., Sporring, J. (eds.) MICCAI 2006. LNCS, vol. 4191, pp. 702–709. Springer, Heidelberg (2006)
[43] Segars, W.P., et al.: Realistic CT simulation using the 4D XCAT phantom. Med. Phys. 35(8), 3800–3808 (2008)
[44] Sjöstrand, K., et al.: Sparse decomposition and modeling of anatomical shape variation. IEEE Trans. Med. Imag. 26(12), 1625–1635 (2007)
[45] Suinesiaputra, A., et al.: Automated detection of regional wall motion abnormalities based on a statistical model applied to multi-slice short-axis cardiac MR images. IEEE Trans. Med. Imag. 28(4), 595–607 (2009)
[46] Tenenbaum, J.B., Freeman, W.T.: Separating style and content with bilinear models. Neural Comput. 12(6), 1247–1283 (2000)
[47] Tobon-Gomez, C., et al.: Automatic construction of 3D-ASM intensity models by simulating image acquisition: Application to myocardial gated SPECT studies. IEEE Trans. Med. Imag. 27(11), 1655–1667 (2008)
[48] Tobon-Gomez, C., et al.: 3D mesh based wall thickness measurement: identification of left ventricular hypertrophy phenotypes. In: EMBS 2010 (2010) (in press)
[49] Trouvé, A.: Diffeomorphisms groups and pattern matching in image analysis. Int. J. Comput. Vision 28(3), 213–221 (1998)
[50] Twining, C.J., Marsland, S.: Constructing an atlas for the diffeomorphism group of a compact manifold with boundary, with application to the analysis of image registrations. J. Comput. Appl. Math. 222(2), 411–428 (2008)
[51] Vercauteren, T., et al.: Non-parametric diffeomorphic image registration with the demons algorithm. In: Ayache, N., Ourselin, S., Maeder, A. (eds.) MICCAI 2007, Part II. LNCS, vol. 4792, pp. 319–326. Springer, Heidelberg (2007)
[52] Young, A.A., Frangi, A.F.: Computational cardiac atlases: from patient to population and back. Experimental Physiology 94(5), 578–596 (2009)
[53] Zhu, Y., et al.: Segmentation of the left ventricle from cardiac MR images using a subject-specific dynamical model. IEEE Trans. Med. Imag. 29(3), 669–687 (2010)
[54] Zimmerman, V., et al.: Modeling the Purkinje conduction system with a non deterministic rule based iterative method. IEEE Computers in Cardiology 36, 461–464 (2009)

Patient-Specific Modeling of the Heart: Applications to Cardiovascular Disease Management

Razvan Ionasec[1,2], Ingmar Voigt[1,3], Viorel Mihalef[1], Saša Grbić[1,2], Dime Vitanovski[1,3], Yang Wang[1], Yefeng Zheng[1], Joachim Hornegger[3], Nassir Navab[2], Bogdan Georgescu[1], and Dorin Comaniciu[1]

[1] Integrated Data Systems, Siemens Corporate Research, Princeton, USA
[2] Computer Aided Medical Procedures, Technical University Munich, Germany
[3] Pattern Recognition Lab, Friedrich-Alexander-University, Erlangen, Germany

Abstract. As decisions in cardiology increasingly rely on non-invasive methods, fast and precise image analysis tools have become a crucial component of the clinical workflow. Especially when dealing with complex cardiovascular disorders, such as valvular heart disease, advanced imaging techniques have the potential to significantly improve treatment outcome as well as to reduce procedure risks and related costs. We are developing patient-specific cardiac models, estimated from available multi-modal images, to enable advanced clinical applications for the management of cardiovascular disease. In particular, a novel physiological model of the complete heart, including the chambers and valvular apparatus is introduced, which captures a large spectrum of morphological, dynamic and pathological variations. To estimate the patient-specific model parameters from four-dimensional cardiac images, we have developed a robust learning-based framework. The model-driven approach enables a multitude of advanced clinical applications. Gold standard clinical methods, which manually process 2D images, can be replaced with fast, precise, and comprehensive model-based quantification to enhance cardiac analysis. For emerging percutaneous and minimal invasive valve interventions, cardiac surgeons and interventional cardiologists can substantially benefit from automated patient selection and virtual valve implantation techniques. Furthermore, the complete cardiac model enables for patient-specific hemodynamic simulations and blood flow analysis. Extensive experiments demonstrated the potential of these technologies to improve treatment of cardiovascular disease.

1 Introduction

Decisions in cardiovascular disease management increasingly rely on non-invasive imaging, with echocardiography currently regarded as the key evaluation technique. Precise morphological and functional knowledge about the cardiac apparatus is highly appreciated today and considered as a prerequisite for the entire clinical workflow including diagnosis, therapy-planning, surgery or percutaneous intervention as well as patient monitoring and follow-up [1]. Nevertheless,

O. Camara et al. (Eds.): STACOM-CESC 2010, LNCS 6364, pp. 14–24, 2010.

most non-invasive investigations to date are based on two-dimensional images, user-dependent processing and manually performed, potentially inaccurate measurements [2].

The quality of acquired information, as well as the accessibility and cost effectiveness of each medical imaging modality has radically improved over the past decades. Techniques like Transesophageal Echocardiography (TEE), cardiac Computed Tomography (CT) and Cardiovascular Magnetic Resonance (CMR) imaging, enable dynamic four dimensional scanning of a beating heart over the whole cardiac cycle. Such volumetric time-resolved data encode rich structural and dynamic information, which however is barely exploited in clinical practice, due to its size and complexity as well as the lack of appropriate medical systems.

We developed a novel patient-specific modeling framework of the complete heart from multi-modal cardiac images to facilitate the management of cardiovascular disease. Our methodology relies on a physiological model of the cardiac apparatus, which includes an explicit representation of the heart valves, and captures anatomical, dynamical and pathological variations. To extract patient-specific parameters from four-dimensional data, we developed a robust and efficient discriminative learning-based system. The estimation is formulated as a multi-scale problem through which models of increasing complexity are progressively learned. Based on the patient-specific cardiac modeling techniques, we developed applications that support the clinical workflow including: comprehensive quantitative analysis, automated patient selection and risk stratification, therapy simulation for percutaneous procedures, and computational fluid dynamics for blood flow analysis. The developed machine learning algorithms and performed clinical experiments are backed by a large database of medical images acquired with CT, Ultrasound and MRI scanners, from 476 patients affected by a large spectrum of cardiovascular diseases.

2 Physiological Modeling and Parametrization

We developed a comprehensive model of the heart, which includes the chambers (left ventricle, left atrium, right ventricle and right atrium) [3] and the heart valves (aortic, mitral, tricuspid and pulmonary valves) [4,5] to capture a large variety of morphological, functional and pathological variations. A modular and hierarchical approach was used to reduce anatomical complexity and facilitate an effective and flexible estimation of individual anatomies. Our model is anatomically-compliant and maintains a consistent parameterization across the cardiac cycle and different patients by utilizing physiological-driven constraints and sampling schemes.

2.1 Parametrization

The global dynamic variation of each heart chamber and valve is parameterized as a temporal dependent similarity transform, which defines the translation, the quaternion representation of the rotation, the similarity transform scaling factors, and the temporal position in the cardiac cycle. A set of 152 anatomical

landmarks for the heart chambers and 33 for the valves, described in the next paragraph, are used to parameterize the complex and synchronized motion pattern of all heart anatomies. Thereby, each landmark is described by a trajectory in a three dimensional space, normalized by the temporal dependent similarity transform. The final model is completed with a set of 9 dense surface meshes to represent the chambers and an additional set of 13 structures for the valves. Each mesh is sampled along anatomical grids of vertices defined through the landmarks [3,4].

2.2 Anatomical Definition

Left ventricle and atrium: The left ventricle is constructed from 78 landmarks (16 mitral lateral, 15 mitral septum, 16 left ventricle output tract and 32 aortic valve control points) and four surface geometries (LV epicardium, LV endocardium and LV output tract). The left atrial surface is connected to it's ventricle via the aortic valve control points (Fig. 1(a)) [3].

Right ventricle and atrium: The right ventricle is composed of 74 landmarks (16 tricuspid lateral, 15 tricuspid septum, 28 tricuspid valve and 18 pulmonary valve control points) and four surface geometries (RV apex, RV output tract and RV inflow tract). The right atrial surface is constrained by 28 tricuspid valve control points and links to the right ventricle (Fig. 1(b)) [3].

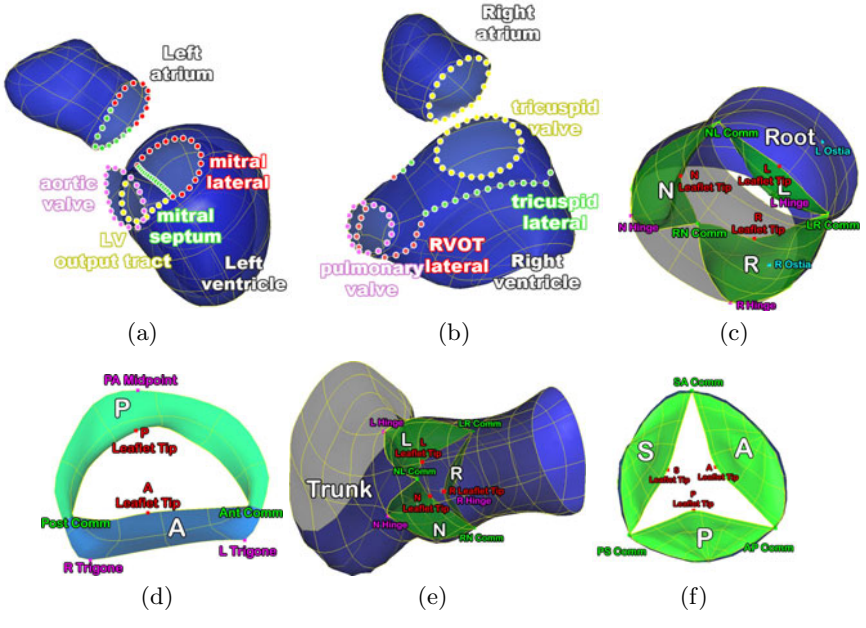

(a) (b) (c)

(d) (e) (f)

Fig. 1. Cardiac model components: (a) the left heart (left ventricle and left atrium), (b) right heart (right ventricle and right atrium), (c) aortic valve, (d) mitral valve, (e) pulmonary valve and (f) tricuspid valve.

Aortic valve: The aortic valve consists of 11 landmarks (3 commissures, 3 hinges, 3 leaflet tips and 2 ostias) and four surface structures (aortic root, N-, L- and R-leaflet). The aortic root is constrained by the hinge and commissure plane and each leaflet is spanned between two commissures and one hinge (Fig. 1(c)) [4].

Mitral valve: The mitral valve is composed of 7 landmarks (3 trigones, 2 commissures and 2 leafleat tips). The anterior leaflet is defined by two trigones, one leaflet tip and two commissures and the posterior leaflet by three trigones, one leaflet tip and one commissure (Fig. 1(d)) [4].

Pulmonary valve: The pulmonary valve is consisting of 9 landmarks (3 commissures, 3 hinges and 3 leaflet tips) and four surface structures (pulmonary root, N-, L- and R-leafet) (Fig. 1(e)) [6].

Tricuspid valve: The tricuspid valve is constructed from four surface geometries (annulus, septal-, anterior- and posterior leaflet) and six anatomical landmarks (three commissures and three leaflet tips) (Fig. 1(f)) [5].

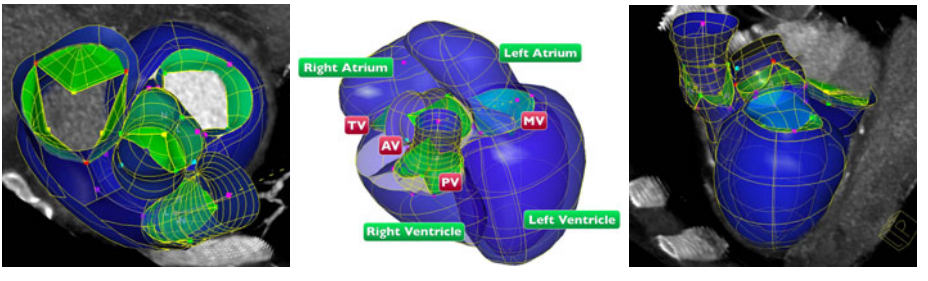

Fig. 2. Examples of personalized model estimated from a multiphase CT sequence.

3 Patient-Specific Parameter Estimation

We developed a robust learning-based framework to estimate the patient-specific parameters of the previously introduced heart model from four-dimensional data. To guarantee robustness against image artifacts and handle the shape and appearance variations encountered in cardiac images, our approach relies on boosting techniques, in particular the Probabilistic Boosting Tree (PBT) [7]. Computation speed is essential to qualify novel technologies for clinical practice. Thus, we developed search space marginalization methods, such as the Marginal Space Learning (MSL) [3] and Trajectory Spectrum Learning (TSL) [8,4], to efficiently perform optimization in multi-dimensional parameter domains.

To handle the problem complexity, the estimation is following a coarse-to-fine strategy based on the natural level of detail of the underlining anatomies. The input data is a temporal sequence of volumetric scans acquired with one of the three modalities: CT, Ultrasound or MRI. The natural first step is to recover the pose and corresponding motion parameters of each model component from the input cardiac data. Through a novel approach, which combines

MSL [3] with RANSAC techniques, we obtained robust and time-coherent object localization [4]. In the second step, the anatomical landmarks' location and motion are simultaneously estimated using the TSL algorithm [8], which employs trajectory-based features and strong trajectory spectrum classifiers. The final stage tackles the boundary delineation of the complete heart surfaces over the entire cardiac cycle. Our method leverages robust boundary detectors together with collaborative trackers and motion manifolds [9].

On average, the precision of the patient-specific estimation is 1.73mm at a speed of 4.8sec per volume for the valvular model and 1.13-1.57mm at a speed of 4.0sec for the chambers. We demonstrated that our automated method is robust with respect to different image modalities and the obtained accuracy is within the inter-user variability.

4 Clinical Applications

In the remainder of this paper we leveraged the patient-specific cardiac model obtained from multiple image modalities to demonstrate a variety of non-invasive analysis procedures, which can lead to reduced therapeutical costs and complication risks, as well as improved treatment outcome.

4.1 Quantitative and Qualitative Analysis

Precise quantification of the anatomy and function is fundamental in the medical management of cardiovascular disease. The clinical gold standard still processes 2D images and performs manual measurements which are tedious to obtain and moreover known to be affected by inaccuracies [2].

We proposed a paradigm shift in the clinical evaluation of the cardiac apparatus, which aims to replace manual analysis based on 2D images with automated model-based quantification from 4D data. The explicit mathematical model is exploited to express a wide-ranging collection of quantitative parameters that support the overall clinical decision making process. In the following we present a selection of clinical experiments.

Valves Analysis: Table 1 presents the system-precision for various dimensions of the aortic-mitral coupling: diameters of the ventricular-arterial junction (VAJ), sinus of valsalva (SV) and sinotubular junction (SJ), aortic valve area (AV area), mitral valve area (MV area), mitral annular circumference (AC) , anteroposterior diameter (APD), anterolateral-posteromedial diameter (AL-PM-D) [4].

Chambers Analysis: The motion pattern of a chamber during a cardiac cycle provides many important clinical measurements of its functionality, e.g., the ventricular ejection fraction, myocardium wall thickness, and dissynchrony within a chamber or between different chambers [3].

The benefits of the proposed model-based analysis are: **Precision** - increased by robust modeling and measuring the natural three-dimensional valve anatomy, **Efficiency** - by automated quantification that outperforms manual measuring

Table 1. Precision for various dimensions of the aortic-mitral coupling along with Bland- Altman plots for the aortic valve area and mitral annular area. The aortic valve experiments were performed on CT data from 36 patients, while the mitral valve was evaluated on TEE data from 10 patients, based on the input of expert cardiologists.

	Mean	STD
VAJ (cm)	0.137	0.017
SV (cm)	0.166	0.043
STJ (cm)	0.098	0.029
AC (cm)	0.846	0.3
APD (cm)	0.325	0.219
AL-PM-D(cm)	0.509	0.37

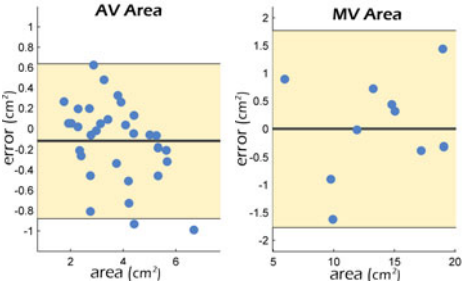

in terms of required analysis time, and **Comprehensiveness** - through analysis that includes four-dimensional information of the morphology and function of the entire cardiac apparatus.

4.2 Computer Aided Diagnosis and Case Retrieval

Clinical decisions are largely based on generic information and rule sets from clinical guidelines and publications, and personal experience of clinicians. Besides investigating the quantitative capabilities of our cardiac models, we also proposed a generic method on how to automatically derive high-level clinical information using learning-based discriminative distance functions [10]. We formulate inference in a comprehensive feature space, which incorporates the complex morphologic and functional information. Generally we address two tasks: retrieval of similar cases using a learned distance function, which measures the similarity of two particular cardiac shapes, and a binary classification problem, based on geometric models and derived features.

For distance learning we considered two techniques, namely learning from equivalence constraints and the intrinsic Random Forest distance. Equivalence constraints are represented using triplets of two model instances' feature vectors

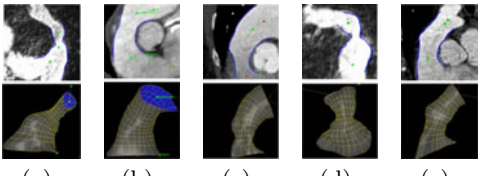

Fig. 3. Types of pulmonary trunk morphologies: (a) pyramidal shape, (b) constant diameter, (c) inverted pyramidal shape, (d) narrowed centrally but wide proximally and distally, (e) wide centrally but narrowed proximally and distally.

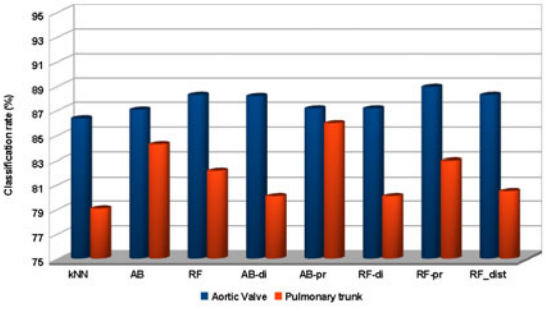

Fig. 4. Classification accuracy for the different learning techniques applied to Aortic Valve Disease classification and PPVI suitability selection.

and a label indicating whether the two instances are similar or dissimilar. Learning from these triplets is often called learning in the product space and demonstrated to be effective for high dimensional data with many correlated, weakly relevant and irrelevant features [10]. The signed margin of models constructed using boosting or Random Forests is used as the required distance function for our experiments with equivalence constraints.

The generic approach enables learning arbitrary user-defined concepts of similarity depending on the application. This is demonstrated with two applications: 1) diagnosis and severity assessment of aortic valves and 2) patient selection for Percutaneous Pulmonary Valve Implantation (PPVI), where classification rates of up to 88.9% and 85.9% could be observed on a set of valve models from 288 and 102 patients respectively (Fig. 4). The morphology of the pulmonary trunk is a major determinant of suitability for PPVI [6]. Intervention in unsuitable patients exposes them to unnecessary invasive catherization. In the classification scheme depicted in Fig. 3 patients from type (a) are considered to be unsuitable for PPVI due to the narrow artery and high probability of device migration. Shape features extracted from the estimated pulmonary trunk are used to learn a discriminative distance function to discriminating anatomies of type (a) from other classes.

4.3 Computational Decision Support for Percutaneous Procedures

Percutaneous approaches are becoming increasingly popular, due to reduced procedural complications and lower follow-up rates [1]. The prosthetic implants are delivered through catheters using transvenous, transarterial or transapical techniques, which obstructs clinicians from a direct view and access to the affected anatomies. Thus, the success of the intervention relies to a large portion on intraoperative images, and the experience and skills of the operator, while a suboptimal deployment location can result in poor hemodynamic performance with severe paravalvular leakages and/or high gradients and suboptimal effective orifice.

We proposed a novel framework for preoperative planning, intraoperative guidance and post-operative assessment of percutaneous aortic valve replacement

Fig. 5. Schematic description of the proposed computational decision support workflow for percutaneous aortic valve implantation.

procedures with stent mounted devices (Fig. 5) [11]. Our model of the aortic valvular complex including aortic valve and aorta ascendens is used to perform an in-silico delivery of the valve implant based on deformable simplex meshes and geometrical constraints. The device is modeled out of the *stent mesh*, which precisely mimics the geometry of the prosthesis and the *computational mesh*, a superimposed 2-simplex mesh, which is used to guide the expansion. The expansion of the device is modeled by balancing external and internal forces as encountered in the actual procedure, using iterative optimization methods Fig. 6). The deformation is described by a finite difference discretization of a second order differential equation. [12].

The predictive power of the model-based in-silico valve replacement was evaluated on 20 patients with pre- and postoperative 3D cardiac CT scans, each by comparing the preoperative prediction result with a ground truth model manually fitted to the real device imaged in the postoperative data (Fig. 5). With an accuracy bellow 2mm at the annular level, we demonstrated the potential of this approach to support preoperative planning by finding the best implant type, size and deployment location and orientation via in-silico implantation under various treatment hypotheses until optimal predicted performance is observed.

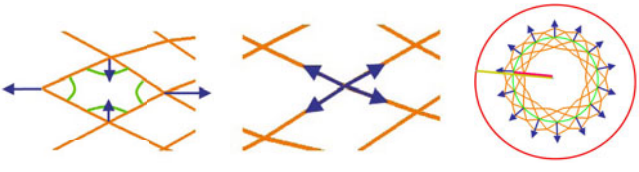

Fig. 6. Forces acting on the model on deployment to converge to the observed geometric properties: (a) f_{angle} enforces the charateristic angles at the strut joints (green), (b) f_{length} maintains the strut lengths. (c) f_{circ} enforces the circumference (green), while f_{ext} dampens and eliminates the all forces acting along the stent mesh normal wheighted by the fraction of distances of strut joint and vessel wall (red) to the stent centroid (magenta/yellow). Please note that (c) shows a short axis cross section of the stent mesh.

4.4 Computational Hemodynamics in the Human Heart

By using the patient-specific cardiac model presented in the previous sections as an input to a 3D Navier-Stokes solver, we derive realistic hemodynamics, constrained by the local anatomy, along the entire heart cycle. This enables us to advance the state-of-the-art in two ways: first, we obtain realistic cardiac blood flow computations for the entire heart, and second, we present a differential assessment of the flow dynamics corresponding to specific heart conditions. The flow computations presented here differ in an essential manner from other works: the realistic patient-specific valve models modulate the blood flow significantly, in accordance to the presence of various cardiac pathologies.

For the computations presented here we essentially enforce a one-way transfer of the heart mesh kinematics to the cardiac blood flow, using the framework presented in [13,14]. The Navier-Stokes equations with viscous terms are solved in a level set formulation, using a fractional step combined with an approximate projection method for the pressure. The equations are discretized on a uniform grid, using finite difference and finite volume techniques. The heart mesh is immersed in the computational domain with the help of a level set function that effectively "thickens" the original triangle mesh by the grid spacing. The interface location is used to impose no-slip boundary conditions to the fluid region. The mesh velocity, which is known at each time step, is extrapolated to the interfacial nodes using extrapolation kernels.

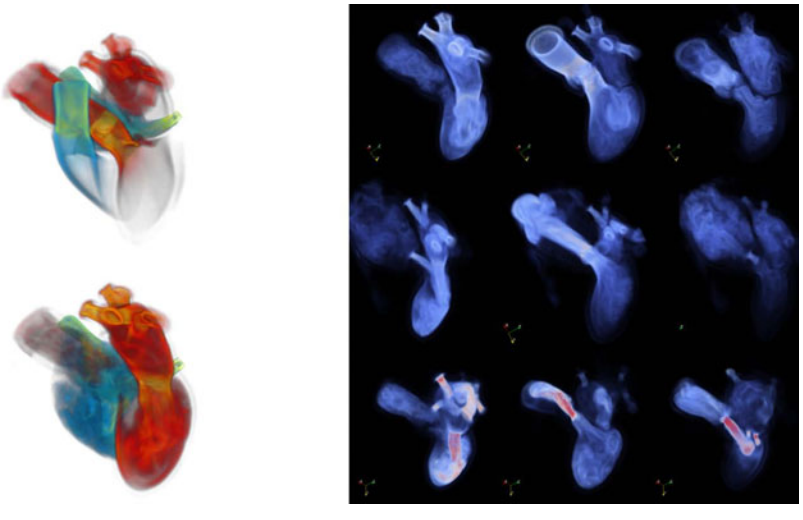

Fig. 7. Left images: visualization of the blood flow vorticity magnitude for whole heart during systole (top) and diastole (bottom). Right images: comparison of diseased hearts. Top: normal heart; Middle: heart with dilated aorta; Bottom: heart with bicuspid valve. First column: peak diastole; Second column: peak systole; Third column: end systole.

The blood flow computations inside both the left and right sides of the heart [14] produced flow curve data qualitatively similar to the flow curves presented in the literature. Very interesting was the comparison of the results of the diseased hearts with the normal one (Fig. 7) [13]. The normal heart displayed strong systolic and diastolic fluxes, with blood jets directed toward the center of the aorta, respectively the center of the left ventricle. The two diseased hearts - one with a dilated aortic root and one with a bicuspid aortic valve - displayed quite different flow characteristics. For the heart with a heavily enlarged aorta the aortic valve never closed, leading to massive aortic regurgitation during diastole and a systolic flow directed straight toward the abnormally enlarged region of the aorta. The bicuspid aortic valve also produced a very strong regurgitation at the beginning of the diastole toward the left ventricle, while a sclerotic mitral valve directed the diastolic jet straight toward the posterior ventricular wall.

The flow computations we performed underline the importance of the patient-specific cardiac geometry and especially of the valve apparatus in determining the hemodynamic characteristics. Our first validation efforts for hemodynamics computations [14], which qualitatively compare the flow curves with measured ultrasound ones, will be augmented with direct comparisons of velocity fields determined using phase-contrast MRI.

5 Conclusion

We described our comprehensive heart model, which includes an explicit representation of the valvular apparatus, and parameterizes morphological, functional and pathological variations of the cardiac apparatus. Subsequently, we presented a robust and efficient learning-based framework to estimate patient-specific model parameters from multi-modal cardiac images. Based on several clinical applications, we demonstrated the relevance of the developed technologies to advance the management of cardiovascular disease. Nevertheless, extensions of the model to include tissue and other biomechanical properties, and further anatomical details, such as papillary muscles, chordae tendineae and trabeculations are necessary future developments.

References

1. Otto, C., Bonow, R.O.: Valvular Heart Disease: A Companion to Braunwald's Heart Disease. Saunders (2009)
2. Bonow, R.O., Carabello, B.A., Chatterjee, K., de Leon, A.C.J., Faxon, D.P., Freed, M.D., Gaasch, W.H., Lytle, B.W., Nishimura, R.A., O'Gara, P.T., O'Rourke, R.A., Otto, C.M., Shah, P.M., Shanewise, J.S.: Acc/aha 2006 guidelines for the management of patients with valvular heart disease: a report of the american college of cardiology/american heart association task force on practice guidelines (writing committee to develop guidelines for the management of patients with valvular heart disease). Circulation 114(5), 84–231 (2006)

3. Zheng, Y., Georgescu, B., Barbu, A., Scheuering, M., Comaniciu, D.: Four-chamber heart modeling and automatic segmentation for 3D cardiac CT volumes using marginal space learning and steerable features. IEEE Transactions on Medical Imaging 27(11), 1668–1681 (2008)
4. Ionasec, R.I., Voigt, I., Georgescu, B., Wang, Y., Houle, H., Vega-Higuera, F., Navab, N., Comaniciu, D.: Patient-specific modeling and quantification of the aortic and mitral valves from 4D cardiac CT and TEE. IEEE Transactions on Medical Imaging (2010) (in press)
5. Grbic, S., Ionasec, R.I., Vitanovski, D., Voigt, I., Wang, Y., Georgescu, B., Navab, N., Comaniciu, D.: Complete valvular heart apparatus model from 4D cardiac CT. In: Proceedings of MICCAI (2010)
6. Vitanovski, D., Ionasec, R., Georgescu, B., Huber, M., Taylor, A., Hornegger, J., Comaniciu, D.: Personalized pulmonary trunk modeling for intervention planning and valve assessment estimated from CT data. In: Yang, G.-Z., Hawkes, D., Rueckert, D., Noble, A., Taylor, C. (eds.) MICCAI 2009. LNCS, vol. 5761, pp. 17–25. Springer, Heidelberg (2009)
7. Tu, Z.: Probabilistic boosting-tree: Learning discriminative methods for classification, recognition, and clustering. In: International Conference on Computer Vision, pp. 1589–1596 (2005)
8. Ionasec, R.I., Wang, Y., Georgescu, B., Voigt, I., Navab, N., Comaniciu, D.: Robust Motion Estimation Using Trajectory Spectrum Learning: Application to Aortic and Mitral Valve Modeling from 4D TEE. In: Society, I.C. (ed.) Proceedings of 12th IEEE International Conference on Computer Vision 2009, pp. 1601–1608 (2009)
9. Yang, L., Georgescu, B., Zheng, Y., Meer, P., Comaniciu, D.: 3d ultrasound tracking of the left ventricle using one-step forward prediction and data fusion of collaborative trackers. In: IEEE Conference on Computer Vision and Pattern Recognition (2008)
10. Voigt, I., Vitanovski, D., Ionasec, R.I., Tsymbal, A., Georgescu, B., Zhou, S.K., Navab, N., Hornegger, J., Comaniciu, D.: Learning discriminative distance functions for valve retrieval and improved decision support in valvular heart disease. In: Proceedings of SPIE Medical Imaging (2010)
11. Voigt, I., Ionasec, R.I., Georgescu, B., Boese, J., Brockmann, G., Hornegger, J., Comaniciu, D.: Computational Decision Support for Percutaneous Aortic Valve Implantation. In: Proceedings of the 5th International Workshop on Medical Imaging and Augmented Reality (2010)
12. Larrabide, I., Radaelli, A., Frangi, A.F.: Fast virtual stenting with deformable meshes: Application to intracranial aneurysms. In: Metaxas, D., Axel, L., Fichtinger, G., Székely, G. (eds.) MICCAI 2008, Part II. LNCS, vol. 5242, pp. 790–797. Springer, Heidelberg (2008)
13. Mihalef, V., Ionasec, R., Wang, Y., Zheng, Y., Georgescu, B., Comaniciu, D.: Patient-specific modeling of left heart anatomy, dynamics and hemodynamics from high resolution 4D CT. In: Proceedings of ISBI (2010)
14. Mihalef, V., Ionasec, R., Sharma, P., Georgescu, B., Huber, M., Comaniciu, D.: Patient-specific modeling of whole heart anatomy, dynamics and hemodynamics from 4D cardiac CT images. In: Proceedings of VPH (2010) (to appear)

The Generation of Patient-Specific Heart Models for Diagnosis and Interventions

Jürgen Weese[1], Jochen Peters[1], Carsten Meyer[1], Irina Wächter[1], Reinhard Kneser[1], Helko Lehmann[1], Olivier Ecabert[1], Hans Barschdorf[2], Raghed Hanna[3], Frank M. Weber[3], Olaf Dössel[3], and Cristian Lorenz[2]

[1] Philips Research Aachen, Weisshausstrasse 2, 52066 Aachen
[2] Philips Research Hamburg, Roengtenstrasse 24, 22335 Hamburg
[3] Karlsruhe Institute of Technology, Institute of Biomedical Engineering, Kaiserstrasse 12, 76128 Karlsruhe

Abstract. A framework for the automatic extraction and generation of patient-specific organ models from different image modalities is presented. These models can be used to extract and represent diagnostic information about the heart and its function. Furthermore, the models can be used for treatment planning and an overlay of the models onto X-ray fluoroscopy images can support navigation when performing an intervention in the CathLab.

1 Introduction

Today's imaging devices such as computed tomography (CT) and magnetic resonance (MR) scanners provide an enormous amount of high-quality images with high resolution in space and time. From these images a wealth of patient-specific information can be obtained that is both diagnostically and therapeutically relevant. For example, for a patient with ischemia and infarction induced by coronary-artery stenosis, information about the heart function, myocardial perfusion and scar tissue can be derived from imaging studies. With the additional information, the therapy can then become more targeted and better adapted to the patient's individual needs and risks. The provision of the patient-specific information during the actual treatment is also beneficial. This applies in particular to interventional procedures in the catheterization laboratory (CathLab) since the anatomical details of the heart are not clearly visible with X-ray imaging.

Even though critical anatomical information is contained in these high resolution CT and MR images, sophisticated image processing techniques are needed to extract the information to make them readily available to benefit routine clinical use. Numerous methods have been developed for this purpose [1]. Time consuming manual approaches pose a serious hurdle in routine clinical practice and the need for an efficient clinical workflow drives the development of automated methods. Also, a suitable representation is needed that allows, for instance, integration of complementary information from different scans as well as the intuitive display of the information during an intervention. We propose to generate a digital patient-specific heart model and integrate all the required information into this model. While the model represents the relevant aspects of the patient's anatomy and associated function, it is independent of

O. Camara et al. (Eds.): STACOM-CESC 2010, LNCS 6364, pp. 25 – 35, 2010.

the actual imaging protocols and modality. To generate the patient-specific heart model, we match a generic heart model to 3-D images of the patient [2]. While previous approaches have been tailored to specific imaging techniques, our framework can be applied across a wide variety of imaging protocols and modalities. This is achieved by separating knowledge about the organ shape from knowledge about image appearance and algorithmic considerations. In this paper, we investigate the generality and portability of our technology by applying it to three different image analysis tasks, 1) the adaptation of a whole heart model with attached major vascular structures to contrast-enhanced CT data, 2) the adaptation of a whole heart model to non-contrast-enhanced MR data, and 3) the adaptation of an accurate model of the aortic valve to contrast-enhanced CT data.

Furthermore, we illustrate the use of our technology for diagnostic and interventional applications. By segmenting time-series of CT images, we can assess the volumes of all four heart chambers over time and provide information about local wall motion. For the guidance of ablation procedures for atrial fibrillation, models of the left atrium and pulmonary veins can be generated from CT, MR and rotational X-ray and used for interventional guidance. Finally, application of the aortic valve model for the guidance of percutaneous aortic valve treatment is outlined.

2 Generation of Patient-Specific Organ Models

As mentioned in the introduction, we generate patient-specific models by adapting generic models to images of a patient. Fig. 1 shows the overall architecture of our framework. The central component of this architecture is a generic organ model, to which a wealth of information can be attached. This generic organ model describes the organ shape, its variability and its appearance for an imaging modality or protocol. The framework separates knowledge about the organ shape from knowledge about

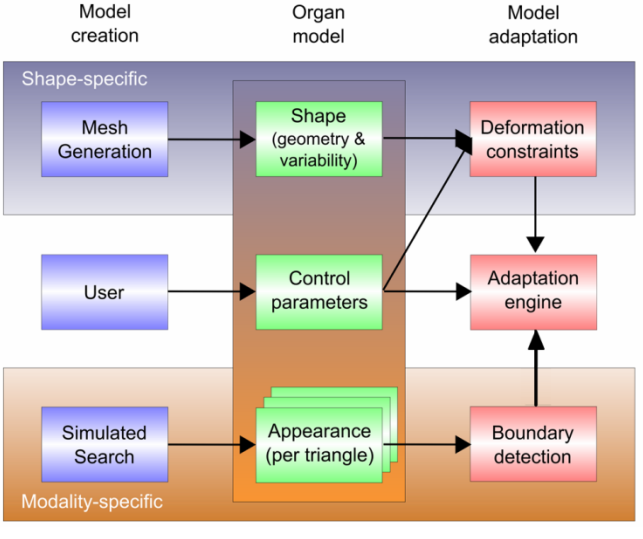

Fig. 1. Diagram illustrating the architecture of our framework for the automatic generation of personalized organ models

image appearance, which facilitates adaptation to new imaging modalities or protocols. In addition, the generic model includes information that controls the sequence and parameters of the steps for model adaptation.

2.1 Generic Model Shape and Variability

To create the generic model shape a representative image is selected and the organ of interest is manually annotated, i.e. each voxel of the image is assigned a label corresponding to the anatomical part of the organ. Based on the annotation a multi-compartment triangular surface mesh is generated. Once annotations of multiple images based on the same mesh topology are available the mean shape of the organ can be generated. For complex models, meshes may also be generated for individual parts and fused in a second step.

Fig. 2 shows the models used in the following sections. The whole heart model comprises the endocardial surfaces of both ventricles and both atria, the epicardial surface of the left ventricular myocardium and the trunks of the great vessels (aorta, pulmonary artery and pulmonary veins). This model has been extended and the major vascular structures (aorta, pulmonary veins, coronary sinus, inferior vena cava, superior vena cava) have been added. The model of the left atrium and pulmonary veins represents a part of this model. The last model represents the detailed anatomy of the aortic valve.

For model adaptation, a parametric model of shape variability is beneficial. We assign for that purpose separate linear transformations (e.g. rigid with scaling, affine) to suitable anatomic sub-regions. To ensure smooth connections between the sub-regions, we linearly interpolate the individual transformations in pre-defined transition regions. For the whole heart model, this description of shape variability turned out to be better than statistical shape models derived from principal component analysis [2]. At the same time, this description can be used to model bending and diameter variations of vascular structures [3].

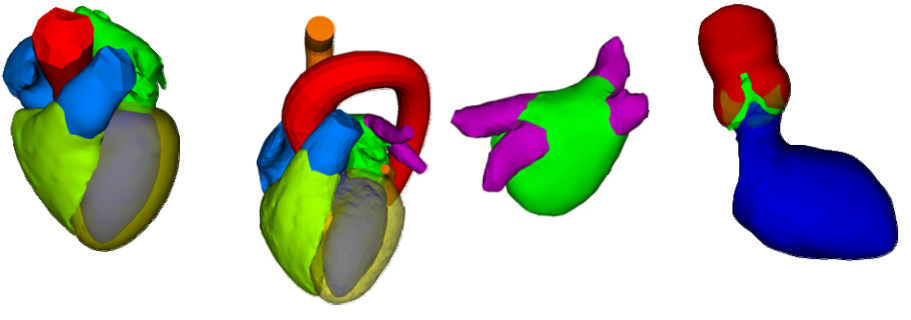

Fig. 2. Whole heart model, whole heart model with major attached vascular structures, model of the left atrium and pulmonary veins, and aortic valve model (from left to right).

2.2 Appearance Model

During model adaptation, the boundaries of the target organ must be detected in the image. Boundary detection is supported by appearance information that is learned

from a set of annotated reference images and corresponding meshes. During a training phase, the images and meshes are used in a first step to create a large number (500 – 10,000) of boundary detection functions which use gradient information and gray value information on one or both sides of the mesh. For gray-value calibration, also information about global gray-value statistics can be used [4]. In a second step, "Simulated Search" assigns an optimal boundary detection function to each triangle [5]. The selection process works as follows for each triangle independently:

1. The pose of the triangles in the reference meshes is slightly disturbed.
2. The boundary detection process using the given boundary detection function is performed.
3. The residual error between the detected point and the reference position is recorded for all tested displacements and all functions candidates.
4. The candidate with the smallest simulated residual error is finally selected

We create the annotated images and corresponding meshes by the following approach. In a first step the mesh is adapted to very few (1-3) manually annotated images. The resulting reference meshes are sufficient to train a first set of boundary detection functions by "Simulated Search". This initial model is then adapted to a larger set of images and the result is thoroughly refined, e.g. by a clinical expert. With the new reference images and meshes, we train a second set of boundary detection functions. The process of automatic adaptation, manual refinement, training of new boundary detection functions is continued until sufficient reference images and meshes are available.

2.3 Adaptation Control

Automatic adaptation of the generic shape model to an image is typically achieved in several steps [2]. Firstly, we use the generalized Hough transform (GHT) to roughly localize the organ in the image and adapt the size. Secondly, the location, orientation and scaling are refined. To this end, boundary detection is performed for each mesh triangle and the parameters of the similarity transformation are modified to minimize the sum of squared distances between the mesh triangles and the detected boundary points. Boundary detection and parameter refinement are iterated until no major changes are observed. Thirdly, the parameters of the combined linear transformations that characterize the shape variability (Section 2.1) are adapted by iterating boundary detection and parameter refinement. Finally, a deformable adaptation is performed. Again boundary detection and mesh refinement are iterated until convergence. In this phase, the locations of all mesh vertices are optimized during mesh refinement until a balance is reached between the geometric constraints defined by the generic shape model and the forces attracting the mesh to the detected boundary points. The process of model adaptation can be modified in various ways. To speed up model adaptation, the adaptation process described above may be done with a low resolution mesh model and a final deformable adaptation step with a high resolution mesh model may be added. Reliable adaptation of vascular structure can, for instance, be achieved by adapting the four heart chambers first and successively activating the tubular segments representing the vascular structures. The information about the adaptation steps that are actually carried out, the mesh resolution or other parameters related to the

different steps as well as information about the adaptation order of different model parts is contained in a control file of the generic organ model.

2.4 Examples

Generation of a generic organ model for a specific imaging modality or protocol requires experience and time. Once available, adaptation to an image and generation of a patient-specific model is normally fully automatic and requires about 10-15s on a standard state-of-the-art workstation. We show results for three examples. First, we show results for the whole heart model with the major attached vascular structures. 35 Computed Tomography Angiography (CTA) data sets from 20 patients (reconstructed at various cardiac phases) were used for building the generic model, while 37 additional data sets from 17 patients have been used for testing model adaptation. Second, we present results for the whole heart model and adaptation to MR images. Here, we used 42 steady-state free-precession MR end-diastolic breathing compensated "whole heart" images, acquired to inspect the coronary arteries. Third, we show results for the aortic valve model based on 16 CTA data sets acquired with scanners from different manufacturers.

The accuracy of model adaptation is assessed by measuring the symmetrized mean Euclidean "surface-to-patch" distance, i.e., the mean distance between the triangle centers of the adapted mesh to an anatomically corresponding patch of maximum geodesic radius r = 10 mm of the "ground truth" reference mesh and vice versa. This distance is averaged over triangles and test images. For the whole heart model with major vascular structures, the distal parts of the coronary sinus and inferior vena cava are excluded. These structures are not contrasted in many images and no "ground truth" could be defined. Furthermore, the triangle positions near the artificial cut planes of the truncated vessels in the whole heart models are excluded from the error measurement, since the cut planes do not relate to actual anatomy. For the aortic valve model only the mesh elements representing the aortic bulbus, the aortic valve, and the outflow tract have been evaluated. For whole heart adaptation to MR images and aortic valve adaptation to CT images, we used the same data sets for training the generic model and model adaptation. To avoid a bias we used a cross-validation approach. We divided the MR images into four clusters of 10/11 images, used 3 clusters for training, 1 cluster for accuracy measurements, and repeated this process for the four clusters. On the CT data, we used a leaving-one-out approach, i.e., we trained the model on all images except the one for testing and repeated this for all images.

Table 1. Accuracy of model adaptation for three examples

Model/Modality	ε_{mean} (mm)
Whole Heart & major vascular structures / CT	0.67
Whole Heart / MR	0.76
Aortic Valve / CT	0.47

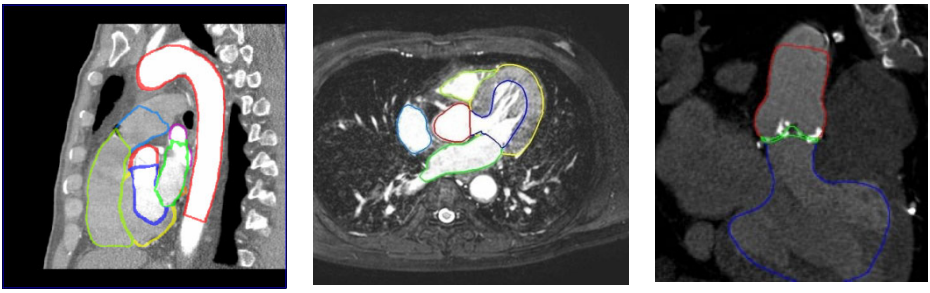

Fig. 3. Typical results of model adaptation for the whole heart with major vascular structures in CT, the whole heart in MR and the aortic valve model in CT (left to right).

Fig. 3 shows typical results and allows visual comparison of the contours of the adapted model with the image structures. Numerical accuracies of model adaptation are between 0.5-0.8mm (see Tab. 1).

2.5 Framework Extensions

The heart models as shown in Fig. 2 are of fixed vascular topology. For the left atrium (LA), the standard case of two by two pulmonary veins (PV) on left and right side is modeled, which represents about 68% of patients [5]. The remaining 32% have three, four, or sometimes five PVs at the right side of the left atrium. To cover these cases, respective LA variant models have been created, that can be attached to the rest of the whole heart model in a modular way. For the selection of the patient specific variant, a hybrid method has been developed, combining model based with a guided region growing based approach. First, a simplified LA model with no right PVs at all, is adapted to the patient. For the subsequent region growing, the simplified model carries marked triangles from which a seed point and a cone-like grow-restriction is defined to prevent leakage. The region growing is prioritized with the seed distance, leading to a spherical grow front. The front splits in case of bifurcations, which is used to detect position and number of PV ostia. Based on this information, the anatomical variant of the patient can be determined and the proper LA variant model can be selected, positioned and adapted to the patient. The procedure is outlined in Fig. 4.

3 Diagnostic and Interventional Applications

On the one hand, patient-specific heart models can be used to extract and represent diagnostic information. This is illustrated for the characterization of the heart function from cardiac CTA images. On the other hand, interventions can be supported by generating models for the specific application and visualizing them in combination with X-ray images in the CathLab.

3.1 Heart Function from CTA

Once, a patient-specific heart model has been derived from an image with sufficient accuracy, volume measurements of the heart chambers are straight forward. Applying

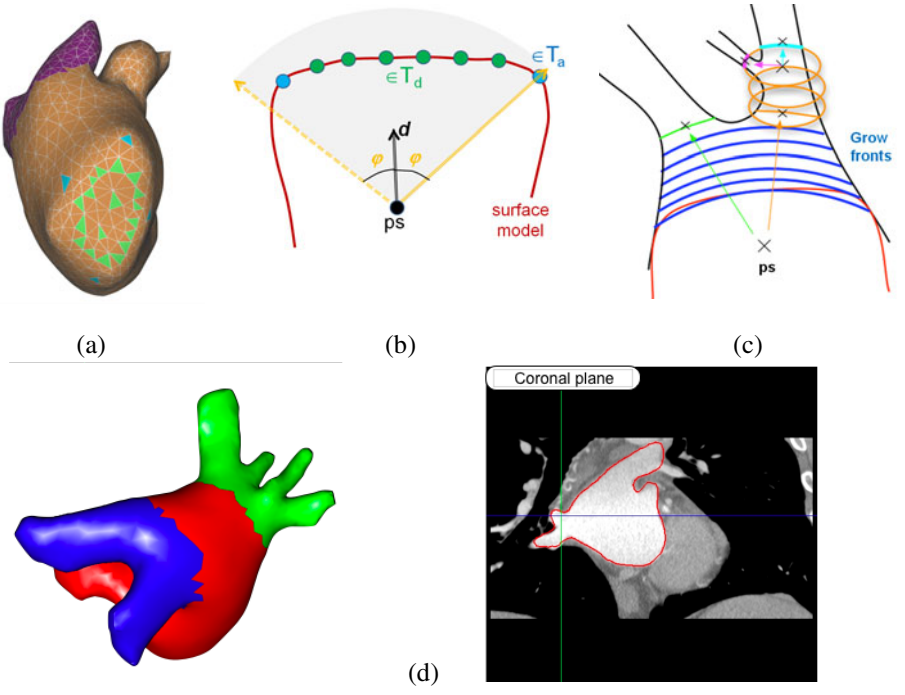

Fig. 4. (a) Simplified triangulated surface model of the left atrium without right pulmonary veins. Marked triangles allow set-up of the region grower. (b) Definition of the seed point and cone-like grow restriction. (c) Detection of the right pulmonary vein ostia. (d) Results for a patient case with 4 pulmonary veins at the right side of the LA.

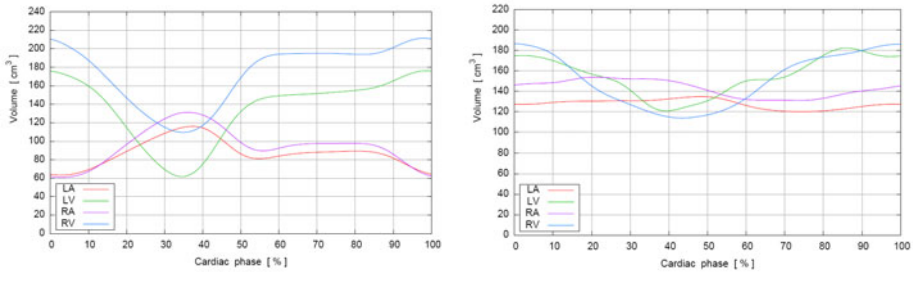

Fig. 5. Volume of the four heart chambers over the heart beat for a patient with a slowly beating heart (53bpm, left) and a patient with an irregularly beating heart (> 80bpm) and small ejection fraction (right).

the method to images of different heart phases enables, therefore, the automatic characterization of global heart function (see Fig. 5). This is confirmed by initial clinical investigations for cardiac CTA [5][8], where our method has been compared to three manual and semi-automatic tools for the assessment of left ventricular volumes and

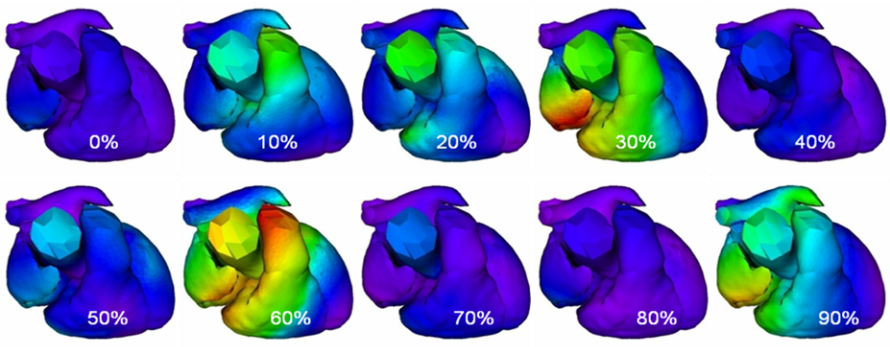

Fig. 6. Velocities over time mapped on a static personalized heart model of a patient for phases at 10% intervals of the heart beat (purple = 0.0, red = 1.5mm/%RR)

related measures. A further clinical study [9] evaluates the use of our method for the assessment of four-chamber cardiac function.

With slight modifications [10] that enhance the consistency of heart model adaptation over the cardiac cycle, the method can also derive information about local heart wall motion from retrospectively gated cardiac CTA images. For that purpose, images have been reconstructed with phase increments of 2% of the RR interval using a gating window width of approximately 15%, an image resolution in the axial plane of 0.86 mm and a slice thickness of 2mm. Fig. 6 shows an example where the local surface velocities have been mapped onto the patient-specific heart model for different heart phases. This information may, for instance, support CT-based asynchrony assessment.

3.2 Atrial Fibrillation Treatment

For patients with recurrent atrial fibrillation radiofrequency ablation has proven to be an effective treatment. Thereby abnormal electrical pathways, in particular those originating from the pulmonary veins, are destroyed using a radiofrequency energy emitting probe. The probe is positioned with the help of a catheter at different sites on the left atrial wall under fluoroscopy guidance. Accurate probe placement is, however, difficult since the atrial wall is hardly visible in X-ray fluoroscopy images. To improve probe placement and support the generation of a continuous line of ablation points, a patient-specific model of the left atrium can be geometrically aligned with the fluoroscopy images and displayed e.g. as an image overlay [11] (Fig. 7, extreme right).

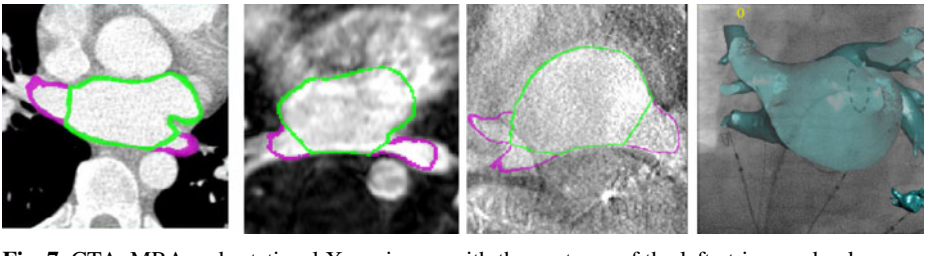

Fig. 7. CTA, MRA and rotational X-ray image with the anatomy of the left atrium and pulmonary veins outlined and an overlay of a patient-specific LAPV model onto fluoroscopy data (left to right)

The patient-specific model may be generated from pre-interventional CTA or MRA images. Recently, we also developed an approach to derive a patient-specific model of the left atrium and pulmonary veins by a rotational X-ray imaging technique during the intervention [12] (Fig. 7).

3.3 Percutaneous Aortic Valve Therapy

Conventional treatment of patients with dysfunctional aortic valves is a highly invasive procedure involving considerable mortality and morbidity risks. To enable treatment of fragile patients, who currently remain largely untreated, new minimally invasive procedures are developed that are carried out under X-ray guidance in the CathLab. During such a procedure, a compressed tissue heart valve is inserted through the femoral artery, positioned over the diseased aortic valve, unfolded and fixed by inflating a balloon. As in the case of radiofrequency ablation for the treatment of atrial fibrillation, the procedure is complicated by the fact that the heart anatomy itself is not clearly visible in the X-ray images.

A patient-specific heart model for this application could accurately model the aortic bulbus, the aortic valve, the outflow tract, the left ventricle and the coronary ostia. Accurate valve placement may then be supported by overlaying the properly aligned model onto X-ray fluoroscopy images (Fig. 8).

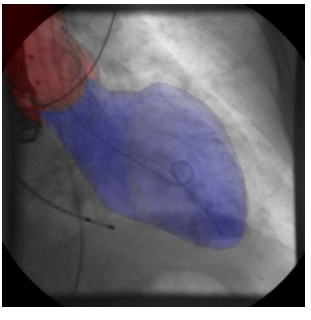

Fig. 8. Overlay of a patient-specific aortic valve model onto an X-ray fluoroscopy image

4 Conclusion and Outlook

A framework for the automatic extraction and generation of patient-specific organ models from different image modalities has been presented. These models can be used to extract and represent diagnostic information about the heart and its function. Furthermore, the models can be used for treatment planning and an overlay of the models onto X-ray fluoroscopy images can support navigation when performing an intervention in the CathLab. In the future, the technology will be extended to other imaging modalities such as ultrasound and complemented by methods for the integration of information from different imaging studies into a single model. The integration of information about scar tissue into a patient-specific heart model illustrates the first step in this direction [13]. Within the EU-funded euHeart project [14], use of the models for biophysical and physiologic simulations that predict the patient's heart function is also being investigated.

Acknowledgment

We thank Philips Healthcare CT and Philips Healthcare CV X-Ray for supporting the development of the cardiac models. For help developing the aortic valve model and the supply of imaging data we thank R. Hoffmann and H. Kühl of the Medical Clinic I, University Hospital of the RWTH Aachen and M. Kelm, J. Balzer and M. Neizel of the Department of Cardiology, Pneumology and Angiology at the Düsseldorf University Hospital.

References

[1] Frangi, A.F., Niessen, W.J., Viergever, M.A.: Three-Dimensional Modeling for Functional Analysis of Cardiac Images: A Review. IEEE Transactions on Medical Imaging 20(1), 2–25 (2001)

[2] Ecabert, O., Peters, J., Schramm, H., Lorenz, C., von Berg, J., Walker, M.J., Vembar, M., Olszewski, M.E., Subramanyan, K., Lavi, G., Weese, J.: Automatic model-based segmentation of the heart in CT images. IEEE Transactions on Medical Imaging 27(9), 1189–1201 (2008)

[3] Peters, J., Ecabert, O., Lorenz, C., von Berg, J., Walker, M.J., Ivanc, T.B., Vembar, M., Olszewski, M.E., Weese, J.: Segmentation of the heart and major vascular structures in cardiovascular CT images. In: Proc. SPIE Medical Imaging, vol. 6914, p. 691417. SPIE, San Jose (2008)

[4] Peters, J., Ecabert, O., Meyer, C., Schramm, H., Kneser, R., Groth, A., Weese, J.: Automatic whole heart segmentation in static magnetic resonance image volumes. In: Ayache, N., Ourselin, S., Maeder, A. (eds.) MICCAI 2007, Part II. LNCS, vol. 4792, pp. 402–410. Springer, Heidelberg (2007)

[5] Peters, J., Ecabert, O., Meyer, C., Kneser, R., Weese, J.: Optimizing boundary detection via Simulated Search with applications to multi-modal heart segmentation. Medical Image Analysis 14, 70–84 (2010)

[6] Marom, E., Herndon, J., Kim, Y., McAdams, H.: Variations in pulmonary venous drainage to the left atrium: implications for radiofrequency ablation. Radiology 230, 824–829 (2004)

[7] Abadi, S., Roguin, A., Engel, A., Lessick, J.: Feasibility of automatic assessment of four-chamber cardiac function with MDCT: Initial clinical application and validation. European Journal of Radiology 74(1), 175–181 (2010)

[8] Plumhans, C., Keil, S., Ocklenburg, C., Mühlenbruch, G., Behrendt, F.F., Günther, R.W., Mahnken, A.H.: Comparison of manual, semi- and fully automated heart segmentation for assessing global left ventricular function in Multidetector Computed Tomography. Investigative Radiology 44, 476–482 (2009)

[9] Ghersin, E., Abadi, A., Yalonetsky, S., Engel, A., Lessick, J.: Clinical evaluation of a fully automated model-based algorithm to calculate left ventricular volumes and ejection fraction using multidetector computed tomography. Acute Cardiac Care 11(1), 43–51 (2009)

[10] Peters, J., Ecabert, O., Schmitt, H., Grass, M., Weese, J.: Local cardiac wall motion estimation from retrospectively gated CT images. In: Ayache, N., Delingette, H., Sermesant, M. (eds.) FIMH 2009. LNCS, vol. 5528, pp. 191–200. Springer, Heidelberg (2009)

[11] King, A.P., Boubertakh, R., Rhode, K.S., Ma, Y.L., Chinchapatnam, P., Gao, G., Tangcharoen, T., Ginks, M., Cooklin, M., Gill, J.S., Hawkes, D.J., Razavi, R.S., Schaeffter, T.: A subject-specific technique for respiratory motion correction in image-guided cardiac catheterisation procedures. Medical Image Analysis 13(3), 419–431 (2009)

[12] Manzke, R., Meyer, C., Ecabert, O., Peters, J., Noordhoek, N.J., Thiagalingam, A., Reddy, V.Y., Chan, R.C., Weese, J.: Automatic Segmentation of Rotational X-Ray Images for Anatomic Intra-Procedural Surface Generation in Atrial Fibrillation Ablation Procedures. IEEE Transactions on Medical Imaging 29(2), 260–272 (2010)
[13] Lehmann, H., Kneser, R., Neizel, M., Peters, J., Ecabert, O., Kühl, H., Kelm, M., Weese, J.: Integrating Viability Information into a Cardiac Model for Interventional Guidance. In: Ayache, N., Delingette, H., Sermesant, M. (eds.) FIMH 2009. LNCS, vol. 5528, pp. 312–320. Springer, Heidelberg (2009)
[14] Ecabert, O., Smith, N.: euHeart: Integrated cardiac care using patient-specific cardiovascular modeling. In: SPIE Newsroom (2008); doi:10.1117/2.1200804.1126

The Cardiac Atlas Project: Rationale, Design and Procedures

Carissa G. Fonseca[1], Michael Backhaus[2], Jae Do Chung[2], Wenchao Tao[1], Pau Medrano-Gracia[2], Brett R Cowan[2], Peter J Hunter[2], J Paul Finn[1], Kalyanam Shivkumar[3], Joao AC Lima[4], David A Bluemke[4], Alan H Kadish[5], Daniel C Lee[5], and Alistair A Young[2]

[1] Diagnostic CardioVascular Imaging, UCLA,
Suite 3371, 10945 Le Conte Avenue, Los Angeles, CA 90095-7206, USA
{cfonseca,wtao,pfinn}@mednet.ucla.edu
[2] Auckland Bioengineering Institute, University of Auckland,
Private Bag 92019, Auckland 1142, New Zealand
{m.backhaus,jaedo.chung,p.medrano,b.cowan}@auckland.ac.nz
{p.hunter,a.young}@auckland.ac.nz
[3] UCLA Cardiac Arrhythmia Center,
BH-307 CHS, 10833 Le Conte Avenue, Los Angeles, CA 90095, USA
kshivkumar@mednet.ucla.edu
[4] Department of Radiology, Johns Hopkins Hospital,
600 N Wolfe Street, Baltimore, MD 21287, USA
{jlima,dbluemke}@jhmi.edu
[5] Bluhm Cardiovascular Institute, Northwestern Memorial Institute
251 E. Huron Street, Feinberg Pavilion 8-536, Chicago, IL 60611, USA
{a-kadish,dlee}@northwestern.edu

Abstract. The Cardiac Atlas Project (CAP) is a NIH sponsored international collaboration to establish a web-accessible structural and functional atlas of the normal and pathological heart as a resource for the clinical, research and educational communities. An initial goal of the atlas is to facilitate statistical analysis of regional heart shape and wall motion characteristics, and characterization of remodeling, between and within population groups. The two main early contributing studies are the Multi Ethnic Study of Atherosclerosis (MESA) and the Defibrillators to Reduce Risk by Magnetic Resonance Imaging Evaluation (DETERMINE) clinical trial. De-identified image and text data from 2864 asymptomatic volunteers from MESA, and 470 myocardial infarction cases from DETERMINE, are currently available in the CAP database. DICOM images were de-identified using HIPAA compliant software based on tools provided by the Center for Computational Biology at UCLA. Only those cases with informed consent and IRB approval compatible with the CAP were included. Researchers requesting permission to access CAP data can apply through the CAP website (www.cardiacatlas.org). All proposals for data access must be approved by the data contributors, and applicants must sign a data transfer agreement with each study from which data is requested. Software to visualize cardiac images and create 3D mathematical models, developed in the CAP, is available open-source from the website.

Keywords: Computational Atlas, Database, Cardiac, Mapping.

O. Camara et al. (Eds.): STACOM-CESC 2010, LNCS 6364, pp. 36 – 45, 2010.

1 Introduction

Cardiac performance in health and disease is defined across multiple levels of structure and function from molecular and cellular organization to gross anatomy, and can be studied using a diversity of both imaging techniques (MRI, CT, echocardiography, coronary angiography) and non-imaging tools (ECG, blood pressure and cholesterol measurements). Mathematical and computer models can be used to integrate data on various aspects of cardiac performance, obtained from a variety of sources, in a standardized way. This approach provides an invaluable, highly detailed and dynamic map of the heart that clinicians can use to characterize a particular patient's function against the range of functional characteristics derived from large populations of patients, with the objective of allowing more precise evaluation of disease and targeting of therapies.

Computational modeling techniques are already being applied in various biomedical projects around the globe, including the Physiome Project [1] which describes whole-body physiology, the International Consortium for Brain Mapping (ICBM) [2], Informatics for Integrating Biology and the Bedside (i2b2) [3], and the Integrative Biology Project [4], to name a few. The Center for Computational Biology (CCB) [5] at UCLA, which hosts the ICBM, provides a number of infrastructural and middleware tools, mainly in the area of brain mapping. In the cardiac domain, the Cardiovascular Research Grid (CVRG) at Johns Hopkins University [6] provides grid computing infrastructure for cardiac research, inspired by the Cancer Bioinformatic Grid (caBIG) [7] and the Biomedical Informatics Research network (BIRN) [8].

The Cardiac Atlas Project (CAP) is a NIH sponsored, international, multi-institutional endeavor which aims to facilitate large scale statistical analysis of heart shape, structure, function and wall motion characteristics across various population groups, using parametric mathematical modeling tools. The initial goals of the Project are i) to develop a database of cardiac Magnetic Resonance Images (MRI) and associated patient data, ii) to develop standardized procedures for the contribution, curation, archival, classification, and sharing of data and derived analyses, and iii) to provide open source software for the mapping and analysis of cardiac morphometry, with particular emphasis on the spatio-temporal characteristics of regional heart wall motion. In collaboration with the CCB, infrastructure created for brain mapping research is being translated to the cardiac domain. The CAP is also developing software tools for accessing and analyzing cardiovascular imaging data, as well as procedures and policies for secure, ethical and efficient data and resource sharing. This paper provides an overview of the design and goals of the CAP, and describes the complex administrative and procedural issues related to the contribution of data to the CAP, standardization and sharing of data and software tools, and the protection of the rights of participants, contributors and users of the database.

2 Data

The CAP database currently includes image and text data of approximately 3000 subjects from two main early contributing studies: the Multi Ethnic Study of Atherosclerosis (MESA) [9] and the Defibrillators to Reduce Risk by Magnetic Resonance Imaging Evaluation (DETERMINE) [10] clinical trial. Several other smaller research studies are also contributing data.

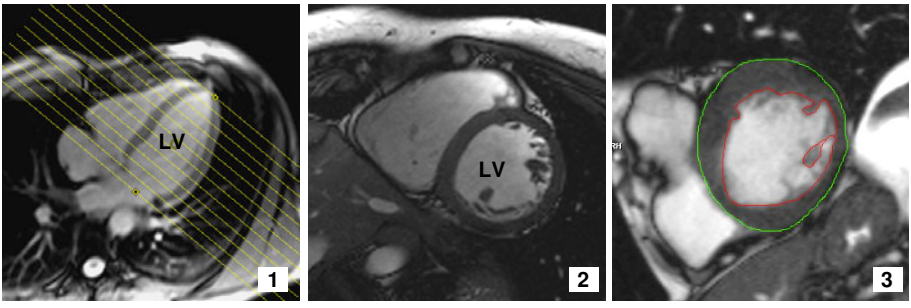

Fig. 1. Routine Cardiac MR images: 1) Cine image of long-axis view of the heart (LV = Left Ventricle) showing planned short-axis imaging planes (yellow lines); 2) Mid ventricular short-axis image; 3) Image analysis contours drawn around the inner (red) and outer (green) borders of the LV wall.

Individual datasets comprise cardiac MR images in DICOM format, together with image analysis files in the form of contours already drawn around the inner and outer borders of the left ventricle by the contributing study (Figure 1). Cases from all studies include cine image series acquired in the short and long axis planes of the heart. The DETERMINE cases also include delayed enhancement viability MR images used for detection and quantification of myocardial infarct.

Text data from the image DICOM headers (e.g. MRI pulse sequence type, image position and orientation, and other MR scan parameters) are automatically extracted and stored in the CAP database. Some limited clinical information is also contributed, including: age (years), gender (M/F), height (cm), weight (kg), systolic and diastolic blood pressure (mmHg), hypertension (y/n), heart rate (bpm), race/ethnicity (class), and classifications for hypertension, diabetes, smoking (Y/N), alcohol (Y/N), angina (y/n), ECG and NYHA classification.

These data are currently stored in two main databases within the CAP: a production database hosted by the CCB at UCLA, and a research database hosted by the University of Auckland, New Zealand.

3 Regulatory and IRB Requirements

Only data that were originally acquired with the approval of a local Institutional Review Board or Ethics Committee, and with informed consent from the participant compatible with data-sharing, may be contributed to the CAP. In observance of the USA HIPAA (Health Insurance Portability and Accountability Act) laws which protect participants' private health information, data must be de-identified at source before upload to the CAP database. Any data that can be used to identify an individual, e.g. names, dates (except for year), social security or medical record numbers, locations or device identifiers, are deleted. At no stage is any identifiable data read, analyzed or stored on any CAP computers.

Some contributing studies, such as DETERMINE, include a section in their own participant information sheet and consent form on the contribution of de-identified

data into the CAP. Participants can give or withhold consent to contribute their data to CAP independent of participation in the contributing study.

Other studies, such as MESA, are inherently designed for data-sharing and have an IRB approved informed consent process compatible with contribution to de-identification and sharing in the CAP project. In the case of MESA, explicit amendments were obtained from each field center's local IRB for the contribution of image and text data to CAP. Only data from those field centers with IRB approval, and those participants with informed consent compatible with CAP, were included in the CAP database.

The Cardiac Atlas Project Investigators themselves obtained the necessary IRB and Ethics Committee approvals to undertake the project at the two CAP centers- the University of Auckland, New Zealand, and the University of California Los Angeles, USA.

4 CAP Policies and Procedures

In order to ensure that all data provided to CAP are managed according to well defined principles, in accordance with the regulatory and ethical requirements associated with de-identified human image and clinical data, a number of policies and procedures related to data ownership, control and sharing have been developed. These policies apply to participants from whom the data is obtained, contributing studies which originally collected and have contributed the data, the CAP investigators and third-party Users who wish to access CAP data. The flow of data in CAP is shown in Figure 2.

4.1 Participants

Participants consent to contribute their de-identified image and text data to the heart disease research community now and in the future. All data are de-identified in a manner compatible with the HIPAA privacy rule, using the CCB's de-identification software with customized mappings [11] where original study identifiers, and private health information are replaced by CAP codes. This occurs at the site of the Contributing Study before upload to the CAP data servers, so the CAP does not receive or retain the original identifiers. There is, therefore, no possibility that CAP investigators, or third party Users of CAP data, can identify individuals, and all researchers must agree not to attempt to identify participants. The key linking CAP codes with original identifiers is retained by the Contributing Study, so that investigators of the Contributing Study could link results from CAP back to the original study if desired. Participants can request withdrawal of their data from the database at any time by requesting removal either via the CAP or directly to the Contributing Study. In this case the Contributing Study must notify CAP of which CAP codes must be deleted.

4.2 Contributors

Each Contributing Study has made substantial monetary, intellectual, and time investments for the collection of the data in a well-controlled manner (*viz.* original study design, recruitment, quality control, analysis, etc.), which represents a valuable scientific resource. Data contributed to CAP is therefore considered the property of

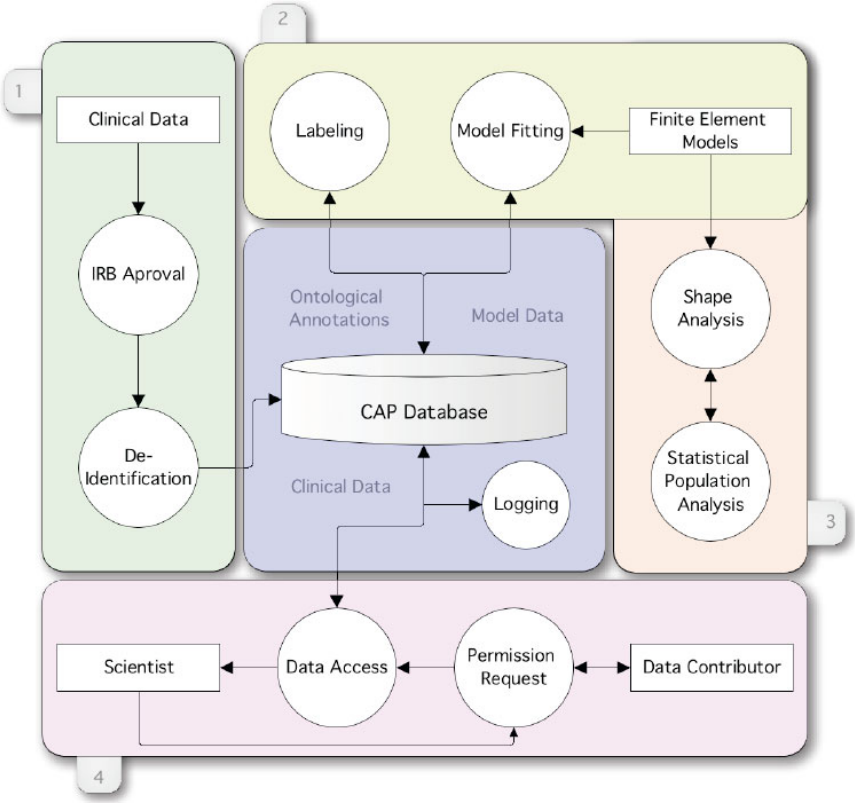

Fig. 2. CAP work-flow diagram visualizing 1) Data Acquisition; 2) Data Processing; 3) Data Analysis and 4) Public Data Access.

the Contributing Study. The Contributing Study Steering Committee controls all use of their data through data distribution agreements, on a case by case basis, as described below.

4.3 Users

Potential CAP users are required to submit a Research Proposal, outlining the rationale and goals of the project, term, and data storage, to the CAP Steering Committee. If acceptable, CAP will liaise with each of the Contributing Studies whose data is required for the Research Project. Each Contributing Study (or nominee) will then review the proposal and assess its eligibility with respect to the goals of the Contributing Study. If the proposal is approved, the User will be required to sign and abide by a Data Distribution (DDA) agreement for each of the Contributing Studies involved. Separate DDA's are required because terms and conditions governing data use are specific to the goals and rationale of each Contributing Study. The DDA defines terms and conditions of the use of the data, including publication policy, acknowledgements, security and intellectual property.

4.4 Intellectual Property

All software produced by the Cardiac Atlas Project (CAP) is freely available, via the CAP website, to researchers and educators in the non-profit sector, such as educational institutions, research institutes, and government laboratories.

CAP database and heart modeling tools, comprising database management, uploading and downloading of images, web browser interface, conversion of data formats, visualization, and parametric modeling of shape and motion, developed using CMGUI (the open source finite element modeling package developed by the University of Auckland Bioengineering Institute) [12], are being made available using the Mozilla Public License (MPL).

Commercialization of enhanced or customized versions of the software, or incorporation of the software or pieces of it into other software packages, is permitted subject to the terms of the license. Researchers are permitted to modify the source code and are strongly encouraged to share modifications with other researchers as well as with the CAP. Intellectual Property pertaining to the endpoints or specific aims of a Contributing Study, for example evaluation of a therapeutic drug or device which formed the primary hypothesis of the Contributing Study, will in general remain the property of the Contributing Study.

Intellectual property developed by third party researchers using CAP data, not relating to the specific character of the Contributing Studies, should remain the property of the developers.

5 End User Tools

5.1 Database

The CAP Database (Figure 3), hosted by the CCB at UCLA, builds upon existing brain mapping infrastructure, which has been modified for cardiac images. Access to the database is secure and privileges are assigned based on the User's needs and intent.

Browsing: The user will be able to browse the data in the CAP database. Data will be sortable by a few key fields, such as Research Group (e.g. DETERMINE), imaging protocol series description (e.g. TruFISP), age, etc.

Searching: The user will be able to perform simple and advanced queries in order to search for data. A simple query might be based on two or three fields (e.g. male + MESA + diabetic) or may contain a 'wildcard' field. (e.g. diabetic). An advanced query would allow the user to search for cases more specifically (e.g. male + MESA + diabetic + 25 < age < 45 years + acquisition date > 2003).

Downloading: Once the User has decided which data s/he would like to use, s/he would need to submit a Research Proposal to CAP for approval. Data may be downloaded only upon the execution of a completed Data Distribution Agreement.

5.2 CAP Client

MRI data may be visualized and patient specific mathematical models created using the open source (Mozilla tri-license) CAP client [13] which can be freely downloaded at the Project website.

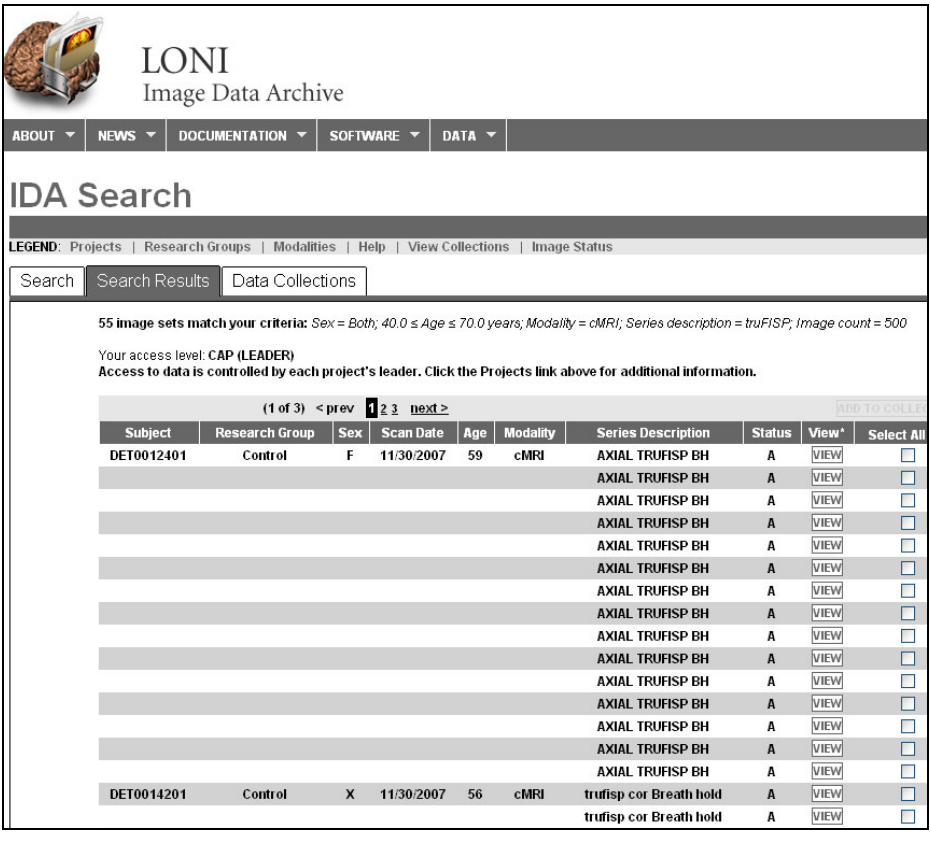

Fig. 3. Example of Search results for the CAP Database hosted by the CCB at the UCLA Laboratory of Neuro Imaging (LONI)

The CAP client provides:

- Retrieval of MRI data from the database across the network and the capability to upload models generated from such data to the database.
- Visualization of 2D CMR images, 3D visualization of the mathematical model constructed from the CMR images, and 4D Visualization (3D Visualization with the temporal dimension as the 4th dimension).
- Fitting of a mathematical model to a series of CMR images with minimal human intervention, enabling a large set of data to be automatically fitted to appropriate models and parameters. The Client software will also provide a means for the human user to be able to interactively and graphically modify the relevant model parameters.
- Tools necessary for the statistical analysis of the data. This will be used for the generation of the parametric distribution models.

The CAP Client is developed in C++ and runs on the Windows, Mac OS X and Linux platforms.

6 Data Analysis

Atlas based methods are now well established for the statistical classification and quantification of shape and wall motion characteristics [14]. These methods enable standardized analysis of statistical variations present within and among patient groups, and enable classification of individual phenotypes within known population distributions. In almost all cases contributed to the CAP, contours are contributed in association with the images and clinical information. These contours can be used in a standardized model-based analysis to establish shape and motion with respect to a standard coordinate system, similar to the Talairach coordinate system used in the brain. Since shape and motion are mathematically mapped, statistical tools such as principal component analysis can be used to quantify the significant modes of variation present in a population. In a preliminary analysis, major modes of variation within the DETERMINE cohort were associated with size, sphericity and mitral valve geometry, each of which are known indices of geometric remodeling. Projection of an individual's shape and motion onto these modes (e.g. sphericity) provides a standardized method for quantifying the amount of each mode present.

7 Future Directions

In accordance with the goals of standardized classification and sharing of data and resources, the CAP is developing and building upon currently available ontological schema to describe the data and will federate cardiovascular modeling software and data to make them available to the cardiovascular research community via the Cardiovascular Research Grid (CVRG) [6].

The CAP database will be interfaced with the CVRG-Core, and modified to implement interfaces and mechanisms compatible with CVRG enabled analysis tools. The CAP client software will also be grid-enabled, in order to be used in standard CVRG workflows, including a portal component to enable interaction with other resources on the grid. The parametric modeling tools and associated ontological schema that are being developed by CAP will be designed to facilitate data fusion between different imaging protocols and modalities as well as other data sources.

The standardized classification and description of CAP data elements (CV images and derived morphological information including contours and parametric geometry descriptions) will occur through registration of an information model and associated semantic annotations, expressed in the Web Ontology Language (OWL) [15], at the National Center for Biomedical Ontologies (NCBO) [16]. This will allow grid-enabled tools to query and access data of the correct type, and databases to declare what type of data are available. Data and derived results from several studies can be labeled and collated in a standardized manner to achieve meta or subgroup analyses via the use of existing domain ontologies, such as the Foundational Model of Anatomy (FMA) for anatomical data [17] and the Systematized Nomenclature of Medicine - Clinical Terms (SNOMED CT) for clinical terms [18]. Where gaps occur, suggested terms will be proposed based on feedback from the radiological and cardiological communities via online resources such as the NCBO BioPortal [16] and WebProtégé [19].

8 Conclusions

The CAP currently hosts approximately 3000 cardiac MRI studies, derived functional analyses and associated subject characteristics data which represents a substantial and valuable resource. Tools for the de-identification of data were developed and validated. These tools were provided to the Contributing studies and were used successfully. The necessary IRB and Ethics Committee approvals were obtained and policies were developed to protect the rights of subject participants, contributors and users of the database. Applications to use the data can now be submitted to the CAP. Applicants who are granted access can browse and query the database as well as view the images therein, and can download the data upon completion of a Data Distribution Agreement. The CAP client, which allows model generation, is also available for download at the Project's website.

Acknowledgement

The project described was supported by Award Number R01HL087773 from the National Heart, Lung, and Blood Institute. The content is solely the responsibility of the authors and does not necessarily represent the official views of the National Heart, Lung, And Blood Institute or the National Institutes of Health.

References

1. ABI Physiome Home Page, http://www.physiome.org.nz/
2. International Consortium for Brain Mapping, http://www.loni.ucla.edu/ICBM
3. Informatics for Integrating Biology and Bedside Home Page, http://www.i2b2.org/
4. Integrative Biology Project Home Page, http://www.integrativebiology.ox.ac.uk/
5. Center for Computational Biology Home Page, http://www.loni.ucla.edu/ccb
6. Cardiovascular Research Grid Home Page, http://www.cvrgrid.org/
7. Cancer Biomedical Informatics Grid Home Page, http://cabig.nci.nih.gov
8. Biomedical Informatics Resarch Network Home Page, http://www.nbirn.net/
9. Bild, D.E., Bluemke, D.A., Burke, G.L., Detrano, R., Diez Roux, A.V., Folsom, A.R., Greenland, P., Jacob Jr., D.R., Kronmal, R., Liu, K., Nelson, J.C., O'Leary, D., Saad, M.F., Shea, S., Szklo, M., Tracy, R.P.: Multi-ethnic study of atherosclerosis: objectives and design. Am. J. Epidemiol. 156, 871–881 (2002)
10. Kadish, A.H., Bello, D., Finn, J.P., Bonow, R.O., Schaechter, A., Subacius, H., Albert, C., Daubert, J.P., Fonseca, C.G., Goldberger, J.: Rationale and design for the Defibrillators to Reduce Risk by Magnetic Resonance Imaging Evaluation (DETERMINE) trial. J. Cardiovasc. Electro-physiol. 20, 982–987 (2009)
11. LONI De-identification Debabelet, http://www.loni.ucla.edu/Software/DiD
12. CMGUI software, http://www.cmiss.org/cmgui
13. Backhaus, M., Britten, R., Chung, J.D., Cowan, B.R., Fonseca, C.G., Medrano-Gracia, P., Tao, W., Young, A.A.: The Cardiac Atlas Project: Development of a Framework Integrating Cardiac Images and Models. In: MICCAI 2010, Workshop on Statistical Atlases and Computational Models of the Heart: Mapping Structure and Function plus a Cardiac Electrophysiological Simulation Challenge (STACOM-CESC 2010), Beijing, China. LNCS (2010) (in press)

14. Young, A.A., Frangi, A.: Computational cardiac atlases: from patient to population and back. Experimental Physiology 94(5), 578 (2009)
15. OWL Web Ontology Language, http://www.w3.org/TR/owl-features/
16. Bioportal 2.0 Home Page, http://www.bioontology.org/tools/alpha.html
17. Foundational Model of Anatomy Home Page, http://sig.biostr.washington.edu/projects/fm/AboutFM.html
18. Ryan, A.: Towards semantic interoperability in healthcare: ontology mapping from SNOMED-CT to HL7 version 3. Australian Computer Society, Inc., Hobart (2006)
19. WebProtégé Home page, http://protegewiki.stanford.edu/index.php/WebProtege

The Cardiac Atlas Project: Preliminary Description of Heart Shape in Patients with Myocardial Infarction

Pau Medrano-Gracia[1], Brett R. Cowan[1], J. Paul Finn[2], Carissa G. Fonseca[2], Alan H. Kadish[3], Dan C. Lee[3], Wenchao Tao[2], and Alistair A. Young[1]

[1] Auckland Bioengineering Institute, University of Auckland,
Private Bag 92019, Auckland 1142, New Zealand
{p.medrano,b.cowan,a.young}@auckland.ac.nz,
http://www.abi.auckland.ac.nz
[2] Diagnostic CardioVascular Imaging, UCLA,
Suite 3371, 10945 LeConte Avenue, Los Angeles, CA 90095-7206, USA
{cfonseca,wtao,pfinn}@mednet.ucla.edu,
http://dcvi.radsci.ucla.edu
[3] Bluhm Cardiovascular Institute, Northwestern Memorial Institute
251 E. Huron Street, Feinberg Pavilion 8-536, Chicago, IL 60611, USA
{a-kadish,dlee}@northwestern.edu

Abstract. The Cardiac Atlas Project seeks to establish a standardized database of cardiovascular imaging examinations, together with derived analyses, for the purposes of statistical characterization of global and regional heart function abnormalities. We present preliminary results from a subset of cases contributed from the Defibrillators to Reduce Risk by Magnetic Resonance Imaging Evaluation (DETERMINE) study of patients with myocardial infarction. Finite element models were fitted to the epicardial and endocardial surfaces throughout the cardiac cycle in 200 patients using a standardized procedure. The control points of the shape model were used in a principal component analysis of shape and motion. The modes were associated with well-known clinical indices of adverse remodeling in heart disease, including heart size, sphericity and mitral valve geometry. These results therefore show promise for the clinical application of a statistical analysis of shape and motion in patients with myocardial infarction.

Keywords: Statistical Shape Model, Principal Component Analysis, Cardiac Magnetic Resonance Imaging (MRI), Finite Element Modeling.

1 Introduction

Cardiac magnetic resonance (CMR) imaging provides an abundant source of detailed, quantitative data on heart structure and function. Model-based image analysis procedures provide a powerful mechanism for the fast, accurate assessment of cardiac MRI data and lend themselves to biophysical analysis and

O. Camara et al. (Eds.): STACOM-CESC 2010, LNCS 6364, pp. 46–53, 2010.

standardized functional mapping procedures. The theory of statistical analysis of cardiac shape and motion has been well developed and applied to the heart for at least a decade [Augenstein and Young, 2001, Frangi et al., 2002]. Principal component analysis (PCA) and independent component analysis (ICA) are the main statistical tools for the study of the variability of function and shape of the heart among and within patient groups [Üzümcü et al., 2003]. The PCA represents a global linear analysis of the major components of variation assuming a multidimensional Gaussian distribution, while the ICA does not require a Gaussian distribution of the data, and allows analysis of more localized shape variations.

Most studies have focused on the left ventricle (LV) due to the prevalence of LV disease, but more comprehensive approaches have also been researched [Lötjönen et al., 2003]. Few studies have examined the shape and motion of the LV from a global 4-D perspective [Papademetris et al., 2002, Remme et al., 2004].

There has been extensive research into modeling cardiac function (see [Frangi et al., 2001] for a review); however, the analysis of large datasets has been limited by the lack of available population studies. Although recent studies have reported findings of up to 100 cases [Ordas et al., 2007], it is well known that these procedures require significantly more cases to achieve robust clinical application.

The Cardiac Atlas Project (CAP) is an international collaboration which aims to facilitate large scale statistical analysis of heart shape, structure, function and wall motion characteristics across various population groups via parametric mathematical modeling tools. One major study contributing data to the CAP is the Defibrillators to Reduce Risk by Magnetic Resonance Imaging Evaluation (DETERMINE) study [Kadish et al., 2009]. The DETERMINE trial is a multicenter, randomized study of patients with coronary artery disease and mild to moderate left ventricular impairment. The primary objective of the study is to test the hypothesis that implantable cardioverter defibrillator (ICD) therapy in combination with medical therapy, in patients with myocardial infarct greater than or equal to 10% of the LV muscle mass (as measured by CMR), improves long term survival compared to medical therapy alone. The baseline CMR examinations were contributed to the CAP, along with associated clinical information. This represents a valuable resource for the study of regional wall motion abnormalities in patients with myocardial infarction.

In this paper we report preliminary results from a subset of 200 cases from the DETERMINE cohort. PCA and ICA were performed and the major components of variation within the dataset were determined using a variety of methods. These components were compared with known clinical characteristics of LV remodeling due to myocardial infarction.

2 Methods

A total of 200 cases were chosen at random from the DETERMINE cohort. The images were acquired using Steady-State Free Precession imaging (SSFP) and the number of frames per case ranges from 20 to 30 [Kadish et al., 2009].

A standardized mathematical model of the LV was customized to each case using guide-point modeling [Young et al., 2000]. Briefly, a 3D finite element model was adaptively optimized to fit each subject's image dataset, using linear least squares optimization. Guide points placed on the images were fitted by a geometric model including epicardial and endocardial surfaces. This method has previously been validated in animals against autopsy LV mass, in patients with regional wall motion abnormalities against manually drawn contours, and in healthy volunteers against flow-derived measurements of cardiac output [Young et al., 2000]. Papillary muscles were included in the blood pool. Fiducial markers were placed by the user on the LV central axis, the mitral valve, and insertions of the right ventricular free wall to the interventricular septum. These markers were used to calculate a pose and scale for the model, and orient a standard coordinate system. In addition, the insertion points of the mitral valve leaflets were marked in all available long axis images, in order to define the basal extent of the LV [Young et al., 2000].

The mathematical model was described in a prolate spheroidal coordinate system [Nielsen, 1987] giving a radial (λ) function of two angular coordinates (μ and θ in eqn. 1). The interpolation of control points used bicubic Hermite functions — in element coordinates (ξ_1, ξ_2, ξ_3) giving C^1 continuity (eqn. 2). This yields an intuitive node parametrization of (λ, μ, θ) with respect to the shape of the heart. The focal length (f) defined the overall scale of the coordinate heart. The radial location of the guide points λ_g was fitted by minimizing eqn. 3 with respect to the nodal parameters.

$$\begin{aligned} x &= f\ \cosh(\lambda)\cos(\mu) \\ y &= f\ \sinh(\lambda)\sin(\mu)\cos(\theta) \\ z &= f\ \sinh(\lambda)\sin(\mu)\sin(\theta) \end{aligned} \tag{1}$$

$$\lambda(\xi_1, \xi_2, \xi_3) = \sum_n \Psi(\xi_1, \xi_2, \xi_3)\lambda^n \tag{2}$$

$$E(\lambda) = S(\lambda) + \sum_g (\lambda(\xi_g) - \lambda_g)^2 \tag{3}$$

The smoothing term $S(\lambda)$ was included to regularize the problem, which can be ill-posed due to the sparse location of the data.

The shape parameters of the model were then analyzed with the Modular Data Processing Toolkit [Zito et al., 2008]. Principal Component Analysis (PCA) and an Independent Component Analysis (ICA using the JADE algorithm [Cardoso, 1999]) was applied to 3 different shape vector configurations, which defined three different shape spaces. Firstly, a rectangular Cartesian shape vector (RC) was formed from a subdivision of the finite element model. Secondly, a prolate spheroidal shape space (*Prolate*) was formed using the focal length and the (λ, μ, θ) nodal model parameterization. Finally, just the λ parameters (*Lambda*) were considered in a separate shape vector, using average values for focal length, μ and θ.

In order to compute the PCA analysis, the data was mean-removed and standardized as in [Young and Frangi, 2009]. The modes were computed to reach a cumulative representation of 95% ($\pm 2\sigma$) of the variability. In the case of ICA, modes were ranked according to the size of the standard deviations (σ) present for each mode in the 200 cases. This paper only considers analysis of the end-diastolic shape; a full temporal analysis of shape and motion is in progress.

3 Results

Figure 1 shows the first six modes for each of the shape spaces (*RC*, *Prolate*, *Lambda*) investigated. The number of modes required to represent 95% of the total variation were 19 for *RC*, 6 for *Prolate* and 31 for *Lambda*. For each mode, the $\pm 2\sigma$ shapes are represented and the relative power of the mode is noted at the bottom of each pair. The modes are ordered according to their relative power.

A close inspection of figures 1 and 2, reveals that common modes appear in all three shape spaces, in both PCA and ICA analysis. This implies that the statistical shape analysis results in a robust signal decomposition.

For example, *Mode 1* (size) from the PCA *Prolate* is also found as *Mode 1* in the *RC* space, whereas in the ICA, it is found in both the *Prolate* and *RC* spaces with different but consistently dominant power. It is not present in the *Lambda* space since the effect of focal length (size) has been removed. *Mode 2* (sphericity) in the PCA *Prolate* analysis is present in *Mode 3* and *Mode 4* in *RC*, and *Mode 1* in *Lambda*, whereas in the ICA, it appears in *Mode 2* and *Mode 4* in *RC*, *Mode 2* in *Prolate* and is still present, but decreasingly so, in *Mode 1* in *Lambda*. This could be related to the fact that ICA does not separate signals well when there is more than one signal with a Gaussian distribution. Finally, *Mode 3* in PCA *Prolate* (mitral valve insertion plane) can be found in all spaces but *Lambda* where it has been removed.

4 Discussion

The three modes present in the statistical shape analysis are also known to be important descriptors of the remodelling of the LV due to myocardial infarction. LV size, sphericity and mitral valve geometry are all recognized clinical indicators of disease, with larger more spherical hearts being indicative of more progressed disease.

The advantage of the rectangular Cartesian analysis is that all data in the shape vector have the same physical meaning (i.e. mm). The quantification of effect size in terms of shape variation is therefore unambiguous. In the Prolate case, however, the focal length has very different scale to the (λ, μ, θ) nodal parameters, so it is therefore unsurprising that the focal length should comprise over 80% of the shape variation in this space. By decoupling size and mitral valve orientation from the shape vector, as in the Lambda space, we see the effects due solely to radial distance from the LV center. In this space sphericity is the dominant mode of variation. The amount of this shape mode present in

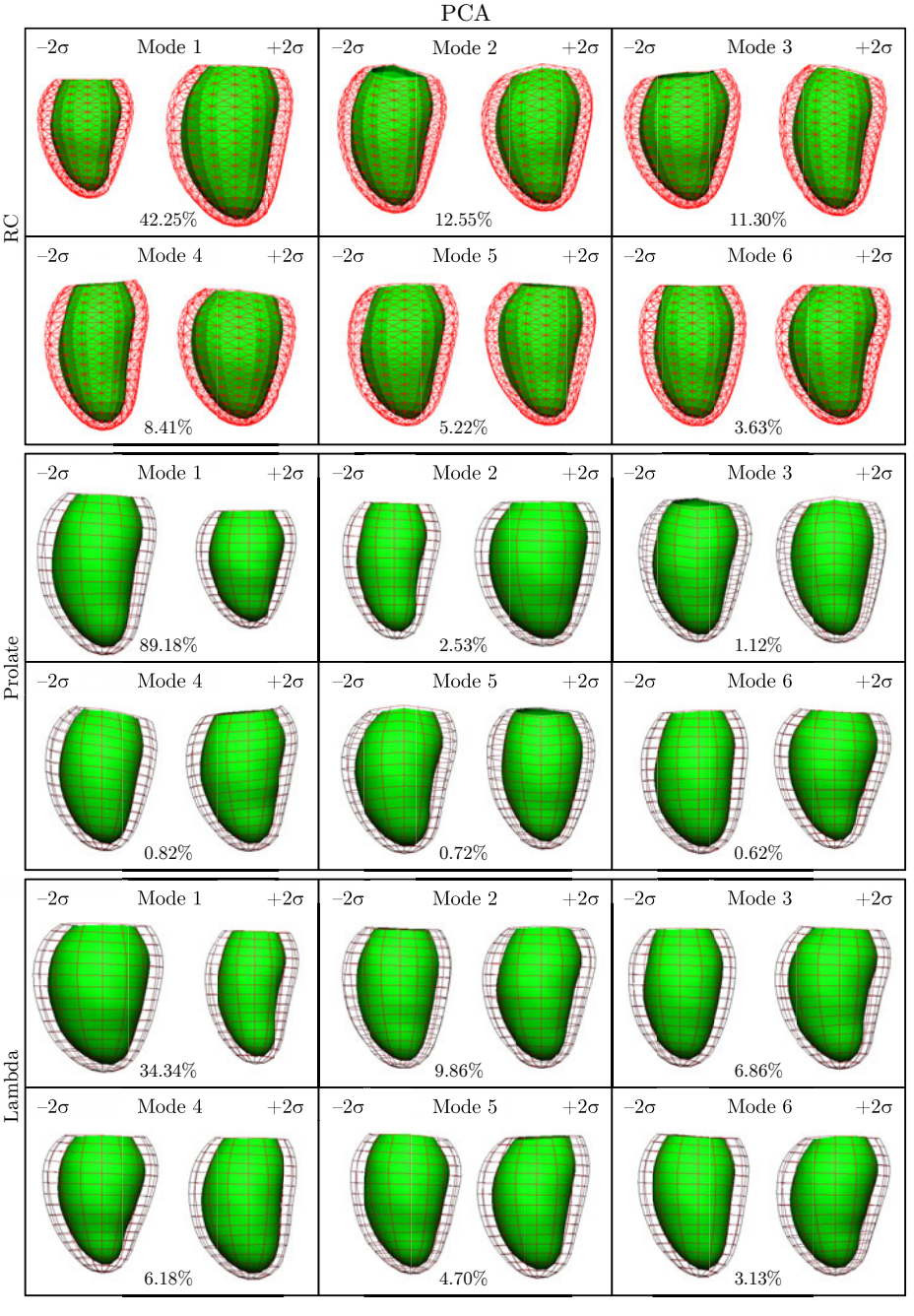

Fig. 1. PCA first six modes in the 3 spaces analyzed

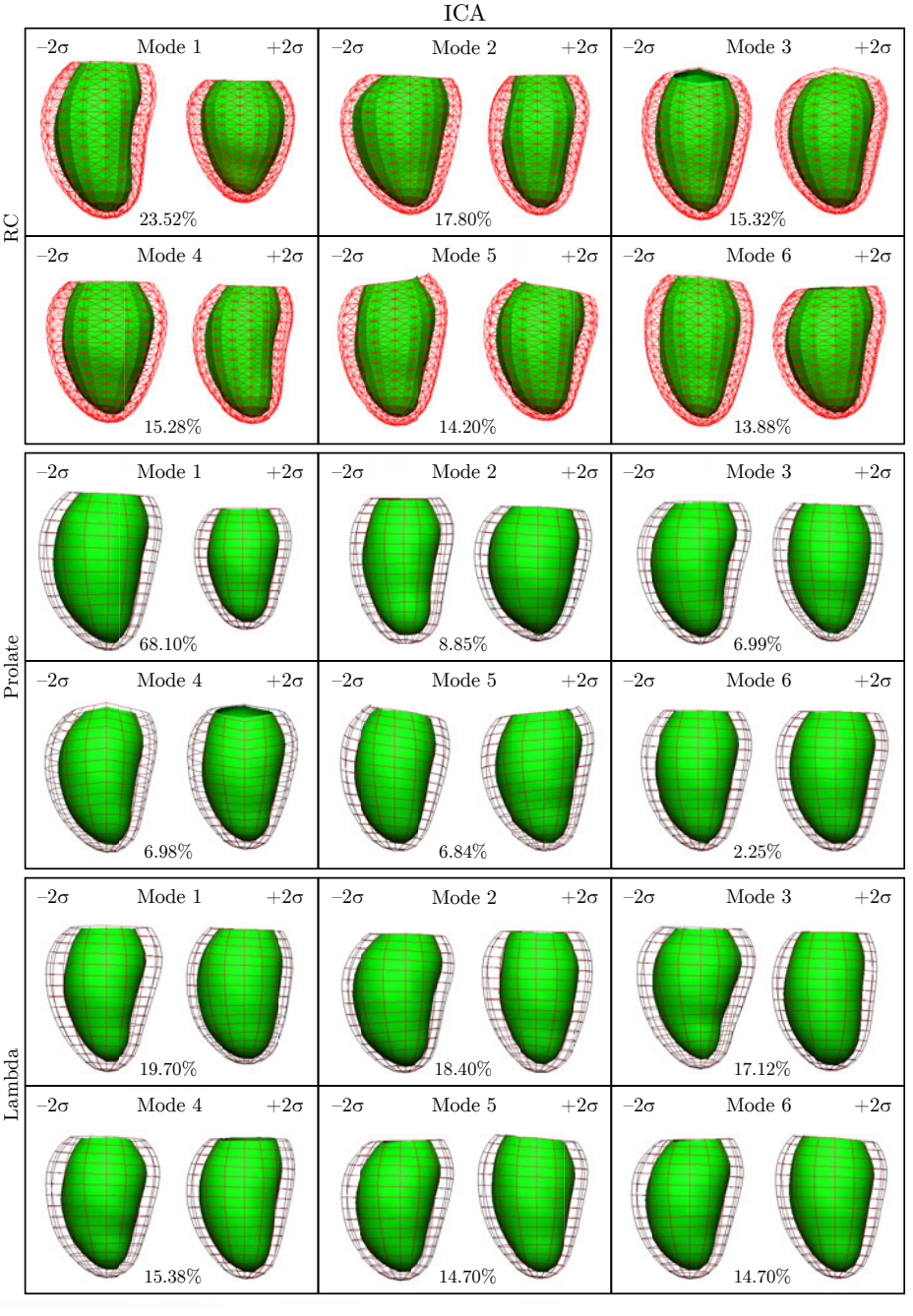

Fig. 2. ICA first six modes in the 3 spaces analyzed

any individual heart could therefore serve as an important quantitative clinical index of disease.

The literature reports more accuracy using ICA in relation to standard error measurements. However, determination of the optimal methodology is highly contingent on the particular application.

5 Future Work

This paper only considered the shape of the LV at end-diastole. A full analysis of shape and motion is in progress. Also, analysis of both right and left ventricular geometry is of interest in cases of congenital heart disease. To this end, this analysis could be extended to include more complicated geometries [Lam et al., 2010].

One limitation of these methods is the lack of precisely identifiable landmarks which presents an interesting area for future research, e.g. [Mansi et al., 2009].

Another topic for research is the comparison of the statistical modes arising from the DETERMINE study with those arising from another study which has contributed data to the CAP — the Multi Ethnic Study of Atherosclerosis (MESA), which comprises asymptomatic volunteers. To date, 2450 MESA cases have been contributed to the CAP, facilitating comparison between "normal volunteers" and patient groups.

6 Conclusion

A statistical analysis of LV shape using a variety of shape measures, and analysis methods, yields consistent major modes of variation, which are known indicators of the severity of disease. This method enables quantification of these modes in a standard way, which will facilitate detailed and precise evaluation of patients.

Acknowledgements

The project described was supported by Award Number R01HL087773 from the National Heart, Lung, and Blood Institute. The content is solely the responsibility of the authors and does not necessarily represent the official views of the National Heart, Lung, and Blood Institute or the National Institutes of Health.

References

[Augenstein and Young, 2001] Augenstein, K., Young, A.: Finite element modeling for three-dimensional motion reconstruction and analysis. In: Measurement of Cardiac Deformations from MRI: Physical and Mathematical Models, pp. 37–58 (2001)

[Cardoso, 1999] Cardoso, J.: High-order contrasts for independent component analysis. Neural computation 11(1), 157–192 (1999)

[Frangi et al., 2001] Frangi, A., Niessen, W., Viergever, M.: Three-dimensional modeling for functional analysis of cardiac images: A review. IEEE Transactions on medical imaging 20(1), 2–5 (2001)

[Frangi et al., 2002] Frangi, A., Rueckert, D., Schnabel, J., Niessen, W.: Automatic construction of multiple-object three-dimensional statistical shape models: Application to cardiac modeling. IEEE Transactions on Medical Imaging 21(9), 1151–1166 (2002)

[Kadish et al., 2009] Kadish, A., Bello, D., Finn, J., Bonow, R., Schaechter, A., Subacius, H., Albert, C., Daubert, J., Fonseca, C., Goldberger, J.: Rationale and design for the defibrillators to reduce risk by magnetic resonance imaging evaluation (DETERMINE) trial. Journal of Cardiovascular Electrophysiology 20(9), 982–987 (2009)

[Lam et al., 2010] Lam, H., Cowan, B., Nash, M., Young, A.: Interactive biventricular modeling tools for clinical cardiac image analysis. Journal of Cardiovascular Magnetic Resonance 12(suppl. 1), 248 (2010)

[Lötjönen et al., 2003] Lötjönen, J., Koikkalainen, J., Smutek, D., Kivistö, S., Lauerma, K.: Four-chamber 3-D statistical shape model from cardiac short-axis and long-axis MR images. In: Ellis, R.E., Peters, T.M. (eds.) MICCAI 2003. LNCS, vol. 2878, pp. 459–466. Springer, Heidelberg (2003)

[Mansi et al., 2009] Mansi, T., Durrleman, S., Bernhardt, B., Sermesant, M., Delingette, H., Voigt, I., Lurz, P., Taylor, A., Blanc, J., Boudjemline, Y., et al.: A Statistical Model of Right Ventricle in Tetralogy of Fallot for Prediction of Remodelling and Therapy Planning. In: Yang, G.-Z., Hawkes, D., Rueckert, D., Noble, A., Taylor, C. (eds.) MICCAI 2009. LNCS, vol. 5761, pp. 214–221. Springer, Heidelberg (2009)

[Nielsen, 1987] Nielsen, P.: The anatomy of the heart: a finite element model. PhD Thesis-University of Auckland (1987)

[Ordas et al., 2007] Ordas, S., Oubel, E., Leta, R., Carreras, F., Frangi, A.: A statistical shape model of the heart and its application to model-based segmentation. In: Proc. SPIE Medical Imaging, San Diego, CA, USA, vol. 6511 (2007)

[Papademetris et al., 2002] Papademetris, X., Sinusas, A., Dione, D., Constable, R., Duncan, J.: Estimation of 3-D left ventricular deformation from medical images using biomechanical models. IEEE Transactions on Medical Imaging 21(7), 786–800 (2002)

[Remme et al., 2004] Remme, E., Young, A., Augenstein, K., Cowan, B., Hunter, P.: Extraction and quantification of left ventricular deformation modes. IEEE Transactions on Biomedical Engineering 51(11), 1923–1931 (2004)

[Young et al., 2000] Young, A., Cowan, B., Thrupp, S., Hedley, W., Dell'Italia, L.: Left Ventricular Mass and Volume: Fast Calculation with Guide-Point Modeling on MR Images. Radiology 216(2), 597 (2000)

[Young and Frangi, 2009] Young, A., Frangi, A.: Computational cardiac atlases: from patient to population and back. Experimental Physiology 94(5), 578 (2009)

[Zito et al., 2008] Zito, T., Wilbert, N., Wiskott, L., Berkes, P.: Modular toolkit for Data Processing (MDP): a Python data processing framework. Frontiers in neuroinformatics, 2 (2008)

[Üzümcü et al., 2003] Üzümcü, M., Frangi, A., Sonka, M., Reiber, J., Lelieveldt, B.: ICA vs. PCA active appearance models: Application to cardiac MR segmentation. In: Ellis, R.E., Peters, T.M. (eds.) MICCAI 2003. LNCS, vol. 2878, pp. 451–458. Springer, Heidelberg (2003)

The Cardiac Atlas Project: Development of a Framework Integrating Cardiac Images and Models

Michael Backhaus[1], Randall Britten[1], Jae Do Chung[1], Brett R. Cowan[1], Carissa G. Fonseca[2], Pau Medrano-Gracia[1], Wenchao Tao[2], and Alistair A. Young[1]

[1] Auckland Bioengineering Institute, University of Auckland, Private Bag 92019, Auckland 1142, New Zealand
{m.backhaus,r.britten,jaedo.chung,b.cowan}@auckland.ac.nz
{p.medrano,a.young}@auckland.ac.nz
http://www.abi.auckland.ac.nz

[2] Diagnostic CardioVascular Imaging, UCLA, Suite 3371, 10945 LeConte Avenue, Los Angeles, CA 90095-7206
{cfonseca,wtao}@mednet.ucla.edu
http://dcvi.radsci.ucla.edu

Abstract. We describe the software design, architecture and infrastructure employed in the Cardiac Atlas Project (CAP), an international collaboration to establish a web-accessible structural and functional atlas of the normal and pathological heart. Cardiac imaging data is de-identified in a HIPAA compliant manner using the LONI Debabeler with customized DICOM mappings. A production database and web-interface were employed based on existing tools developed by LONI. A new open-source database and web interface have been developed for research purposes. After consideration and evaluation of several software frameworks, the research database has been implemented based on a 3-tier architecture utilizing MySQL, JBoss and Dcm4chee. Parts of Dcm4chee have been extended to enable access to MRI specific attributes and arbitrary search parameters. An XML schema has been designed representing the elements associated with the creation and curation of volumetric shape models. The research database is implemented compliant to the DICOM standard, thus providing compatibility with existing clinical networks and devices. A modeling tool, the CAP client, has been developed to enable browsing of 3D image data and creation and modification of volumetric shape models. All software components developed by the CAP are open source and are freely available under the Mozilla license.

Keywords: Computational Atlas, Database, Parametric Shape Models.

1 Introduction

Cardiovascular diseases (CVDs) are the number one cause of death globally: more people die annually from CVDs than from any other cause. By 2030, almost 23.6 million people will die from CVDs, mainly from heart disease and

O. Camara et al. (Eds.): STACOM-CESC 2010, LNCS 6364, pp. 54–64, 2010.

stroke [39]. To help with understanding the disease and planning intervention, integrative models of cardiac physiology are important. Anatomical, functional and clinical data must be integrated across many scales, from molecular interactions to organ system function [2]. The CAP aims to provide access to Cardiac Magnetic Resonance (CMR) images and derived data for the clinical, research and educational communities. The data and tools provided will assist the scientific community with large scale studies for a better understanding of CVDs. The proposed research has three primary objectives.

1. **Establish a database of CMR examinations**. The two main contributing studies, MESA and DETERMINE, provide CMR image and text data from 2864 cases representing asymptomatic volunteers (MESA), and 470 cases representing patients with myocardial infarction (DETERMINE). Upon upload to the CAP, cardiac magnetic resonance (CMR) images are de-identified and stored in a database with advanced MRI search options.
2. **Develop open source software** for the mapping and analysis of cardiac morphometry. A client software is used to generate volumetric models. CMR Images can be loaded into the software and visualized in 3D over time. A finite element model of the heart can be customized to the images using markers placed by an analyst or contour information contributed from the original studies. The models are stored with the CMR images in the CAP database.
3. **Develop standardized procedures** for the contribution, curation, archival, classification, and sharing of CMR data and derived analyses, These methods are used to facilitate statistical analysis of regional heart shape and wall motion characteristics, and characterization of remodeling, between and within population groups. CMR images and models are labeled and classified using ontological terms and contribute to a publicly accessible knowledge base of cardiac images and models.

The following sections describe the developed software and procedures implemented to satisfy the research objectives. For details about the work-flow for users and contributing studies please refer to [23].

2 Data De-identification

2.1 Privacy and Security

The Health Insurance Portability and Accountability Act (HIPAA) Privacy and Security Rules [29] regulate the use and disclosure of patient information. They define requirements and conditions which control secure data access and transfer, as well as Protected Health Information (PHI). PHI are any data that can be used to identify an individual, and must be replaced or removed (de-identified) to protect the identity of patients. The HIPAA allows a limited data set for research purposes which may contain elements of dates related to a person. Having IRB approval for use of a limited data set, the CAP retains the patient age and year of scan in the database.

2.2 DICOM Data Elements

Medical images used by the CAP are acquired in the Magnetic Resonance Imaging (MRI) modality type and stored as DICOM Objects. These objects contain Data Elements (DE) representing information associated with the scanned object. The DICOM Standard defines 27 Value Representations (VR) [26] as valid data types for DEs. The VR of each DE is listed in the DICOM Data Dictionary [26]. The dictionary further defines an Attribute Name (AN) and Value Multiplicity (VM) per DE. The current DICOM Standard (v2009) contains more than 2800 DEs, also known as public attributes or tags. In addition, many manufacturers of medical devices encode proprietary information in private attributes.

2.3 De-identification

The CAP uses the UCLA Laboratory for Neurological Imaging (LONI) Debabeler [1], a HIPAA compliant software tool, for the de-identification of DICOM images. The Debabeler is used to create and customize translations between medical image file formats. We have created a CAP specific Debabeler translation with rules to encrypt or replace attributes that could potentially contain PHI. The de-identification works in the following manner:

1. **Split by tag**: DICOM tags that are known to be safe are left unchanged.
2. **Split by VR**: DICOM tags not selected in step 1. are left unchanged if they have allowed VRs.
3. **Discard**: DICOM tags not selected in step 2. are discarded.
4. **Replace**: Out of all the DICOM tags in steps 1., 2., and 3., the values of specified tags are replaced.

The output of the Debabbler includes a key linking CAP case codes to the original identifiers, which is kept by the contributing study. CAP personnel, and third party CAP users, are prohibited from accessing this key. The CAP Debabeler mapping is available from the subversion repository at the sourceforge project site [30].

3 Database

3.1 Production Database

The CAP production database is hosted by the LONI as an extension of existing brain mapping infrastructure. The purpose of this database is to provide a mechanism by which approved third party users can access the de-identified data and derived information. The LONI Image Data Archive (IDA) is a server farm consisting of Linux computers running the MySQL database engine and Tomcat web application servers with a built-in load balancer that manages the requests to the web servers. The IDA database has been extended to enable the storage and browsing of time-resolved cardiovascular MRI data.

3.2 Research Database

A goal of the CAP is to establish an open source web accessible structural and functional atlas of the heart [9]. The project requirements include storage and retrieval of medical images, ontological mappings and volumetric shape models.

Framework Evaluation. Based on a confidentiality and integrity evaluation of the CAP requirements, the atlas framework had to be developed using a 3-tier architecture (web-, application- and database-server) including secure authentication and monitoring. Several frameworks have been evaluated regarding features like security, database connectivity, web-services, testing frameworks, etc. In order to evaluate development efforts and extensibility, 3 prototypes were implemented using the most suitable frameworks.

1. **Prototype A** based on MySQL [7] / Zope [31] / Plone [32]
   Pro: User control management, Integration with the Physiome Model Repository [33];
   Con: No native web-service support; limited documentation; small developers group; low maintenance;
2. **Prototype B** based on MySQL / GlassFish [8] / Liferay [10]
   Pro: User control management; Java Portlets [11] supported by a variety of application servers and CMSs;
   Con: Limited Ajax support for Portlets (JSR168);
3. **Prototype C** based on MySQL / JBoss [34] / Dcm4chee [6]
   Pro: Mature architecture and code basis; active development, maintenance and support; DICOM compliant implementation; compatibility with other Java APIs; compatibility with other international research projects [5] [37];
   Con: Large code base.

Due to its advantages and compatibility with other research projects, Prototype C was chosen as the software framework for the development of the CAP research database.

Image Archive. Dcm4chee is a clinical data manager system based on a J2EE [12] and JMX [13] software architecture and is deployed within the JBoss Application Server. It provides a number of clinical services of which the most important for the CAP are:

1. **DICOM Interfaces** - Acting as an archive, Dcm4chee is able to store, query, and retrieve any type of DICOM object;
2. **WADO and RID Interfaces** - WADO (Web Access to DICOM Objects) and RID (IHE Retrieve Information for Display) interfaces enable access to the archived content from the Web;
3. **Web-based User Interface** - Dcm4chee contains a robust user interface which runs entirely in a Web browser;
4. **Audit Record Repository** - IHE ATNA audit logging [16].

Extended DICOM Queries. The Dcm4chee application logic, database schema and web-application have been extended to provide access to MRI specific

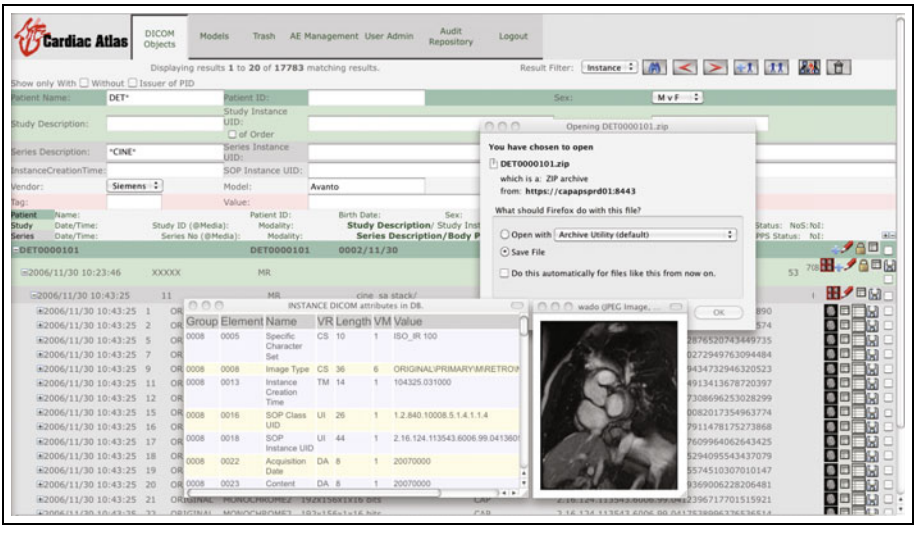

Fig. 1. CAP web-application, based on Dcm4chee, providing extended MRI search options

attributes as defined in the DICOM Standard MR Image Module [26]. Further, vendor and model of the scanner used to record the images are stored. The database fields are populated at image import using extended methods from the Dcm4chee Enterprise Java Beans (EJBs).

The web-application extension provides the ability to include all added attributes as search options (see Fig. 1). Using the web-front-end for querying the CAP database, a researcher might be interested in specific studies, cine series or individual images that satisfy the search parameters. For this purpose, a search filter has been added to generate a result-set providing direct access to Patient, Study, Series or Instance data.

To be able to search for arbitrary (including private) DICOM attributes, an XPath query [28] has been implemented. An XML tree [14] representing the DICOM structure of the imported images is generated, stripped of binary and large values (but keeping the DICOM tag) and stored in the database. Using MySQL XML Functions [27], an XPath query on 600,000 images, searching for instances with the scanning sequence "Spin Echo" stored in tag "0018,0020", takes several minutes to complete (depending on the speed of the storage system). For comparison, the same query in a relational database on an indexed text field takes only seconds to complete. The XPath query time can be significantly improved by limiting the search space, e.g. through specification of a Patient ID. However, this shows the limitations of querying large XML data-sets without the ability to specify indices on values. This limitation could be overcome by moving the XPath query functionality to an optimized XML database (e.g. *eXist* [3]).

Model Storage. In order to store volumetric models generated with the CAP client application, an XML schema has been designed representing the elements associated with volumetric shape model creation and curation. This includes input parameters, such as images, contours and markers, calculated output parameters, mesh files representing the model, as well as provenance information (see Fig. 2).

CAP models are stored by serializing the XML model and mesh files. The models are imported to the CAP database, where they are de-serialized and

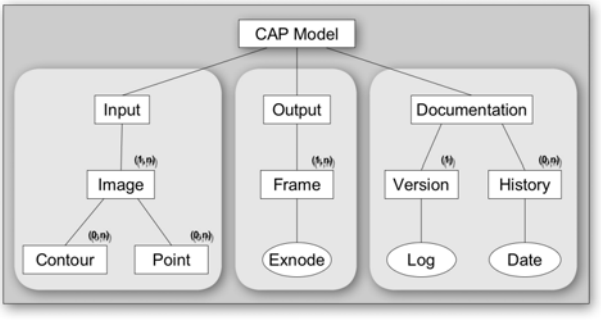

Fig. 2. CAP model structure diagram visualizing the basic model components

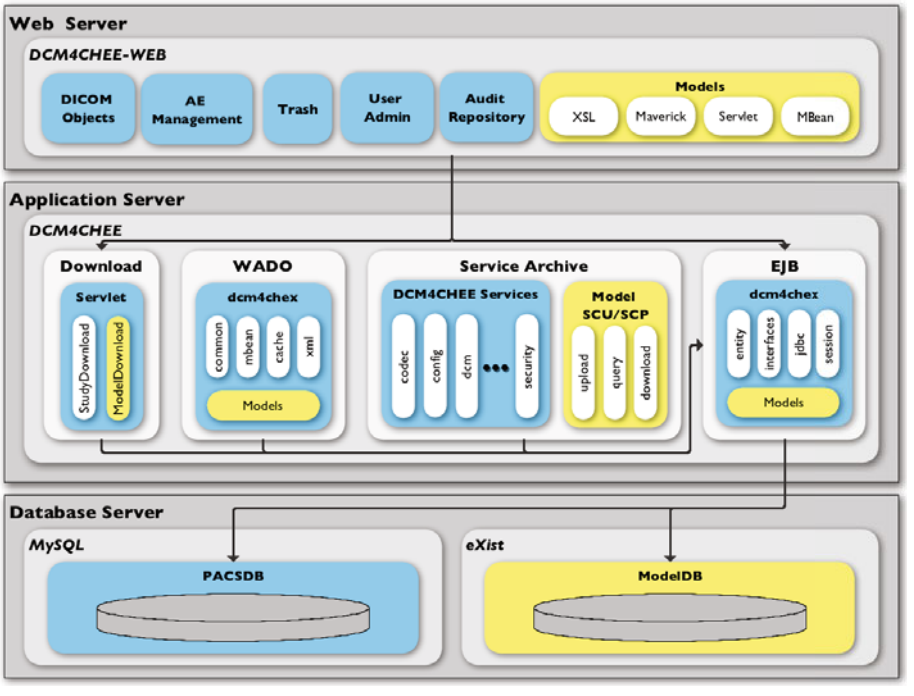

Fig. 3. 3-tier architecture of the CAP Model Implementation based on Dcm4chee. Blue boxes represent basic Dcm4chee classes, yellow boxes represent CAP specific model extensions.

checked for consistency of referenced file-associations. A simple versioning implementation stores models with incremental version numbers allowing reversion to earlier versions. The XML model files are stored in the *eXist* XML database, which provides core database features, such as indexing and transaction recovery, allowing for fast search and retrieval of model related data. The consistency check and versioning methods, as well as import and export of models, are implemented as extensions to the Dcm4chee architecture (see Fig. 3). This provides a tight integration with the solid code structure and logging facilities of Dcm4chee, as well as model accessibility via DICOM network interfaces WADO and SCP.

Download. The download functionality of the Dcm4chee web-application has been extended to allow the download of complete DICOM studies and series. Further, models can be downloaded with optional referenced data. This functionality is achieved by implementing a servlet that collects requested data and provides it in a compressed archive to the user.

4 CAP Client

4.1 Overview

The CAP Client is the client side software tool for the visualization and the analysis of the MRI cases stored in the CAP database. Given a set of CMR images, the CAP client can be used to perform:

1. **Image Browse and Labeling** - Reading the DICOM header information of all images and presenting the information in a graphical user interface on which the user can browse through, select and label the images for further use in model fitting;
2. **Visualization** - Display cine images in their correct position and orientation in 3D+time;

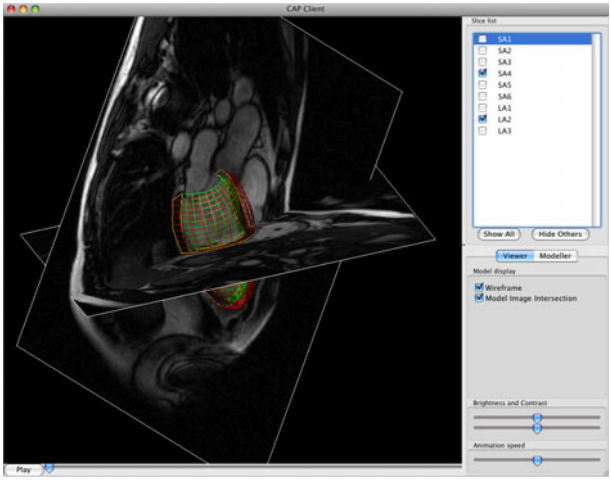

Fig. 4. Screenshot of the CAP Client running on Mac OS X

3. **Model Fitting** - A finite element model of the left ventricle is fitted to a set of images using fiducial markers and data points;
4. **Data Export** - Fitted model parameters along with images and contour information are stored in an XML file format (see Section 3.2).

4.2 Design and Implementation

The development of the CAP Client has been greatly influenced by the use of the CMGUI library [35], an advanced visualization software library developed at the Auckland Bioengineering Institute (ABI). Other software considered was GIMIAS [24] and CardioViz3D [25]. Through the use of CMGUI, we can refer to existing knowledge at the ABI about using the finite element method for the model fitting and the involved computational complexity and graphical visualization. Important objectives for the software development include:

1. **Performance** - To allow the user to view and manipulate large sets of CMR images in 3D and fit models to them in an interactive manner, performance is a critical design factor. In order to meet the real-time requirements regarding the 3D graphics and numerical computation, the C++ programming language was chosen for its superior time efficiency and the availability of high performance numerical libraries. The CAP client uses hardware-accelerated OpenGL API for graphics rendering and the GMM++ linear algebra library [36] for the model fitting.
2. **Ease of Use** - The CAP client is expected to be used by non-technical users for educational and research purposes, therefore ease of use is an important design goal. All features of the CAP client are accessible through an intuitive graphical user interface.
3. **Extensibility and Maintainability** - In order to encourage external developers to extend the CAP client to suit their needs, the source code is structured to easily accommodate such extensions. Various object oriented techniques were adopted to increase the extensibility of the software. For example, the abstract factory design pattern [22] and the adaptor design pattern [21] were used to ease the possible replacement of the linear algebra library.
4. **Portability** - The CAP client was designed to be portable across different platforms and currently runs on Microsoft Windows, Mac OS X and Linux. This portability is achieved using cross-platform libraries such as wxWidgets [17], boost [38] and GMM++, as well as build and testing tools such as CMake and Google Test.

The CAP client is open source under the Mozilla tri-license and the source code is available from the mercurial repository at the CAP sourceforge project site [30].

5 Future Work

Ontologies: For classification and standardization purposes, the CAP framework will be extended to allow labeling of 2D and 3D regions of interest using

anatomical terms from the Foundational Model of Anatomy (FMA) [18] and clinical terms from Systematized Nomenclature of Medicine (SNOMED-CT) [19]. The ontological annotations will be expressed using the web ontology language (OWL) [20].

Grid enabling: The CAP seeks to federate cardiovascular modeling software and data resources to make them available to the cardiovascular research community via the Cardiovascular Research Grid (CVRG) [37]. CVRG provides infrastructure tools in the cardiovascular domain to enable researchers to easily access distributed resources through standardized interfaces, based on tools developed in the BIRN [4] and caBIG [5] projects. The CAP research database will be interfaced with the CVRG-Core, and modified to implement interfaces and mechanisms compatible with CVRG enabled analysis tools.

CAP Client database access: The CAP Client will be enabled to interface with the CAP research database using the DICOM SCP, SCU, and WADO protocol (cf. Fig. 3).

6 Conclusion

We designed and implemented procedures and tools to facilitate a workflow from the acquisition of CMR images towards a statistical analysis of volumetric models. CMR images used within the CAP are de-identified in a HIPAA compliant manner and are accessible to the scientific community via the CAP database. The database is compliant to the DICOM standard and provides sophisticated image attribute search options. The CAP Client software allows the user to import images from the database and fit a finite element model using markers and contour information. Volumetric shape models are stored in XML and CMGUI specific file formats and are available to the research community via the CAP database.

References

1. Neu, S.C., Valentino, D.J., Toga, A.W.: The LONI Debabeler: a mediator for neuroimaging software. NeuroImage 24(4) (2005)
2. Young, A.A., Frangi, A.F.: Computational cardiac atlases: from patient to population and back. Experimental Physiology (2009)
3. Meier, W.: eXist: An Open Source Native XML Database. LNCS, vol. 2593. Springer, Berlin (2009)
4. Philip, M.P.: Building Cyber-Infrastructure for the Biomedical Informatics Research Network. IEEE Computer Society, Los Alamitos (2006)
5. Cimino, J.J., Hayamizu, T.F., Bodenreider, O., Davis, B., Stafford, G.A., Ringwald, M.: The caBIG terminology review process. Journal of Biomedical Informatics 42(3), Auditing of Terminologies (2009)
6. Warnock, M.J., Toland, C., Evans, D., Wallace, B., Nagy, P.: Benefits of Using the DCM4CHE DICOM Archive. Journal of Digital Imaging (2007)

7. Widenius, M., Axmark, D., DuBois, P.: Mysql Reference Manual. O'Reilly & Associates, Inc., Sebastopol (2002)
8. Heffelfinger, D.: Java EE 5 Development using GlassFish Application Server. Packt Pub. Ltd. (2007)
9. Backhaus, M., Chung, J., Cowan, B.R., Fonseca, C.G., Tao, W., Young, A.A.: The Cardiac Atlas Project: Towards a Map of the Heart. In: Kerckhoffs, R. (ed.) Patient-specific modeling of the cardiovascular system. Springer, Heidelberg (in press)
10. Sezov, R.: Liferay Portal Administrator's Guide, 3rd edn. Liferay Press, Los Angeles (2009)
11. Bellas, F.: Standards for second-generation portals. IEEE Internet Computing (2004)
12. Alur, D., Crupi, J., Malks, D.: Core J2EE patterns. Prentice Hall PTR, Englewood Cliffs (2003)
13. Fleury, M., Lindfors, J.: JMX: Managing J2EE with Java Management Extensions. Sams, USA (2002)
14. Bray, T., Paoli, J., Sperberg-McQueen, C.M., Maler, E., Yergeau, F., Cowan, J.: Extensible markup language (XML) 1.1. W3C Recommendation (2006)
15. Parisot, C.: The DICOM standard: A breakthrough for digital information exchange in cardiology. The International Journal of Cardiac Imaging 11(3) (1995)
16. Gregg, B., DAgostino, H., Toledo, E.G.: Creating an IHE ATNA-Based Audit Repository. Journal of Digital Imaging (2006)
17. Smart, J., Hock, K., Csomor, S.: Cross-Platform GUI Programming with wxWidgets. Prentice Hall PTR, Englewood Cliffs (2005)
18. Rosse, C., Mejino Jr., J.L.V.: A reference ontology for biomedical informatics: the Foundational Model of Anatomy. Journal of Biomedical Informatics (2003)
19. Stearns, M.Q., Price, C., Spackman, K.A., Wang, A.Y.: SNOMED clinical terms: overview of the development process and project status. In: Proc. AMIA Symp. (2001)
20. McGuinness, D.L., van Harmelen, F.: OWL web ontology language overview, W3C recommendation (2004)
21. Gamma, E., Helm, R., Johnson, R., Vlissides, J.: Design patterns: elements of reusable object-oriented software. Lavoisier (1995)
22. Nguyen, D.: Abstract Factory Design Pattern. Connexions (2008)
23. Fonseca, C.G., Backhaus, M., Chung, J.D., Tao, W., Medrano-Gracia, P., Cowan, B.R., Hunter, P.J., Finn, J.P., Shivkumar, K., Lima, J.A.C., Bluemke, D.A., Kadish, A.H., Lee, D.C., Young, A.A.: MICCAI 2010 Workshop on Statistical Atlases and Computational Models of the Heart: Mapping Structure and Function plus a Cardiac Electrophysiological Simulation Challenge (STACOM-CESCÕ 2010), Beijing, China. LNCS. Springer, Heidelberg (2010) (in press)
24. Larrabide, I., Omedas, P., Martelli, Y., Planes, X., Nieber, M., Moya, J.A., Butakoff, C., Sebastian, R., Camara, O., De Craene, M., Bijnens, B.H., Frangi, A.F.: GIMIAS: An Open Source Framework for Efficient Development of Research Tools and Clinical Prototypes. LNCS. Springer, Heidelberg (2009)
25. Toussaint, N.: CardioViz3D: Cardiac Simulation Data Processing and Visualization, User Manual, INRIA Sophia-Antipolis (2008)
26. Digital Imaging and Communications in Medicine (DICOM) (2009)
27. MySQL 5.1 Reference Manual, Functions and Operators, XML Functions, `http://dev.mysql.com/doc/refman/5.1/en/xml-functions.html`
28. XML Path Language (XPath) 2.0, W3C Recommendation (2007), `http://www.w3.org/TR/xpath20/`

29. U.S. Department of Health and Human Services, Privacy Rule, 45 CFR Parts 160, 162, and 164
30. CAP Sourceforge project site, http://sourceforge.net/projects/cardiacatlas/
31. Zope, http://www.zope.org/
32. Plone, http://plone.org/
33. Physiome Model Repository, http://www.cellml.org/tools/pmr
34. JBoss Application Server, JBoss Inc. (2002)
35. CMGUI, http://www.cmiss.org/cmgui
36. Gmm++ Library, http://download.gna.org/getfem/html/homepage/gmm/index.html
37. Cardiovascular Research Grid, http://www.cvrgrid.org/
38. Boost C++ Libraries, http://www.boost.org/
39. World Health Organization, Fact sheet No. 317 (Updated September 2009)

Atlas-Based Quantification of Myocardial Motion Abnormalities: Added-value for the Understanding of CRT Outcome?

Nicolas Duchateau[1], Mathieu De Craene[1], Gemma Piella[1], Corné Hoogendoorn[1], Etelvino Silva[2], Adelina Doltra[2], Lluís Mont[2], M^a Angeles Castel[2], Josep Brugada[2], and Marta Sitges[2], and Alejandro F. Frangi[1,3]

[1] CISTIB, Universitat Pompeu Fabra, CIBER-BBN, Barcelona, Spain
[2] Hospital Clínic - IDIBAPS - Universitat de Barcelona, Spain
[3] ICREA, Barcelona, Spain

Abstract. In this paper, we present the use of atlas-based indexes of abnormality for the quantification of cardiac resynchronization therapy (CRT) outcome in terms of motion. We build an atlas of normal motion from 21 healthy volunteers to which we compare 88 CRT candidates before and after the therapy. Abnormal motion is quantified locally in time and space using a statistical distance to normality, and changes induced by the therapy are related with clinical measurements of CRT outcome. Results correlate with recent clinical hypothesis about CRT response, namely that the correction of specific mechanisms responsible for cardiac dyssynchrony conditions the response to the therapy.

1 Introduction

Cardiac resynchronization therapy (CRT) has become one of the main treatments for improving the condition of patients with advanced heart failure [1]. However, around 30% of the patients implanted with a CRT device fail to clinically respond (around 50% concerning echocardiographic response) [2]. Measuring mechanical dyssynchrony was recently targeted by a large number of trials, looking for a better selection parameter that could outperform the criteria currently used in clinical practice (symptomatic heart failure with long QRS length and low ejection fraction) [3].

Single dyssynchrony indexes based on echocardiographic images showed low predictive value, mainly due to their poor reproducibility in a multi-center context [4]. In addition, the choice of a single parametric approach discards the complexity of the mechanisms responsible for the dyssynchrony of each patient, which explains such a low predictive value [5]. A mechanism-based patient selection strategy has recently been proposed in [6], and contrasts with the previous approaches. The authors first classified patients into specific etiologies of mechanical dyssynchrony, and then studied the response of each class. They concluded that CRT response mainly depends on the ability to correct these specific abnormal mechanisms. Such a strategy also confirmed that understanding the patho-physiological

O. Camara et al. (Eds.): STACOM-CESC 2010, LNCS 6364, pp. 65–74, 2010.

mechanisms amenable to CRT may result more optimal for patient selection than arbitrarily relying on the currently established selection criteria.

Despite these conclusions, the classification of patients and the observations made after the therapy largely relied on visual observations, which questions their reproducibility. More novel methods based on myocardial deformation have also been proposed to study abnormal patterns associated with dyssynchrony [7] [8], but their use in a CRT context is also limited by the reproducibility of the measurements. Higher reproducibility can be achieved by accurately synchronizing patient data to a common spatiotemporal reference anatomy. Patient comparison in terms of cardiac motion and deformation was proposed in [9], [10] and [11], using the framework of statistical atlases. In particular, an atlas-based pipeline for the quantification of myocardial motion abnormalities has recently been described in [12]. This pipeline characterized myocardial velocities of the studied patients according to their distance to normality, in a similar fashion than proposed in [13] for the detection of brain abnormalities. The technique was evaluated in the context of CRT, using a reduced set of patients with one clear specific pattern related to left ventricle (LV) dyssynchrony, namely septal flash (SF) [6].

In this work, we apply this framework to a large database of CRT candidates with a wide spectrum of ventricular dyssynchrony. Our aim is to demonstrate the added value of such an atlas-based distance to normality for the study of response to CRT. We use the local abnormality indexes proposed in [12] to accurately quantify improvements in wall motion induced by CRT. We finally relate the changes in local abnormalities with information about CRT outcome, in order to understand the causes of non-response to the therapy.

2 Methods

2.1 Patient Population

For the present study, data was collected from 21 healthy volunteers, and 88 patients that were candidates for CRT based on current international clinical guidelines (ejection fraction $< 35\%$, QRS duration $> 120ms$, and NYHA classification III-IV). The study protocol was approved by our local ethics committee and written informed consent was obtained from all patients. The baseline characteristics for these subjects are summarized in Tab. 1. Clinical response was defined at follow-up, as an increase $\geq 10\%$ in the 6 min walking test as compared to baseline, or a NYHA functional class reduction ≥ 1 point, in alive patients without heart transplantation. Echocardiographic response was defined as a reduction $\geq 15\%$ in the LV end-systolic volume [2], as measured by one experienced observer. Patients who died or had heart transplantation during the study were considered as non-responders.

Echocardiographic (2D US) sequences in a zoomed-in 4-chamber view were acquired for all these subjects, using a commercially available system (Vivid 7, General Electric, Milwaukee, WI, USA). The examination was performed at baseline (OFF), 24-72 hours after device implantation (ON) and at follow-up

Table 1. Clinical and echocardiographic characteristics for the population of CRT candidates and for the set of volunteers

		CRT candidates		Volunteers
		Baseline	Follow-up	
Age (years)		68 ± 9		30 ± 5
Male gender		64 (73 %)		14 (67 %)
QRS width (ms)		178 ± 29	.	81 ± 10
6 min walking test (m)		289 ± 82	399 ± 130	.
NYHA funcional class	I	0	15 (17 %)	21 (100 %)
	II	23 (26 %)	49 (56 %)	0
	III	56 (64 %)	19 (22 %)	0
	IV	7 (8 %)	0	0
LV end-diastolic volume (mL)		247 ± 88	212 ± 78	104 ± 27
LV end-systolic volume (mL)		186 ± 76	147 ± 66	41 ± 9
LV ejection fraction (%)		25 ± 8	33 ± 9	60 ± 5

(FU), which corresponded in average to 11 ± 2 months after the implant. The sequences were acquired with a breath-hold constraint to minimize the influence of respiratory motion. Resolution was optimized during the acquisition of healthy subjects sequences, and corresponds to an average frame rate of 60 frames/s and a pixel size of 0.24×0.24 mm^2. The temporal resolution of the sequences is lower for the set of CRT candidates (around half the frame rate), as they have dilated hearts and therefore require the use of a broader US sector. Their average pixel size is 0.26×0.26 mm^2.

The choice of using 2D US and in particular the 4-chamber view was lead by the fact that this view is the one used in clinical routine for the assessment of fast abnormal motion patterns related to LV dyssynchrony, as described in [6]. However, the concepts developed in this paper could readily be applied to 3D US and other imaging modalities once the required temporal resolution is available in standard clinical acquisition protocols. The use of real-time 3D echocardiography [14] [15] is particularly of interest to capture out-of-plane motion, which may increase the accuracy of the proposed analysis, and extend it to specific 3D motion patterns currently not captured by our method, such as torsion.

2.2 Atlas-Based Abnormality Indexes

The atlas pipeline described in [12] was applied on the 4-chamber sequences of the two populations described in Sec. 2.1. The choice of a reference among the set of healthy volunteers was addressed using the group-wise normalized mutual information metric proposed in [16], and criteria based on image quality (LV fully visible along the whole sequence, and low heart rate to achieve a higher temporal resolution of the atlas). Statistics on myocardial velocities were computed locally in time and space, at every anatomical location $(\mathbf{x}, t)$ of the reference anatomy. Normal motion was first quantified by computing the average and covariance of myocardial velocities for the set of healthy volunteers. Motion abnormalities were then computed for each individual (both volunteers [using leave-one-out

cross-correlation] and CRT candidates) by calculating a statistical distance to the velocity distribution of the atlas population (Hotelling's T-square statistic). This computation returned a p-value at every location $(\mathbf{x}, t)$ of the myocardial wall, low p-value meaning high degree of abnormality. As these abnormality maps are defined on a 2D+t space, one way of visualizing them is to unfold the LV wall around its medial line and to use time as a second dimension. The representation of the p-value in this space is similar to M-mode echocardiographic images, classically used to visualize wall motion over time. Examples of this representation are given in Fig. 2, focusing on the septum region.

3 Relevance of the Atlas Population

The computation of a distance to normality assumes that we can trust the atlas population as being representative of normality. In this study, the atlas population has non-dilated hearts, no antecedent of cardiac dysfunction, and its baseline characteristics match with the values found in the literature for a population of patients with normal cardiac function [17]. In addition, this population is relatively young (age 30 ± 5 years), which means its cardiac function is preserved from lower efficiency raising up when subjects become older.

Number of subjects. To justify that the statistics are not biased due to the number of subjects in the atlas population ($N = 21$), we computed the evolution of the abnormality index (p-value) depending on the number of subjects $N_s < N$ involved in its computation. This experiment is summarized in Fig. 1, in which the indexes were computed for a reduced set of 14 CRT candidates at each spatiotemporal location $(\mathbf{x}, t)$. These values were normalized towards the value obtained for the largest atlas population, so that the evolution is represented in the same magnitude scale (%). The plot on the left represents this evolution for

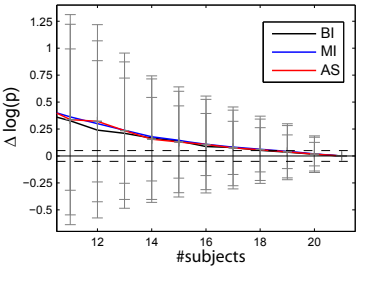

Segment	IVC*	Systole\IVC†	Diastole
BI	17.0 ± 1.6	16.8 ± 1.2	17.9 ± 1.3
MI	16.7 ± 1.0	17.1 ± 1.5	18.0 ± 1.1
AS	17.9 ± 1.5	19.3 ± 1.5	19.4 ± 1.6

* Isovolumic contraction

† Systole excluding the IVC period

Fig. 1. Left: Normalized evolution of the abnormality indexes of one CRT candidate, versus the size of the atlas population. Average over the cardiac cycle and the septal segments (basal inferoseptal [BI], mid inferoseptal [MI], and apical septal [AS]). Error bars represent the standard deviation over 100 random combinations of $N_s < N$ subjects. Right: values above which this evolution stabilizes to its final value ±5% (dashed line), per cardiac segment and temporal window of the cardiac cycle. Average ± standard deviation values over a set of 14 CRT candidates.

Table 2. Shapiro-Wilk (SW) and Lilliefors (LF) tests for the distribution of myocardial velocities from 21 healthy volunteers, at each septal segment. Both components of velocities (radial $\mathbf{v}_\rho$ and longitudinal $\mathbf{v}_\theta$) were treated independently. Bottom line: generation of 21 normally distributed random numbers, repeated 10000 times.

(%)	Segment	SW	LF
$\mathbf{v}_\rho$	BI	89.6 ± 7.4	17.2 ± 5.0
	MI	90.2 ± 7.4	17.0 ± 5.3
	AS	90.3 ± 7.3	16.8 ± 5.0
$\mathbf{v}_\theta$	BI	90.9 ± 7.5	15.9 ± 4.7
	MI	91.2 ± 7.3	15.6 ± 4.7
	AS	90.2 ± 7.4	16.7 ± 5.2
randn(21, 10000)		95.2 ± 0.3	13.1 ± 3.1

the three septal segments of one CRT candidate. For each value of $N_s < N$, the experiment was repeated for 100 random combinations of N_s subjects (vertical error bars). In each spatiotemporal region, the number of subjects above which this evolution stabilizes to its final value $\pm 5\%$ is summarized in the table on the right (average $\pm$ standard deviation over the set of 14 CRT candidates). Based on these values, we can reasonably trust an atlas built with all the available population of subjects (21 volunteers).

Statistical distribution assumptions. The p-value used for the quantification of motion abnormalities is computed from the Hotelling's T-square statistic, under the assumption that the distribution of myocardial velocities over the set of the 21 volunteers is gaussian. We computed the Shapiro-Wilk and the Lilliefors tests at each location $(\mathbf{x}, t)$ to justify this assumption. The results are summarized in Tab. 2, which shows the average values and standard deviation of these tests over the three septal segments, for both components of the velocities treated independently. The last line presents the values of these tests for the generation of 21 normally distributed random numbers, repeated 10000 times. Based on these values, we can reasonably consider that the distribution of velocities is gaussian at each point $(\mathbf{x}, t)$.

4 Clinical Outcome After CRT

4.1 Atlas-Based Quantification of CRT Outcome

We computed p-value maps of abnormality for the set of 88 CRT candidates, as described in Sec. 2.2. These maps are illustrated in Fig. 2 at baseline and follow-up, focusing on the septum region for three candidates. The p-value is represented in logarithmic scale, and pondered by the sign of radial velocity $\mathbf{v}_\rho$ at the same location $(\mathbf{x}, t)$. This mode of representation highlights inward and outward motion of the septum: blue color represents high abnormality with inward motion of the septum, red color being high abnormality for an outward motion. Characteristic

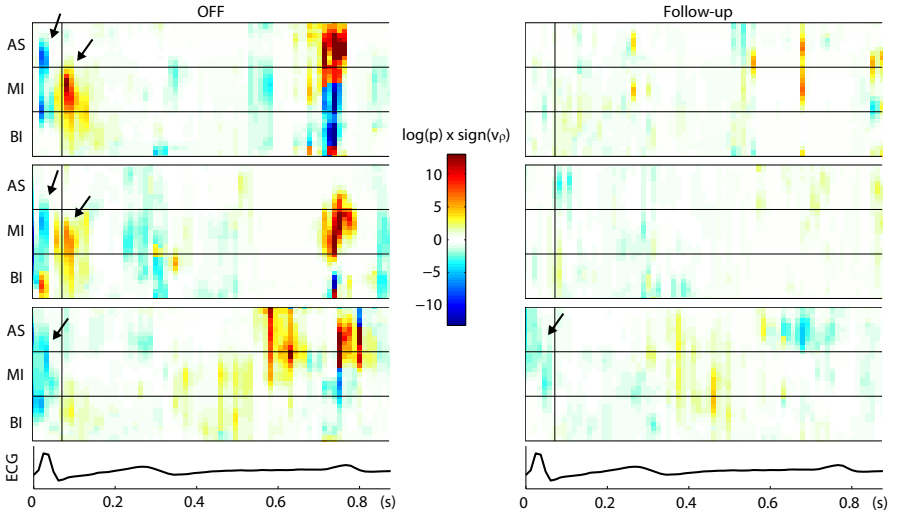

Fig. 2. Abnormality maps in the septal region (vertical axis) for three CRT candidates, at baseline and follow-up: two with SF (top and middle, inward and outward events of SF being indicated by the black arrows), and one with left-right interaction (bottom). The color scale encodes the amount of p-value in logarithmic scale, pondered by the sign of the radial velocity. The vertical line indicates the end of the IVC period.

abnormality patterns are visible on these three patients before the therapy, and can be related to specific types of dyssynchrony: the patients at top and middle rows show a fast succession of blue/red color during the IVC period, corresponding to the inward/outward events of SF. This pattern is not visible anymore on the maps at follow-up. In contrast, the bottom row patient has only inward abnormality during the IVC, corresponding to a left-right interaction dyssynchrony. This pattern, despite a slight reduction, is still visible at follow-up.

4.2 Relation between Abnormality Reduction and CRT Outcome

The follow-up parameters for the set of CRT candidates are displayed in Tab. 1. One patient died during the study, and was therefore considered as non-responder. This patient had SF. Among the 87 remaining patients, experimented clinicians visually detected SF at baseline for 58 of them (67%). This pattern was still present after the therapy for 7 patients (8%). The amount of responders and non-responders for these populations is summarized in Tab. 3.

Regional abnormalities were then compared to CRT outcome for the whole set of CRT candidates, looking for differences between responders and non-responders. Boxplots in Fig. 3 represent the average of the abnormality indexes over temporal intervals of the cardiac cycle and the three septal segments. The indexes were computed at baseline (OFF), after implant (ON), and at follow-up (FU). Indexes for the atlas population are displayed in gray. In this figure, we mainly observe a reduction of systolic abnormalities (IVC and Systole\IVC),

Table 3. Clinical and echocardiographic responders (R) and non-responders (NR) among the set of 88 CRT candidates, the set of 59 patients with SF detected at baseline (58 survived), and the 7 patients for which SF is still present after the therapy

		Clinical	
		R	NR
Echo	R	42	7
	NR	30	9

88 CRT candidates

		Clinical	
		R	NR
Echo	R	36	5
	NR	15	3

59 SF (OFF)

		Clinical	
		R	NR
Echo	R	3	2
	NR	2	0

7 SF (FU)

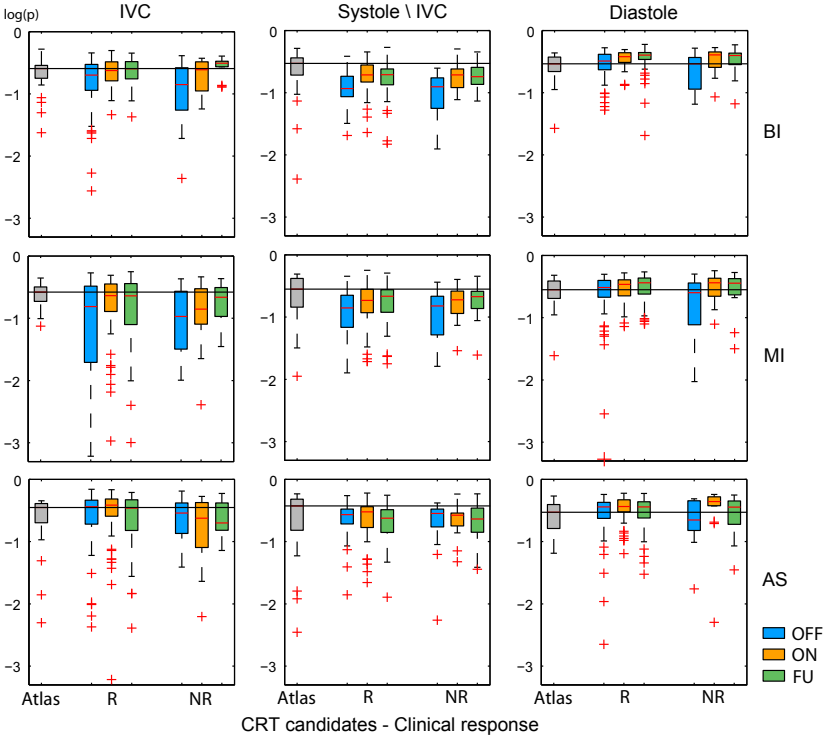

Fig. 3. Comparison of regional abnormality indexes (p-value in logarithmic scale) at baseline (OFF), after implant (ON), and at follow-up (FU). Clustering between responders (R) and non-responders (NR). Average over specific temporal intervals of the cardiac cycle (columns) and septal segments (rows).

at basal inferoseptal and mid inferoseptal levels. Responders show a slightly higher reduction of abnormalities at mid inferoseptal level during the IVC. However, abnormality changes before and after CRT are similar for both responders and non-responders at the other spatiotemporal regions, showing that the therapy improves the motion and the coordination of the cardiac chambers in both groups. This also suggests that global computations of abnormality and in general of dyssynchrony cannot distinguish between responders and non-responders.

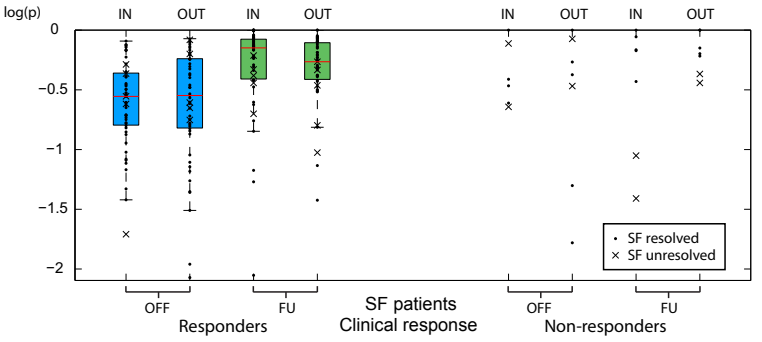

Fig. 4. Comparison of abnormality indexes (p-value in logarithmic scale) for the inward (IN) and outward (OUT) events of SF, at baseline (OFF) and follow-up (FU). Average over the IVC period and the whole septum. Cross symbols indicate patients for which SF is still observed at FU.

Such a conclusion echoes the clinical scepticism about the limited value of single dyssynchrony indexes for the study of CRT response [4] [5].

As a consequence, we specifically looked at the evolution of abnormalities corresponding to SF, with the underlying objective of confirming the hypothesis that the reduction of specific abnormal patterns may be a better predictor of CRT response. This comparison is illustrated in Fig. 4, for the set of 58 patients who were visually diagnosed as SF at baseline, and for which FU information is available. The displayed points represent the average of the abnormality over the whole septum, and over the temporal windows corresponding to the inward ($\mathcal{IN}$) and outward ($\mathcal{OUT}$) events of SF, defined as:

$$\mathcal{IN} = \left\{ t \in IVC \;\middle|\; \mathbf{v}_\rho(t) < 0 \;,\; t < \mathcal{OUT} \right\}$$
$$\mathcal{OUT} = \left\{ t \in IVC \;\middle|\; \mathbf{v}_\rho(t) > 0 \;,\; t > \mathcal{IN} \right\}$$

In this figure, we observe a large reduction of SF abnormalities for the whole set of responders, confirming that a correction of this specific pattern stands for a good predictor of CRT response. As a comparison, in [6], all the patients for which SF was corrected by CRT were responders.

In our study, there were 7 non-responders among the SF population (12 %), for which a case by case examination helps understanding the reasons for non-response: 2 conserved the SF pattern after the therapy (cross symbols on Fig.4); 1 had still highly abnormal dyssynchronous motion, even if SF was resolved; 1 had ambiguous SF at baseline; 2 showed an increase in the 6 min walking test that was not enough to pass the threshold for being considered as clinical responder; and 1 fails to respond without any of these reasons.

Limitations. Myocardial velocities were computed under a small displacements hypothesis and assuming stationarity between the acquired frames, as justified in [12]. This partially limits artifacts resulting from differences in temporal resolution between the set of healthy volunteers and CRT candidates respectively.

The use of 2D+t diffeomorphic tracking of the anatomy [15] will be included to our pipeline in further work to reach better accuracy along the continuous timescale.

In this study, results are displayed against clinical response. The observations made with echocardiographic response lead to less conclusions. This can be interpreted by the fact that CRT is able to correct motion abnormalities and therefore improving patient condition (clinical response), without necessarily reversing cardiac remodelling (echocardiographic response). Complementary details discussing the relevance of clinical and echocardiographic response can be found in [2].

5 Conclusion

In this paper, we demonstrated the use of atlas-based abnormality indexes for the local quantification of cardiac motion improvements induced by CRT, which is particularly relevant for the understanding of CRT outcome. The conclusions from this work correlate with the hypothesis demonstrated in recent clinical trials, namely that the reduction of specific patterns of dyssynchrony conditions the response to CRT. The prediction of response based on baseline data will be studied in further work, and will include the comparison of individuals to groups of patients for which response is known. Future work will also extend the analysis to strain measurements, as the presence of local infarction might affect CRT response, and is not currently taken into account by indexes focusing on motion only.

Acknowledgments. This research has been partially funded by the Industrial and Technological Development Center (CDTI) under the CENIT-CDTEAM and CENIT-cvREMOD programs and by the European Commission's project euHeart (FP7-ICT-224495). Gemma Piella was supported by the Ramón y Cajal Programme from the Spanish Ministry of Science and Innovation. Adelina Doltra was supported by a Post-Residency Award from Fundació Clínic.

References

1. St. John Sutton, M.G., Plappert, T., Abraham, W.T., Smith, A.L., DeLurgio, D.B., Leon, A.R., Loh, E., Kocovic, D.Z., Fisher, W.G., Ellestad, M., Messenger, J., Kruger, K., Hilpisch, K.E., Hill, M.R.S.: Effect of cardiac resynchronization therapy on left ventricular size and function in chronic heart failure. Circulation 107(15), 1985–1990 (2003)
2. Bleeker, G.B., Bax, J.J., Fung, J.W.-H., van der Wall, E.E., Zhang, Q., Schalij, M.J., Chan, J.Y.-S., Yu, C.-M.: Clinical versus echocardiographic parameters to assess response to cardiac resynchronization therapy. American Journal of Cardiology 97(2), 260–263 (2006)
3. Bax, J.J., Abraham, T., Barold, S.S., Breithardt, O.A., Fung, J.W., Garrigue, S., Gorcsan, I., John, D.L.H., Kass, D.A., Knuuti, J., Leclercq, C., Linde, C., Mark, D.B., Monaghan, M.J., Nihoyannopoulos, P., Schalij, M.J., Stellbrink, C., Yu, C.-M.: Cardiac Resynchronization Therapy: Part 1–Issues Before Device Implantation. Journal of the American College of Cardiology 46(12), 2153–2167 (2005)

4. Voigt, J.-U.: Rocking will tell it. European Heart Journal 30(8), 885–886 (2009)
5. Fornwalt, B.K., Delfino, J.G., Sprague, W.W., Oshinski, J.N.: It's time for a paradigm shift in the quantitative evaluation of left ventricular dyssynchrony,". Journal of the American Society of Echocardiography 22(6), 672–676 (2009)
6. Parsai, C., Bijnens, B.H., Sutherland, G.R., Baltabaeva, A., Claus, P., Marciniak, M., Paul, V., Scheffer, M., Donal, E., Derumeaux, G., Anderson, L.: Toward understanding response to cardiac resynchronization therapy: left ventricular dyssynchrony is only one of multiple mechanisms. European Heart Journal 30(8), 940–949 (2009)
7. Delgado, V., Ypenburg, C., Van Bommel, R.J., Tops, L.F., Mollema, S.A., Marsan, N.A., Bleeker, G.B., Schalij, M.J., Bax, J.J.: Assessment of left ventricular dyssynchrony by speckle tracking strain imaging: Comparison between longitudinal, circumferential, and radial strain in cardiac resynchronization therapy. Journal of the American College of Cardiology 51(20), 1944–1952 (2008)
8. Rutz, A.K., Manka, R., Kozerke, S., Roas, S., Boesiger, P., Schwitter, J.: Left ventricular dyssynchrony in patients with left bundle branch block and patients after myocardial infarction: integration of mechanics and viability by cardiac magnetic resonance. European Heart Journal 30(17), 2117–2127 (2009)
9. Rao, A., Chandrashekara, R., Sanchez-Ortiz, G.I., Mohiaddin, R., Aljabar, P., Hajnal, J.V., Puri, B.K., Rueckert, D.: Spatial transformation of motion and deformation fields using nonrigid registration. IEEE Transactions on Medical Imaging 23(9), 1065–1076 (2004)
10. Chandrashekara, R., Mohiaddin, R., Rueckert, D.: Comparison of cardiac motion fields from tagged and untagged MR images using nonrigid registration. In: Frangi, A.F., Radeva, P.I., Santos, A., Hernandez, M. (eds.) FIMH 2005. LNCS, vol. 3504, pp. 425–433. Springer, Heidelberg (2005)
11. Rougon, N.F., Petitjean, C., Preteux, F.J.: Building and using a statistical 3D motion atlas for analyzing myocardial contraction in MRI. In: Proc. SPIE Medical Imaging, vol. 5370, pp. 253–264 (2004)
12. Duchateau, N., De Craene, M., Silva, E., Sitges, M., Bijnens, B.H., Frangi, A.F.: Septal flash assessment on CRT candidates based on statistical atlases of motion. In: Yang, G.-Z., Hawkes, D., Rueckert, D., Noble, A., Taylor, C. (eds.) MICCAI 2009. LNCS, vol. 5762, pp. 759–766. Springer, Heidelberg (2009)
13. Commowick, O., Fillard, P., Clatz, O., Warfield, S.K.: Detection of DTI white matter abnormalities in multiple sclerosis patients. In: Metaxas, D., Axel, L., Fichtinger, G., Székely, G. (eds.) MICCAI 2008, Part I. LNCS, vol. 5241, pp. 975–982. Springer, Heidelberg (2008)
14. Soliman, O.I., Geleijnse, M.L., Theuns, D.A., van Dalen, B.M., Vletter, W.B., Jordaens, L.J., Metawei, A.K., Al-Amin, A.M., ten Cate, F.J.: Usefulness of left ventricular systolic dyssynchrony by real-time three-dimensional echocardiography to predict long-term response to cardiac resynchronization therapy. American Journal of Cardiology 103(11), 1586–1591 (2009)
15. De Craene, M., Piella, G., Duchateau, N., Silva, E., Doltra, A., D'Hooge, J., Camara, O., Sitges, M., Frangi, A.F.: Temporal diffeomorphic free-form deformation for strain quantification in 3D-US images. In: Proc. MICCAI LNCS 2010. LNCS, Springer, Heidelberg (2010) (to appear)
16. Hoogendoorn, C., Whitmarsh, T., Duchateau, N., Sukno, F.M., De Craene, M., Frangi, A.F.: A groupwise mutual information metric for cost efficient selection of a suitable reference in cardiac computational atlas construction. In: Proc. SPIE Medical Imaging, vol. 7623, p. 76231R (2010)
17. Feigenbaum, H.: Echocardiographic measurements and normal values. In: Echocardiography, pp. 658–695. Lea and Febiger, Philadelphia (1994)

Towards High-Resolution Cardiac Atlases: Ventricular Anatomy Descriptors for a Standardized Reference Frame

Ramón Casero[1], Rebecca A.B. Burton[2], T. Alexander Quinn[2], Christian Bollensdorff[2], Patrick Hales[3], Jürgen E. Schneider[3], Peter Kohl[2], and Vicente Grau[4]

[1] Computational Biology Group, Computing Laboratory, University of Oxford, Wolfson Building, Parks Rd, Oxford OX1 3QD, UK
ramon.casero@comlab.ox.ac.uk
[2] Cardiac Mechano-Electric Feedback lab, Dept of Physiology, Anatomy and Genetics, University of Oxford, Sherrington Building, Parks Rd, Oxford OX1 3PT
[3] Department of Cardiovascular Medicine, Wellcome Trust Centre for Human Genetics, University of Oxford, Roosevelt Dr, Oxford OX3 7BN, UK
[4] Institute of Biomedical Engineering, Dept of Engineering Science, and the Oxford e-Research Centre, University of Oxford, Parks Rd, Oxford OX1 3QD, UK

Abstract. Increased resolution in cardiac Magnetic Resonance Imaging (MRI) and growing interest in the effect of small structures in electrophysiology of the heart pose new challenges for cardiac atlases. In this paper we discuss the limitations of current atlas-building models when trying to incorporate cardiac small structure and argue for the need of developing a standard coordinate system for the heart that separates this from the macro-structure common to all individual hearts, in a way analogous to the stereotactic coordinate system from brain atlases. With this goal, we propose a set of methods to obtain two descriptors of the ventricular macro-structure that can be used to build a standardized reference frame: the central curve on the Left Ventricle cavity and the smoothed internal envelope of the Right Ventricle crest (i.e. the curve in the endocardial surface marking the junction between the right ventricular free wall and the septum).

Keywords: computational biology, cardiac atlas.

1 Introduction

Modern work on atlases in medical imaging can arguably be traced back to the identification of anatomical areas in the brain associated to language function by Paul Broca and Carl Wernicke in the second half of the 19th century.

The first brain anatomical atlas was published over a century later [19]. Talairach and Tournoux made two fundamental contributions. First, they proposed a standard coordinate system or reference frame for the brain (the Talairach stereotactic or stereotaxic proportional grid); this coordinate system is uniquely

O. Camara et al. (Eds.): STACOM-CESC 2010, LNCS 6364, pp. 75–84, 2010.

determined by 3 anatomical features: the anterior commissure and posterior commissure points, and the vertical midsagittal plane. Second, they approximately segmented Brodmann areas by visual inspection on each slice of the atlas. While this approach has been very valuable, in particular to analyze information from low-resolution imaging modalities, single-subject or *target* anatomical atlases have limited ability to generalize, do not allow evaluation of morphometric variability and rely on tedious and error-prone visual segmentation of anatomical structures by experts.

To produce a multi-subject or *reference* probabilistic atlas, the Montreal Neurological Institute (MNI) 305 atlas automatically registered 55 Magnetic Resonance Imaging (MRI) brains to the MNI 250 atlas. The MNI 250 atlas was built from 250 normal MRI scans, hand segmented and registered to the Talairach and Tournoux atlas [9]. This atlas was an average of all 305 registered MRI volumes to produce a blurred-out image of the brain's macro-structure.

Building on these approaches, the International Consortium for Brain Mapping (ICBM) was formed in 1993 to develop a probabilistic reference system for the human brain. It has produced to date[1] a target brain from a single subject, the reference ICBM 452 T1 Atlas brain (a probabilistic atlas that is both an average of intensities and shape), and cytoarchitectonic maps registered to the ICBM 452 reference atlas.

Cardiac reference or probabilistic atlas research followed in the steps of brain atlases from the late 1990s. For example, Lelieveldt et al. [14] constructed a very coarse scale three-dimensional (3D) model of heart surfaces (and other thorax organs) from 11 subjects using a hyperquadric implicit shape model and using fuzzy boundary templates for variability. Frangi et al. [11] proposed a probabilistic atlas of ventricular shape truncated at the base, using 3D point distribution models (14 normal subjects). Lorenzo-Valdés et al. [15] extended this work with an intensity probabilistic atlas. A coarse division of the LV in segments (the 16- or 17-segment models [8]) is routinely used in clinical practice, and a prolate spheroid standard coordinate system was proposed in [13].

For a recent review of the field, see Young and Frangi [21], who noted that "probabilistic maps of heart and motion in health and disease, is now an active area of research". Yet, cardiac research is arguably still catching up with some areas of brain research. For example, the ICBM's target brain is labelled and segmented, while the Auckland 2D MRI Cardiac Atlas[2] is labelled but not segmented. Also, the ICBM has scanned thousands of subjects (normal persons, aged 18 to 90 years, with a wide ethnic and racial distribution) [16], compared to the 100 subjects of one of the largest-scale statistical atlases built so far [21].

A challenge for statistical descriptions of anatomy is the distinction between common macro-structure features (e.g. the number of main cavities in the heart) and small details that vary between individuals (e.g. papillary muscles or vessel trees). This becomes more important as advances in imaging and computational models allow studying the effects of microstructure. For the brain, the Zuse

[1] http://www.loni.ucla.edu/ICBM/Downloads/Downloads_Atlases.shtml
[2] http://atlas.scmr.org/

Institute Berlin released a Honeybee Standard Brain atlas[3], that consists of a reference mean shape with the macro-structure of the bee brain, onto which small stochastic structures (e.g. neurons) and function can be mapped [4]. In the heart, this approach has not yet been attempted.

Current shape models typically build on the Point Distribution Model (PDM) paradigm based on Principal Component Analysis (PCA) introduced by Cootes et al. [10] in computer vision in the early 1990s (see e.g. [6] sec. 4.5 for an overview). These models have considered smoothed out versions of cardiac surfaces, possibly for several reasons. First, shapes are built mostly from MRI and Computed Tomography (CT) images, and to date these modalities cannot provide resolutions fine enough *in vivo* to visualize small structures like trabeculae, vessels or the free-running Purkinje System. Second, even if available, high resolution modalities, like histology, produce amounts of data and registration challenges that are at the boundaries of what is feasible computationally and in the wet-lab today. Third, PDMs require a one-to-one correspondence between landmarks and are thus ill-suited to represent small structures that have no correspondence between subjects. Fourth, "Models should be as simple as possible, yet as complex as necessary to address a given question" [12], and clinical global and local function evaluation have historically used measurements that are either qualitative or quantitative at a macro scale, precluding the need for very fine structures (see e.g. [6] Ch. 3 for a detailed review).

While with current technology it is not possible to obtain high resolution *in vivo* images of the whole heart, state of the art wet-lab and *ex vivo* image acquisition techniques make it possible to obtain MRI volumes with paracellular resolution [5,18,20], as illustrated by Fig. 1. Recent results suggest that trabeculae and intramural vessels may affect excitation wavefronts in ways not present in coarser scale models and relevant to arrhythmia induction [1], a wide anatomical variability for the free-running Purkinje System [3], and the role of the intramuscular Purkinje System in the synchronization of activation times in ventricular walls [17]. For most of these structures, their typical distribution and variability within a species and between species is unknown. Hence, it is of great interest to gain a better understanding of this variability from high resolution *ex vivo* images and eventually build mathematical small structure models that can be used to enhance resolution-limited clinical scans improving the realism of computational models.

Current methods to build cardiac probabilistic atlases typically register the images in the training data set to optimize a measure (e.g. sum of squared errors, mutual information) between the voxel intensities or derived features from the images. While these methods have been proven useful in low-resolution analysis, they cannot tackle highly detailed models since, in general, small structures have no anatomical correspondence between images (see Fig. 1). Adding a regularization term to the registration algorithm or downsampling the images removes the small structure information blindly, and thus is not a solution for the given problem.

[3] http://www.neurobiologie.fu-berlin.de/beebrain/

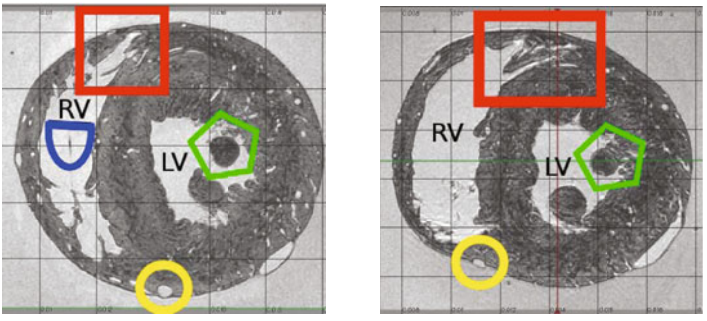

Fig. 1. Structure details in similar short-axis slices in two different MRI rat hearts from our data set: Right Ventricle (RV) crest trabeculae (red rectangle), Left Ventricle (LV) papillary muscle (green pentagon), left descending coronary artery (yellow circle), free running Purkinje network branch (blue semi-ellipse, only in left image)

We propose to find some macro-structure features or descriptors, as in the Talairach stereotactic system, to span a standard coordinate system that allows one to make comparisons between subjects, quantify variability and establish anatomical correspondences. We also propose to follow an approach similar to the Honeybee Standard Brain atlas [4] in the sense of separating the macro-structure of the heart from small anatomical structures. We consider macro-structure the deterministic scaffolding of the heart and main landmarks. All hearts have four chambers (left and right atria and ventricles), four main valves (aortic, mitral, pulmonary and tricuspid) and an apex. Smaller structures (including trabeculae, vessels, the Purkinje System and papillary muscles) are found also in all hearts, but with different topologies and a stochastic distribution. In this paper we present methods for the definition of macro-structure descriptors. We propose two structures present in all hearts, with a clear, simple geometrical definition, anatomically relevant and, most importantly, sufficient to define a coordinate reference system for the two ventricles: the central curve in the Left Ventricle (LV) cavity and the smoothed internal envelope of the RV crest (i.e. the curve on the endocardial surface marking the junction between the right ventricular free wall and the septum), and we propose a sequence of methods to compute them on any heart. Initial results show the ability of the method to detect these structures in high-resolution rat MRI data sets.

2 Wet-Lab Methods and Anatomical Imaging

All investigations reported in this study conformed to the UK Home Office guidance on the Operation of Animals (Scientific Procedures) Act of 1986. Sprague Dowley rat (≈300g, n = 14) hearts were excised and swiftly mounted to a Langendorff system for coronary perfusion with normal tyrode [5]. The hearts were cardioplegically arrested with high K^+ (20mM) solution in their slack (resting) state and fixed via coronary perfusion. Fixation was achieved by perfusing the

heart with Karnovsky fixative [5], being careful to avoid excessive pressure gradients, which have been seen to cause volume overload in the ventricles. Hearts were left overnight in fixative containing 4 mM gadodiamide contrast agent, then washed for 30 min in sodium cacodylate buffer, and embedded in bubble-free 2% low melting agar (containing 4mM gadodiamide).

Anatomical MRI scans were performed using a Varian 9.4 T (400 MHz) MR system (Varian Inc, Palo Alto, CA), and a birdcage coil with an inner diameter of 28mm (Rapid Biomedical, Wurzburg, Germany) to transmit / receive the NMR signals. A 3D gradient echo pulse sequence was used for data acquisition [18,20], with a total scan time of 12 hours. Data were acquired at a typical experimental resolution of $43 \times 43 \times 19$ μm, which was zero filled and written to a stack of TIFF images with a final resolution of 25.4 μm in-plane, 12.7 μm inter-plane.

3 Method for Reference Frame Descriptors

In this section we present a method to obtain two macro-structure descriptors sufficient to establish a standard reference frame of rat ventricle anatomy. In brief, the method produces a central curve in the LV cavity, and an envelope for the RV crest, and it involves a minimum amount of user interaction. Image analysis methods were written using a combination of Matlab functions, and the open source platform Seg3D [4].

1) Cardiac tissue segmentation. The MRI volumes obtained as described above showed a clear tissue/background differentiation and low bias field. We used a threshold, followed by a morphological closing and a subsequent identification of the largest connected component to extract cardiac tissue. A final hole filling algorithm was applied.

2) Computer-assisted hand segmentation of the four ventricular valve annulae. The four main valve annulae were segmented by two experts using the Spline Tool in Seg3D [7], specifically developed for this purpose. The experts scrolled through the MRI volume placing landmarks on each annulus, aided by real-time visualisation of the interpolated curve provided by the tool [7].

3) Ventriculo-atrial surface interpolation. Anatomically, the four annulae belong in a connective tissue layer that electrically insulates the atria from the ventricles. Interpolation of the valve annulae with a smooth surface provides an approximation to the connective tissue layer and a natural boundary between the ventricle and atrium cavities, and the ventricle cavities and pulmonary/aortic arteries. Similar to the method described in [7], PCA was applied to the cloud of annulus landmarks to obtain the three eigenvectors $v_1,\ v_2,\ v_3$ where the corresponding eigenvalues $\lambda_1 \geq \lambda_2 \geq \lambda_3$. The valve plane was made horizontal by computing $\tilde{s}'_i = [v_1\ v_2\ v_3]^\top\ \tilde{s}_i$, for each centered annulus landmark $\tilde{s}_i$, thus avoiding the presence of folds on the valve plane. The rotated annulus points were interpolated using a $f : (x_i,\ y_i) \mapsto z_i$ thin-plate spline (TPS) [2]. Surface points were computed with the TPS, rotated back to span the whole MRI image, and used to segment ventricles from atria (Fig. 2).

[4] http://www.seg3d.org

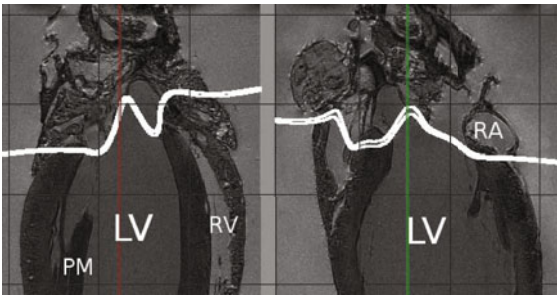

Fig. 2. Detail of interpolated ventriculo-atrial surface in two orthogonal planes. Left ventricle (LV), right ventricle (RV), right atrium (RA), papillary muscle (PM).

4) Ventricle cavities segmentation. The segmented background was eroded by 2 voxels so that it did not touch the external wall of the heart. The ventriculo-atrial surface segmentation was loaded and dilated by 4 voxels. The Connected Component Filter was seeded on the background near the apex to segment the space external to the heart, and dilated by 2 voxels so that it touched the cardiac wall again. This segmentation was combined with the ventriculo-atrial surface using a logical OR operation, producing a boundary for the cavities. Finally, the inverse of the tissue segmentation was loaded again, and the LV and RV cavities segmented using the Connected Component Filter, as illustrated by Fig. 3.

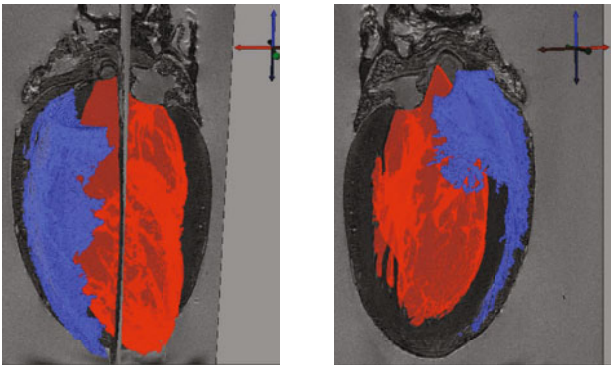

Fig. 3. Segmentation of LV (red) surrounded by RV (blue) cavities. Right image shows the RV outflow tract.

5) Initial calculation of LV reference frame. PCA was computed separately on the coordinates of segmented tissue and LV voxels, to obtain the orthogonal bases of eigenvectors $\{v_1,\ v_2,\ v_3\}$ and $\{w_1,\ w_2,\ w_3\}$, respectively, such that the largest eigenvalue corresponds to v_3, w_3 and the basis is right-hand oriented. A new non-orthogonal basis $\{v_2,\ v_3,\ w_1\}$ was orthogonalized applying Gram-Schmidt with w_1 fixed, i.e. computing matrix Q in a QR decomposition

of $[w_1,\ v_2,\ v_3]$. In this way, the vertical orientation is determined by the LV segmentation (making the LV long axis aligned with the z axis), and the XY-plane orientation is determined by the whole tissue segmentation (making the axis from LV to RV aligned with the X axis). The Q matrix represents a 3D rotation; the centre of rotation m was chosen to be the LV segmentation centroid. The MRI volume and segmentations were centered around m and rotated by $Q^\top$ leaving the heart in a normalised orientation.

6) Papillary muscles segmentation. The middle slice of the LV segmentation was selected, and the regions between the convex hull and the cavity found with an XOR operator. Connected components were computed, and those with large areas were assumed to belong to papillary muscles. Each component was eroded by 25% r voxel, where $a = \pi r^2$, a the component's area in voxel^2, and dilated by 50% r. The resulting area was propagated to the next slice to constrain the search region for papillary muscle voxels. This process iterated slices until the papillary muscle component had no voxels left. An example is provided in Fig. 4.

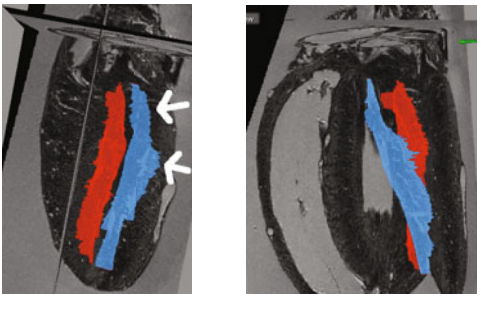

Fig. 4. Segmentation of two papillary muscles (depicted in red and blue) in LV. While small errors in the segmentation are visible in some slices (top white arrow: segmentation beyond chordae tendineae; bottom white arrow: segmentation overflow), for our purpose only an approximate delineation was required to "fill the gaps" in the LV segmentation.

7) Calculation of final coordinate reference frame. The coordinate reference frame calculated in step 5 is affected by the presence of papillary muscles, and thus we recomputed it after eliminating these from the segmented object.

8) Centroid curve from LV cavity extraction. A centroid was computed for each LV segmentation slice. All centroids were interpolated with an approximating natural cubic spline with centripetal parametrisation with smoothing factor $p = 0.999$.

9) RV crest segmentation. The centroid m_{RV} for each RV segmentation slice was computed. Azimuth values were computed for each RV voxel with respect to the LV centroid m_{LV} closest to m_{RV}. The voxels with the most negative and positive values were identified as belonging to the RV crest, i.e. the curve at the junction between the LV and RV. Crest points were replaced by

part of the tricuspid annulus when the azimuth method did not produce a good result in that region.

10) Internal envelope of RV crest computation. The crest segmentation from step 9 is affected by inter-individual variability in the location of RV trabeculae, which is precisely what we want to avoid as explained in detail in the Introduction. Smoothing the crest with a spline is similar to computing a local mean, or downsampling the MRI volume, and is thus not a suitable solution. Instead, we compute the internal envelope of the crest from the point of view of the LV centroids.

The shortest distance d from each crest point to the LV centroid curve was computed. The resulting function was extended on both ends to make it cyclic. Local minima were computed in d, and linearly interpolated to a curve $d_{\min}$. In order to remove local oscillations, the $d_{\min}$ curve was filtered removing $d_{\min}(i)$ if $d_{\min}(i) > d_{\min}(i-1)$ and $d_{\min}(i) > d_{\min}(i+1)$. The remaining points were interpolated with a shape-preserving piecewise cubic curve d_{env} (function `interp1(...,'cubic')` in Matlab) to avoid ringing. The envelope points were computed as an intermediate point at d_{env} on the straight line connecting the crest point and its corresponding LV centroid. The resulting envelope is smooth in the radial direction, but follows the trabeculae in the azimuth direction. Azimuth variations were smoothed out using an approximating natural cubic spline with centripetal parametrisation and smoothing factor $0.90 \leq p \leq 0.99$. The results are displayed for three rat hearts in Fig. 5.

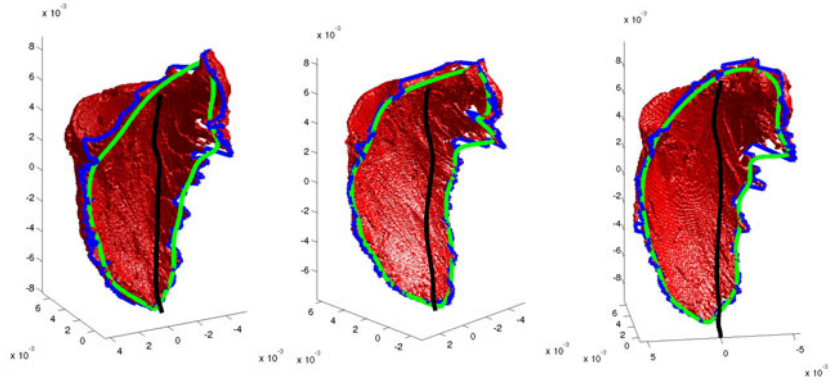

Fig. 5. Reference frame for three rat hearts. RV cavity (red), LV centroid curve (vertical black), RV crest (rugged blue), RV crest envelope (smooth green).

4 Results and Discussion

The methods above were applied to three high-resolution MRI scans of rat hearts acquired as described above. Results of ventriculo-atrial surface interpolation, ventricular cavities segmentation and definition of the reference structures are shown in Figures 2-5. The similarity between the results for three rat hearts

suggests that the descriptors are able to remove the variability caused by small structures while retaining enough information about the macro-structure of the ventricles. Remarkably, the crest envelope produces a corner at the apex, a structure whose reliable discrimination has been a challenge so far. The descriptors also highlight the need to take into consideration the RV outflow tract and the base of the LV in anatomical modelling. These features have usually been ignored in the literature by truncating the ventricles at the base (see e.g. [21]).

There are fundamental difficulties for a quantitative validation since ground truth is not well defined; further validation will arrive with the application of this framework to all 14 hearts available and the study of specific small structures. Also, the robustness of the steps involving manual interaction will be evaluated with inter- and intra-observer variability studies.

The descriptors are sufficient to form the basis of a reference frame for both LV and RV coordinates. As illustrated in Fig. 5, we can define a coordinate reference frame using ideas similar to the prolate spheroidal one described e.g. in [13], extended to include the RV. Similarly to the honey bee project, future work will extract smooth surface boundaries for the inside and outside of the LV and RV. Unlike the honey bee project, though, said surfaces will not be computed from average probabilistic maps, but from surface envelopes (analogous to the RV crest envelope) that separate macro-structure from small details like trabeculae. Mapping the hearts to the reference system will allow one to evaluate and model both macro and small structure variability.

Acknowledgements

The authors thank the financial support of the BBSRC-funded Oxford 3D Heart Project (BB E003443). RC is a postdoctoral researcher in project preDiCT (EC FP7). TAQ is an EPSRC Postdoctoral Fellow. PK is a Senior Fellow of the British Heart Foundation. VG is a Research Councils UK Fellow. This work was made possible in part by software from the NIH/NCRR Center for Integrative Biomedical Computing, P41-RR12553-10; and by the spline computation software in the Qwt project (http://qwt.sf.net).

References

1. Bishop, M.J., et al.: Development of an anatomically detailed MRI-derived rabbit ventricular model and assessment of its impact on simulations of electrophysiological function. Am. J. Physiol. Heart Circ. Physiol. 298, H699–H718 (2010)
2. Bookstein, F.L.: Principal warps: Thin-plate splines and the decomposition of deformations. PAMI 11(6), 567–585 (1989)
3. Bordas, R., et al.: Integrated approach for the study of anatomical variability in the cardiac purkinje system: from high resolution MRI to electrophysiology simulation. In: IEEE EMBC 2010, Buenos Aires (2010) (in press)
4. Brandt, R., et al.: Three-dimensional average-shape atlas of the honeybee brain and its applications. J. Comp. Neurol. 492(1), 1–19 (2005)

5. Burton, R.A.B., et al.: Three-dimensional models of individual cardiac histoanatomy: tools and challenges. Ann. NY Acad. Sci. 1080, 301–319 (2006)
6. Casero, R.: Left ventricle functional analysis in 2D+t contrast echocardiography within an atlas-based deformable template model framework, PhD Thesis, University of Oxford (2008)
7. Casero, R., et al.: Cardiac Valve Annulus Manual Segmentation Using Computer Assisted Visual Feedback in Three-Dimensional Image Data. In: IEEE EMBC 2010, Buenos Aires (2010) (in press)
8. Cerqueira, M.D., et al.: Standardized myocardial segmentation and nomenclature for tomographic imaging of the heart: A Statement for Healthcare Professionals From the Cardiac Imaging Committee of the Council on Clinical Cardiology of the American Heart Association. Circulation 105(4), 539–542 (2002)
9. Collins, D.L.: 3D model-based segmentation of individual brain structures from magnetic resonance imaging data, PhD Thesis, McGill University, Montreal (1994)
10. Cootes, T.F., et al.: Training models of shape from sets of examples. In: BMVC 1992, pp. 266–275 (1992)
11. Frangi, A.F., et al.: Automatic Construction of Multiple-Object Three-Dimensional Statistical Shape Models: Application to Cardiac Modeling. TMI 21(9), 1151–1166 (2002)
12. Garny, A., et al.: Dimensionality in cardiac modelling. Prog. Biophys. Mol. Biol. 87, 47–66 (2005)
13. LeGrice, I., et al.: The architecture of the heart: a data-based model. Phil. Trans. R Soc. Lond. A 359, 1217–1232 (2001)
14. Lelieveldt, B.P.F., et al.: Anatomical Model Matching with Fuzzy Implicit Surfaces for Segmentation of Thoracic Volume Scans. TMI 18(3), 218–230 (1999)
15. Lorenzo-Valdés, M., et al.: Atlas-Based Segmentation and Tracking of 3D Cardiac MR Images Using Non-rigid Registration. In: Dohi, T., Kikinis, R. (eds.) MICCAI 2002. LNCS, vol. 2488, pp. 642–650. Springer, Heidelberg (2002)
16. Mazziotta, J., et al.: A Four-Dimensional Probabilistic Atlas of the Human Brain. J. Am. Medical Informatics Association 8(5), 401–430 (2001)
17. Romero, D., et al.: Effects of the Purkinje System and Cardiac Geometry on Biventricular Pacing: A Model Study. Ann. Biomed. Eng. 38(4), 1388–1398 (2010)
18. Schneider, J.E., et al.: Long-term stability of cardiac function in normal and chronically failing mouse hearts in a vertical-bore MR system. Magnetic Resonance Materials in Physics, Biology and Medicine 17(3-6), 162–169 (2004)
19. Talairach, J., Tournoux, P.: Co-Planar Stereotaxic Atlas of the Human Brain: 3-Dimensional Proportional System. An Approach to Cerebral Imaging. Thieme Medical Publishers (1988)
20. Plank, G., et al.: Generation of histo-anatomically representative models of the individual heart: tools and application. Phil. Trans. Series A, Math., phys., and eng. sciences 367(1896), 2257–2292 (2009)
21. Young, A.A., Frangi, A.F.: Computational cardiac atlases: from patient to population and back. Experimental Physiology 94(5), 578–596 (2009)

Robust Atlas-Based Segmentation of Highly Variable Anatomy: Left Atrium Segmentation

Michal Depa[1], Mert R. Sabuncu[2], Godtfred Holmvang[3], Reza Nezafat[4], Ehud J. Schmidt[5], and Polina Golland[1]

[1] Computer Science and Artificial Intelligence Lab, MIT, Cambridge, MA, USA
[2] Martinos Center for Biomedical Imaging, Massachusetts General Hospital, Boston, MA, USA
[3] Cardiac MRI Unit, Massachusetts General Hospital, Boston, MA, USA
[4] Department of Medicine (Cardiovascular Division), Beth Israel Deaconess Medical Center, Boston, MA, USA
[5] Department of Radiology, Brigham & Women's Hospital, Boston, MA, USA

Abstract. Automatic segmentation of the heart's left atrium offers great benefits for planning and outcome evaluation of atrial ablation procedures. However, the high anatomical variability of the left atrium presents significant challenges for atlas-guided segmentation. In this paper, we demonstrate an automatic method for left atrium segmentation using weighted voting label fusion and a variant of the demons registration algorithm adapted to handle images with different intensity distributions. We achieve accurate automatic segmentation that is robust to the high anatomical variations in the shape of the left atrium in a clinical dataset of MRA images.

Keywords: Atlas-based segmentation, left atrium segmentation, cardiac segmentation, label fusion, non-rigid registration.

1 Introduction

The high anatomical variability of the heart's left atrium makes its segmentation a particularly difficult problem. Specifically, the shape of the left atrium cavity, as well as the number and locations of the pulmonary veins connecting to it, vary substantially across subjects (Fig. 1). In this paper, we propose and demonstrate a robust atlas-based method for automatic segmentation of the left atrium in contrast-enhanced magnetic resonance angiography (MRA) images.

Clinically, left atrium segmentation is a highly relevant problem. Atrial fibrillation is known to be one of the most common heart conditions. It manifests itself by causing irregular contractions of the heart's atria and can have serious consequences such as stroke and heart failure [1,2]. Catheter-based radiofrequency ablation has recently emerged as a treatment for this condition. It involves burning the cardiac tissue that is responsible for the re-entry electrical currents that cause fibrillation. The high anatomical variability of the left atrium shape and the pulmonary veins that enter it presents significant difficulties for

O. Camara et al. (Eds.): STACOM-CESC 2010, LNCS 6364, pp. 85–94, 2010.

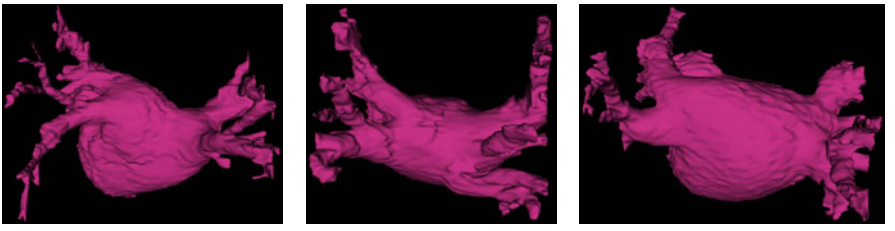

Fig. 1. Manual segmentations of the left atrium in three different subjects, illustrating the variability of the anatomy

cardiac ablation since it is commonly performed at the junction of the atrial body and pulmonary veins. Consequently, accurate visualization of the patient's left atrium promises to substantially improve intervention planning. The knowledge of the shape of the left atrium can also aid in the subsequent segmentation of the resulting ablation scars and thus in the evaluation of the outcome of the procedure [3].

One approach to segment the left atrium is whole heart segmentation, where all of the heart chambers, and sometimes other structures, are included in a single model and segmented simultaneously. Unfortunately, most whole heart segmentation methods do not model the pulmonary veins of the left atrium [4,5]. An exception is [6], where the geometrical model of the heart constructed from CT images includes the pulmonary veins. However, the approach involves building a mean shape model that will face considerable challenges in the presence of topological differences in anatomy.

An alternative approach is to focus on segmentation of the left atrium by first extracting the whole blood pool by intensity thresholding and then separating it into different heart chambers by making cuts at narrowings [7]. This work was extended to allow tracking of centerlines of the pulmonary veins entering the atrium [8,9]. The method however suffers from requiring several thresholds to be set manually because of varying intensity distributions and anatomies of the left atrium across patients.

In this work, we perform the segmentation via a label fusion algorithm [10,11] that uses a training set of MRA images of different patients with corresponding manual segmentations. We first align the training images to the test subject image to be segmented and apply the resulting deformations to the corresponding manual segmentation label maps to yield a set of left atrium segmentations in the coordinate space of the test subject. These form a non-parametric subject-specific statistical atlas. We then use a weighted voting algorithm to assign every voxel to the left atrium or to the background. A similar approach was demonstrated in [12] for segmentation of the aorta and heart extent in CT images. In contrast, we aim to delineate the considerably more complex structure of the left atrium. This requires more powerful label fusion and registration algorithms. Notably, we use a weighted label fusion scheme that assigns higher weights to voxels in training segmentations that are located deeper within the structure of

interest and that have similar intensities in training and test images [11]. We also handle varying intensity distributions between images by incorporating iterative intensity equalization in a variant of the demons registration algorithm [13,14] used for the registration of the training images to the novel test image.

We demonstrate fully automatic, accurate segmentations of both the atrial body and pulmonary veins connected to it on a set of 16 clinical MRA images. Our method captures all of the pulmonary veins in all patients in our dataset. Comparison to traditional atlas-based segmentation and majority voting non-parametric segmentation demonstrates the advantage of the proposed method for this problem.

2 Methods

In this section we describe the registration and segmentation algorithms we employ in this work. We let $\{I_i\}$ be the set of N training images, $\{L_i\}$ be the set of corresponding expert manual segmentations and $\{\Phi_i\}$ be the warps from the training images $\{I_i\}$ to the test image I. Our goal is to estimate the label map L of the test image I.

2.1 Diffeomorphic Demons Registration with Intensity Equalization

We perform pairwise registrations by first aligning the images affinely using a mutual information metric [15], then using a diffeomorphic variant of the demons registration algorithm [16]. The method represents warps Φ with a smooth and stationary velocity field v using a one-parameter subgroup of diffeomorphisms [17]. In this formulation, $\Phi(x) = \exp(v)(x)$, i.e., the flow of the velocity field at time one is equal to its equivalent deformation. In addition to guaranteeing diffeomorphic registration, this parametrization is computationally efficient and offers convenient access to the inverse deformation $\Phi^{-1}(x) = \exp(-v)(x)$. At each iteration, the incremental update velocity field u is found by minimizing the energy function [13]:

$$E(I_F, I_M, \Phi, u) = ||I_F - I_M \circ \Phi \circ \exp(u)||^2 + ||u||^2, \tag{1}$$

where I_F and I_M are the fixed and moving images respectively, and Φ is the warp at the current iteration. The new updated velocity field is then smoothed to optimize a regularization constraint.

One disadvantage of demons registration algorithms is that they are driven by intensity differences between images I_F and I_M. Although the MRA images we work with are of the same modality, the intensity distribution varies from one image to the next. To address this problem, we introduce an intensity transformation:

$$\tilde{I}_M(x) = \sum_{k=1}^{K} \theta_k b_k(I_M(x)) = B(I_M(x))\,\theta, \tag{2}$$

where $\{b_1(\cdot)\dots b_K(\cdot)\}$ is the set of basis functions and $\theta = \{\theta_1 \dots \theta_K\}$ is the vector of corresponding coefficients. This transformation effectively modifies the energy function we are optimizing:

$$E(I_F, I_M, \Phi, u) = ||I_F - B[I_M \circ \Phi \circ \exp(u)]\,\theta||^2 + ||u||^2. \tag{3}$$

Similar to [18], we use polynomial basis functions up to degree K. For a fixed velocity field u, Eq. (3) reduces to a standard linear least squares problem. We thus alternate between estimating coefficients $\{\theta_i\}$ from corresponding voxel pairs in $I_M \circ \Phi$ and I_F (using robust least squares with outlier detection) and performing the standard demons iteration.

2.2 Label Fusion Segmentation

Rather than summarize the training set through average statistics, label fusion algorithms keep the atlas in the form of the original training images with their expert manual segmentations. After registering the training images $\{I_i\}$ to the test image I, we obtain a non-parametric subject-specific atlas composed of N warped images and corresponding label maps.

To perform the segmentation, we use a weighted voting scheme at each voxel, taking into account not only the number of occurrences of each label, but also their locations in the manually segmented structures and the similarity between the intensities of corresponding voxels in the training and test images, similar to [11]. Formally, we compute the maximum a posteriori (MAP) estimate of the label map:

$$\hat{L} = \arg\max_L p(L|I, \{L_i, I_i, \Phi_i\}) = \arg\max_L p(L, I|\{L_i, I_i, \Phi_i\}). \tag{4}$$

We make a simplifying assumption that each voxel is generated from the training set independently from all other voxels. Furthermore, we assume that each training image is equally likely to generate any particular voxel a priori. The MAP estimation then reduces to an independent decision at each voxel:

$$\hat{L}(x) = \arg\max_{l \in 1,\dots,\mathcal{L}} \sum_{i=1}^{N} p(L(x) = l, I(x)|L_i, I_i, \Phi_i) \tag{5}$$

$$= \arg\max_{l \in 1,\dots,\mathcal{L}} \sum_{i=1}^{N} p(L(x) = l|L_i, \Phi_i) p(I(x)|I_i, \Phi_i), \tag{6}$$

where $\mathcal{L}$ is the total number of possible labels ($\mathcal{L} = 2$ in our case). Eq. (6) assumes that the label and intensity values at each voxel of the test image are conditionally independent given the warp Φ_i and the fact that they were generated from training subject i. This decision rule can be viewed as weighted soft voting with $p(L(x) = l|L_i, \Phi_i)$ providing the vote and $p(I(x)|I_i, \Phi_i)$ serving as a weight. We set weights using a Gaussian image likelihood:

$$p(I(x)|I_i, \Phi_i) = \frac{1}{\sqrt{2\pi\sigma^2}} e^{-\frac{1}{2\sigma^2}(I(x) - \tilde{I}_i(\Phi_i(x)))^2}, \tag{7}$$

where $\tilde{I}_i(\Phi_i(\cdot))$ is the training image I_i, registered to the test image I and intensity equalized by applying the intensity transformation estimated during the registration step. The weight is higher when the two corresponding voxels in the aligned images have similar intensities. We define the votes through the label likelihood term:

$$p(L(x) = l|L_i, \Phi_i) \propto e^{\rho D_i^l(\Phi_i(x))}, \tag{8}$$

where $D_i^l(\Phi_i(\cdot))$ is the signed Euclidean distance map of the manual segmentation of the training subject i in the coordinate space of the test subject and ρ is the slope parameter. Voxels that are inside the structure and farther from the boundary are assigned higher votes.

3 Results

We validate our method on a set of 16 electro-cardiogram gated Gadolinium-DTPA (0.2 mmol/kg) contrast-enhanced MRA images (CIDA sequence, TR= 4.3ms, TE=2.0ms, θ=40°, in-plane resolution varying from 0.51mm to 0.68mm, slice thickness varying from 1.2mm to 1.7mm, ±80 kHz bandwidth, atrial diastolic ECG timing to counteract considerable volume changes of the left atrium). We perform leave-one-out experiments by treating one subject as the test image and the remaining 15 as the training set, and repeating for each subject in the dataset. We use the Dice overlap score [19] between the automatic and expert manual segmentations as a quantitative measure of segmentation quality. Dice scores vary from 0 to 1, with 1 corresponding to perfect overlap.

In the label fusion segmentation algorithm, we set $\sigma = 100$ and $\rho = 1.5$. We explored the parameter space by varying σ between 50 and 500, and ρ between 0.3 and 2.5. During this process, we confirmed that our method is in fact robust to the choice of the parameters. The difference between the best and the worst Dice scores obtained for each subject while varying the parameters was 0.05 ± 0.03. We also explored different values for the polynomial degree of the intensity transformation in the registration algorithm. We varied the degree from 1 to 5 and found that it had similarly little effect on the results, with a 0.008 ± 0.007 difference between the best and worst overlap scores for each subject. We chose a degree of 3 because it provided the highest overall Dice scores.

We compare our method of weighed voting (WV) label fusion to three alternative atlas-based approaches: majority voting (MV) label fusion, parametric atlas thresholding (AT) and atlas-based EM-segmentation (EM). The majority voting label fusion is similar to weighted voting, except it assigns each voxel to the label that occurs most frequently in the registered training set at this voxel [10,20]. We also construct a parametric atlas that summarizes all 16 subjects in a single template image and a probabilistic label map by performing group-wise registration to an average space. After registering this new atlas to the test subject, we segment the left atrium using two different approaches. In atlas thresholding, we simply threshold the warped probabilistic label map at 0.5 to obtain the segmentation. We also use this parametric atlas as a spatial prior

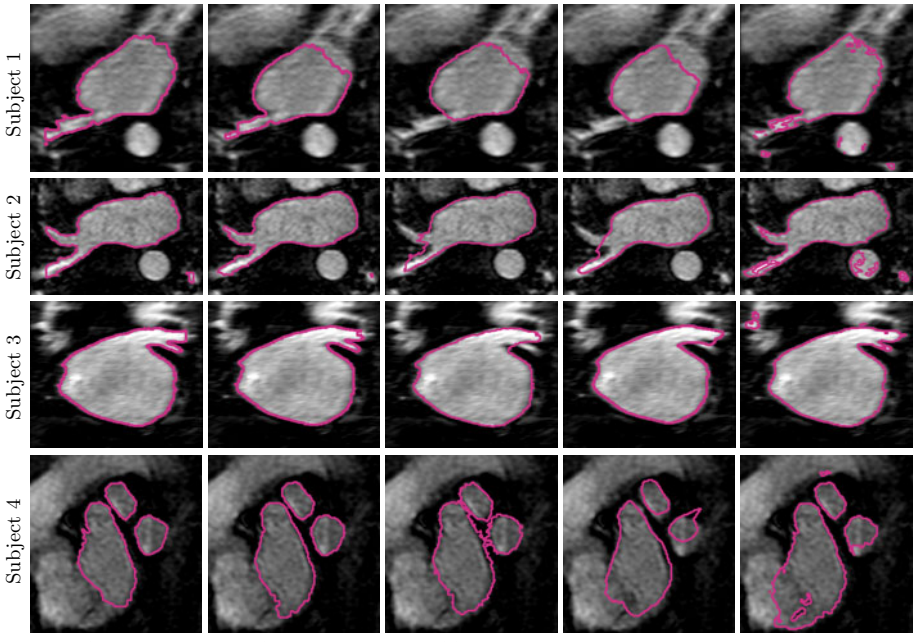

Fig. 2. Example segmentations of four different subjects: (a) expert manual segmentation, (b) weighted voting label fusion (WV), (c) majority voting label fusion (MV), (d) parametric atlas thresholding (AT) and (e) EM-segmentation using the parametric atlas as a spatial prior (EM)

in a traditional model-based EM-segmentation [21]. Note that this construction favors the baseline algorithms as it includes the test image in the registration of all subjects into a single coordinate frame.

In our application, correctly segmenting all of the pulmonary veins of the left atrium is crucial. Therefore it is important to visually inspect the resulting segmentations to fully evaluate them. Fig. 2 shows segmentation outlines of expert manual segmentations and the four methods we compare on corresponding slices of four different subjects. In the first row, majority voting and atlas thresholding miss a pulmonary vein that is correctly identified by our approach. EM-segmentation segments that vein only partially while at the same time producing false positives in the aorta and atrial body. The second and third rows show similar situations. In the last row, all methods correctly segment the pulmonary veins, but our method produces the most accurate outlines. Detailed analysis of all subjects shows that our method does not miss a single pulmonary vein in the whole dataset, in spite of the high anatomical variability.

Fig. 3 reports the segmentation accuracy for each method, as measured by the volume overlap Dice scores. We also report the differences in segmentation accuracy between our method and the benchmark algorithms. To compute the difference

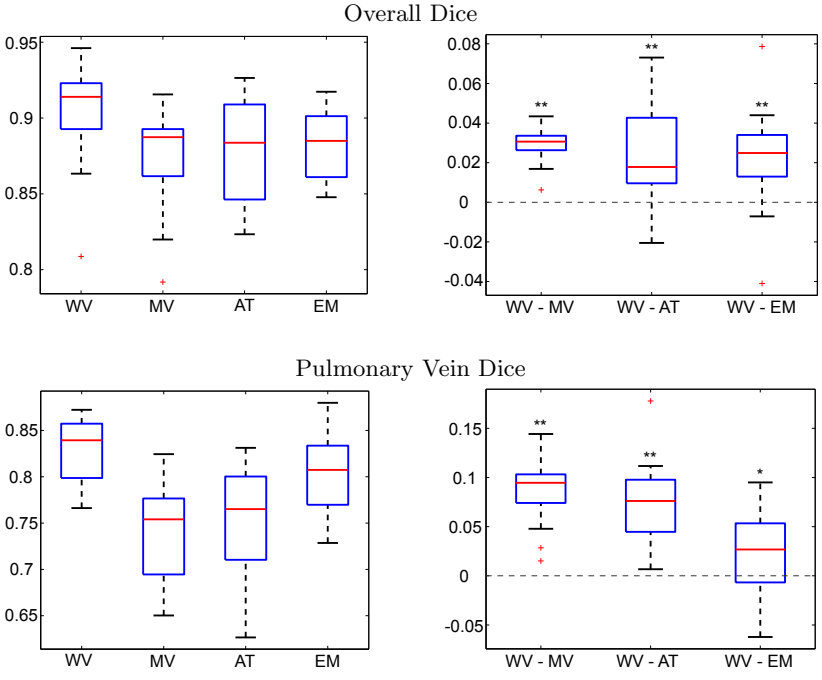

Fig. 3. Dice scores of results for weighted voting label fusion (WV), majority voting label fusion (MV), parametric atlas thresholding (AT) and atlas-based EM-segmentation (EM). For each box plot, the central red line indicates the median, the boxes extend to the 25^{th} and 75^{th} percentiles, and the whiskers extend to the most extreme values not considered outliers, which are plotted as red crosses. Stars indicate that the weighted label fusion method achieves significantly more accurate segmentation than the baseline method (single-sided paired t-test, *: $p < 0.05$, **: $p < 0.01$).

between two methods, we subtract the Dice score of the second method from the score of the first for each subject. Our approach clearly outperforms other algorithms (WV vs. MV: $p < 10^{-9}$, WV vs. AT: $p < 0.002$, WV vs. EM: $p < 0.003$; single-sided paired t-test). To focus the evaluation on the critical part of the structure, we manually isolate the pulmonary veins in each of the manual and automatic segmentations, and compare the Dice scores for these limited label maps. Again, we observe consistent improvements offered by our approach (WV vs. MV: $p < 10^{-7}$, WV vs. AT: $p < 10^{-7}$, WV vs. EM: $p < 0.03$; single-sided paired t-test). Since atlas-based EM-segmentation is an intensity based method, it performs relatively well in segmenting pulmonary veins, but suffers from numerous false positives in other areas, which lower its overall Dice scores.

In Table 1, we present the computational cost for the different methods. The computation time consists of the time needed to perform the registrations and the time required by the segmentation step. We use an ITK implementation of the diffeomorphic demons registration algorithm [14] and implement the segmentation

Table 1. Computation times for different methods

Method	Registration	Segmentation	Total
WV	8 min × 15	5 min	125 min
MV	8 min × 15	0.5 min	120.5 min
AT	8 min	0.1 min	8.1 min
EM	8 min	15 min	23 min

step in MATLAB. The weighted voting and majority voting label fusion methods register all of the training images (15 in our case) to the test subject. Each registration takes on average 8 minutes. The parametric atlas can be computed without any knowledge about the test image. Therefore, the parametric atlas thresholding and the atlas-based EM-segmentation require only a single registration of the atlas to the test subject.

4 Discussion and Conclusions

We demonstrated a non-parametric atlas-based method for automatic left atrium segmentation. This label fusion style approach first registers the whole training set to the test subject and then combines weighted votes from training subjects to make decisions. These votes are computed independently at each voxel and depend on the intensity similarity between the training and test images, as well as the voxel's location in the structure of interest. To handle global shifts in the intensity distribution across images, we modified the diffeomorphic demons registration algorithm to perform iterative intensity equalization during registration.

Experimental results illustrate the capacity of our method to handle high anatomical variability, yielding accurate segmentation and detecting all pulmonary veins in all subjects. By explicitly modeling the anatomical variability represented in the label maps and the corresponding training images, the proposed method outperforms traditional atlas-based segmentation algorithms and a simple label fusion benchmark.

This increased accuracy however comes at the cost of additional computation time since the whole training set needs to be registered to every test subject that is being segmented. Although the weighted voting label fusion approach is more computationally expensive than the other methods, this requirement does not pose a problem in our application because the left atrium segmentation does not need to be produced in real-time. The computation time can be substantially reduced by parallelizing the registration step since the registrations are independent from each other. Moreover, clustering training images, similar to the approach in [22], and using cluster centers as training templates can further reduce the number of necessary registrations. The registration algorithm itself also clearly affects the overall segmentation results and a careful study will be necessary to inform future development of the method.

We found that there was no clear relationship between our method's performance on a specific subject and the number of similar examples in the training set. For example, one subject in our dataset had a pulmonary vein that was not present in any of the other patients. Our method still produced an accurate segmentation of that vein, even with no similar left atrium anatomy in the training set. A more detailed analysis of the effects of sub-populations in the training set on the quality of the resulting segmentations is an interesting future research topic.

In addition to the benefits automatic segmentation offers for the planning stages of cardiac ablation, our method can also assist in the evaluation of the procedure outcome. Segmentation of the ablation scars in post-procedure images is a clinically relevant but difficult problem. Using left atrium segmentation as a prior for scar location is a promising future direction of research we will pursue.

Acknowledgments. This research was supported in part by NAMIC (NIH NIBIB NAMIC U54-EB005149), the NAC (NIH NCRR NAC P41-RR13218), the NIH NINDS R01-NS051826 grant, the NSF CAREER 0642971 grant, and the NIH R01EB008743-01A2 grant. Michal Depa was supported by the Irwin Mark Jacobs and Joan Klein Jacobs Presidential Fellowship and the Julie Payette NSERC Research Scholarship.

References

1. Flegel, K.M., Shipley, M.J., Rose, G.: Risk of stroke in non-rheumatic atrial fibrillation. Lancet 1, 526–529 (1987)
2. Cha, Y.M., Redfield, M.M., Shen, W.K., Gersh, B.J.: Atrial fibrillation and ventricular dysfunction: a vicious electromechanical cycle. Circulation 109, 2839–2843 (2004)
3. Reddy, V.Y., Schmidt, E.J., Holmvang, G., Fung, M.: Arrhythmia recurrence after atrial fibrillation ablation: Can magnetic resonance imaging identify gaps in atrial ablation lines? Journal of Cardiovascular Electrophysiology, 434–437 (2007)
4. Ecabert, O., Peters, J., Weese, J.: Modeling shape variability for full heart segmentation in cardiac computed-tomography images. In: Proc. of SPIE Medical Imaging: Image Processing (2006)
5. Zheng, Y., Barbu, A., Georgescu, B., Scheuering, M., Comaniciu, D.: Four-chamber heart modeling and automatic segmentation for 3D cardiac CT volumes using marginal space learning and steerable features. IEEE Transactions on Medical Imaging 27(11), 1668–1681 (2008)
6. Lorenz, C., von Berg, J.: A comprehensive shape model of the heart. Medical Image Analysis 10(4), 657–670 (2006)
7. John, M., Rahn, N.: Automatic left atrium segmentation by cutting the blood pool at narrowings. In: Duncan, J.S., Gerig, G. (eds.) MICCAI 2005. LNCS, vol. 3750, pp. 798–805. Springer, Heidelberg (2005)
8. Karim, R., Mohiaddin, R., Rueckert, D.: Left atrium segmentation for atrial fibrillation ablation. In: Proc. of SPIE Medical Imaging: Visualization, Image-guided Procedures, and Modeling (2008)
9. Karim, R., Mohiaddin, R., Rueckert, D.: Left atrium pulmonary veins: Segmentation and quantification for planning atrial fibrillation ablation. In: Proc. of SPIE Medical Imaging: Visualization, Image-guided Procedures, and Modeling (2009)

10. Heckemann, R.A., Hajnal, J.V., Aljabar, P., Rueckert, D., Hammers, A.: Automatic anatomical brain MRI segmentation combining label propagation and decision fusion. NeuroImage 33(1), 115–126 (2006)
11. Sabuncu, M.R., Yeo, B.T., Van Leemput, K., Fischl, B., Golland, P.: Nonparametric mixture models for supervised image parcellation. In: Proc. of PMMIA 2009: MICCAI Workshop on Probabilistic Models for Medical Image Analysis, pp. 301–313 (2009)
12. Išgum, I., Staring, M., Rutten, A., Prokop, M., Viergever, M.A., van Ginneken, B.: Multi-atlas-based segmentation with local decision fusion – application to cardiac and aortic segmentation in CT scans. IEEE Transactions on Medical Imaging 28(7), 1000–1009 (2009)
13. Vercauteren, T., Pennec, X., Perchant, A., Ayache, N.: Diffeomorphic demons: Efficient non-parametric image registration. NeuroImage 45(1), S61–S72 (2009)
14. Dru, F., Vercauteren, T.: An ITK implementation of the symmetric log-domain diffeomorphic demons algorithm. Insight Journal (2009)
15. Wells, W.M., Viola, P., Atsumi, H., Nakajima, S., Kikinis, R.: Multi-modal volume registration by maximization of mutual information. Medical Image Analysis 1(1), 35–51 (1996)
16. Thirion, J.P.: Image matching as a diffusion process: an analogy with Maxwell's demons. Medical Image Analysis 2(3), 243–260 (1998)
17. Arsigny, V., Commowick, O., Pennec, X., Ayache, N.: A log-euclidean framework for statistics on diffeomorphisms. In: Larsen, R., Nielsen, M., Sporring, J. (eds.) MICCAI 2006. LNCS, vol. 4190, pp. 924–931. Springer, Heidelberg (2006)
18. Guimond, A., Roche, A., Ayache, N., Meunier, J.: Three-dimensional multimodal brain warping using the demons algorithm and adaptive intensity corrections. IEEE Transactions on Medical Imaging 20(1), 58–69 (2001)
19. Dice, L.R.: Measures of the amount of ecologic association between species. Ecology 26(3), 297–302 (1945)
20. Rohlfing, T., Brandt, R., Menzel, R., Maurer, C.R.: Evaluation of atlas selection strategies for atlas-based image segmentation with application to confocal microscopy images of bee brains. NeuroImage 21(4), 1428–1442 (2004)
21. Van Leemput, K., Maes, F., Vandermeulen, D., Seutens, P.: Automated model-based tissue classification of MR images of the brain. IEEE Transactions on Medical Imaging 18(10), 897–908 (1999)
22. Sabuncu, M.R., Balci, S.K., Shenton, M.E., Golland, P.: Image-driven population analysis through mixture modeling. IEEE Transactions on Medical Imaging 28(9), 1473–1487 (2009)

Atlas-Based Reduced Models of Blood Flows for Fast Patient-Specific Simulations

Kristin McLeod[1], Alfonso Caiazzo[2], Miguel A. Fernández[2], Tommaso Mansi[1], Irene E. Vignon-Clementel[2], Maxime Sermesant[1], Xavier Pennec[1], Younes Boudjemline[3], and Jean-Frederic Gerbeau[2]

[1] INRIA Méditerranée, Asclepios Project, Sophia Antipolis, France
[2] INRIA Rocquencourt, Reo Project, Rocquencourt, France
[3] Service de Cardiologie Pédiatrique, Hôpital Necker-Enfants Malades, Paris, France

Abstract. Model-based interpretation of the complex clinical data now available (shape, motion, flow) can provide quantitative information for diagnosis as well as predictions. However such models can be extremely time consuming, which does not always fit with the clinical time constraints. The aim of this work is to propose a model reduction technique to perform faster patient-specific simulations with prior knowledge built from simulations on an average anatomy. Rather than simulating a full fluid problem on individual patients, we create a representative 'template' of the artery shape. A full flow simulation is carried out only on this template, and a reduced model is built from the results. Then this reduced model can be transported to the individual geometries, allowing faster computational analysis. Here we propose a preliminary validation of this idea. A well-posed framework based on currents representation of shapes is used to create an unbiased template of the pulmonary artery for 4 patients with Tetralogy of Fallot. Then, a reduced computational fluid dynamics model is built on this template. Finally, we demonstrate that this reduced model can represent a specific patient simulation.

1 Introduction

When considering a large set of patient geometries, full flow simulations can be rather costly if they need to be carried out individually on each patient. However, often relevant information about the fluid solution can be extracted from *reduced models*. We present a method which combines an atlas-based technique and model reduction approaches, in order to create a database of *pre-computed* flow characteristics, which enables fast patient-specific flow simulations. This work investigates the validity of applying reduced models and atlas-based methods to decrease flow computational cost, and in particular to examine under which conditions these methods can be useful for obtaining clinically relevant features.

Let us assume to be given a set of individual patient geometries. We construct a template (also called an 'atlas') of the pulmonary artery based on the "currents" approach, as described in detail in [1,2]. In [1], a "forward" model is proposed where the set of shapes (in this case surfaces) are considered as random deformations of an unknown "ideal" template plus some residuals. A key advantage of this

O. Camara et al. (Eds.): STACOM-CESC 2010, LNCS 6364, pp. 95–104, 2010.

framework is that the template is unbiased. Our idea is to perform a full fluid simulation, later called a *direct* simulation, only on an atlas of the population. Results can be used to extract a reduced model which, opportunely mapped back onto particular geometries, can be used to perform faster *reduced* simulations. In particular, the reduced model is based on a Proper Orthogonal Decomposition (POD) of the fluid solution, i.e. a description of the flow field in a lower dimensional space, with a considerably lower number of degrees of freedom.

To illustrate the approach, we applied this method to Tetralogy of Fallot (ToF) patients. ToF is a severe congenital heart defect that requires open heart surgical repair within the first year of life. Understanding the shape of the pulmonary artery and the flow of blood through the artery is crucial for follow-up treatment planning. A fast and effective method to retrieve relevant information about the patient-specific blood flow in the pulmonary artery of ToF patients is motivated by the need of assisting cardiologists in determining the optimal placement and size for valve replacement. But CFD simulations are known to be very time consuming. A model reduction approach could therefore be useful in this context.

Here, considering a data set of 4 ToF patients, we present a preliminary *a posteriori* validation of the model reduction method, comparing the full solution on individual patients with its projection on the POD basis mapped from the template.

2 Model Reduction with Atlas-Based Methods

The pulmonary artery of each patient was segmented from MR angiography as described in Sec. 3.1. Initially, an unbiased template of the artery shape was constructed to serve as a reference atlas for the population.

Blood flow inside the template was simulated numerically, and a proper orthogonal decomposition (POD) of the solution was derived. This decomposition, transported to the individual geometries, may allow to reduce the computational expenses of individual flow simulations. This method is summarized in fig. 1.

2.1 Unbiased Template of the Pulmonary Artery in ToF Patients

The pulmonary artery template is created using the *forward* strategy proposed in [1]. This approach is particularly suited for our purposes as it is non-parametric since shapes are represented by currents, so that the framework can be used for meshes that initially have no point correspondences. However, when the template is mapped to an individual, a one-to-one correspondence between points is established between the template and the mapped individual, which is a useful feature for later applying reduced models that necessitate such a parameterization. Also, the framework has the advantage in that the template is unbiased with respect to the population used to create it. What this means is that adding new patients drawn from the same population at the template creation step will have little effect to the final template.

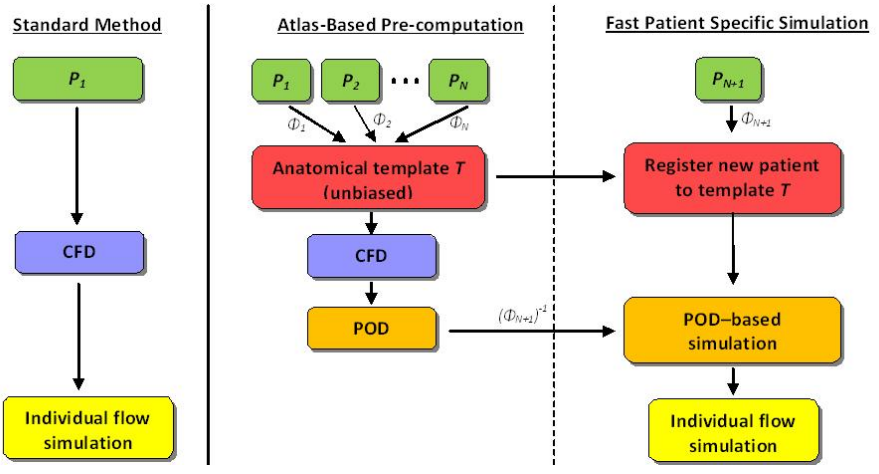

Fig. 1. Left column: the standard method for individual fluid flow simulation. Centre column: pre-computed Computational Fluid Dynamic (CFD) simulation using atlas-based methods, with model reduction using Proper Orthogonal Decomposition (POD). Right column: using the pre-computed fluid simulation and model reduction, fluid simulation can be applied to a new patient quickly, by first registering the template to the patient, then deforming the POD modes using the inverse of this deformation.

The pulmonary artery surfaces $\mathcal{T}^i$, or shapes, are modelled as the sum of a diffeomorphic deformation φ^i of the template $\widehat{\mathcal{T}}$ and a residual term ϵ^i standing for the shape features that cannot be represented by the template (topology changes, acquisition artefacts, etc.): $\mathcal{T}^i = \varphi^i(\widehat{\mathcal{T}}) + \epsilon^i$. Currents are used to represent the shapes, the residuals and the deformations in the same common framework. They enable the usual operations (mean, variance...) on shapes as they form a vector space. Intuitively, currents can be seen as objects that give the flux of any vector field $\omega \in W$ across the shapes. W is a Reproducing Kernel Hilbert Space, RKHS, of infinite dimension generated by a Gaussian kernel $K_W(\mathbf{x}, \mathbf{y}) = \exp(-\|\mathbf{x} - \mathbf{y}\|^2/\lambda_W^2)$ that defines an inner product in W (and also in the dual space of W, W^*). W^* is therefore a vector space of linear mappings from W to $\mathbb{R}$, which is defined as the space of currents.

More precisely, a triangle centred at $\mathbf{x}$ with normal α is represented by the Dirac delta current $\delta_{\mathbf{x}}^{\alpha}$. Therefore, a discrete mesh is encoded by the sum of the currents of its triangles $\mathcal{T}^i = \sum_k \delta_{\mathbf{x}_k^i}^{\alpha_k^i}$. The residuals ϵ^i are modelled as a Gaussian distribution on the α_k^i. The deformation φ^i that registers the template $\widehat{\mathcal{T}}$ to the current $\mathcal{T}^i$ is estimated using the Large Deformation Diffeomorphic Mappings (LDDMM) framework [3]. φ^i is parameterised by a smooth initial vector speed $\mathbf{v}_0^i$, which also belongs to a Gaussian RKHS V with variance λ_V^2. Moreover, this initial speed vector field is completely defined by the *moment* vectors β^i centred at the same point location as the template moments: $\mathbf{v}_0^i(\mathbf{x}) = \sum_k K_V(\mathbf{x}_k, \mathbf{x})\beta_0^i(\mathbf{x}_k)$. Finally, the template $\widehat{\mathcal{T}}$ and the deformations φ^i towards

each patient are estimated by means of an alternate two-step strategy, initialised with the mean current of the population.

2.2 Blood Flow Simulation on the Reference Geometry

Let us denote with $\widehat{\Omega}$ the three dimensional domain defined by the template surface $\widehat{\mathcal{T}}$. This domain is discretized using a tetrahedral mesh $\widehat{\Omega}_h$ (h being the level of refinement of this discretization, see fig. 2, right). Blood flow is simulated solving numerically the incompressible Navier-Stokes equations with a Lagrangian P1 finite element (FE) formulation. In the following, $(\widehat{v}_1, \ldots, \widehat{v}_M)$ denotes the finite element basis, and $(\widehat{\mathbf{u}}_h, \widehat{p}_h)$ denote the velocity and pressure fields computed on the reference domain. For example, the pressure field is decomposed as $\widehat{p}_h(x) = \sum_{j=1}^{M} p_j \widehat{v}_j(x)$, where p_j is the value of p_h at node j. A similar decomposition is used for the velocity.

A flow rate is prescribed at the inlet, with a mean value of 4.2L.min^{-1}. At the outlet a Windkessel model (zero-dimensional model) was coupled to the three-dimensional model to represent the impedance of the distal pulmonary vasculature [4]. Values of the proximal resistance, capacitance and distal resistance are chosen so that the average pressure is 10mmHg and that the pressure ranges from 0mmHg to 25mmHg (since at this stage, these patients have no functioning valve).

Proper Orthogonal Decomposition (POD). A proper orthogonal decomposition (POD) of a numerical solution (or, in general, of a given set of data, see, *e.g.*, [5,6,7]) consists of finding a set of basis functions (orthogonal w.r.t. a given scalar product) which, even containing a small number of elements, can represent sufficiently well the numerical solution. This approach, besides reducing the data size without losing relevant information, allows to perform faster numerical simulations, by restricting the space of the solution to the subspace generated by the POD basis functions.

We computed a POD basis $\left\{\widehat{\boldsymbol{\phi}}_i^{\mathbf{u}}, \widehat{\phi}_i^p\right\}_{i=1}^{N_\text{m}}$ containing N_m modes, with $\widehat{\boldsymbol{\phi}}_i^{\mathbf{u}} : \widehat{\Omega} \to \mathbb{R}^3$ (velocity POD basis functions) and $\widehat{\phi}_i^p : \widehat{\Omega} \to \mathbb{R}$ (pressure POD basis functions), for $i = 1, \ldots, N_\text{m}$. For example, a pressure POD basis function $\widehat{\phi}_i^p$ is known through its decomposition on the finite element basis: $\widehat{\phi}_i^p(x) = \sum_{j=1}^{M} \phi_{i,j}^p v_j(x)$, where $\phi_{i,j}^p$ denotes the value of ϕ_i^p at node j.

2.3 Mapping POD on Individual Geometries

POD provides a reduced description of the flow solution on the template shape. In order to obtain in further studies a suitable representation of the flow in individual patient geometries, with a reduced computational cost, our aim is to transport the template POD on the individual geometry.

Deformation of the Reference Domain. To fix the notation, let us denote with Ω a particular patient geometry, and with $\mathcal{T}$ its external surface. As for the template, we will call Ω_h and $\mathcal{T}_h$ the discretizations of, respectively, Ω and $\mathcal{T}$

(see fig. 2, right). We consider the individual geometry as a *deformation* of the template, assuming to be given a deformation map‘

$$\mathcal{A} : \widehat{\Omega} \to \Omega \tag{1}$$

which maps the reference template onto the individual (deformed) domain. Let $F = \nabla \mathcal{A}$ be the deformation gradient and $J = \det F$ its Jacobian.

Reference POD Transported to Individual Geometries. Through $\mathcal{A}$ we can define a change of variables between the template $\widehat{\Omega}$ and the particular geometry Ω. Hence, the transported pressure POD basis function ϕ_i^p is defined as

$$\phi_i^p(\mathbf{x}) = \widehat{\phi}_i^p\big(\mathcal{A}^{-1}(\mathbf{x})\big) \tag{2}$$

for all $\mathbf{x} \in \Omega$. Yet, for solenoidal vector fields like $\widehat{\boldsymbol{\phi}}_i^{\mathbf{u}}$, the simple change of variables (2) is no longer appropriate. Instead, following [8], we transport the velocity POD basis using the relation

$$\boldsymbol{\phi}_i^{\mathbf{u}}(\mathbf{x}) = \frac{1}{\big|J\big(\mathcal{A}^{-1}(\mathbf{x})\big)\big|} F\big(\mathcal{A}^{-1}(\mathbf{x})\big) \widehat{\boldsymbol{\phi}}_i^{\mathbf{u}}\big(\mathcal{A}^{-1}(\mathbf{x})\big) \tag{3}$$

for all $\mathbf{x} \in \Omega$. Equation (3) is known as the (inverse) Piola transform (see, *e.g.*, [9]). It has the remarkable property that the transform of a divergence free vector field, in $\widehat{\Omega}$, is also divergence free, in Ω.

Computation of the deformation gradient. In practice, information about geometries is only based on a discretization of the surfaces. However, knowing $\mathcal{A}|_{\mathcal{T}}$, even if only on a discretization of the surface, will be sufficient for our purposes. Indeed, in case of moderate deformations, the map $\mathcal{A}$ in the complete volume can be generated as a harmonic extension of $\mathcal{A}|_{\mathcal{T}}$. Next, from the discrete form of $\mathcal{A}$, one can compute an approximation F_h of the deformation gradient,

$$F_h^{\alpha\beta}(\widehat{\mathbf{x}}) = \sum_{i=1}^{M} F_i^{\alpha\beta} \widehat{v}_i(\widehat{\mathbf{x}}),$$

by projecting (for the L^2 norm) $\nabla \mathcal{A}$ on the finite element basis. This can be done solving the linear systems

$$\widehat{M} \left[F_i^{\alpha\beta} \right]_{i=1,\dots,M} = \left[\int_{\widehat{\Omega}} \partial_\beta \mathcal{A}_\alpha(\widehat{\mathbf{x}}) \widehat{v}_i(\widehat{\mathbf{x}}) \, \mathrm{d}\widehat{\mathbf{x}} \right]_{i=1,\dots,M},$$

for each coordinate $\alpha, \beta = x, y, z$, with $\widehat{M} = \left[\int_{\widehat{\Omega}} \widehat{v}_i \widehat{v}_j \right]_{i,j=1,\dots,M}$ the so-called mass matrix. Note that this procedure is convenient to easily get a nodal definition of the deformation gradient (but other options are also possible).

3 Experiments and Results

3.1 Data Collection

Subjects and Image Preparation. We selected 4 young adult patients. MRI angiography of the heart were acquired with a 1.5T MR scanner (Signa HDx, GE Medical Systems). Images were acquired in the short-axis view covering entirely both ventricles and the pulmonary artery (isotropic in-plane resolution: $0.78 \times 0.78mm^2$ to $1.7 \times 1.7mm^2$; slice thickness: 2mm; spacing between slices 1mm).

Surface Meshes Preparation. We segmented the pulmonary artery from MR angiography through image thresholding and manual corrections. The artery was segmented from the pulmonary valve annulus, which connects the artery to the right ventricle, to about 1-2cm after the pulmonary branches, which go towards the lungs. From the resulting binary mask, meshes were extracted using marching cubes algorithm. The meshes were then pre-processed for CFD simulations with 3-MATIC[1] to impose more easily usable boundary conditions. Inlet and outlets were cut by a plane and extended by approximately 1cm (see fig. 2).

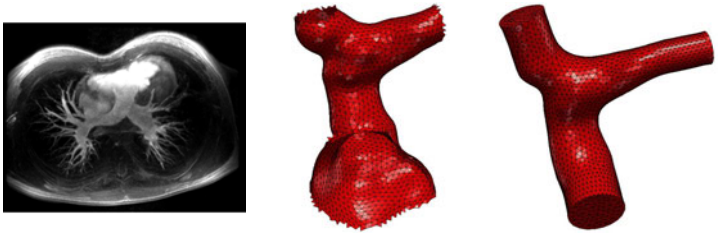

Fig. 2. Left: The raw image before segmentation. Centre: The pre-processed segmented mesh. Right: The same mesh after processing.

3.2 Statistical Shape Model of the Pulmonary Arteries

To estimate the template $\widehat{\mathcal{T}}$, two parameters must be set (Sec. 2.1): λ_V, which defines the "stiffness" of the non-linear deformations (larger λ_V values give more global transformations, i.e. rigid body); and λ_W, which characterises the resolution of the currents representation (for lower λ_W values more subtle shape features can be analysed). As we were mainly interested in the regional ToF alterations (dilation, valve enlargement, regional bulging), these parameters were set to $\lambda_W = 30$mm, $\lambda_V = 5$mm for the template.

Four iterations of the alternate minimisation for the shape template were needed to reach convergence. The resulting template $\widehat{\mathcal{T}}$ was well centred (mean over standard deviation of the deformations was *0.42575*, see fig. 3). Creation of the template took under 16 hours using parallel implementation of the algorithm on Xeon 2.66Ghz cores. In this way, patient-to-template registration is implemented simultaneously, which means that the template creation is minimally

[1] `www.materialise.com`

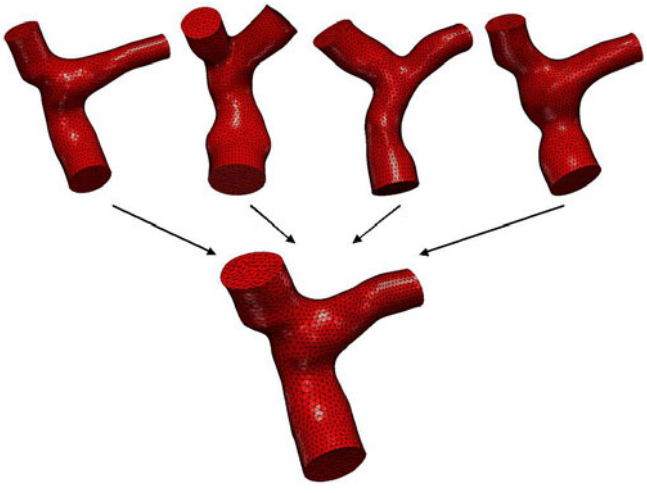

Fig. 3. The four segmented (processed) patient meshes (top row) used to create the template (bottom row)

dependent of the number of patients used to create it. The initialized template creation took under 15 minutes, each parallel implementation of the template-to-patient registration took under 15 minutes, and each template update took between $4 - 6$ hours.

3.3 Validation of Atlas-Based Flow Simulations on the Pulmonary Artery

To verify that the template is unbiased, we created a template with the four patient meshes from this study plus an extra mesh not used in this study, and compared that with template created with four patients. The meshes are shown in fig. 4. As we can see, the templates are very close. The main goal of POD

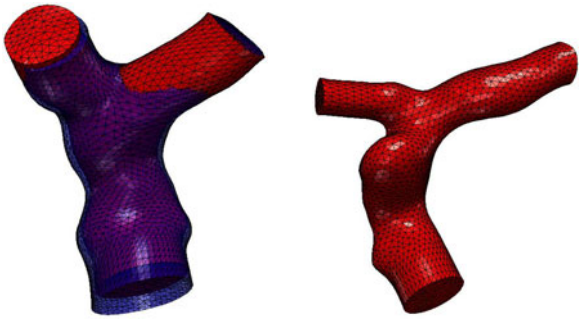

Fig. 4. Left: the template created using five patients (blue) compared to the template created with four patients (red) Right: the extra patient mesh included in the template creation with five patients

is that, once having reduced the number of degrees of freedom of the discrete problem, one can look for a *reduced* numerical solution belonging to the subspace spanned by the POD basis. Hence, POD basis on each individual geometry could be extremely useful to perform fast fluid simulations, without the need of solving a full problem on each new patient geometry. However, it is not assured that the basis computed from the template geometry can represent well the fluid solution on a particular shape. Actually, it is even likely that the transported basis is in general unable to represent correctly the solution in the new geometry. Nevertheless, in the case of Tetralogy of Fallot, we may hope that the variability is sufficiently moderate so that the proposed approach is reasonably accurate.

To assess this conjecture, we performed direct numerical simulations of the flow on the template (fig. 5) and on the four particular geometries, with the same boundary conditions. These numerical solutions $(\mathbf{u}_h, p_h)$ are then L^2-projected onto the spaces

$$U = \text{span}\{\boldsymbol{\phi}_i^{\mathbf{u}}\}_{i=1}^{N_\text{m}}, \quad P = \text{span}\{\phi_i^p\}_{i=1}^{N_\text{m}}$$

spanned by the transported POD basis (given by (3) and (2)). For comparison purposes, the following quantities were computed:

- instantaneous L^2-norm difference in velocity and pressure :

$$\frac{\left\|\mathbf{u}_h - \Pi_U(\mathbf{u}_h)\right\|_{L^2(\Omega)}}{\max_t \left\|\mathbf{u}_h\right\|_{L^2(\Omega)}}, \quad \frac{\left\|p_h - \Pi_P(p_h)\right\|_{L^2(\Omega)}}{\max_t \left\|p_h\right\|_{L^2(\Omega)}};$$

- instantaneous difference in mean inlet and outlet pressures:

$$\max_{i=1,2} \left\{ \frac{\left| p_h|_\text{inlet} - p_h|_{\text{outlet}_i} - \left(\Pi_P(p_h)|_\text{inlet} - \Pi_P(p_h)|_{\text{outlet}_i}\right)\right|}{\left|p_h|_\text{inlet} - p_h|_{\text{outlet}_i}\right|} \right\},$$

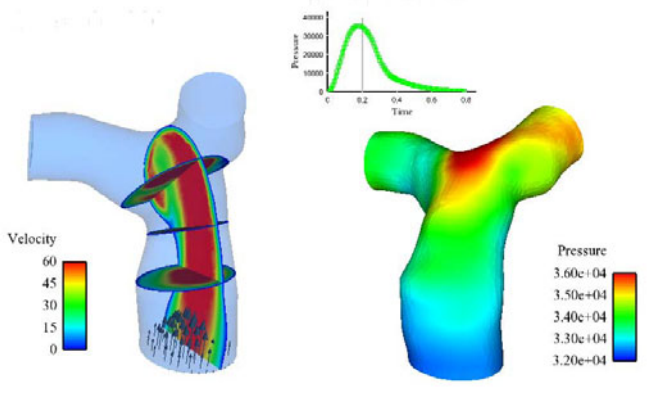

Fig. 5. Flow simulation on the template. Left: velocity (absolute value) on different cutting planes. Right: pressure on the external wall. The curve on top shows the outlet pressure.

where Π_U (resp. Π_P) stands for the L^2-projection onto U (resp. P), given by

$$\int_\Omega \big(\Pi_U(\mathbf{u}_h)\big)(\mathbf{x}) \cdot \boldsymbol{\phi}_i^{\mathbf{u}}(\mathbf{x})\, \mathrm{d}\mathbf{x} = \int_\Omega \mathbf{u}_h(\mathbf{x}) \cdot \boldsymbol{\phi}_i^{\mathbf{u}}(\mathbf{x})\, \mathrm{d}\mathbf{x} \quad i = 1, \ldots, N_{\mathrm{m}}$$

and similarly for the pressure.

The length of time to compute the flow simulations were between $15-20$ mins for a blood cycle. The obtained error curves for the four patients are shown in fig. 6. In three of the four cases, we obtained encouraging results. Taking into account a relatively small number of POD basis functions, relative errors for the fluid solution were below 30%. Here, we chose 20 modes for a time dependent solution represented by 100 snapshots, based on the fact that taking more modes did not significantly decrease the error. One shall remark that the worst behaving case was also the one with largest deformation. Similarly, comparing pressure difference we obtained relatively small errors (from 5% to 20%, for the most deformed geometry).

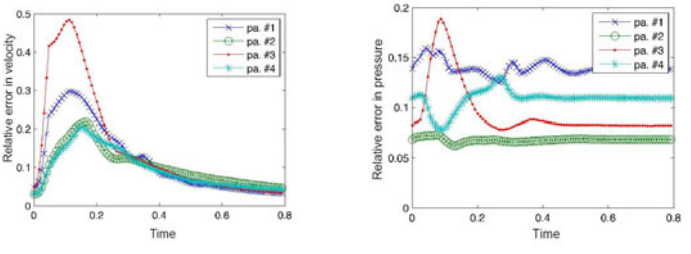

Fig. 6. Error in velocity (norm L^2) and pressure (difference between inlet and outlet) between the full fluid solution on the patient meshes (1,2,3,4) and their projections on the deformed POD basis

4 Discussion and Future Work

The idea proposed in this paper consists of using an atlas of geometries to build reduced order models based on POD. In this preliminary study, we have only tested the approximation properties of the transported POD bases. Owing to the well-known sensitivity of the flow to the geometry, it was not expected to get a high accuracy for details of the flow. Nevertheless, in the case of Tetralogy of Fallot, we have illustrated that it may be possible to get a reasonable accuracy for some quantities of interest like the pressure drop between inlet and outlet. For the template creation, four iterations were required to satisfy the conditions for convergence, therefore the total time to create the template was lengthy. However, visual inspection of the corresponding meshes showed very small changes along these iterations. In future work it may be interesting to investigate further the best convergence conditions for the template update to optimize the template creation time while preserving the necessary features of the shape for flow simulation. The quality of the results could also be improved

by computing the template POD basis for more snapshots, coming from different template geometries and different physiological situations. The transported bases will then be used to actually discretize the model and run reduced order simulations, with patient specific boundary conditions.

References

1. Durrleman, S., Pennec, X., Trouvé, A., Ayache, N.: A forward model to build unbiased atlases from curves and surfaces. In: Pennec, X., Joshi, S. (eds.) Proc. of the International Workshop on the Mathematical Foundations of Computational Anatomy, (MFCA 2008) (2008)
2. Durrleman, S., Pennec, X., Trouvé, A., Ayache, N.: Statistical Models of Sets of Curves and Surfaces based on Currents. Medical Image Analysis 13(5), 793–808 (2009)
3. Vaillant, M., Glaunes, J.: Surface matching via currents. In: Christensen, G.E., Sonka, M. (eds.) IPMI 2005. LNCS, vol. 3565, pp. 381–392. Springer, Heidelberg (2005)
4. Vignon-Clementel, I., Figueroa, C., Jansen, K., Taylor, C.: Outflow boundary conditions for 3D simulations of non-periodic blood flow and pressure fields in deformable arteries. Computer Methods in Biomechanics and Biomedical Engineering 111(3), 502–513 (2010)
5. Wu, C., Liang, Y., Lin, W., Lee, H., Lim, S.: A note on equivalence of proper orthogonal decomposition methods. J. Sound Vibration 265(5), 1103–1110 (2003)
6. Bergmann, M., Bruneau, C., Iollo, A.: Enablers for robust POD models. Journal of Computational Physics 228(2), 516–538 (2009)
7. Rathinam, M., Petzold, L.: A new look at proper orthogonal decomposition. SIAM Journal on Numerical Analysis 41(5), 1893–1925 (2004)
8. Løvgren, A., Maday, Y., Rønquist, E.: The reduced basis element method for fluid flows. In: Analysis and simulation of fluid dynamics. Adv. Math. Fluid Mech., pp. 129–154. Birkhäuser, Basel (2007)
9. Ciarlet, P.: Mathematical elasticity. Vol. I. Studies in Mathematics and its Applications, vol. 20. North-Holland Publishing Co., Amsterdam (1988); Three-dimensional elasticity

Image and Physiological Data Fusion for Guidance and Modelling of Cardiac Resynchronization Therapy Procedures

YingLiang Ma[1,*], Simon Duckett[1], Phani Chinchapatnam[1], Anoop Shetty[1], C. Aldo Rinaldi[2], Tobias Schaeffter[1], and Kawal S. Rhode[1]

[1] Division of Imaging Sciences, King's College London, The Rayne Institute, St Thomas' Hospital, London SE1 7EH, United Kingdom
[2] Department of Cardiology, Guy's and St Thomas' Hospitals NHS Foundation Trust, London SE1 7EH, United Kingdom
y.ma@kcl.ac.uk

Abstract. Cardiac resynchronization therapy (CRT) can be an effective procedure for patients with heart failure but 30% of patients do not respond. This may be partially caused by the sub-optimal placement of the left ventricular (LV) lead. Detailed cardiac anatomy and dyssynchrony information could improve optimal LV lead placement. As a pre-interventional imaging modality, cardiac magnetic resonance (MR) imaging has the potential to provide all the relevant information. Whole heart MR image data can be processed to yield detailed anatomical models including the coronary veins. Cine MR data can be used to measure the motion of the LV to determine which regions are late-activating. Finally, late Gadolinium enhancement imaging can be used to detect regions of scarring. This paper presents a complete software solution for the guidance of CRT using pre-procedural MR data combined with live X-ray fluoroscopy. The platform was evaluated using 7 live CRT cases. For each patient, a detailed cardiac model was generated and registered to the X-ray fluoroscopy using multiple views of a catheter looped in the right atrium. There was complete freedom of movement of the X-ray system and respiratory motion compensation was achieved by tracking the diaphragm. The registration was validated using balloon occlusion coronary venograms. The mean 2D target registration error for 7 patients was 1.3 ± 0.68 mm. All patients had a successful left lead implant.

Keywords: cardiac resynchronization therapy, fluoroscopy overlay, motion compensation, interventional guidance.

1 Introduction

Cardiac resynchronization therapy (CRT) can be an effective procedure for patients with heart failure but more than 30% of patients do not respond [1]. X-ray imaging alone is used to guide placement of pacemaker leads for CRT, but this modality provides little functional or anatomical information to the cardiologist. Lead placement is performed by steering relatively "blindly" which contributes to procedural failure

* Corresponding author.

O. Camara et al. (Eds.): STACOM-CESC 2010, LNCS 6364, pp. 105–113, 2010.

rates of 5 to 12%. Furthermore, leads placed in sub-optimal positions may contribute to the high non-response rate [2]. Previous work with overlay technology has demonstrated that fusion of computed tomography and fluoroscopy may support electrophysiologists in more accurate delivery of therapy during atrial fibrillation ablation [3]. Recent examples [4, 5] have demonstrated that a similar overlay approach using magnetic resonance imaging (MRI) fused to X-ray fluoroscopy is a powerful combination for CRT procedure guidance. MRI offers unique soft tissue contrast without the use of ionizing radiation for depicting coronary vein morphology, quantifying myocardial dyssynchrony, and identifying scar tissue. It is widely believed that these elements are key determinants of clinical outcomes for CRT and that they should be used for patient selection, procedural planning, and guidance.

Cardiac magnetic resonance (CMR) imaging provides a potential complete imaging solution for CRT patients. Whole heart MRI can provide knowledge of the anatomy of the coronary veins which is increasingly important in CRT. Failure to implant a left ventricular (LV) lead is often due to inability to cannulate the coronary sinus (CS) or unfavorable venous anatomy resulting in the inability to find a stable lead position [6]. In addition, the whole heart MRI data can be processed with automatic segmentation tools to produce patient-specific ventricular and atrial anatomical models [7]. The combination of the chamber and coronary venous models can then be used as a 3D roadmap for procedure guidance. Furthermore, cine MRI can provide information about the motion of the LV. Automatic motion analysis software, such as the TomTec 4D LV Analysis tool (TomTec Imaging Systems, Munich, Germany), can give information about the latest activating regions, thought to be important targets for lead delivery. This functional information is often provided to the cardiologist using the standard 16 segment American Heart Association (AHA) model of the LV. CMR also allows assessment of myocardial scar using late Gadolinium enhancement. It is known that positioning an LV lead within areas of scar reduces response to CRT. Segmenting and registering the position and extent of myocardial scar and overlaying this information on to X-ray fluoroscopy could assist the cardiologist during the implant to avoid these areas.

The fusion of anatomical and functional data from CMR to X-fluoroscopy is not only useful for the guidance of CRT procedures but also provides rich data for the validation and testing of patient-specific cardiac biophysical models [8]. The fusion environment allows the mapping of catheter-based measurements to the CMR data [9], providing more data for i*n-silico* modelling.

In this paper, a complete software solution for the guidance of CRT by using preprocedural MRI data combined with live X-ray fluoroscopy is presented. The proposed solution explores all the ideas described above and has been tested on 7 live clinical CRT cases. This patient cohort was used to evaluate the performance of the software in terms of registration accuracy and robustness to the clinical workflow, with the aim that the software will be used at a later stage for a large scale randomized clinical study looking at the clinical outcomes of image-guided versus non-guided implantation.

2 Methods

All patients fulfilled the criteria for CRT. Prior to their implants, they all underwent CMR (Philips 1.5T Achieva, Phillips Healthcare, Best, The Netherlands)). All image-guided

CRT procedures were performed using a single plane flat-panel cardiac X-ray system (Philips Allura Xper FD10) in the catheterization laboratory by a single experienced operator. The overall workflow of the CRT overlay is shown in figure 1.

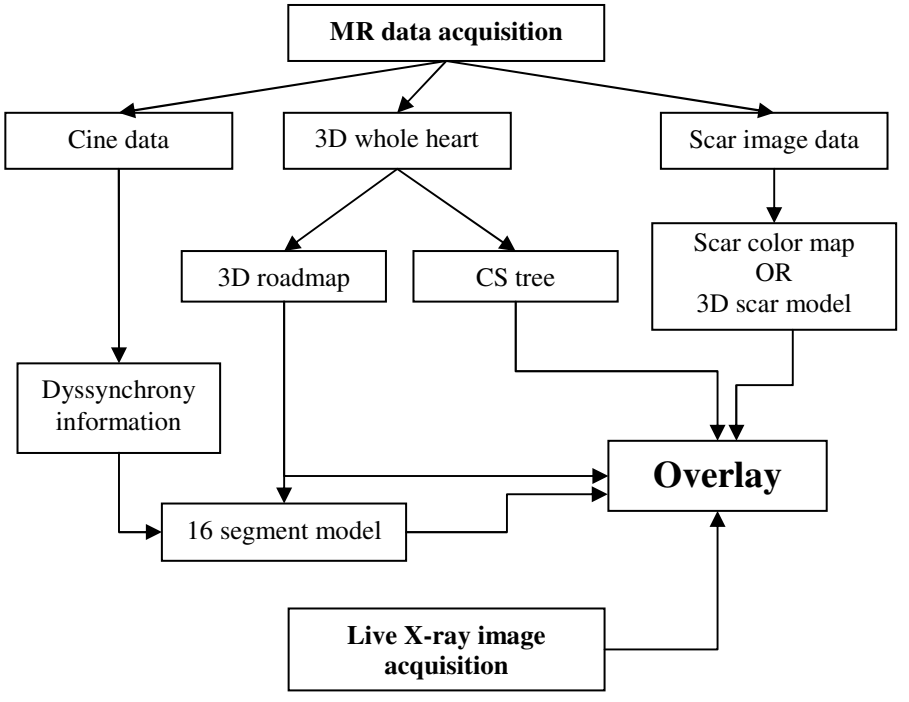

Fig. 1. The overall workflow of the CRT overlay

2.1 MR Imaging and Anatomical Model Generation

For all patients both respiratory- and cardiac-gated CMR images were acquired prior to the implant on a Philips Achieva 1.5T MR system. Cardiac synchronization was performed with vector electrocardiography (VECG). After localization and coil sensitivity reference scans, an interactive real-time scan was performed to determine the geometry of the short axis (SA), four (4CH), three (3CH) and two chamber (2CH) views. A multiple slice (M2D) cine steady state free precession (SSFP) scan was performed in SA orientation to assess the ventricular function (FA=60°, TR/TE=2.9/1.5ms, resolution 2.2x2.2x10mm, 30 heart phases). Visual assessment of the 3Ch view (FA=60°, TR/TE=3.0/1.5ms, 60 heart phases) was used to determine end-systole. For contrast enhanced MRI of the coronary veins, dimeglumine-gadobenate (Gd-BOPTA) (Bracco Imaging SpA, Milan, Italy) was infused with subsequent saline flushing as proposed by Bi *et al.* [10] for coronary arteries. In order to determine the optimal start point of the whole heart coronary vein MR-scan, a dynamic ECG-triggered 2D-scan with inversion recovery (IR) preparation (TI=300ms) was used. For coronary vein visualization, an ECG-triggered respiratory navigated 3D IR-SSFP MR-scan was applied to acquire the

whole-heart during a short interval (60-80ms) in end-systole using the following parameters: FA=50°, TI=300ms, TR/TE=4.25/1.44ms, resolution was 1.5 x 1.5 x 2mm (contiguous slices). A SA stack of late Gadolinium enhancement imaging was performed after the 3D whole heart imaging.

The endocardial surfaces of the right ventricle, left atrium and right atrium and the epicardial surface of the LV were extracted automatically by using a model-based segmentation algorithm [7] from the 3D IR-SSFP whole heart image data. The reason for using the epicardial surface of the LV is that the implanted left lead is placed on the epicardial surface through the coronary veins. All segmentations allowed for manual adjustments when required. In addition, the CS was manually segmented from whole heart image data by a clinical expert using ITK-SNAP [11] to yield a highly detailed anatomical model, which included the CS main branch and three sub-branches (figure 2).

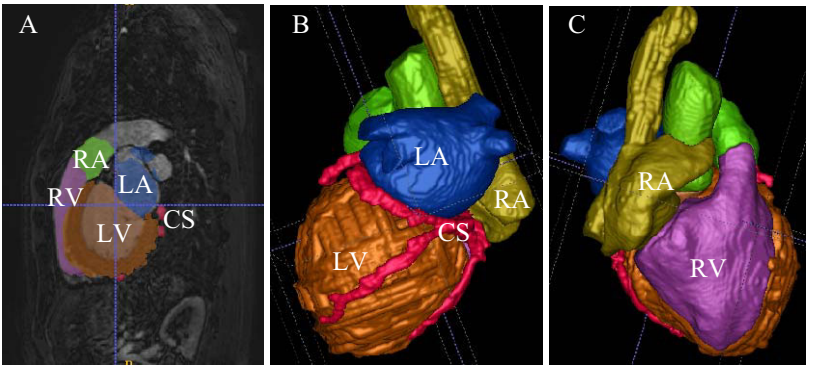

Fig. 2. Whole heart segmentation using a model-based segmentation algorithm. There were some manual corrections to the LV and right atrium (RA). The CS was manually segmented. LA = left atrium. RV = right ventricle. (A) Color labeled whole heart segmentation. (B)(C) 3D anatomical models.

2.2 LV Motion Analysis

TomTec 4D LV Analysis is a software solution to analyze and visualize LV function and LV dyssynchrony in cardiac cine MR image data. As shown in figure 3A, the LV surface has been divided into 16 segments according to the definition of the AHA model (figure 3B). Based on regional volume, 16 mechanical delay motion curves are generated (figure 3C). Prior to the CRT procedure, the cardiologist chooses the segment which has the latest activation according to the motion analysis. As the TomTec software does not support export of the 16 segment model, functionality to generate the AHA model from the MR image data was added to the guidance software solution and the latest activating segment was marked.

2.3 Scar Processing

In patients with myocardial scarring, the position and extent was determined from the late Gadolinium enhanced MR images. These image data were registered to the whole

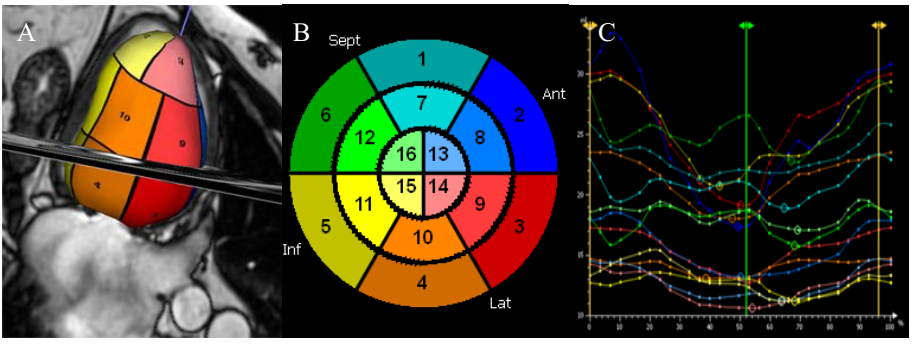

Fig. 3. (A) 16 segment AHA model generated from whole heart MR image data. (B) Bull's eye definition. (C) 4D LV mechanical delay motion curves.

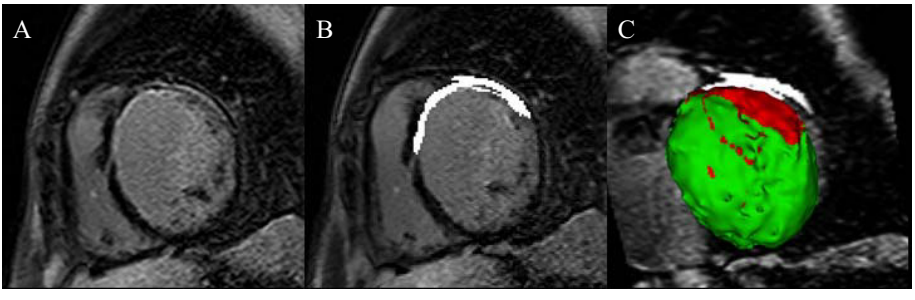

Fig. 4. (A) Original MR late Gadolinium enhancement image. (B) Manual segmentation of myocardial scar. Scar tissue is labeled in white. (C) The 3D scar was presented as a binary map on the LV surface. Scar tissue is labeled in red on the LV surface.

heart MRI data. The scar information was transferred to the anatomical models in 2 ways: firstly, the 3D myocardial scar was manually segmented by a clinical expert using ITK-SNAP. The scar was then visualized as a 3D entity as part of the anatomical model; secondly, a more automated approach was taken as described in [12]. In this approach, the scar information is projected on to the LV epicardial surface using a maximum intensity projection. This data is then binarised to give a regional distribution of scar on the LV epicardial surface (figure 4). Both methods were used and the cardiologist was able to select either type of visualisation during the implant.

2.4 Fluoroscopy Overlay

An overlay platform was developed based on the Philips EP Navigator environment and as an extension to our guidance system for cardiac electrophysiology procedures [13, 14]. This platform allows for the manual registration of pre-procedural anatomical data to live X-ray images. For each patient, the anatomical model was imported and overlaid on to the live X-ray images to guide the procedure. The registration of the MRI and the X-ray data was achieved using multiple views (at least 3) of a catheter looped in the right atrium as a feature for manual registration (figure 5A), taking

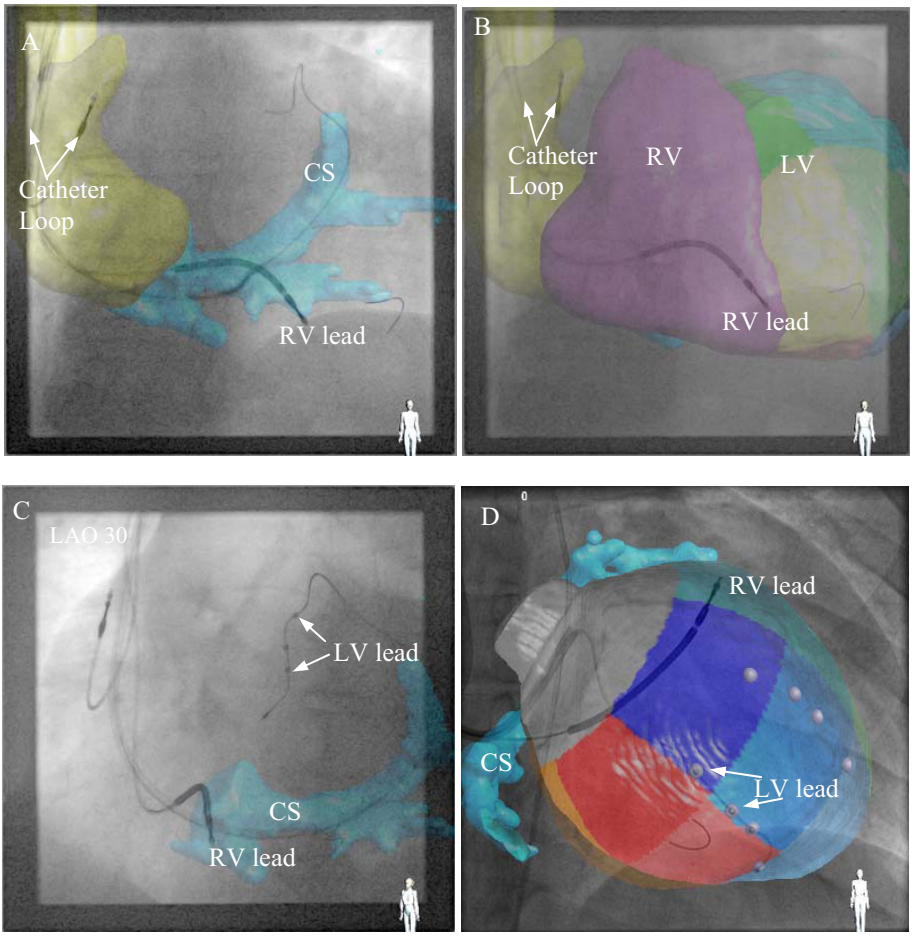

Fig. 5. (A) Using a catheter loop to register the 3D anatomical model with the X-ray fluoroscopic images. (B) The clinical overlay screenshot shows RV (right ventricle), RA (right atrium) and CS. (C) This screenshot shows the CS overlay in LAO (left anterior oblique) 30 view. (D) Using the 16 segment AHA model to show latest activating region. Grey spheres are the 3D LV lead positions (current and previous), which have been projected to the LV surface.

less than 5 minutes. As the guidance platform received the live X-ray stream from the Philips Allura X-ray system and the positions of the C-arm and X-ray table during the implant procedure, alignment between the anatomical model and the live X-ray images was automatically maintained throughout the procedure as long as the patient did not move on the X-ray table. To compensate respiratory motion in real-time, the left or right hemi-diaphragm was tracked in the 2D X-ray images using mean squared difference between a current image and a reference image within a pre-defined region of interest (figure 6A). The 1D translation along the long axis of the region of interest was calculated. A simple translational model similar to the one commonly employed

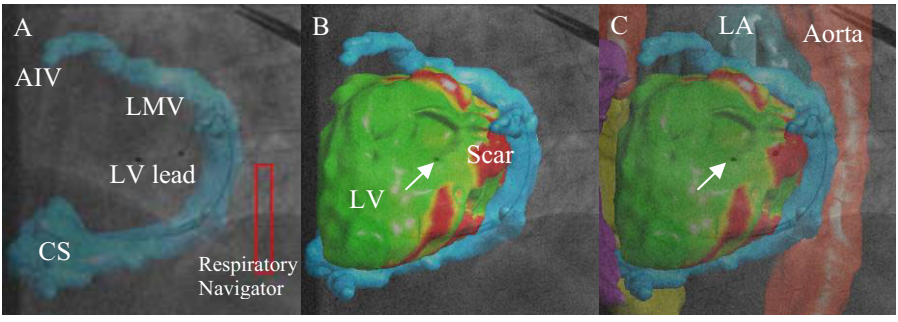

Fig. 6. Anatomical models derived from 3D cardiac whole heart MR images registered as an overlay to real-time fluoroscopy. This patient had myocardial scar which has been registered to the LV and is depicted as the red region on the overlay. (A) to (C) LAO projections showing the overlay being used for implantation of the LV lead. The left marginal vein (LMV) is being used and it can be seen that this is close to an area of scar. In figures (B) and (C) the arrow shows the position of the LV lead. AIV=Anterior inter-ventricular vein.

in MRI image acquisition [15] was used to apply the 1D displacement of diaphragm to the 3D anatomical roadmap. The 1D motion correlation factor between diaphragm and heart was 0.6. The 3D heart roadmap was translated along the head to foot vector of the patient.

2.5 Validation of 2D-3D Registration

During the procedures, several screenshots of the guidance platform software were taken when venography was performed with an occlusion balloon catheter (figure 7A, 7B). Those screenshots were used to evaluate the accuracy of registration between the 3D anatomical models and the live X-ray fluoroscopy. The distance errors between the centre line of the main branch of the CS in the 3D anatomical models and the occlusive venogram in the 2D X-ray images were calculated (figure 7C). The centre line of main branch of CS was determined from the venogram as well as a centre line

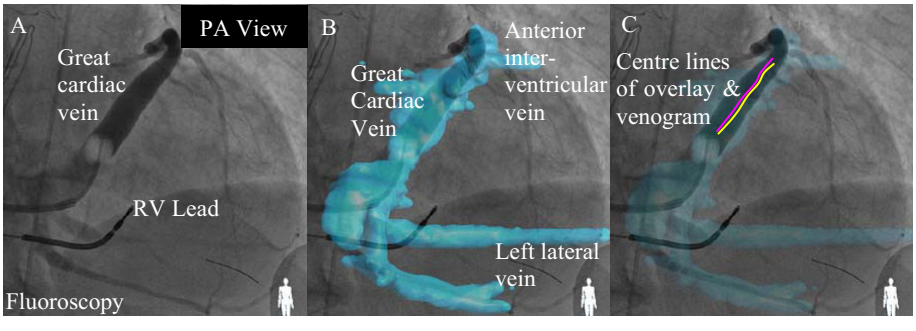

Fig. 7. (A) shows an occlusive venogram. (B) shows how the overlaid coronary veins appeared to the operator during an implant. (C) shows the overlay of the 3D CS segmentation from the CMR data with a centre line for both the venogram and the CS. This was used to determine the registration error.

for the overlay in a fluoroscopic overlay. The error was defined as the root mean squared distance error between 10 points on the centre line of CS overlay geometry and the 10 nearest points on the centre line of the CS venogram.

3 Results

For all 7 patients, the CMR data was of sufficient quality to allow the generation of clinically useable anatomical models of the cardiac chambers and the coronary venous system. Scar information was added when present and the models were registered successfully to the X-ray fluoroscopic data is all 7 cases during the implantation procedure. The mean distance error between the centre lines of the CS on the overlays and the venograms was 1.3 ± 0.68mm, showing accurate registration with low variability. The guidance platform was used to guide the pacemaker lead positioning and all patients had successful CS cannulation and left lead deployment.

4 Discussion and Conclusions

The overlay guidance platform for CRT procedures described in this paper allows the real-time visualization of the cardiac chamber & coronary vein morphology, myocardial scar distribution, and functional information overlaid onto X-ray fluoroscopy to guide the implanter. It can achieve high 2D-3D registration accuracy and facilitated successful LV lead implants in all 7 of the patients in this study. It was of particular help in a patient with a persistent left-sided superior vena cava in which balloon occlusion CS angiography was not possible due to CS dilatation. In this case, the overlay guidance platform offered a potentially unique method of displaying the branches of the CS to guide LV lead implantation. Such techniques therefore may offer the potential to reduce procedure time, contrast dose, X-Ray exposure and complication rates, particularly with inexperienced operators. Also, displaying myocardial scars on the LV model as well as motion information may allow more appropriate targeting for the LV lead. The fused data produced by the guidance platform will be invaluable when validating and testing *in-silico* cardiac biophysical models for CRT, which may provide patient-specific predictive optimal LV lead positions in the future.

Acknowledgments

This work is co-funded by Philips Healthcare (Best, The Netherlands), the EPSRC (project *Grand Challenge: Translating Biomedical Modelling into the Heart of the Clinic*), and the EU FP7 (project *euHeart*).

References

1. Ypenburg, C., Westenberg, J.J., et al.: Noninvasive imaging in cardiac resynchronization therapy–part 1: selection of patients. Pacing Clin. Electrophysiol. 31(11), 1475–1499 (2008)

2. Bleeker, G.B., Kaandorp, T.A., et al.: Effect of posterolateral scar tissue on clinical and echocardiographic improvement after cardiac resynchronization therapy. Circulation 113(7), 969–976 (2006)
3. Knecht, S., Skali, H., et al.: Computed tomography-fluoroscopy overlay evaluation during catheter ablation of left atrial arrhythmia. EuroPACE 10, 931–938 (2008)
4. Duckett, S.G., Ginks, M.R., et al.: A novel cardiac magnetic resonance imaging protocol to guide successful CRT implantation. Case report in Circulation Heart Failure (2010) (in press)
5. Manzke, R., Bornstedt, A., et al.: Respiratory motion compensated overlay of surface models from cardiac MR on interventional x-ray fluoroscopy for guidance of cardiac resynchronization therapy procedures. In: SPIE Medical Imaging 2010: Visualization, Image-Guided Procedures, and Modeling, vol. 7625 (2010)
6. Kautzner, J., Riedlbauchová, L., et al.: Technical aspects of implantation of LV lead for cardiac resynchronization therapy in chronic heart failure. PACE 27, 783–790 (2004)
7. Peters, J., Ecabert, O., et al.: Automatic whole heart segmentation in static magnetic resonance image volumes. In: Ayache, N., Ourselin, S., Maeder, A. (eds.) MICCAI 2007, Part II. LNCS, vol. 4792, pp. 402–410. Springer, Heidelberg (2007)
8. Sermesant, M., Peyrat, J.M., et al.: Towards patient-specific myocardial models of the heart. Heart Fail. Clin. 4(3), 289–301 (2008)
9. Gao, G., Chinchapatnam, P., et al.: An MRI/CT-based cardiac electroanatomical mapping system with scattered data interpolation algorithm. In: ISBI (2010)
10. Bi, X., Carr, J.C., et al.: Whole-heart coronary magnetic resonance angiography at 3 Tesla in 5 minutes with slow infusion of Gd-BOPTA, a high-relaxivity clinical contrast agent. Magnetic Resonance in Medicine 58, 1–7 (2007)
11. Yushkevich, P.A., Piven, J., et al.: User-guided 3D active contour segmentation of anatomical structures: Significantly improved efficiency and reliability. Neuroimage 31(3), 1116–1128 (2006)
12. Knowles, B., Caulfield, D., et al.: Three-dimensional visualization of acute radiofrequency ablation lesions using MRI for the simultaneous determination of the patterns of necrosis and edema. IEEE Trans. Biomedical Engineering 57(6), 1467–1475 (2010)
13. Rhode, K.S., Hill, D.L.G., et al.: Registration and tracking to integrate X-ray and MR images in an XMR facility. IEEE Transactions on Medical Imaging 24(11), 810–815 (2003)
14. Rhode, K.S., Sermesant, M., et al.: A system for real-time XMR guided cardiovascular intervention. IEEE Trans. Med. Imaging 24, 500–513 (2005)
15. Wang, Y., Riederer, S.J., et al.: Respiratory motion of the heart: kinematics and the implications for the spatial resolution in coronary imaging. Magnetic Resonance in Medicine 33(5), 713–719 (1995)

A Multi-method Approach towards Understanding the Pathophysiology of Aortic Dissections – The Complementary Role of In-Silico, In-Vitro and In-Vivo Information

Paula A. Rudenick[1], Maurizio Bordone[2], Bart H. Bijnens[3], Eduardo Soudah[2], Eugenio Oñate[2], David Garcia-Dorado[4], and Arturo Evangelista[4]

[1] Universitat Pompeu Fabra, Carrer Tanger, 122-140, E-08018 Barcelona, Spain
[2] International Center for Numerical Methods in Engineering (CIMNE), Universitat Politècnica de Catalunya, Barcelona, Spain
[3] ICREA-Universitat Pompeu Fabra, Carrer Tanger, 122-140, E-08018 Barcelona, Spain
[4] University Hospital Vall d'Hebron, Barcelona, Spain

Abstract. Management and follow-up of chronic aortic dissections continues to be a clinical challenge due to progressive aortic dilatation. To predict dilatation, guidelines suggest follow-up of the aortic diameter. However, dilatation is triggered by haemodynamic parameters (pressure and wall shear stresses (WSS)), and geometry of false (FL) and true lumen (TL). We aimed at a better understanding of TL and FL haemodynamics by performing in-silico (CFD) and in-vitro studies on an idealized dissected aorta and compared this to a typical patient. We observed an increase in diastolic pressure and wall stress in the FL and the presence of diastolic retrograde flow. The inflow jet increased WSS at the proximal FL while a large variability in WSS was induced distally, all being risk factors for wall weakening. In-silico, in-vitro and in-vivo findings were very similar and complementary, showing that their combination can help in a more integrated and extensive assessment of aortic dissections, improving understanding of the haemodynamic conditions and related clinical evolution.

Keywords: Aortic dissection, Computational Fluid Dynamics, In-vitro phantoms, Aortic diseases.

1 Introduction

Aortic pathologies represent an important subgroup within cardiovascular diseases, and while their prevalence is limited, they are associated with a very high morbidity and mortality (>50% in the acute phase). Despite improved diagnostic and therapeutic techniques, the management and follow-up of aortic dissections continue being a challenge in clinical practice.

Classic aortic dissection is believed to begin with the formation of a tear in the aortic intima that exposes an underlying media layer to the pulsatile pressure of the intraluminal blood (Fig. 1) leading to a longitudinal cleaving of the media layer along the aortic wall, causing the dissection. The dissection process extends typically antegrade (driven by the forward force of the aortic blood flow) but sometimes retrograde from the site of the intimal tear. The lumen will be divided into two parts, the true

O. Camara et al. (Eds.): STACOM-CESC 2010, LNCS 6364, pp. 114–123, 2010.

(TL) and the false lumen (FL). In 90% of cases TL and FL are communicated through entry and exit sites in the dissection flap. The distension of FL during the pulsatile pressure inside the lumina can cause intimal flap movement, distorting the TL shape and narrowing its calibre, potentially leading to TL collapse obstructing side branches and inducing visceral ischemia.

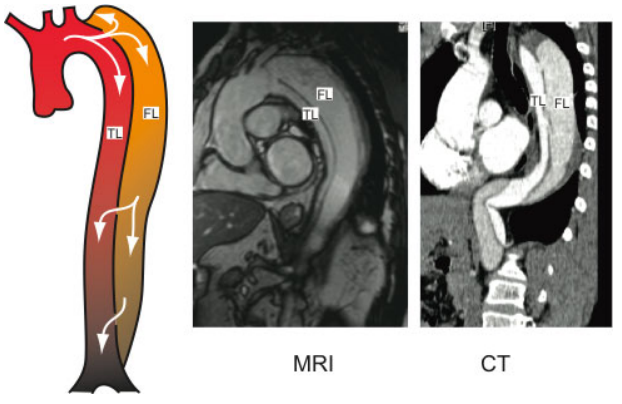

Fig. 1. A classic dissection of the descending aorta (Left). The typical clinical appearance on magnetic resonance (middle) and computed tomography (right) images. TL: True Lumen; FL: False Lumen.

While acute ascending aortic dissections require immediate surgery, descending aortic dissections are often treated medically and persist in the chronic phase [1]. However, these patients still have high mid/long term mortality during the chronic phase, mainly due to the progressive dilatation of the aorta and subsequent rupture.

In current clinical practice, prediction of outcome is mainly based on maximum total aortic diameter, which is compared with guidelines for deciding the best therapeutic approach. However, previous work has shown that maximum diameter is not a reliable determinant of rupture and progression [1-4]. In addition to it, haemodynamic parameters (intra-luminal pressure and flow conditions/wall shear stresses), geometric factors (such as the shape and curvature of the aorta and the communications between FL and TL), and intrinsic wall properties, all play an important role in the progress of dilatation and risk of rupture.

Whereas an integrated clinical approach towards the biomechanics and haemodynamics of the dissected aorta is still lacking, based on clinical observations and patient registries, several markers have been suggested to assist in the prediction of dilatation. The patency of the descending aorta FL may be responsible for progressive aortic dilation [1] and partial thrombosis of the FL has been found as a predictor of post-discharge mortality in patients with type B acute aortic dissection [5].

It was also observed that prognosis of patients with open communication between TL and FL is poorer than in those without such communication, and free communication with high flow rates carries a higher risk for reoperation because of the high flow pressure and wall stress. Nevertheless, complete obliteration of the FL can occur despite open communication and is possibly related to the size of communication [6]. Poor inflow in the TL and lack of outflow in the FL may have impact in FL dilation and rupture during follow-up period [7].

Therefore, from clinical observations, the importance of tear size and location is clear. However, the contradictory findings on which situations are leading to further

dilatation of the FL show that there is still a lack of understanding of the interplay of all variables.

Another factor that could affect the dilation of the FL is the compliance or mechanical strength of the dissected aortic wall. Arteries respond to changes in blood pressure and flow conditions by remodelling. Wall shear stress (WSS) is the tangential force resulting from the friction that the flowing blood exerts on the luminal surface. It has been shown that WSS can change the morphology and orientation of the endothelial cell layer [8]. Prolonged high WSS is known to cause vessel dilation and internal elastic lamina fragmentation, and may be the responsible for dissection initiation [9]. On the other hand, inflammatory and atherosclerotic pathways, triggered by low WSS, could also play an important role in dissection pathogenesis. Excessively low WSS could lead to atherosclerotic inflammatory infiltration and thereby cause deterioration of the aortic wall that could lead to mechanical weakening and rupture [10].

Therefore, it is expected that better aortic morphologic and hemodynamic analysis will be much more predictive for aortic dilatation and will improve the clinical stratification of the risk of these patients, facilitating a better therapeutic management.

The aim of this study is to assess whether an integrated approach towards TL and FL haemodynamics will allow us to define risk markers of severe aortic enlargement. For this, in-silico and in vitro studies were performed to investigate the impact of morphological characteristics on the haemodynamics of the TL and FL and the findings were compared to a typical patient from our hospital.

2 Methods

2.1 In-Vivo

In our hospital, chronic aortic dissection patients undergo regular follow-up with trans-thoracic and trans-oesophageal echocardiography for the quantification of changes in aortic size. Additionally, an MRI study, including short-axis phase-contrast acquisition of blood flow in the distal FL and TL (**Fig. 2**) is performed and when clinically indicated, a CT study is additionally done.

Fig. 2. Typical results from a clinical MRI phase-contrast study. Left: instantaneous volume flow in FL (blue) and TL (red); Middle: measurements in TL; Right: measurements in FL

2.2 In-Silico

Idealized geometry. A Computational 3D model of typical type B aortic dissections was constructed with the CAD software GID (CIMNE, Barcelona) (Fig. 3) [11]. The

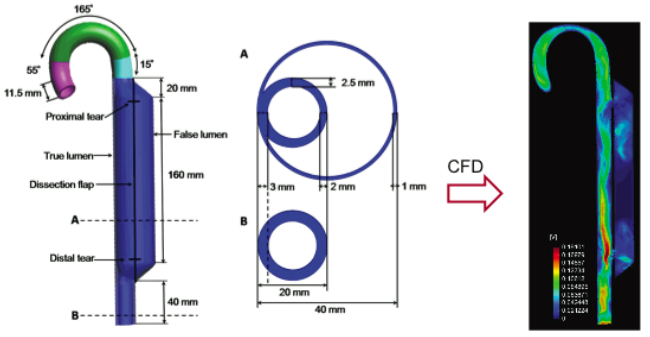

Fig. 3. Left: Idealized geometry of an aortic dissection including the dissected section (A) and the non-dissected aortic section (B); Right: The result of the CFD simulations, showing the velocities at the longitudinal mid-plane of the dissection.

dimensions of the model, including the aortic arch and the ascending aorta, were selected based on anatomical measurements [12,13]. These are: aortic diameter: 20 mm; dissected segment diameter: 40 mm; FL length: 160 mm; TL thickness: 3 mm; dissection flap thickness: 2 mm; and FL thickness: 1 mm. A proximal and distal tear was included with 10 mm diameter, corresponding to 25% of the dissected segment diameter.

Computational fluid dynamics (CFD) simulation. The computational mesh consisted of approximately 1.1 million tetrahedral elements with a size range of 0.5-1.0 mm and was created with GID (CIMNE, Barcelona). The CFD simulation was performed using CFD-Tdyn (CompassIS, Barcelona), solving the Navier Stokes equations. The no-slip wall of the dissection model was assumed to be rigid, assuming that in chronic dissection there is reduced flap motion, so that a rigid flap is a good first approximation. Additionally, several studies suggested that the difference in flow induced pressure variations and consequent wall stress between rigid and elastic aortic models is negligible [14,15]. Realistic time dependent velocity and pressure waveforms (adapted from [16]) were applied at the inlet and outlet of the fluid domain respectively. We assessed intra-luminal pressure and instantaneous volume flow in the FL and TL at the distal and proximal descending aorta, respectively. The WSS distribution at the TL and FL surface was calculated and the velocity vectors at the mid-plane of the dissected geometries were analyzed.

2.3 In-Vitro

Phantom. A simplified physical phantom (without the aortic arch), similar to the 3D geometry used for the in-silico approach, was made from a compliant and flexible material to meet the tensile strength of the aorta. The model was constructed from two individual parts to simulate the dissection: the TL and the FL. These parts were joined together to form the final model. The TL consisted of a silicone tube of 16mm inner diameter and 2mm wall thickness in which holes were made to create the tears.

The FL part was custom made by first creating the geometry using modelling clay and PVC tubes. Next, from this, a two-part silicone (RTV) mould is made, which can be used to create multiple wax casts of the FL. Both halves of the mould are held together for casting a replica from beeswax. After solidifying, any mould marks remaining on the wax were carefully polished away. The wax replica was used in a lost-wax technique to create a latex (Kryolan) phantom by dipping the replica in

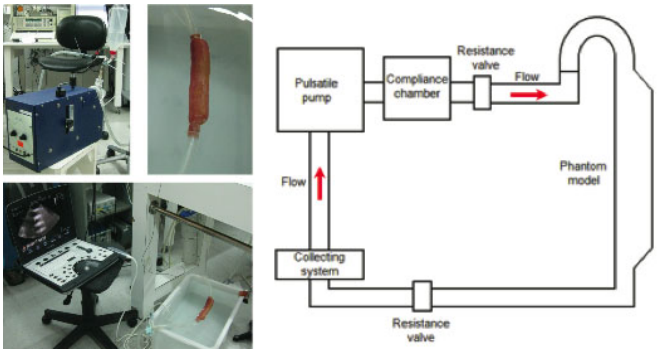

Fig. 4. Experimental set up for the in-vitro measurements. Right: diagram of the circuit. Left: different components of the circuit (top left: pulsatile pump; top right: latex phantom; bottom: portable ultrasound machine and phantom in a water tank).

liquid latex many times at intervals of 1 hour. Once the coating was finished, the model was heated, to remove the wax.

Experimental set up. A dynamic flow circuit, mimicking the human circulatory system, was set up to evaluate flow and morphological characteristics under controlled conditions (Fig. 4). The circuit consisted of a pulsatile pump, a compliance chamber, the dissection model, and a collecting system, connected in series. The flow pump (Harvard Apparatus) was programmed to simulate pulsatile left ventricle output with a heart rate=70bpm; stroke volume=70ml; and systolic/diastolic phase ratio=30/70. Peripheral resistance and systemic pressure were adjusted with the use of resistors (adjustable valves) placed proximal and distal from the phantom.

Measurements/Imaging. TL and FL pressure waveforms were measured with a fluid filled catheter at the distal and proximal sections. Flow was measured using an ultrasonic flow meter (Transonic Systems Inc). Pressure and flow waveforms were digitized using a PowerLab 16/30 with LabChart Pro acquisition and analysis software (ADInstruments, Colorado Springs, CO, USA). Phantom geometry as well as fluid appearance and velocities within the phantom were assessed by two-dimensional and Doppler ultrasound using a high-end portable clinical ultrasound scanner (Vivid Q - GE Healthcare) (Fig. 7).

3 Results

3.1 CFD Simulations

At the distal tear, higher FL pressures were observed at the onset of the cycle, resulting in an antegrade jet through the tear, whereas the FL/TL pressure gradient inverted at the end of the cycle leading to deceleration and inversion of the velocities and resulting in retrograde flow through the distal tear.

Fig. 5 shows the resulting absolute volumetric flows. FL flow variations are remarkably different from the TL, with a biphasic pattern and high early systolic flow.

Fig. 6 shows the normalized velocities during the cycle, obtained at different positions in the model. As can be observed, flow direction in the TL is dominantly antegrade (positive), except at the proximal section were its direction slightly reverses during early diastole. However, in the FL, fluid velocities begin to be retrograde from late systole, resulting in the reverse flow shown in the flow pattern plots (Fig. 7).

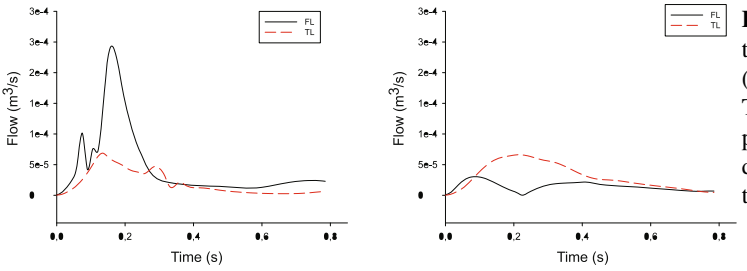

Fig. 5. The instantaneous flow (modulus) in the TL and FL at proximal (left) and distal (right) sections

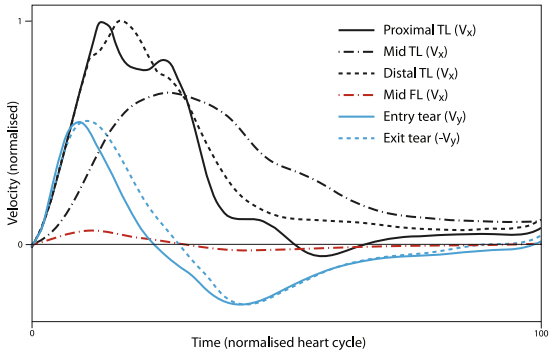

Fig. 6. Normalized mean velocities changes of TL and FL, at different positions of the phantom, and in the entry and exit tears.

Through the entry tear, we can observe a clear inflow during systole and outflow during diastole, while there is outflow during systole and inflow during diastole through the exit tear. The magnitudes of the velocities at both tears are similar. However, there is a shift in the time course indicating the propagation of the fluid wave.

From the assessment of the flow pattern in the dissected region (Fig. 7), we observe a bidirectional flow in the FL with a prominent retrograde during diastole. The most significant elevation in WSS is seen at the impact zone of the entry jet at end-systole, whereas during diastole there was a high variability of WSS in the distal zone.

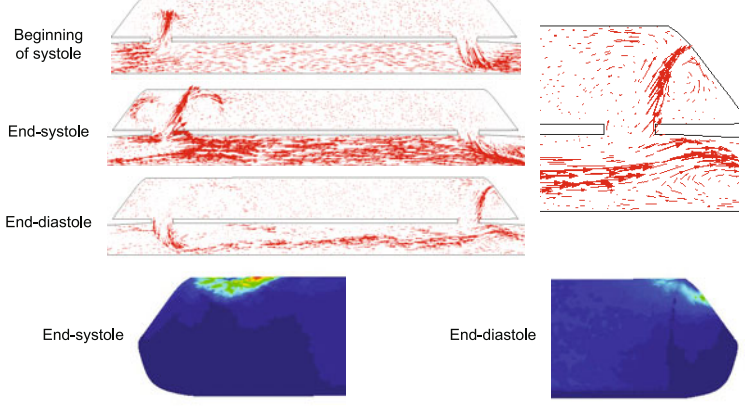

Fig. 7. Top: flow patterns at beginning and end-systole and end-diastole. The zoomed area shows the presence of FL diastolic retrograde flow at the exit tear. Bottom: WSS distributions at the FL surface. Left: the entry tear at end-systole; right: the exit area at end-diastole.

3.2 In-Vitro Measurements

Fig. 8 shows the echocardiographic image and measured Doppler flows for the in-vitro setup. The morphology of TL, FL and exit-tear can be easily recognised and the Doppler traces show the systolic forward flow and diastolic retrograde flow.

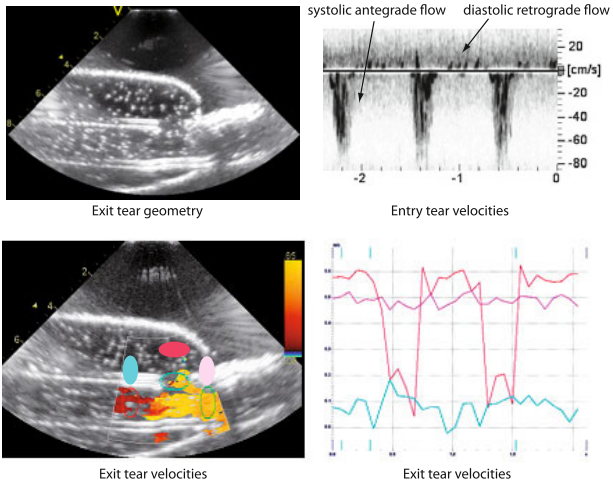

Fig. 8. Echocardiography of the in-vitro setup. Left: longitudinal cut of the phantom at the distal part and colour flow Doppler. Top right: pulsed Doppler velocity waveform at the entry tear; bottom right: colour Doppler velocity waveforms at the exit tear: Red: velocity through the exit tear; Pink: TL velocity distal from the exit tear; Cyan: TL velocity proximal to the exit tear.

Fig. 9 shows the pressure measurements at distal and proximal section in TL and FL. Distal pressures were higher than proximal pressures, also coinciding with the high WSS area detected in the CFD simulations. Comparing pressures between lumina, diastolic pressures in the FL were higher than in the TL. A high pressure gradient between TL and FL is measured at the distal section, which explains the presence of a remarkable reverse flow at the distal tear of the phantom.

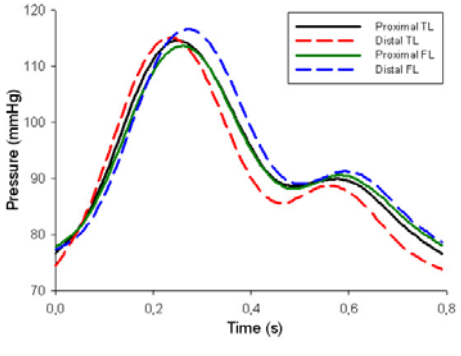

Fig. 9. Measured pressure profiles at proximal and distal sections of TL and FL.

3.3 Comparison of In-Silico and In-Vivo Data

Fig. 10 shows the comparison of the instantaneous flow profiles of the simulated geometry and from one of the patients in our clinic (obtained from MRI phase-contrast velocity measurements). This patient had a large entry tear (12mm) and showed rapid dilatation of the FL over the course of the follow-up (10%/year over 10 years). As can

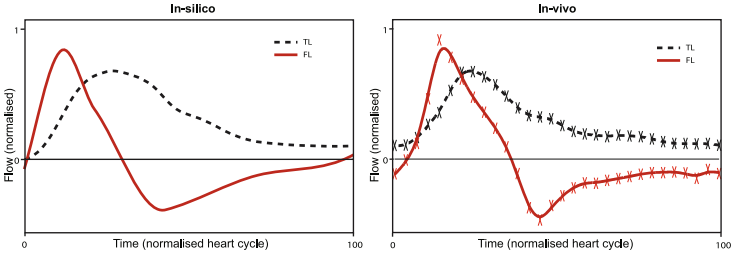

Fig. 10. Comparison of the in-silico instantaneous flow with the measurements from a typical patient

be seen, the observed profiles are remarkably similar, illustrating the usefulness of the in-silico approach to study the haemodynamics of typical patients.

4 Discussion

The dilatation of the dissected aorta depends on multiple factors. The cyclic wall stress in the FL is determined by the blood pressure changes, in interaction with the wall properties. Wall properties themselves are related to genetics, chronic pressure levels and flow (in particular WSS).

In our findings, the diastolic pressure in the FL was higher than in the TL, exposing the already weak and thin FL wall to higher wall stress. Additionally, pressures are higher at the distal section than at the proximal section, explaining the distal propagation of dissections.

Complex flow patterns have been thought to increase inflammatory cell infiltration in artery wall, increasing risk rupture [17,18]. We show both in-silico and in-vitro that the entry-jet and flow reversals result in complex flow patterns in the FL. A concentrated, jet-like flow is noted, directly impinging on the FL wall at the proximal and distal site during peak systole and diastole, respectively. This fast proximal jet might explain the eccentric dilatation of the proximal FL observed in a subset of patients.

An important hemodynamic factor that influences vascular remodelling, aortic expansion and rupture is WSS. WSS influences the morphology and orientation of endothelial cells [8]. An acute increase in WSS leads to an increase of the aortic diameter and weakening of the aortic wall because of loss of elastic tissue, change of muscle cell orientation, and acceleration of cell deterioration. On the other hand, the exposure of the arterial wall to low or variable WSS may increase intercellular permeability and increase the vulnerability of these regions of the vessel to atherosclerosis and weakening that could ultimately lead to rupture.

The cumulative effect of increases in pressure (wall stress) and changes in elastic properties, initiated by altered WSS, results in increased risk of further dilatation and rupture.

Limitations: There are many limitations in both in-silico and in vitro studies of an aortic dissection. We used a flexible dissection phantom to mimic the aortic wall compliance. Despite being an idealized model, its dimensions are based on clinical measurements and this generic model is ideal for parametric studies.

Whereas the overall flow and pressure waveforms were very similar, we had some differences of values between the results obtained with the in-silico and in-vitro models. It was mainly because we compared a flexible physical phantom with a rigid

computational model, and boundary conditions did not correspond exactly to the ones of the in-vitro model. Furthermore, the resistance and compliance of the experimental set up was not perfect, resulting in rather flat velocities when pressure waveforms were adjust to mimic human measurements.

Despite these mentioned differences, in-silico and in-vitro results follow a similar behaviour and are thus useful and complementary as a first validation of our results and in helping to explain clinical observations. Additionally, a wider range of dissection geometries, corresponding to the variety of patients' appearances in clinical practice, should be studied to obtain a full understanding of the haemodynamics in aortic dissection.

Clinical relevance. At present, follow-up and treatment of patients with aortic dissection seem to be non-ideal and it remains difficult to balance the high morbidity and mortality rates registered during the chronic phase of the disease with the severe side effects and risks of surgical or endovascular interventions. In current clinical practice, prediction of outcome in aortic dissections is mainly based on maximum total aortic diameter, which is compared to clinical guidelines for deciding the best therapy. However, this has proven to show severe limitations in assessing the genesis and evolution of aortic dissection [3,4]. So, the need for better predictors of the evolution of aortic dissection is evident, especially to assess FL dilatation and to evaluate and titrate a better pharmacological management.

Our study provides a methodology to assess haemodynamic and WSS differences originating from different geometrical configuration. Understanding these differences and assessing them in clinical practice with imaging modalities such as Magnetic Resonance Imaging (MRI), Transesophageal Echocardiography (TEE) and Computed Tomography (CT), will play an important role in the diagnosis and follow-up of aortic dissections. Combining measurements from imaging together with computational flow analysis using patient-specific geometries and boundary conditions could additionally enable to obtain a much more detailed view on the haemodynamic and wall stress conditions in aortic dissections, thus helping to provide an integrated view on the patient and enable the prediction of local remodelling that could be induced.

5 Conclusion

We evaluated haemodynamic parameters in the TL and FL of a chronic aortic dissection. For this, we have constructed a model of a type B dissection which allows studying aortic geometries, including different tear locations and sizes, both using in-silico computer simulations and in-vitro phantom measurements and if which the results can be directly compared to clinical patients. From one of these experimental in-vitro and in-silico models we showed the flow dynamics in the FL, contributing to novel ways for a better understanding of the haemodynamic conditions and related clinical evolution in patients with a chronic aortic dissection.

References

1. Nienaber, C.A., Haverich, A., Erbel, R.: Diseases of the aorta and trauma to the aorta and the heart. In: Camm, J., Lüscher, T.F., Serruys, P. (eds.) The ESC textbook of cardiovascular medicine. Blackwell, Oxford (2006)

2. Bernard, Y., Zimmermann, H., Chocron, S., Litzler, J.-F., Kastler, B., Etievent, J.-P., Meneveau, N., Schiele, F., Bassand, J.-P.: False lumen patency as a predictor of late outcome in aortic dissection. Am. J. Cardiol. 87, 1378–1382 (2001)
3. Nollen, G.J., Groenink, M., Tijssen, J.G., Van Der Wall, E.E., Mulder, B.J.: Aortic stiffness and diameter predict progressive aortic dilatation in patients with Marfan syndrome. Eur. Heart J. 25, 1146–1152 (2004)
4. Neri, E., Barabesi, L., Buklas, D., Vricella, L.A., Benvenuti, A., Tucci, E., Sassi, C., Massetti, M.: Limited role of aortic size in the genesis of acute type A aortic dissection. Eur. J. Cardiothorac. Surg. 28, 857–863 (2005)
5. Tsai, T.T., Evangelista, A., Nienaber, C.A., Myrmel, T., Meinhardt, G., Cooper, J.V., Smith, D.E., Suzuki, T., Fattori, R., Llovet, A., Froehlich, J., Hutchison, S., Distante, A., Sundt, T., Beckman, J., Januzzi Jr., J.L., Isselbacher, E.M., Eagle, K.A.: International Registry of Acute Aortic Dissection: Partial thrombosis of the false lumen in patients with acute type B aortic dissection. N. Engl. J. Med. 357, 349–359 (2007)
6. Erbel, R., Oelert, H., Meyer, J., Puth, M., Mohr-Katoly, S., Hausmann, D., Daniel, W., Maffei, S., Caruso, A., Covino, F.E., et al.: Effect of medical and surgical therapy on aortic dissection evaluated by transesophageal echocardiography. Implications for prognosis and therapy. The European Cooperative Study Group on Echocardiography, Circulation 87, 1604–1615 (1993)
7. Tsai, T.T., Schlicht, M.S., Khanafer, K., Bull, J.L., Valassis, D.T., Williams, D.M., Berguer, R., Eagle, K.A.: Tear size and location impacts false lumen pressure in an ex vivo model of chronic type B aortic dissection. J. Vasc. Surg. 47, 844–851 (2008)
8. Levesque, M.J., Liepsch, D., Moravec, S., Nerem, R.M.: Correlation of endothelial cell shape and wall shear stress in a stenosed dog aorta. Arteriosclerosis 6, 220–229 (1986)
9. Shaaban, A.M., Duerinckx, A.J.: Wall shear stress and early atherosclerosis: a review. AJR Am. J. Roentgenol. 174, 1657–1665 (2000)
10. Malek, A.M., Alper, S.L., Izumo, S.: Hemodynamics shear stress and its role in atherosclerosis. JAMA 282, 2035–2042 (1999)
11. GiD - The personal pre and postprocessor, CIMNE (2006), http://www.gidhome.com/
12. Williams, D.M., LePage, M.A., Lee, D.Y.: The dissected aorta: part I. Early anatomic changes in an in vitro model. Radiology 203, 23–31 (1997)
13. Strotzer, M., Aebert, H., Lenhart, M., Nitz, W., Wild, T., Manke, C., Völk, M., Feuerbach, S.: Morphology and hemodynamics in dissection of the descending aorta. Assessment with MR imaging, Acta Radiol. 41, 594–600 (2000)
14. Leung, J.H., Wright, A.R., Cheshire, N., Crane, J., Thom, S.A., Hughes, A.D., Xu, Y.: Fluid structure interaction of patient specific abdominal aortic aneurysms: a comparison with solid stress models. Biomed. Eng. Online 5, 1–15 (2006)
15. Borghi, A., Wood, N.B., Mohiaddin, R.H., Xu, X.Y.: Fluid-solid interaction simulation of flow and stress pattern in thoracoabdominal aneurysms: a patient-specific study. J. Fluids Struct. 24, 270–280 (2008)
16. Reymond, P., Merenda, F., Perren, F., Rüfenacht, D., Stergiopulos, N.: Validation of a one-dimensional model of the systemic arterial tree. Am. J. Physiol. Heart Circ. Physiol. 297, H208–H222 (2009)
17. Gimbrone Jr., M.A., Topper, J.N., Nagel, T., Anderson, K.R., Garcia-Cardeña, G.: Endothelial dysfunction, hemodynamic forces, and atherogenesis. Ann. N Y Acad. Sci. 902, 230–240 (2000)
18. Davies, P.F., Spaan, J.A., Krams, R.: Shear stress biology of the endothelium. Ann. Biomed. Eng. 33, 1714–1718 (2005)

Endowing Canonical Geometries to Cardiac Structures

Jaume Garcia-Barnes, Debora Gil, and Aura Hernandez*

Computer Vision Center, Dep. Ciències de la Computació
Universitat Autònoma de Barcelona, Bellaterra, Spain
{jaumegb,aura,debora}@cvc.uab.cat

Abstract. In this paper, we show that canonical (shape-based) geometries can be endowed to cardiac structures using tubular coordinates defined over their medial axis. We give an analytic formulation of these geometries by means of B-Splines. Since B-Splines present vector space structure PCA can be applied to their control points and statistical models relating boundaries and the interior of the anatomical structures can be derived. We demonstrate the applicability in two cardiac structures, the 3D Left Ventricular volume, and the 2D Left-Right ventricle set in 2D Short Axis view.

1 Introduction

The Myocardium presents two main attributes when seen in medical images: shape and appearance. The shape of the volume enclosed by myocardial walls is an intrinsic attribute that represents its anatomy and is easily captured by different anatomical imaging modalities such as CT or MR. In contrast, the appearance is image-dependent given that different modalities and/or acquisition protocols yield different (complementary) physiological information(perfusion, motion or fiber architecture). Statistical analysis of both attributes is a powerful tool that provides good indicators for disease diagnosis, progression and therapy planning and should handle complementary information coming from different sources.

First attempts to relate shape and appearance features were pioneered by Cootes *et al.* in order to improve their Active Shape Model (ASM) search [1]. They considered appearance patterns by sampling image intensities along fixed-length profiles projected orthogonally from the boundary. However, this approach was not able to capture the whole appearance contained inside the object boundaries. In order to solve this, the same authors later introduced Active Appearance Models (AAM) [2], that relate the whole object appearance and its boundary. However, since AAMs are based on warps registering images, they do not provide a canonical way of performing this relation.

* This work was supported by the Spanish projects PI071188, TIN2009-13618 and CONSOLIDER INGENIO 2010 (CSD2007-00018). The second author has been supported by The Ramon y Cajal Program.

O. Camara et al. (Eds.): STACOM-CESC 2010, LNCS 6364, pp. 124–133, 2010.

A natural way of associating shape and appearance attributes on the whole anatomic domain is by means of a parametrization (in the manifold sense) providing coordinates, inside the object, related to the boundary anatomy. Endowing geometry to shape models is achieved by using representations explicitly describing the structure geometry, like medial axis representations [3,4,5] or shape parametrizations [6]. Medial axis representations (*m-reps* [5]) describe geometry using the centres and radius of osculating spheres. Since osculating spheres are those interior spheres having more than one point tangent to the object boundary, they describe geometry by means of the structure boundary principal curvatures. However, *m-reps* present two main inconveniences. On one hand, they are discrete representations which might decrease accuracy of the model [7]. On the other hand, they do not provide a direct description of geometry and have a non-vectorial structure, which requires statistics in Riemmanian spaces [4].

The framework of differential geometry provides suitable tools for describing shape geometry by means of object parametrization in the manifold sense. A main shortcoming is that parametric maps are an infinite dimensional space without vector structure. Although there are a number of authors who have contributed to statistical analysis on Riemmanian manifolds [8], in the infinite case, computation of descriptive statistics is a delicate step not thoroughly solved [9]. A practical way of approaching parametrization of anatomical structures for shape analysis is by using basis functions for the formulation of the parametric map. In this manner, the space of parametric maps is vectorized and PDM approaches serve to compute statistical models. One of the first works is the spherical harmonic (SPHARM) parametrization for the hippocampus modelling used in [6]. The framework is suitable for structures diffeomorphic to spheres (i.e. admitting angular parameters), but the methodology does not generalize to more complex cardiac structures (like the right-left ventricle set, homeomorf to a double torus).

A more recent approach are *cm-reps* models [10] which are continuous explicit generalizations of *m-reps*. The parametrization of the shape is based on a parametrization of the medial axis which is extended to the whole domain by an inverse skeletonization process. In this manner, shape-based ("natural") coordinates are consistently defined over the anatomical structures. These coordinates allow to establish correspondences between structures across different subjects, and also allows to map intensities in these structures into a canonical (fixed for all subjects) reference frame in which shape differences between subjects have been effectively removed. Since these coordinates are defined by finding an analytical relationship between the structure medial axis (skeleton) and its boundaries, the framework naturally handles the combined analysis of shape and appearance. In its current formulation, the methods has two shortcomings. The inverse skeletonization requires solving a biharmonic PDE with nonlinear boundary conditions, which implies a high computational cost. In addition, this approach only provides well defined coordinates along the radial direction, but not in the medial surface manifold, which is represented as a mesh. We consider, that endowing shape based coordinates to a biological structure should apply

to the whole anatomy, especially in the cardiac context where 3 main directions naturally arise: circumferential, radial and, in the 3D case, longitudinal.

In this work, we transfer the philosophy of the combined analysis of shape and appearance hold in *cm-reps* to cardiac imaging. That is, we define shape-based coordinates to 2D and 3D cardiac structures by endowing them with a canonical geometry. This geometry is obtained using tubular coordinates given by normal sections to the medial axis of the structure that, in turn, is parametrized in a consistent manner, taking into account anatomical features. We show the potential of the proposed framework by modelling the shape of the left ventricle including the basal ring and the right and left ventricle joined geometry in 2D short axis views. In this last case, the left-right ventricles set, that is not a "simple object".

2 Differential Geometry Background

An $n-$dimensional differential manifold, $\mathcal{M}$, can be thought as the result of doing patchwork. That is, it can be made by "cutting" pieces of $\mathbb{R}^n$, "deforming" them and smoothly "gluing" them together until the geometric shape is covered. Mathematically, this states that there exists an open covering of the manifold, $(U_\alpha)_{\alpha \in A}$ homeomorphic to $\mathbb{R}^n$ via bijective continuous maps:

$$\begin{array}{rcl} \Phi_\alpha : \mathcal{U}_\alpha & \longrightarrow & U_\alpha \subset \mathbb{R}^n \\ \mathbf{x} = (x_1, \ldots, x_n) & \longmapsto & \mathbf{u}(\mathbf{x}) = (u_1(\mathbf{x}), \ldots, u_n(\mathbf{x})) \end{array}$$

such that, for any two indexes α, β, the composition $\Phi_\alpha \circ \Phi_\beta^{-1}$ is differentiable. The pair $(\mathcal{U}_\alpha, \Phi_\alpha)$ is called *local chart* or *local coordinate system*, $U_\alpha = \Phi(\mathcal{U}_\alpha)$ is called parametric domain and $\Psi_\alpha = \Phi_\alpha^{-1}$ parametrization.

The set of local charts endows the manifold with a topology (i.e., neighbours). The geometry arises with the definition of directions (e.g., left-right, up-down) in each open neighbourhood. Directions in differentiable manifolds are given at each point $\mathbf{x}$ by its tangent space. The elements of the tangent space are called tangent vectors at $\mathbf{x}$ and, intuitively, they describe all possible "directions" through $\mathbf{x}$.

The tangent space is given by the columns of the Jacobian matrix and has dimension n. The vectors perpendicular to tangent vectors are a vector bundle of dimension $d = m - n$ called normal space.

The normal space of a differentiable manifold defines tubular coordinates in $\mathbb{R}^m$ around $\mathcal{M}$ by means of normal sections. If we denote $\overrightarrow{n}_{\mathbf{x}}$ the normal space at $\mathbf{x}$, tubular coordinates are defined as:

$$\begin{array}{rcl} U_\alpha \times V_\beta \in \mathbb{R}^n \times \mathbb{R}^d & \longrightarrow & \mathbb{R}^m \\ (\mathbf{u}, \mathbf{r}) & \longmapsto & \Psi(\mathbf{u}) + \mathbf{r}\overrightarrow{n}_{\Psi(\mathbf{u})} \end{array}$$

for $\mathbf{r}\overrightarrow{n}_{\Psi(\mathbf{u})} := \sum_{i=1}^{d} r_i \overrightarrow{n}_{\Psi(\mathbf{u})}$. That is, for each point $\Psi(\mathbf{u})$ we can move on its normal direction along radial coordinate. It follows that, by means of radial coordinates, we have a distance map to $\Psi(\mathbf{u})$.

3 Canonical Coordinates over Anatomical Manifolds

Anatomical structures define volumetric domains in the ambient space which admit tubular coordinates by means of their medial axis. The medial axis is given by interior points equidistant to two or more boundary points [3]. It follows that its associated tubular coordinates parameterize the anatomical volume.

In the case of anatomical structures, their medial axis is a compact manifold that might be parametrized in angular coordinates. It follows that, by periodicity, the tubular coordinates change is given in a single chart covering the whole structure volume.

In order to provide a canonical geometry, tubular coordinates might be defined such that two manifolds, $\mathcal{M}_1, \mathcal{M}_2$, representing the same anatomical structure, share a common (fixed) parametric domain.

Anatomical structures present several landmarks common to any subject and easily identifiable. The implicit registration is achieved by assigning to anatomical landmarks normalized tubular coordinates codifying their position relatively to the geometry of the organ. We note that, in this manner, parametric coordinates have an anatomical meaning.

The parametrization map Ψ can be analitically approximated by means of basis functions. In our case we choose m-dimensional B-Splines since they are easy to implement and computationally efficient:

$$\Psi(\mathbf{u}, \mathbf{r}) = \sum_{J}^{M_J} \sum_{I}^{M_I} B_I(\mathbf{u}) \cdot B_J(\mathbf{r}) \cdot P_{IJ} \tag{1}$$

Here, $\mathbf{u}$ and $\mathbf{r}$ are the medial axis and the tubular parameters respectively.

Although B-Splines are not as general as, for instance, NURBS, they provide enough flexibility for the biological structures considered in this work.

Parametrizations expressed in terms of basis functions present vector space structure. Thus, the components in the chosen basis can be statistically analysed by means of standard PCA. In our case, PCA is applied to the control points of the B-Spline.

The tubular parametric map given by (1) is computed in two steps:

1. **Medial axis parametrization.** It corresponds to setting $r = 0$ in equation (1). Therefore, it is defined as soon as anatomical coordinates ensuring implicit registration are assigned to points on the medial axis. Such requirement is fulfilled by assigning given angular ranges to curvature extremum and junctions on the medial axis. Once we have pairs $(\mathbf{x}, \mathbf{u})$ of points and their corresponding parameters, the B-spline parametrization is obtained by minimizing:

$$\sum_{i=1}^{N} \|\Psi(\mathbf{u}_i, 0) - \mathbf{x}_i\|^2 \tag{2}$$

2. **Volume parametrization.** The parametric map for $r > 0$ is defined by extending the coordinate $\mathbf{u}$ along radial directions. Since radial coordinates correspond to the distance to the medial axis, $\Psi(\mathbf{u}_i, 0)$ is extended by means

of the distance map to the medial axis. By definition of medial axis, this is equivalent to deforming a B-spline snake to fit the structure boundaries. In order to ensure the implicit registration requirement, unitary radial parameters ($\|\mathbf{r}\| = 1$) are assigned to points on the structure boundaries.

4 Application to Cardiac Structures

We apply our framework to provide a canonical geometry in two cardiac structures of interest, the Left-Right Ventricle set (LV/RV) seen in 2D Short Axis (SA) slices, and the 3D LV volume. In both cases we use LV-RV junctions as landmarks and, in the 3D case, we also consider the apical cap and the basal ring. These landmarks are used to define an affine anatomic reference $\{O; V_x, V_y, V_z\}$ in order to remove variability in subject-device relative position as follows:

V_z is defined as the tangent vector to the line passing through the apical cap, A, and the centroid of the endocardial basal ring, B: $V_z = (B - A)/\|B - A\|$. The positions of A and B manually are determined in Long Axis (LA) views. The origin is defined along V_z-axis as: $O = A + 2/3(B - A)$ in order to account for any translation among different subjects. The vector V_x, is a unitary vector starting at O and pointing to the junction of the right and left ventricles the septum and the inferior walls. Since V_x points the same anatomical location for any LV, by setting V_x as the origin of angles, we handle any rotational disparity among different subjects. The vector V_y is chosen to make $\{V_x, V_y, V_z\}$ a negatively oriented orthonormal system. Figure 1 illustrates the orientation of the anatomical affine reference and the anatomical landmarks. Stars indicate the right and left ventricle junctions used to orient the reference in short axis views.

4.1 3D Left Ventricle Including the Basal Ring

The medial axis of the left ventricle volume is a surface that it is diffeomorphic to the sphere. Thus, it can be parametrized using circumferential and longitudinal

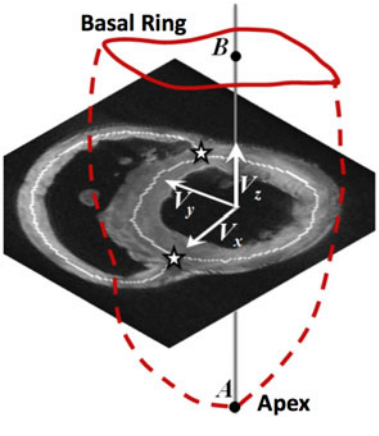

Fig. 1. Anatomical Affine Reference and Landmarks of the Myocardium

coordinates. We note (u, v, r) the parametric coordinates standing for the circumferential, longitudinal and radial directions.

Parameter directions on the medial axis are assigned as follows. The circumferential parameter u is assigned by mapping the same circumferential range $[0, u_S]$ to non-septal segments and the complementary $[u_S, 2\pi]$ to the septal one:

$$u = \begin{cases} \frac{u_S}{\theta_S}\theta, & \theta \leq \theta_S \\ \frac{2\pi - u_S}{2\pi - \theta_S}\theta + 2\pi\frac{\theta_S - u_S}{2\pi - \theta_S} & \theta \geq \theta_S \end{cases} \tag{3}$$

for θ the angle in the anatomical reference system $\{O; V_x, V_y, V_z\}$ and θ_S the angle between V_y and V_x. The septum angular proportion, u_S, is computed as the average of septal angular ranges. The longitudinal parameter v is the angle between a medial axis point and the V_z axis:

$$v = \pi - \arccos\left(\frac{V_z \cdot \mathbf{x}}{\|\mathbf{x}\|}\right) \tag{4}$$

for $\cdot$ the scalar product. Apical points are assigned $v \equiv 0$ and the basal ring $v \equiv \pi$. Finally, the radial parameter r is defined by enforcing that epicardium is given by $r \equiv -1$, endocardium by $r \equiv 1$ and the medial axis by $r \equiv 0$.

Canonical coordinates have been obtained parametrizing the LV volume with cubic blending functions for the angular parameters and linear for the radial one. The number of considered control points is $17 \times 7 \times 2$. Figure 2 (a) shows canonical geometry inside the LV volume.

4.2 LV-RV Set in 2D SA View

Since short axis views are given by perpendicular planes to LV LA, in this case, the medial axis is a curve, γ, that is homeomorph to a double torus. Inspired

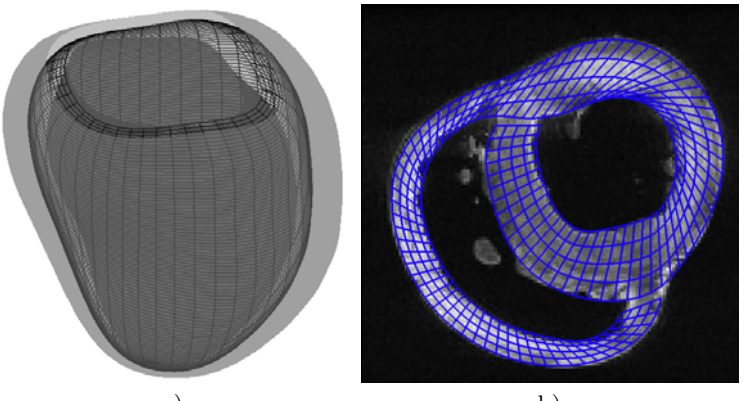

a) b)

Fig. 2. a) Canonical coordinates over the LV volume. b) Canonical coordinates over the LV-RV set.

by dissection methods [11], we use a clock-wise circumferential coordinate, u, starting at V_y and parameterizing first the right ventricle and then the left one. In order to completely unfold the left and right ventricles, the angular coordinate must account for the number of loops, n_l, of the medial axis around the origin O. That is, the angular coordinate is given by the lift of the medial axis path on its universal covering $\mathbb{R}^1$. For each $p \in \gamma$, the lifted angular coordinate, θ_l, is computed by adding $2\pi(nl-1)$ to the angle, θ, measured from V_y to p: $\theta_l = \theta + 2\pi(nl-1)$, for the number of loops n_l given by the number of intersections between the radius through the point p and γ. The circumferential parameter is assigned by mapping the right ventricle and the septal segments to the same angular range $[0, u_S]$ in the parametric domain:

$$u = \begin{cases} \frac{u_S}{\theta_S}\theta + 2\pi(n_l - 1), & \theta \leq \theta_S \\ \\ \frac{2\pi - \theta_S}{2\pi - u_S}\theta + 2\pi\frac{\theta_S - u_S}{2\pi - u_S} & \theta \geq \theta_S \end{cases} \tag{5}$$

for θ_S the angle between V_y and V_x and the angular proportion u_S computed as the average of septal angular ranges [12]. Finally we reverse u in order to follow the medial path from right to left ventricle: $u \rightarrow 2\pi + u_s - u$. Again, the radial parameter, r, is defined by assigning $r \equiv -1$ to epicardium, $r \equiv 1$ to endocardium and $r \equiv 0$ to the medial axis.

Figure 3 shows an example of the parametrization of the myocardium in short axis view using tubular coordinates. The assignment of the circumferential parameter following the dissection path is given in fig. 3(a). The modelling of endocardial (green solid line) and epicardial (red solid line) walls together with the medial axis (black dashed line) is shown in fig.3(b).

Canonical coordinates have been obtained parametrizing the LV-RV set with cubic blending functions for the angular parameter and linear for the radial one. Since the joined geometry of both ventricles is more complex than the left

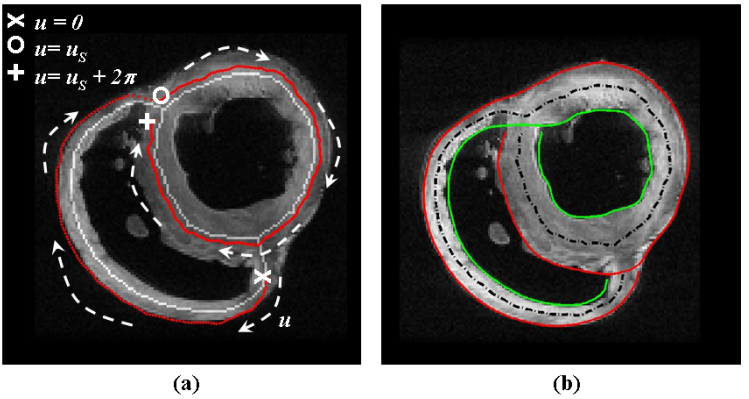

Fig. 3. Parametrization of the joined geometry of the right and left ventricles: circumferential parameter for the medial axis, (a), and tubular parametrization, (b)

ventricle alone, the number of control points has increased to 25×2. Figure 2 (b) shows canonical geometry over the LV-RV set.

5 Statistical Models

In both, the 2D and 3D cases, we use the analytical formulations of the canonical coordinates, given by B-Spline parametrizations and apply PCA to their control points. This provides an statistical model codifying the relation between the object boundaries and its interior.

Regarding LV volume we considered, as training set, $N = 8$ DTI unweighted volumes belonging to normal canine hearts, freely available at web of The Center for Cardiovascular Bioinformatics and Modeling (`www.ccbm.jhu.edu`). Since the number of instances in the training set is smaller than the space dimension, at most N eigenvectors (spanning the subspace generated by the elements in the training set) can be obtained. In this case we have taken the first 6 modes of variation (which explain a 99.25% of the total shape variability). The variability associated to the first 5 modes is shown in figure 4 (above).

Regarding LV-RV structure we considered, as training set, 45 standard MR SA slices belonging to both, Basal and Mid levels. For the statistical model we have taken the first 5 modes of variation (which explain a 95.6% of the total shape variability). The variability associated to the first 5 modes is shown in figure 4 (below). Each row corresponds to a mode of variation (from left to right) in the range $\pm 2\sqrt{\lambda_n}$ (for $\sqrt{\lambda_n}$ the standard deviation associated to the mode).

6 Final Remarks

We have presented a mathematical framework for endowing canonical geometries to anatomical structures, by means of tubular coordinates. This establishes correspondences between subjects allowing the combined analysis of shape and appearance. This framework facilitates moving over the target structure and is suitable for defining regular meshes, facilitating further simulation or finite differences schemes.

Analytical formulation of the geometry is given using B-Splines. Since they have vector space structure, statistical analysis measuring the variability in the relations between boundaries and their interior, are obtained applying PCA to the control points.

We have applied our methodology to two challenging cardiac imaging applications. On one hand, we have provided a model of the left ventricle including the basal ring, which cannot be easily modelled using regular meshes or diffeomorphic maps. On the other hand, we have approached the geometry of the right and left ventricles, which, by their loop distribution, is a delicate step. Currently we are extending the methodology to the 3D LV-RV set and preliminary results are promising, however the extension to the whole heart (including atria) seems unfeasible so far.

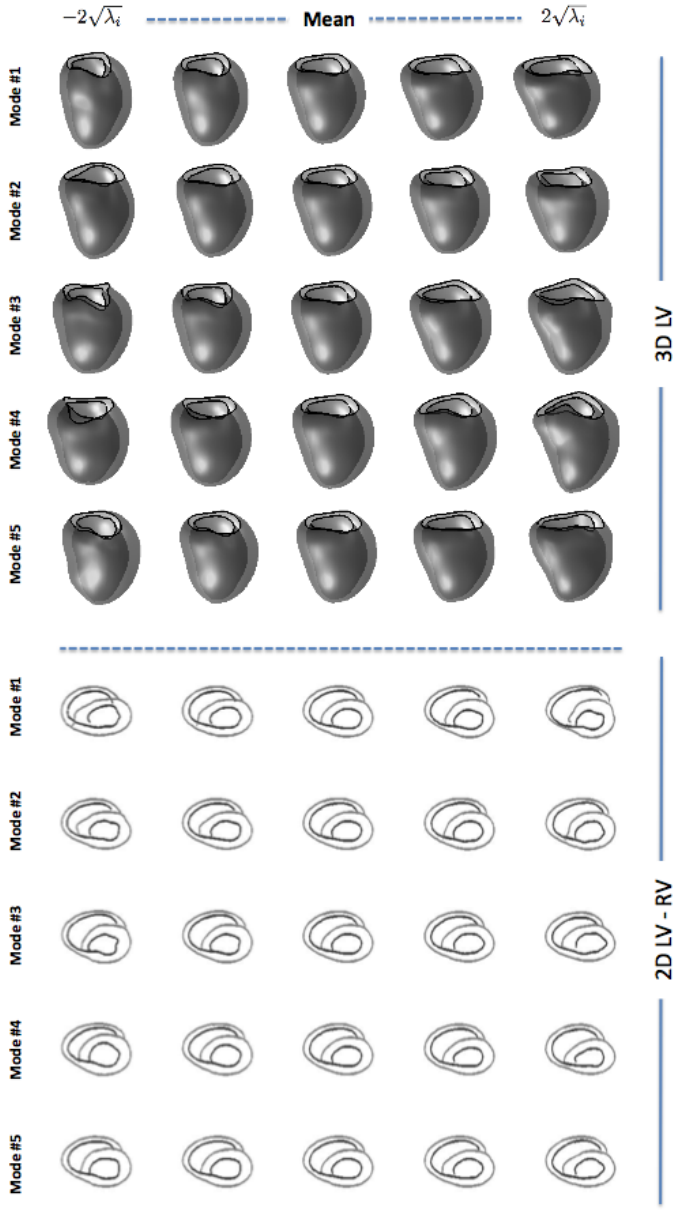

Fig. 4. First 5 Modes of variation performed over the control points of the B-Spline parametric maps that endow a canonical geometry to the LV volume (above) and to the 2D SA LV-RV set (below)

The proposed methodology is easy to implement and computationally is more efficient than other proposed approaches based on PDE. The framework is fed by a ROI enclosing the object under study: the LV in the 3D case and the LV-RV

set in the 2D case. Thus, the speed of the whole process mostly depends on the chosen segmentation method (which is out of the scope of this work). Regarding landmarks, Apical Cap and Basal Ring points can be automatically detected from the 3D ROI, whereas LV-RV junctions require manual intervention. In the 2D case, junction points are directly selected from the MR image and in the 3D case these 2 landmarks are selected over the image obtained after considering the mean along the Z-direction of the unweighted DTI volume.

References

1. Cootes, T., Taylor, C.: Using grey-level models to improve active shape model search. In: Proc. ICPR, pp. 63–67 (1994)
2. Cootes, T., Edwards, G., Taylor, C.: Active appearance models. In: Burkhardt, H., Neumann, B. (eds.) ECCV 1998. LNCS, vol. 1407, pp. 484–498. Springer, Heidelberg (1998)
3. Blum, H.: A transformation for extracting new descriptors of form. In: Whaten-Dunn, W. (ed.) Models for the Perception of Speech and Visual Form, pp. 362–380. MIT Press, Cambridge (1967)
4. Fletcher, P.T., Lu, C., et al.: Principal geodesic analysis for the study of nonlinear statistics of shape. IEEE Trans. Med. Imag. 23(8), 995–1005 (2004)
5. Pizer, S., Fletcher, P., et al.: Deformable m-reps for 3d medical image segmentation. International Journal of Computer Vision 55(2), 85–106 (2003)
6. Kelemen, A., Szekely, G., Gerig, G.: Elastic model-based segmentation of 3-d neuroradiological data sets. IEEE Trans. Med. Imag. 18, 828–839 (1999)
7. Yushkevich, P., Zhang, H., Gee, J.: Continuous medial representation for anatomical structures. IEEE Trans Med Imaging 25(12), 1547–1564 (2006)
8. Pennec, X.: Intrinsic statistics on riemannian manifolds - basic tools for geometric measurements. Journal of Mathematical Imaging and Vision 25, 127–154 (2006)
9. Bossa, M., Hernandez, M., Olmos, S.: Contributions to 3d diffeomorphic atlas estimation: Application to brain images. In: Ayache, N., Ourselin, S., Maeder, A. (eds.) MICCAI 2007, Part I. LNCS, vol. 4791, pp. 667–674. Springer, Heidelberg (2007)
10. Yushkevich, P.: Continuous medial representation of brain structures using the biharmonic pde. NeuroImage 45(1), 99–110 (2009)
11. Ballester, M., Ferreira, A., Carreras, F.: The myocardial band. Heart Failure Clinics 4, 261–272 (2008)
12. Garcia-Barnés, J., Gil, D., Badiella, L., Hernàndez-Sabaté, A., Carreras, F., Pujades, S., Martí, E.: A normalized framework for the design of feature spaces assessing the left ventricular function. IEEE Trans. on Medical Imaging 29(3), 733–745 (2010)

Automatic Segmentation of Left Atrial Geometry from Contrast-Enhanced Magnetic Resonance Images Using a Probabilistic Atlas

R. Karim[1,3], C. Juli[2], L. Malcolme-Lawes[3], D. Wyn-Davies[3], P. Kanagaratnam[3], N. Peters[3], and D. Rueckert[1]

[1] Department of Computing, Imperial College London, 180 Queen's Gate, South Kensington, London SW7 2AZ
[2] Imaging Department, St. Mary's Hospital, Praed Street, London W2 1NY
[3] National Heart and Lung Institute, Imperial College London, 180 Queen's Gate, South Kensington, London SW7 2AZ
rkarim@imperial.ac.uk

Abstract. Left atrium segmentation and the extraction of its geometry remains a challenging problem despite of existing approaches. It is a clinically-relevant important problem with an increasing interest as more research into the mechanism of atrial fibrillation and its recurrence process is undertaken. Contrast-Enhanced (CE) Magnetic Resonance Angiography (MRA) produces excellent images for extracting the atrial geometry. Nevertheless, the variable anatomy of the atrium poses significant challenge for segmentation. To overcome the inherent difficulties with this segmentation, we propose a technique that utilizes the Voronoi subdivision framework for the segmentation. In addition, the segmentation is based on the minimization of a Markov Random Field based energy functional defined within the Voronoi framework. The method also incorporates anatomical priors in the form of a probabilistic atlas. We show how the model is efficient in segmenting atrium images by comparing results from manual segmentations.

Keywords: Segmentation, Left atrium, Graph Cuts, Magnetic Resonance Angiography.

1 Introduction

Atrial fibrillation (AF) is a clinically challenging cardiac arrhythmia that occurs in epidemic proportions with an increasing prevalence worldwide even after accounting for the aging population [10]. The electrical isolation of AF-causing circuits with catheter ablation has emerged as an interventional treatment for AF. High radiofrequency energy inducing thermal damage creates lesions or scars in the left atrium, whereby the electrical conduction pathways of abnormal circuits are disrupted. AF recurrence is not uncommon in patients who underwent ablation treatment and is generally caused by the rejuvenation of scarred tissues. Understanding the temporal process of scar formation and whether scar

O. Camara et al. (Eds.): STACOM-CESC 2010, LNCS 6364, pp. 134–143, 2010.

reduces or expands over time has become important in determining whether some patients are more susceptible to AF recurrence than others [11].

The quantification of the extent of left atrial scar tissue has now become possible due to recent advancements in imaging techniques. However, for assessing scar information it is important to visualize them on the atrial geometry. Contrast-enhanced Magnetic Resonance Angiography provides good quality imaging data for segmenting the atrial anatomy. Previous work on the segmentation of the left atrium include segmentation from MRA/CTA [1,4], CT [7] and X-ray angiography [8]. Our proposed method adopts the Voronoi framework of [1,4]. However, the segmentation method is based on the minimization of an energy functional with a spatial and intensity prior. With a high degree of variability in the anatomy of the atrium, a probabilistic atlas created from training images makes the segmentation approach more robust.

2 Building a 3D Probabilistic Atlas of the Atrium

2.1 Segmentation of Training Images

The variability of atrial anatomy is documented in the clinical literature [5]. The number and branching patterns of pulmonary vein drainages to the left atrium are known to vary across patient subjects. For modelling this variable anatomy, 20 left atrium images were manually segmented from contrast-enhanced Magnetic Resonance Angiography (MRA) images. Noting the possible anatomical variations from [5], we classified our training left atrium images into the different anatomical groups. The most common anatomical variations found were: 1) two drainages to the right and left sides (4-drainage), and 2) a single drainage to the left and two drainages to the right sides (3-drainage). After segmenting the images, shape based interpolation [12] was used to resample the images to isotropic voxels of size 1 mm $\times$ 1 mm $\times$ 1 mm.

2.2 Registration of Training Images

The training images from each anatomical group were registered to a common co-ordinate frame. A left atrium image from each anatomical group was selected as the target image for that group. It was ensured that the atrium selected as reference was a good representative of the anatomy, based on an expert radiologist's opinion. Each training image was then registered to its respective group's reference image. For registration, landmark points were selected on each training atrium: 3 or 4 points, depending on the anatomy, selected at the centre of the opening of the pulmonary drainage and a single point at the centre of the atrial chamber. An affine registration allowing 9 degrees of freedom were used to align the atria and initialize the final registration process. Using the marching cubes algorithm [2], a dense triangulation (pseudo-landmarks) of the boundary surfaces of each segmented atria were generated. The correspondence between each pseudo-landmark was then achieved using a surface based registration method using B-Splines [9]. This aligned all atria images to its respective reference anatomical shape.

2.3 Atlas Construction

A probabilistic atlas for each anatomical group is constructed from the aligned atria images. The atlas is formed by averaging segmentations for each group. A blurring of the segmentations with a Gaussian kernel prior to averaging is needed. With a relatively small population of training images, Gaussian blurring compensates by alleviating undesirable sharp transitions in the probability map. We selected a Gaussian kernel with width 10.0. Too small a kernel creates sharp transitions in foreground probabilities and too large a kernel can suppress the drainage networks in the atlas. Fig. 1 shows the probabilistic atlas for the 4-drainage network.

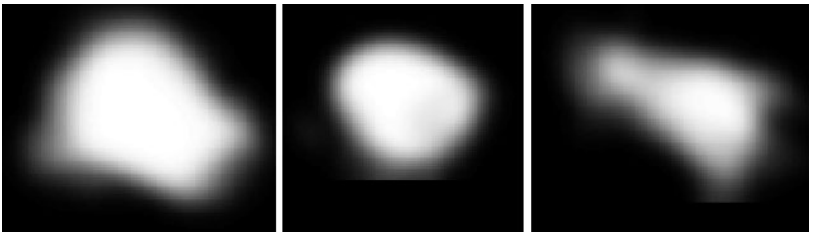

Fig. 1. The probabilistic atlas for the 4-drainage showing transverse (left), sagittal (middle) and coronal (right) planes

3 The Segmentation Framework

3.1 Voronoi Tessellation of the Distance Transform Space

The left atrium in CE-MRA images is connected to neighbouring structures via narrow junctions. These junctions were exploited in [1,4] by making the appropriate cuts and separating the atrium from the rest of the image. For finding narrow junctions within a binary image, a Voronoi Tessellation of the Euclidean Distance Transform (EDT) image is computed.

Each Voronoi cell is analogous to a maximally inscribed sphere, where a narrow junction between two structures is analogous to a smaller sphere between two larger spheres. Although the technique performs well on contrast-enhanced images of the atrium, with no anatomical priors incorporated into the model, this rather ad-hoc approach is unable to segment images that are not contrast-enhanced. In addition to this, it requires manual interaction as it relies heavily on a merging-threshold parameter. We adopt the same Voronoi framework for segmentation. However, we incorporate an anatomical prior with the probabilistic atlas. In addition to this, we use a MRF based energy function which is optimized using graph-cuts.

The left atrium blood pool in the CE-MRA consists of structures other than the atrium, such as the aorta and pulmonary arteries. This blood pool is extracted using a region-growing technique with automatic Otsu thresholding [13].

The EDT of this blood pool is computed. Thus, each pixel in the distance transform is assigned the shortest distance to the left atrium blood pool boundary. Local maxima in this EDT image are assigned centres of the Voronoi cells and thus form the basis of our Voronoi tessellation. By definition, each Voronoi cell only comprise of voxels that are *closest* to its centre. As in [1], each Voronoi cell has a size and the *separating surface* between cells are also given a size. The separating surface are shared borders with a neighbouring cell and illustrated in Fig. 3. The sizes of the cells and separating surfaces are simply the computed EDT values of their inner-most point (i.e. centre). Every voxel in the atrium blood pool is assigned a Voronoi cell of which it is a member; this is its closest Voronoi cell. Thus the closest Voronoi cells for each voxel (i.e. cell memberships) can be computed using gradient ascent on the distance transform.

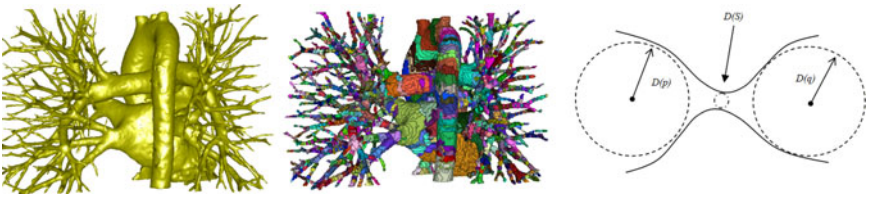

Fig. 2. The blood pool image (left) subdivided into its Voronoi cells (middle), with each cell assigned a random colouring. Right image: Adjacent Voronoi cells are analogous to maximally inscribed circles with a diameter $D(p)$ and $D(q)$. The separating surface also has a diameter $D(\mathcal{S})$

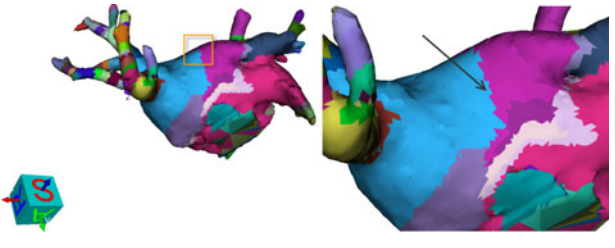

Fig. 3. A left atrium with each Voronoi cell uniquely coloured (left). A close-up of the surface showing shared borders of adjacent or neighbouring cells (right). As cells are 3D entities, these shared borders are surfaces in 3D.

3.2 Energy-Based Formulation

With the image subdivided into Voronoi cells p, segmenting the left atrium is equivalent to assigning a label $f_p \in \{0, 1\}$ to every cell in the image P. The segmentation is based on the observed intensities in the image and the anatomical prior. MRF provides a sound background to model context dependent image segmentation

in which segmentation is formulated as an energy minimization problem. Utilizing our Voronoi framework, an MRF-based energy function is given by:

$$E_P(f) = \lambda \sum_{p \in P} D_p(f_p) + \sum_{p,q \in \mathcal{N}} V_{p,q}(f_p, f_q) \tag{1}$$

where the data term $D_p(f_p)$ is a function of the observed image data and explains how well label f_p can be assigned to the Voronoi cell p based on a probabilistic model. $V_{p,q}(f_p, f_q)$ is a smoothness term penalizing discontinuities in a neighbourhood system of Voronoi cells $\mathcal{N}$. As The parameter λ weighs the influence of the data and smoothness terms.

3.3 The Data and Smoothness Terms

The data term in the MRF model is a combination of the spatial and intensity priors. The probabilistic atlas constructed from pre-segmented training images provides each voxel a prior probability of its label being foreground or background. However, as the MRF model is built over the Voronoi framework, the mean probability over all voxels within a Voronoi cell is used as an estimate of its prior probability. The intensity model is derived from the unseen target image. To model the foreground, a Gaussian distribution is used where the mean and variance are determined from the image intensities of voxels (of the unseen target) labelled as foreground by at least 90% of the training images. In CE-MRA images of good quality, the perfusion of contrast into pulmonary arteries is not as evident as it is in the atrial blood pool. Thus the signal intensity is expected to be higher in the blood pool than in the arteries, thereby making a Gaussian intensity foreground model sensible. The data term for each Voronoi cell is thus given by:

$$D_p(f_p) = \mu \frac{1}{N} \sum_{n_p \in p} p(f_p) + P(I|f_p) \tag{2}$$

where $p(f_p)$ is the spatial prior from the atlas averaged over all voxels n_p of the Voronoi cell and $P(I|f_p)$ is the intensity model. Parameter μ weighs the influence of the two terms.

The regularizer or the smoothness term in the image relates two adjacent Voronoi cells and allows appropriate cuts to be made in the image. As cuts are sought within narrowing regions in the image, the relative sizes of adjacent Voronoi cells are incorporated into the smoothness term. The relative sizes η of two adjacent Voronoi cells p and q is given by $\eta = \min\{D(p), D(q)\} - D(\mathcal{S}_{p,q})$. where $D(\cdot)$ is the diameter function of a Voronoi cell and $\mathcal{S}$ is the separating surface or interface between two adjacent cells. Following [1] and [4], we use $D(\cdot)$ as the EDT value of the cell and surface centres. Larger values of η indicate a Voronoi neighbourhood with a narrowing. The smoothness term $V_{p,q}$ is thus set to a monotonically decreasing function of the relative diameter such as its reciprocal:

$$V_{p,q} = 1/(1 + \eta) \tag{3}$$

3.4 Optimization

The MRF energy model defined in Eq. 1 over the Voronoi framework is a complex functional of the segmentation $\mathbf{f}$. Local optimization methods like simulated annealing are not guaranteed to find a global minimum in polynomial time. However, for MRF functionals of the form defined (Eq. 1) it is possible to find the global optimum using graph cuts [6]. In this method, the functional is converted to a graph $\mathcal{G} = \langle \mathcal{V}, \mathcal{E} \rangle$ with two special s, t *terminal* nodes representing the foreground and background labels. The segmentation labelling problem is solved by computing the minimum s-t cut.

As each Voronoi cell must be marked as foreground or background in the segmentation problem, a node $v \in \mathcal{V}$ is assigned for each Voronoi cell p in image P. Neighbouring cells and thus their nodes are connected by edges $e \in \mathcal{E}$ enforcing continuity in the segmentation. Every node vertex also has edges to the terminal s and t nodes representing the fact that they may be marked either as foreground or background. Edge weights are given by the data term (Eq. 2) for node-to-node connections and by the smoothness term (Eq. 3) for node-to-terminal connections. See Fig. 4 for an illustration. By determining the minimum s-t cut in $\mathcal{G}$, the segmentation problem is solved by assigning a label to each node [3].

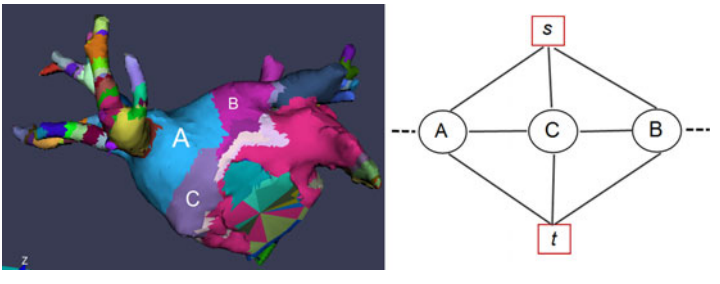

Fig. 4. The Voronoi cells in a segmented left atrium (left). A subset of the graph constructed for optimizing the MRF energy model (right). Note the terminal nodes s and t. Only Voronoi cell nodes A, B and C are shown here as an example. Note also that there is a path from A to B, excluded in the diagram for maintaining clarity.

4 Experiments

4.1 Image Acquisition

We acquired 30 CE-MRA images of the left atrium from different subjects for our study. All subjects were diagnosed for AF and imaged prior to their ablation. We selected 20 images for our training data, as described in section 2.1. Out of the 20 images, 11 atria images had a 4-drainage network and 9 images with a 3-drainage network. The rest of the images were used for validating our proposed model. All images were acquired at 1.5T using a Siemens Avanto scanner. The image

size ranges between $250 \times 250 \times 30$ to $380 \times 380 \times 100$ voxels. The slice thickness ranges between 1.0-3.0 mm. Gadovist was used as the contrasting agent.

4.2 Comparison with Manually Outlined Data

Segmentations of the atrium were generated using the proposed model on 10 images of the left atrium CE-MRA data. The probabilistic atlas was registered to the unseen instance using affine registration and the minimum graph cut produced the segmentation with no manual intervention. For manual segmentations, for each of the images, 5 slices through the data were selected at equally spaced intervals and the outline of atrium manually delineated in each slice. These slices were selected from the most interesting areas of the image, i.e. in and around the atrial chamber and including the drainages. It is worth noting that the network of veins emanating from the atrium has little clinical importance in the context of ablation procedures, and thus has been excluded from our manual segmentations. Each slice is compared against segmentations from the proposed model using an overlap measure O_s defined over the manual $\mathcal{M}$ and computer-assisted segmentation $\mathcal{C}$ as:

$$O_s = \frac{\text{Area}(\mathcal{M} \bigcap \mathcal{C})}{\text{Area}(\mathcal{M})} \tag{4}$$

In addition to this, surface visualizations of the segmented left atrial geometry were generated to allow an assessment of whether segmentations included all the drainages to the atrium only as far as the first bifurcation. In visualizing scars that are only made in and around the atrial chamber and drainage openings, this is more clinically relevant than achieving a voxel-wise accuracy of the segmentations.

4.3 Results

The results of evaluating the segmentations obtained from the proposed method against manual segmentations are given in Table 1 for each selected slice of image data. Figure 5 compares the mean overlaps found for each subject. The proportion of overlap is between 0 and 1, where an overlap of 1.0 represents complete agreement with the manual segmentation. Note the occasional low overlap values, for example: patient 1 slice 1, patient 8 slice 1, patient 8 slice 3. This is primarily for slices with the atrium-ventricle junction at the mitral valve, which is not particularly visible in CE-MRA images. The algorithm relies on the atlas for finding the mitral valve junction and with no explicit model of the valve, this often is an approximation based on the mean atrial shape. However, it is clear from the segmentations that the probabilistic atlas allows the exclusion of the extensive vessel drainage network in angiography images. This produces vessel-free segmentations allowing a clear visualization of the anatomy (see Fig. 6). All segmentations were computed in under 5 secs on a 2 Ghz PC.

Table 1. Overlap between manual segmentation and the proposed method. A value of 1.0 represents complete overlap.

	Subjects									
	1	2	3	4	5	6	7	8	9	10
slice 1	0.50	0.00	0.84	0.99	0.78	0.99	0.85	0.31	0.68	0.66
slice 2	0.98	0.99	0.99	0.99	0.99	0.97	0.94	0.97	0.90	0.97
slice 3	0.98	0.99	0.99	0.98	0.99	0.97	0.99	0.25	0.99	0.90
slice 4	0.98	0.99	0.99	0.99	0.99	0.99	0.99	0.98	0.99	0.99
slice 5	0.98	0.99	0.92	0.99	0.99	0.89	0.99	0.99	0.97	0.97
mean	0.89	0.80	0.95	0.99	0.95	0.97	0.96	0.70	0.91	0.90

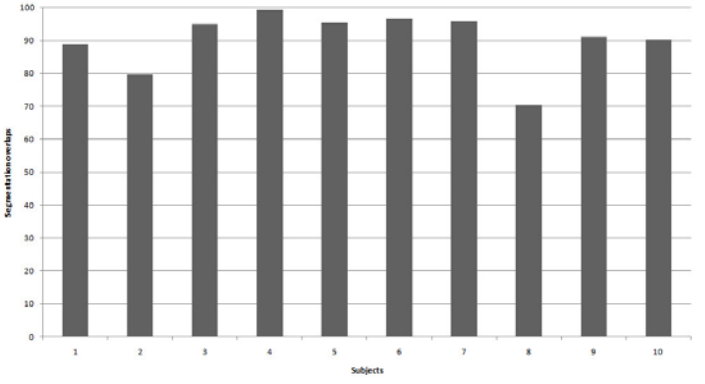

Fig. 5. The mean overlap (between manual and our segmentation) over the selected 5 slices for each of the 10 subjects

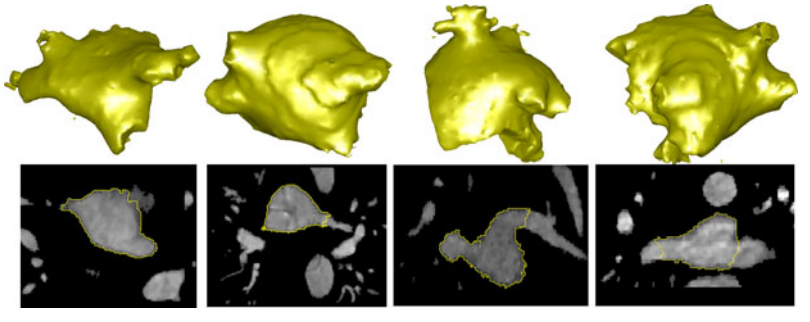

Fig. 6. (Top row) 3D surface rendering of segmented atria obtained from the proposed approach. (Bottom row) The outlines of the segmentations on the angiography images

5 Discussion

This paper describes a new and novel approach for segmenting the left atrium from CE-MRA images via an energy minimization approach. Existing approaches for

segmentation [4,7,1] mostly use ad-hoc methods for separating the atrium from surrounding structures. The exclusion of the ventricle, the extensive vessel drainage network and the pulmonary arteries makes our approach unique. Without prior information of the anatomy, it is difficult to compute a segmentation that only obtains the clinically relevant structures which are the atrial chamber and the drainages as far as the first bifurcation. Our segmentations have shown that only structures of interest can be obtained for different anatomical configurations. In all the cases the ventricle, pulmonary arteries and the drainage networks were excluded. The incorporation of a probabilistic spatial atlas provides the model with an effective prior. Comparison with manual segmentations indicate positive results.

The atrial geometry obtained from the segmentations are important for Electrophysiology (EP) mapping systems such as Ensite NavX and Biosense CARTO. The MRI segmentations can be loaded during a procedure to provide a more detailed anatomy than the one constructed on-site using a catheter. Also, new research into atrial fibrosis and scarring has made it essential to map scar (from pre-procedural imaging) and intra-procedural voltage information to the anatomy (see Fig. 7). Studying the temporal process of scar formation is providing new insights into the progression and recovery of the disease process [11]. With a better atlas, the method is promising and has the potential of being applied to other imaging modalities such as free-breathing non-contrast MRA, a new recent technique in imaging.

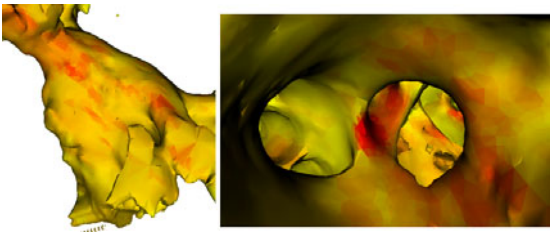

Fig. 7. Left atrial scar information can be mapped and fused to the extracted atrial geometry (left). Endocardial view (right)

References

1. John, M., Rahn, N.: Automatic Left Atrium Segmentation by Cutting the Blood Pool at Narrowings. In: Duncan, J.S., Gerig, G. (eds.) MICCAI 2005. LNCS, vol. 3750, pp. 798–805. Springer, Heidelberg (2005)
2. Lorensen, W.E., Cline, H.E.: Marching cubes: A High Resolution 3D Surface Construction Algorithm. In: Proc. of the 14th Annual Conference on Computer Graphics and Interactive Techniques (1987)
3. Boykov, Y., Veksler, O., Zabih, R.: Fast Approximate Energy Minimization via Graph Cuts. IEEE Tran. on Patt. Analysis and Machine Intelligence 23(11), 1222–1239 (2001)
4. Karim, R., et al.: Left Atrium Segmentation for Atrial Fibrillation Ablation. In: Proceedings of SPIE Medical imaging, Florida, vol. 7261, p. 95 (2009)

5. Marom, E.M., et al.: Variations in Pulmonary Venous Drainage to the Left Atrium. Radiology 230(3), 824–829 (2004)
6. Greig, D.M., Porteous, B.T., Seheult, A.H.: Exact Maximum a posteriori Estimation for Binary Images. Jour. of the Royal Stat. Society. 51(2), 271–279 (1989)
7. Cristoforetti, A., Faes, L., Ravelli, F., Centonze, M., Del Greco, M., Antolini, R., Nollo, G.: Isolation of the left atrial surface from cardiac multi-detector CT images based on marker controlled watershed segmentation. Medical Engineering and Physics 30(1), 48–58 (2008)
8. Meyer, C., Manzke, R., Peters, J., Ecabert, O., Kneser, R., Reddy, V.Y., Chan, R.C., Weese, J.: Automatic Intra-operative Generation of Geometric Left Atrium/Pulmonary Vein Models from Rotational X-Ray Angiography. In: Metaxas, D., Axel, L., Fichtinger, G., Székely, G. (eds.) MICCAI 2008, Part II. LNCS, vol. 5242, pp. 61–69. Springer, Heidelberg (2008)
9. Hartkens, T., Rueckert, D., Schnabel, J.A., Hawkes, D.J., Hill, D.L.G.: VTK CISG Registration Toolkit: An Open Source Software Package for Affine and Non-rigid Registration of Single and Multimodal 3D Images. In: Bildverarbeitung für die Medizin, pp. 409–412 (2002)
10. Benjamin, E.J., Wolf, P.A., D'Agostino, R.B., Silbershatz, H., Kannel, W.B., Levy, D.: Impact of Atrial Fibrillation on the Risk of Death: The Framingham Heart Study. Circulation 98(10) (1998)
11. Oakes, R.S., Badger, T.J., Kholmovski, E.G., Akoum, N., Burgon, et al.: Detection and Quantification of Left Atrial Structural Remodeling with Delayed-enhancement Magnetic Resonance Imaging in patients with Atrial Fibrillation. Circulation 6(2) (2009)
12. Raya, S.P., Udupa, J.K.: Shape-based Interpolation of Multidimensional Objects. IEEE Trans. Med. Imaging 9(1), 32–42 (1990)
13. Otsu, N.: A threshold selection method from gray-level histogram. IEEE Transactions on Systems, Man and Cybernetics 9(1), 62–66 (1979)

Interactive Cardiac Image Analysis for Biventricular Function of the Human Heart

Hoi-Ieng Lam[1], Brett R. Cowan[2], Martyn P. Nash[1,3], and Alistair A. Young[1,2]

[1] Auckland Bioengineering Institute, University of Auckland, New Zealand
[2] Auckland MRI Research Group, University of Auckland, New Zealand
[3] Department of Engineering Science, University of Auckland, New Zealand
{h.lam,b.cowan,martyn.nash,a.young}@auckland.ac.nz

Abstract. We developed an interactive tool for biventricular function analysis from cardiac magnetic resonance (MR) images based on the guide point modelling (GPM) approach [1]. First we built a deformable model of both ventricles of the human heart which consisted of 138 nodes and 82 hexahedral elements, each with bicubic-Bézier-linear interpolation. The model was fitted to a digitized human data set for use as the prior shape in the GPM scheme, which we modified to have a 'predictor' step that used a host mesh fitting algorithm [2] to generate predicted points (PPs) based on the user-defined guide points (GPs). Then the model was fitted towards both GPs and PPs through linear least square minimization. The inclusion of the PPs significantly improved the numerical stability of the linear least square fit and significantly accelerated the solution time. This methodology requires further validation for future application in clinical biventricular analysis.

Keywords: biventricular function, right ventricle, guide point modelling, host mesh fitting.

1 Introduction

Over the years, the role of the right ventricle (RV) of the heart in interventricular dependence and maintaining normal overall haemodynamics has become much more recognized. Measurements of cavity volume, mass and shape of not only the left ventricle (LV), but also the RV, are essential for quantifying normal and impaired cardiac function. In particular, RV volume and function are important indicators when monitoring patients with valvular heart disease [3] and also those with congenital heart disease, where eight out of every thousand infants are affected [4].

A variety of automated image segmentation algorithms such as [5] and [6] for cardiac magnetic resonance (MR) images had been applied to segment both ventricles. Only a few of them were capable of 4D (3D+time) analysis. Moreover, segmentation of the RV endocardium is prone to errors due to the relatively coarse trabeculation of the RV and the unpredictability of RV shape variations under pathological conditions. Also, many of these algorithms only segmented

O. Camara et al. (Eds.): STACOM-CESC 2010, LNCS 6364, pp. 144–153, 2010.

the cavity volume (i.e. the ventricles' blood pool volumes) because segmentation of the epicardium is more problematic. Compared to these image segmentation algorithms, model-based analysis, which has been adopted by a number of studies [1,7,8,9,10] on cardiac image analysis, generally yielded more successful outcomes. The guide point modelling (GPM) technique [1] is one of the model-based analysis methods that enables rapid visualization and analysis of cardiac MR images for the LV in 3D space and through time. It allows minimal yet efficient user interaction to aid the fitting of a deformable finite element (FE) model of the LV to cardiac MR images. The mass, volume and ejection fraction of the LV throughout the cardiac cycle can be obtained.

In this paper, we propose a modelling tool for analysing biventricular function from cardiac MR images based on the GPM approach. Sections 2.1 to 2.4 describe how we developed a biventricular model of the human heart. Then Sect. 2.5 describes how the GPM approach was modified to perform faster by including an extra step of host mesh fitting [2]. The modified GPM was applied to a normal volunteer data set as described in Sect. 3 and we conclude with a discussion in the last section.

2 Method

2.1 Digitization of Human Heart Geometry

We used a set of MR images of a healthy male human volunteer acquired at end-diastole provided by the Centre for Advanced MRI (Auckland, New Zealand). The acquisition parameters were: navigator-gated whole heart 3D sequence with a T2 preparation pulse, 50 short-axis images and 30 long-axis images, each with 192×192 voxels of dimension $0.94 \times 0.94 \times 1.30\,\text{mm}^3$ and $1.35 \times 1.35 \times 1.30\,\text{mm}^3$ respectively, on a 1.5T Siemens MRI scanner (MAGNETOM Avanto System). Manual segmentations were drawn on the endocardial surfaces of the left and right ventricles, the epicardial surface of the whole heart, and around the four valve orifices (namely, the mitral, aortic, tricuspid and pulmonary valves) of the heart.

2.2 Initial Geometry

A porcine FE model [11] was used as the initial approximation of the anatomical geometry of the human heart. It consisted of 88 hexahedral elements with 156 nodes, encompassing both LV and RV. This biventricular model also contained the four valve orifices of the heart, which was the main reason why we chose it among a number of other biventricular models (e.g. for dog [7,12,13,14], rabbit [15], etc.) as the initial geometry.

The model was defined in rectangular Cartesian coordinates, with z-axis pointing from the base towards the apex, y-axis pointing from the centre of the LV towards the centre of the RV and x-axis pointing from posterior to anterior of the heart. Within each element, cubic Hermite basis functions were used to interpolate the element coordinates, ξ_1, ξ_2 and ξ_3, which were aligned approximately in

the circumferential, longitudinal, and transmural directions of the heart, respectively. The position at a given $\boldsymbol{\xi}$ position within an element can be calculated as a weighted average of nodal positions $\mathbf{x}_n$ by

$$\mathbf{x}(\boldsymbol{\xi}) = \sum_{n=1}^{N} \Psi_n(\boldsymbol{\xi})\mathbf{x}_n \tag{1}$$

where Ψ_n is the basis function n evaluated at $\boldsymbol{\xi}$ and $\boldsymbol{\xi} \in [0, 1]$.

2.3 Modifications

Several modifications were done to minimize the number of degrees of freedom (DOFs) of the porcine model to enable fast clinical analysis. The major modifications made to the model are described in the following paragraphs.

Coordinate System. The porcine model was transformed to be in a standard cardiac coordinate system, where the x-axis was oriented along the LV central axis and directed towards the LV apex, the y-axis directed from the LV centre towards the RV centre and the z-axis directed from anterior towards posterior of the heart. The origin of this coordinate system was placed on the LV central axis one third of the distance from the base to the apex. This was done so that the model would be in the same coordinate system convention as previously used for GPM [1].

Interpolation Scheme. We changed the interpolation scheme in the ξ_3 direction (i.e. transmural direction) to be linear. As a result of this, the nodal derivatives with respect to ξ_3 were no longer needed. Secondly, when the ξ_1 or ξ_2 direction of an element coincided with a ξ_3 direction of an adjacent element, the ξ_1 or ξ_2 direction of the first element would need to be constrained to be linearly interpolated. For example, this was done for the elements at the RV insertion. Also, we changed the model's cubic Hermite interpolation to be cubic Bézier basis functions in ξ_1 and ξ_2 directions (i.e. circumferential and longitudinal directions respectively). Bézier basis functions provide derivative continuity between the elements without the need of nodal derivatives to be specified. To achieve derivative continuity at the nodes, a global-to-local parameter mapping [16] was used.

RV Apex Geometry. In the original porcine model, the RV apex had a thicker wall than the LV apex as shown in Fig. 1(a), where there were two layers of elements beneath the RV cavity. However, human hearts usually have approximately equal thickness at both LV and RV apexes from observation. Therefore we extended the RV cavity by splitting apart the layer of initially adjacent elements which were directly below the RV cavity (see Fig. 1(a)).

Basal Geometry. We simplified the complicated basal geometry of the model by removing the 6 basal elements which originally surrounded the inner side of the valves. Then we collapsed the $\xi_2 = 1$ face of the 12 basal elements which

surrounded the outer side of the valves. This ensured all endocardial surfaces were smoothly interpolated by cubic Bézier polynomials, without any inconsistency of ξ directions between adjacent elements. Also, the element between the LV inflow and outflow tract was being collapsed in the ξ_3 direction at every node such that it became a surface element. (See Fig. 1(b).)

Gap removal. The original porcine model had hanging nodes at the LV and RV outflow tracts, which resulted in gaps in some element boundaries due to different level of subdivision between adjacent elements at their common boundary. As some basal elements were removed as described in the previous paragraph, the hanging node at the LV outflow tract no longer exists in the model. For the remaining hanging nodes on the RV outflow tract, we adjusted the position of each hanging node to lie half way along the boundary of the bigger element by assigning its position to be the average of its nearest vertices [16]. This constraint was enforced in the global-to-local map of the model.

2.4 Final Geometry

After all the modifications, the simplified biventricular model consisted of 82 bicubic-Bézier-linear elements and 138 nodes. The total number of geometric DOFs in the model was reduced from 5981 to 1791.

Fitting to Human Data. Before fitting to the digitized human data set, the surfaces of the simplified biventricular model was triangulated such that there were 32 triangles on each element surface that formed the endocardial or the epicardial surface. Also, the model was translated, rotated and uniformly scaled so that it was well-positioned within the data cloud prior to fitting. We used linear least square minimization to penalize the observed ($\mathbf{z}_d$) and the predicted ($\mathbf{u}(\boldsymbol{\xi}_d)$) data displacements. The objective function to be minimized is given by

$$E(\mathbf{u}_n) = \sum_{d=1}^{D} \left\| w_d \left(\mathbf{u}(\boldsymbol{\xi}_d) - \mathbf{z}_d \right) \right\|^2 + E_s(\mathbf{u}_n) \tag{2}$$

$$\mathbf{u}(\boldsymbol{\xi}_d) = \mathbf{x}^{final}(\boldsymbol{\xi}_d) - \mathbf{x}^{initial}(\boldsymbol{\xi}_d) \tag{3}$$

$$\mathbf{z}_d = \mathbf{h}_d - \mathbf{x}^{initial}(\boldsymbol{\xi}_d) \tag{4}$$

where D is the total number of data points, w_d is the weight for each data point which is generally kept at 1.0 for geometric fitting, $\mathbf{h}_d$ is the global coordinates of the data points, and $\mathbf{x}^{initial}(\boldsymbol{\xi}_d)$ and $\mathbf{x}^{final}(\boldsymbol{\xi}_d)$ are the positions of the vertices on the model surface closest to the data points before and after the fit, respectively. Since $\mathbf{u}(\boldsymbol{\xi}_d) = \sum_{n=1}^{N} \Psi_n(\boldsymbol{\xi}_d)\mathbf{u}_n$ according to (1), (2) can be rewritten as

$$E(\mathbf{u}_n) = \sum_{d=1}^{D} \left\| w_d \left(\Psi_n(\boldsymbol{\xi}_d)\mathbf{u}_n - \mathbf{z}_d \right) \right\|^2 + E_s(\mathbf{u}_n) \tag{5}$$

The second term in the objective function is a Sobelov smoothing penalty function which helps to maintain the smoothness of the model.

Minimizing (5) and equating that to zero would result in a linear system of equations in the form of $Ax = b$, where A is a square matrix and consists of two terms $A = A_d + A_s$. These two terms correspond to those two in the objection function, i.e. the first relates to the data points to be fitted and the second one relates to the smoothing. Solving this system of equations would give the displacements $\mathbf{u}_n$ and hence $\mathbf{u}(\boldsymbol{\xi}_d)$ could be obtained. Then, the positions of the closest vertices after each fit was found by substituting $\mathbf{u}(\boldsymbol{\xi}_d)$ into (3). Due to the geometric complexity of the heart, the fitted model was slightly manually adjusted at places where necessary. The resultant fitted model is shown in Fig. 1(d), with a root mean squared error of 0.99 mm (2 s.f.).

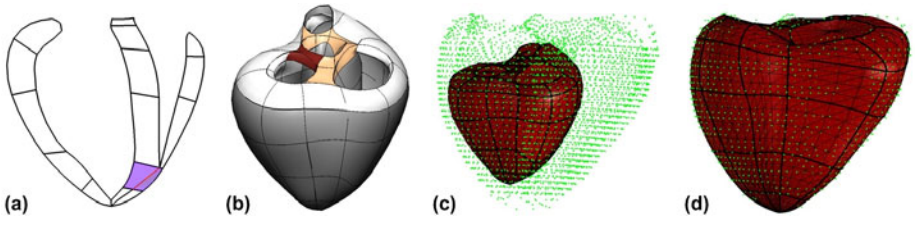

Fig. 1. (a) A horizontal long-axis view of the porcine model. To allow the RV cavity to extend further towards the apex, the shaded elements were split apart along the edge highlighted in red. (b) The original porcine model with elements colored in light orange to be removed, those colored in white to have their $\xi_2 = 1$ face collapsed and the element in dark red to be collapsed into a surface element. (c) The biventricular model before fitting to the human data (green points). (d) The fitted model. Note that the triangles shown are not elements but act as visualization aids and their vertices were used in the fitting process.

2.5 Implementation of Human Heart Model to Modified GPM

Figure 2 gives a summary of the modified GPM. The biventricular model is interactively fitted to guide points (GPs), predicted points (PPs) and image-derived data. The model updates in real-time accordingly, where mass and volume are also recalculated. Each step is summarized in the following paragraphs.

Initialization. We implemented the biventricular model obtained in the previous section into the GPM framework as the prior shape to be customized for different patient data. For biventricular function analysis, the user needed to define a set of fiducial markers which includes: (i) the centres of the LV cavity on apical and basal short-axis images; (ii) the centre of the RV cavity on a basal short-axis image; (iii) the RV insertion points which are located at the intersection of the endocardial RV free wall with the interventricular septum on all appropriate short-axis images; (iv) (optional) the centroids of the four valve orifices on appropriate long-axis images and (v) the LV epicardial apex on a long-axis image. A scale factor for the heart model was obtained based on the distance between the most basal marker (usually one of the valve centroid markers) and the most apical marker (the LV epicardial apex).

Customization. An interactive environment was provided for the user to place GPs sparsely on the endocardial surfaces of the left and right ventricles, the epicardial surfaces of the whole heart and the four valve orifices of the heart. GPs were generally placed on the end-diastolic, end-systolic and end of rapid-filling phases, before placing them on other phases as needed. A non-rigid registration algorithm [17] was employed to track the contours (model-image intersections) throughout each phase of the cardiac cycle. Also, an automatic image segmentation algorithm [18] was implemented to obtain edge information but the usage of this algorithm is optional.

Solution. The fitting algorithm of GPM was basically the same as the linear least square minimization approach described in Sect. 2.4, except that preconditioning was also employed when solving the linear system of equations $Ax = b$. Preconditioning is a process that transforms the $Ax = b$ system into $M^{-1}Ax = M^{-1}b$, where M is called the preconditioner. If M is well chosen, $M^{-1}Ax = M^{-1}b$ would have more favourable properties for iterative solution to have a faster convergence [19]. Thus, we would like to construct a preconditioner M that is close enough to A but also attempts to reduce the condition number of the coefficient matrix. As mentioned in the previous section, $A = A_d + A_s$. The second term, A_s, can be pre-calculated before the iterative solution process commences. However, the first term, A_d, cannot be pre-calculated. This is because A_d depends on $\boldsymbol{\xi}_d$, the local coordinates of the model surface vertices that are closest to the GPs, which vary according to the user input. For simplicity, the original GPM scheme took A_s to be the preconditioner, i.e. $M^{-1} = A_s^{-1}$. However, it was found that using A_s as the preconditioner performed poorly for biventricular analysis.

Predictor Step. To circumvent this poor preconditioning and to add a more intuitive interactivity to the model, we added an extra 'predictor' step, which took place before the actual linear least square minimization, to the GPM scheme. In this step, we introduced computer-generated data points which we call 'predicted points' (PPs). Their initial positions were defined to be the nodal positions $\mathbf{x}_n$ of our biventricular model, thus there were a total of 138 PPs. When GPs were added or edited during the interactive GPM analysis, model surface vertices closest to the GPs would be calculated. Then a host mesh consisting of a single hexahedral trilinear element would be constructed to encompass the closest surface vertices, the GPs and the PPs. The element coordinates ($\boldsymbol{\xi}$) of the closest surface vertices and PPs within the host mesh were calculated. The host mesh would be deformed to minimize the distances between the GPs and their corresponding surface vertices in a similar fashion as in Sect. 2.4, but with nodal parameters in (5) corresponding to the nodes of the host mesh. When the mesh deformed, since a unique material point is always identified by the same local coordinate value, the PPs would undergo the same deformation as the mesh. Therefore the updated PPs provide information on how the model would deform and thus we could fit our model to the GPs as well as the updated PPs, along with other image-derived data. But lower weights were applied on the PPs than the GPs to ensure that the model would be fitted closely to the user inputs.

With the addition of PPs, A_d, the first term of the A matrix of the linear system, becomes dependent on the $\boldsymbol{\xi}$ coordinates of the model surface vertices which correspond to the GPs as well as those of the nodal vertices which correspond to the PPs. This means that $A_d = A_g + A_p$, where A_g refers to the part of A_d that depends on the GPs and A_p is related to PPs. Hence, $A = A_g + A_p + A_s$. Since the PPs would always exist in the model fit and always correspond to the same nodal vertices, the preconditioner could be set up as $M = A_p + A_s$.

There is a second advantage with the introduction of PPs to the GPM scheme for biventricular analysis. The valve centroids are landmarks that can be easily located on images that cross through the inflow and outflow tracts of the ventricles. Hence it would be advantageous to make use of them when fitting the biventricular model where possible. However the valve centroids do not reside within any elements of the biventricular model, therefore it is impossible to incorporate GPs placed at the valve centroids into the model fit. But we can incorporate the GPs for the valve centroids into the host mesh fit because they can be embedded into the same host mesh in which all PPs and the closest surface vertices are also embedded within. Hence, when user defines a GP for one of the valve centroids, the model would be fitted implicitly to that GP by fitting towards the PPs that would have been updated based on the valve centroid GP.

3 Results

We fitted our biventricular model to a set of 9 user-defined fiducial GPs placed on cine MR images of a normal volunteer at end-diastole (cardiac-gated spin echo, 8 short-axis images and 2 long-axis images, each with 192×256 voxels of dimension $1.41 \times 1.41 \times 5.00\,\text{mm}^3$), using the original GPM and also the modified GPM approach.

Table 1 shows that the solution time was significantly faster and the accuracy significantly improved using the modified GPM method. Without PPs and using only the smoothing terms in the preconditioner, the solution still had not converged after 200 conjugate gradient iterations. Figure 3 shows the model after being fitted to endocardial and epicardial GPs, as well as the first 9 GPs mentioned above using the modified GPM approach.

Table 1. Comparison between the original and the modified GPM technique when the model was fitted to 9 user-defined fiducial GPs (1 for LV epicardial apex, 6 for RV insertion positions, 1 for mitral valve and 1 for tricuspid valve). The maximum number of iterations was pre-defined to be 200 and the tolerance was set to be 10^{-6}.

	Model Fit Only			Host Mesh Fit + Model Fit		
	X	Y	Z	X	Y	Z
Number of Iterations	200	200	200	8	7	8
Time taken (s)	0.92	0.92	0.92	0.047	0.032	0.047
Residual (mm)	0.095	0.12	0.047	2.2×10^{-11}	4.7×10^{-7}	4.0×10^{-11}

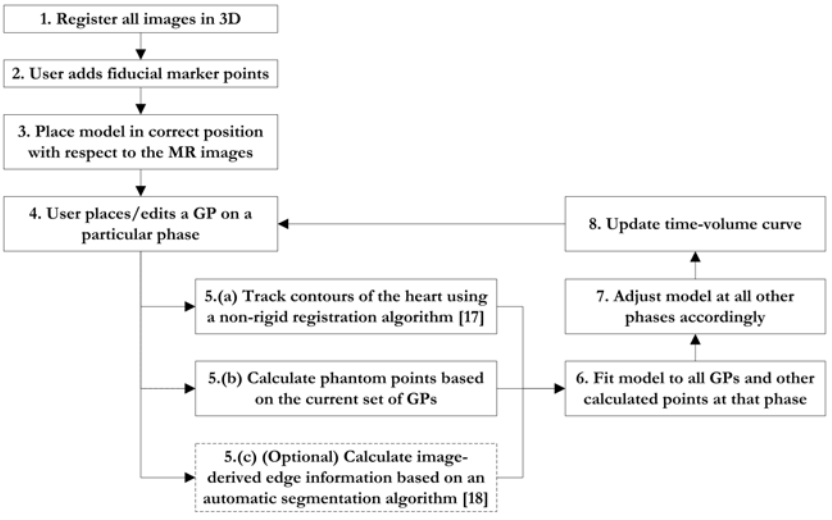

Fig. 2. An overview of the modified GPM for biventricular function analysis. The box surrounded by dotted line is an optional routine.

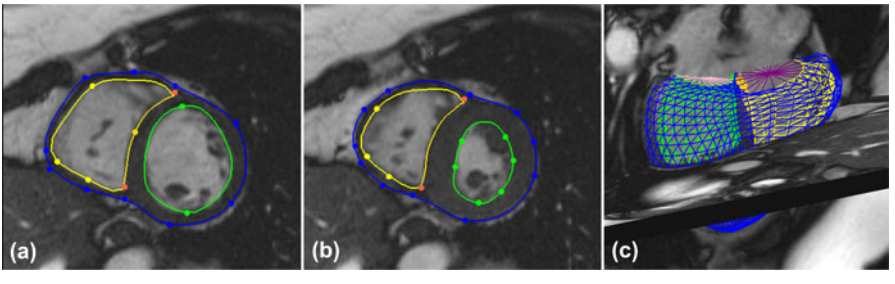

Fig. 3. Application of the modified interactive GPM to image data of a normal volunteer (only GPs are shown) at (a) end-diastole and (b) end-systole. (c) The fitted biventricular model in 3D with short and long axis MR images.

4 Conclusions and Discussions

The relatively thin wall of the RV, and also its complicated, asymmetric geometry has made it much more difficult than the LV to model its geometry and motion. Thus we developed a biventricular model for the human heart and implemented that into the 4D spatial-temporal interactive GPM technique. We modified the GPM technique such that there was an extra step of host mesh fitting and the result of that was fed into the next step where the actual model fit was performed. The host mesh fit acted to give a rough prediction how the model would deform according to the user-defined GPs and this information was incorporated as some constraints in the system of linear equations of the model fit. This significantly

improved the stability of the system of linear equations to be solved, hence a significant improvement in the speed of convergence. The interactive modelling technique developed here could be adapted to work with other biventricular models such as those mentioned in Sect. 2.2. Also, it would not be difficult to include myocardial fibre orientation into the human-customized model since the original porcine model had myocardial fibre orientation incorporated.

In conclusion, we demonstrated the capability of our interactive biventricular modelling tool on a normal volunteer study. The result so far is promising but certainly requires validation before clinical application can be done. Another possible future work includes optimizing the values of smoothing weights.

Acknowledgments. Hoi-Ieng Lam is funded by the Tertiary Education Committee of New Zealand and the University of Auckland, New Zealand. Alistair A. Young is supported by Award Number R01HL087773 from the National Heart, Lung and Blood Institute (USA). Martyn P. Nash is supported by a James Cook Fellowship administrated by the Royal Society of New Zealand on behalf of the New Zealand Government.

References

1. Young, A.A., Cowan, B.R., Thrupp, S.F., Hedley, W.J., Dell'Italia, L.J.: Left Ventricular Mass and Volume: Fast Calculation with Guide-Point Modeling on MR Images. Radiology 216, 597–602 (2000)
2. Fernandez, J.W., Mithraratne, P., Thrupp, S.F., Tawhai, M.H., Hunter, P.J.: Anatomically Based Geometric Modelling of the Musculo-Skeletal System and Other Organs. Biomech. Model. Mechanobiol. 2, 139–155 (2003)
3. Nagel, E., Stuber, M., Hess, O.M.: Importance of the Right Ventricle in Valvular Heart Disease. Eur. Heart J. 17, 829–836 (1996)
4. Lilly, L.S. (ed.): Pathophysiology of Heart Disease: A Collaborative Project of Medical Students and Faculty, 2nd edn. Williams & Wilkins, USA (1998)
5. Lorenzo-Valdes, M., Sanchez-Ortiza, G., Elkingtonb, A., Mohiaddinb, R., Rueckert, D.: Segmentation of 4D Cardiac MR Images Using a Probabilistic Atlas and the EM Algorithm. Med. Image Anal. 8, 255–265 (2004)
6. Cocosco, C.A., Niessen, W.J., Netsch, T., Vonken, E.J., Lund, G., Stork, A., Viergever, M.A.: Automatic Image-Driven Segmentation of the Ventricles in Cardiac Cine MRI. J. Magn. Reson. Imaging 28, 366–374 (2008)
7. Sermesant, M., Forest, C., Pennec, X., Delingette, H., Ayache, N.: Deformable Biomechanical Models: Application to 4D Cardiac Image Analysis. Medical Image Analysis 7(4), 475–488 (2003)
8. Lötjönen, J., Kivistö, S., Koikkalainen, J., Smutek, D., Lauerma, K.: Statistical Shape Model of Atria, Ventricles and Epicardium from Short- and Long-Axis MR Images. Med. Image Anal. 8, 371–386 (2004)
9. Bistoquet, A., Oshinski, J., Skrinjar, O.: Left Ventricular Deformation Recovery from Cine MRI using an Incompressible Model. IEEE Trans. Med. Imag. 26(9), 1136–1153 (2007)
10. Zhang, H., Wahle, A., Johnson, R.K., Scholz, T.D., Sonka, M.: 4-D Cardiac MR Image Analysis: Left and Right Ventricular Morphology and Function. IEEE Trans. Med. Imaging 29(2), 350–364 (2010)

11. Stevens, C., Remme, E., LeGrice, I., Hunter, P.: Ventricular Mechanics in Diastole: Material Parameter Sensitivity. J. Biomech. 36(5), 737–748 (2003)
12. Nielsen, P.M.F., LeGrice, I.J., Smaill, B.H., Hunter, P.J.: Mathematical Model of Geometry and Fibrous Structure of the Heart. Am. J. Physiol. 260, H1365–H1378 (1991)
13. LeGrice, I.J., Hunter, P.J., Smaill, B.H.: Laminar Structure of the Heart: a Mathematical Model. Am. J. Physiol. 272, H2466–H2476 (1997)
14. Kerckhoffs, R.C.P., Bovendeerd, P.H.M., Prinzen, F.W., Smits, K., Arts, T.: Intra- and Interventricular Asynchrony of Electromechanics in the Ventricularly Paced Heart. J. Eng. Math. 47, 201–216 (2003)
15. Vetter, F.J., McCulloch, A.D.: Three-Dimensional Analysis of Regional Cardiac Function: a Model of Rabbit Ventricular Anatomy. Prog. Biophys. Mol. Biol. 69, 157–183 (1998)
16. Nielsen, P.M.F.: The Anatomy of the Heart: A Finite Element Model. PhD Thesis, University of Auckland (1987)
17. Li, B., Young, A.A., Cowan, B.R.: GPU Accelerated Non-rigid Registration for the Evaluation of Cardiac Function. Med. Image Comput. Comput. Assist. Interv. 11(Pt. 2), 880–887 (2008)
18. Singleton, H.R., Pohost, G.M.: Automatic Cardiac MR Segmentation using Edge Detection by Tissue Classification in Pixel Neighborhoods. Magn. Reson. Med. 37, 418–424 (1997)
19. Trefethen, L.N., Bau III, D.: Numerical Linear Algebra. S.I.A.M., Philadelphia (1997)

Cardiac Motion Estimation Using a ProActive Deformable Model: Evaluation and Sensitivity Analysis

Ken C.L. Wong[1], Florence Billet[1], Tommaso Mansi[1], Radomir Chabiniok[2], Maxime Sermesant[1,3], Hervé Delingette[1], and Nicholas Ayache[1]

[1] INRIA, Asclepios project, 2004 route des Lucioles, Sophia Antipolis, France
[2] INRIA, Macs project, Rocquencourt, Le Chesnay, France
[3] King's College London, St Thomas Hospital, Division of Imaging Sciences, London, UK

Abstract. To regularize cardiac motion recovery from medical images, electromechanical models are increasingly popular for providing *a priori* physiological motion information. Although these models are macroscopic, there are still many parameters to be specified for accurate and robust recovery. In this paper, we provide a sensitivity analysis of a proactive electromechanical model-based cardiac motion tracking framework by studying the impacts of its model parameters. Our sensitivity analysis differs from other works by evaluating the motion recovery through a synthetic image sequence with known displacement field as well as cine and tagged MRI sequences. This analysis helps to identify which parameters should be estimated from patient-specific data and which ones can have their values set from the literature.

1 Introduction

Cardiac motion recovery has been an active research area for decades, aiming at accurate and robust estimation of patient-specific myocardial motions from cardiac images. Although medical image modalities, such as magnetic resonance images (MRI), can provide observations of cardiac anatomy and apparent motion, the motion information is often sparse, spatially and temporally noisy, and leads to qualitative rather than quantitative estimations. Therefore, *a priori* motion information is often required to regularize the motion estimation. To this end, electromechanical models have been increasingly popular because of their physiological meaningfulness [1,2,3].

Macroscopic electromechanical models applied to cardiac image analysis usually consist of three key components: transmembrane potential wave propagation, active contraction forces, and passive biomechanics. Although these models are somewhat simplified compared to cellular cardiac models, they still have many parameters to be specified for clinically relevant recovery. Some authors [4,5] have already published some sensitivity analyses in which the effects of model parameter variations were quantified on simulated cardiac functions. These studies are

O. Camara et al. (Eds.): STACOM-CESC 2010, LNCS 6364, pp. 154–163, 2010.

useful to assess the relative impact of those parameters, however, without any validation on *in vivo* patient data, the analyses cannot provide any hints about the validity of the model for a given patient.

In this paper, we present a sensitivity analysis of electromechanical model parameters for patient-specific cardiac motion recovery from medical images. Through synthetic images for which the ground truth is available, and patient cine MRI for which the corresponding cardiac motion was estimated by experts from tagged MRI, we studied the sensitivity of the motion recovery framework proposed in [1] with respect to the model parameters. This analysis can aid finding which parameters should be estimated from patient-specific measurements and which can have their values set from the literature. It also evaluates the physiological plausibility of the adopted cardiac electromechanical model by comparing the simulated displacements with the expert-estimated motions from the tagged MRI.

2 Motion Recovery with Electromechanical Model

The cardiac motion recovery framework in [1] was tested, which uses the ProActive Deformable Model whose dynamics equation is:

$$\mathbf{M}\ddot{\mathbf{U}} + \mathbf{C}\dot{\mathbf{U}} + \mathbf{K}\mathbf{U} = \mathbf{F}_b + \alpha\mathbf{F}_c + \beta\mathbf{F}_{\text{img}} \tag{1}$$

with $\mathbf{M}$, $\mathbf{C}$, and $\mathbf{K}$ the mass, damping, and stiffness matrices respectively. $\mathbf{F}_b$ comprises different external loads from boundary conditions. $\mathbf{F}_c$ and $\mathbf{F}_{\text{img}}$ are the vectors for active contraction forces and image-derived forces respectively. α and β are scaling parameters involved in the sensitivity analysis.

To obtain the contraction force vector $\mathbf{F}_c$, the electrical activation times computed using a multi-front anisotropic Eikonal approach were used to provide the contraction forces along given fiber orientations [6]. The blood pressures on the ventricular walls were provided by prescribed atrial pressures in the filling phase, a three-element Windkessel model in the ejection phase, and ventricular volumetric constraints in the isovolumetric phases. The image force vector $\mathbf{F}_{\text{img}}$ was computed using a correlation-based 3D block-matching algorithm [7] combined with image intensity gradients, tracking the motions of the salient cardiac features on the heart surfaces. The linear and anisotropic biomechanical properties are included in $\mathbf{K}$, whose stiffness is specified by the Young's moduli along and across the fibers (E_f, E_{cf}). The sensitivity analysis of cardiac motion recovery can be performed by solving (1) with varying parameters.

3 Experiments

3.1 Experimental Setup

The sensitivity analysis is focused on parameters related to biomechanics. For each data set, we first obtained a simulation which is similar to the apparent

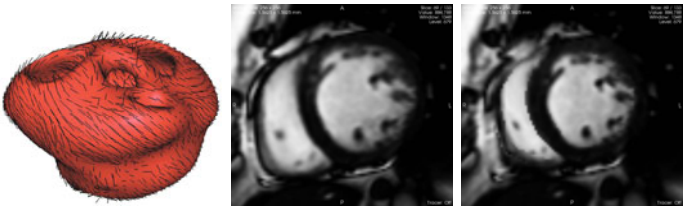

(a) Synthetic data.

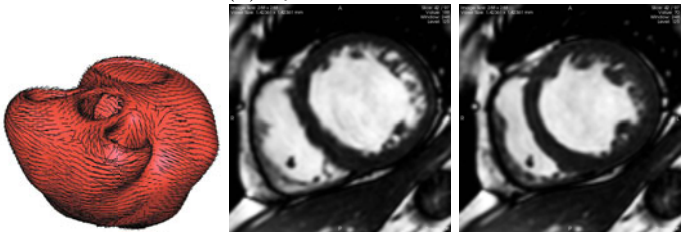

(b) Patient data set 1.

Fig. 1. Data used in the experiments. Left to right: heart geometry segmented from patient MRI with synthetic fiber orientations, image frame at the end of diastole, and image frame at the end of systole. For (a), both images were synthesized from the MRI at the mid-diastole with the simulated deformation.

cardiac motion in the images, then we performed cardiac motion recovery with (11) by varying different parameters. The tested parameters include the active force scaling parameter ($\alpha = 0, 0.6, 0.8, 1.0, 1.2$) which controls the amount of myocardial contraction, the image force scaling parameter ($\beta = 0, 5, 15, 25, 45$) which controls the amount of image forces, the Young's modulus across the fiber direction ($E_{cf} = 25, 50, 75$ kPa, with $E_f = 75$kPa, i.e. from transversely isotropic to isotropic), and with or without ventricular blood pressures as boundary conditions. Different sets of fiber orientations (epicardium to endocardium: $-\theta$ to $+\theta$, $\theta = 20^o, 40^o, 60^o, 80^o$ for both left and right ventricles) were also tested. We varied only one parameter at a time for each test.

To analyze the sensitivity of the motion recovery framework corresponding to the above parameters, experiments were performed on one synthetic image sequence and two patient cine MRI sequences. No patient electrophysiological data were used during the recoveries.

Synthetic Data. The synthetic image sequence was obtained through a simulation using the measurements of a patient diagnosed with left bundle branch block. The electromechanical model used in the simulation is highly nonlinear compared with the ProActive Deformable Model used in this analysis. This nonlinear model uses the Ciarlet-Geymonat material as the nonlinear passive mechanical model and the Bestel-Clement-Sorine model as the active stress model with the consideration of actin-myosin interactions [8]. The anatomical MRI at the mid-diastole was segmented using the semi-automatic segmentation in CardioViz3D [9] to provide the heart geometry including the four basal valvular rings of the ventricles (Fig. 1(a)), with the synthetic fiber orientations generated

according to the literature (-70^o to $+70^o$ for the left ventricle, and -50^o to $+50^o$ for the right ventricle). The myocardial electrical activation was simulated using the Eikonal model with the patient electrophysiological data from the LV endocardium. A cycle of cardiac deformation of 1.054 s was simulated. By extrapolating the obtained deformation field to the whole image space, the image from which the heart geometry was segmented was warped into a synthetic image sequence, with 34 ms/frame, and isotropic spatial resolution resolution of 1.5625 mm/voxel. In the sensitivity analysis, the models and pathological situations were assumed to be unknown, thus the parameters used in the ProActive Deformable Model were nominal as described in [1].

Patient Data. Two cine MRI sequences from patients with dilated cardiomyopathy were used in the experiments. Data set 1 contains a cardiac cycle in 0.87 s, with temporal resolution 29 ms/frame, 10 mm inter-slice spacing, and in-plane resolution 1.42 mm/pixel (Fig. 1(b)). Data set 2 contains a cardiac cycle in 0.73 s, with temporal resolution 25 ms/frame, 10 mm inter-slice spacing, and in-plane resolution 1.45 mm/pixel. Both data sets have corresponding tagged MRI sequences collected at similar time instants, therefore experts could perform manual tracking of the tag plane intersections to extract the short-axis myocardial displacements as references. Furthermore, the expert-estimated ejection fractions of data set 1 and 2 are 25% and 15% respectively.

3.2 Results and Discussions

The results of the synthetic and patient data were evaluated with the same approach for consistency. For the patient data, as the tagged MRI were not well-registered with the cine MRI, and the tag plane intersections were too sparse to provide meaningful strains from the manually tracked displacements, direct point-to-point comparisons between the recovered deformation and the reference tag motions could not be performed. To cope with this, we compared the regional displacements using the 17 AHA segments [10]. For both recovered and reference motions, the mean radial and circumferential displacements of each segment were computed, which were used to compute the *displacement difference magnitude*:

$$\frac{\sum_i \|\bar{\mathbf{u}}_{\text{recovery}}(i) - \bar{\mathbf{u}}_{\text{reference}}(i)\|}{n} \tag{2}$$

with $\bar{\mathbf{u}}_{\text{recovery}}(i)$ and $\bar{\mathbf{u}}_{\text{reference}}(i)$ the mean displacement vectors (radial or circumferential) of the recovered and reference motions in segment i respectively, and n the number of segments utilized. As the short-axis tagged MRI cannot provide accurate motions around the apex, only segments 1 to 12 corresponding to the basal and the mid-ventricular levels were used. The results of the synthetic data were evaluated similarly with the reference motions from the displacement field of the simulated ground truth.

Fig. 2 shows the recovered geometries at the end of systole. For the synthetic data, the heart geometry recovered without image forces (i.e. pure simulation with the ProActive Deformable Model) is quite far from the ground truth, but

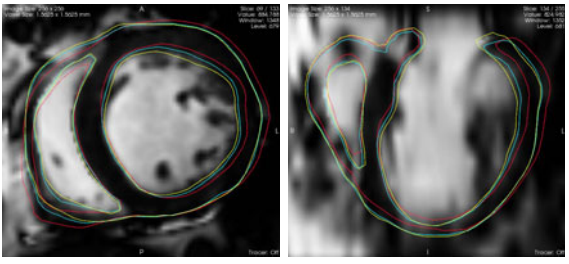

(a) Synthetic data.

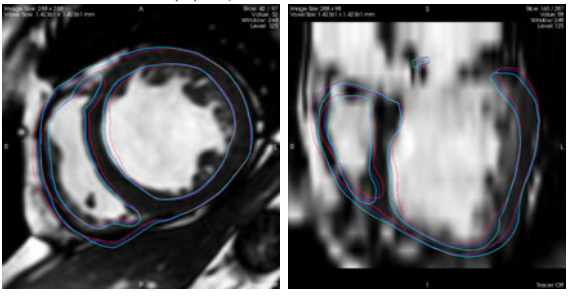

(b) Patient data set 1.

Fig. 2. Recovered geometries at the end of systole. Left to right: short-axis and long-axis views of recovered geometries overlapped with images. (a) Yellow line represents the ground truth, and red and cyan lines represent the recovered geometries with the image force scaling parameter $\beta = 0$ and 45 respectively. (b) Red, blue, and cyan lines represent the recovered geometries with the image force scaling parameter $\beta = 0$, 15, and 45 respectively.

the one recovered with large image forces is much closer. Interestingly, in some locations such as the endocardium of the left ventricle, the recovered geometry with large image forces is even closer to the apparent heart surfaces than the simulated ground truth. This shows that the recovery framework is capable of correcting imperfectness of initial segmentation by using image intensity gradients. Similarly, for the patient data sets, the larger the image forces, the more subject-specific the recovered geometries.

Fig. 3, 4, 5, and 7 show the changes of the displacement difference magnitude versus the changes of model parameters under different image forces. Similar to the observations in Fig. 2, in all tests, the larger the image forces, the closer the recovered motions to the reference motions. Furthermore, in most cases, the image forces show greater influences on the radial displacements rather than the circumferential displacements. This is reasonable as cine MRI, different from tagged MRI, can mainly provide apparent radial motions of the myocardium instead of circumferential motions.

Comparing the sensitivities between parameters, the anisotropy of mechanical stiffness is the least sensitive (Fig. 3, 4, and 5). The displacement difference magnitudes show relatively small changes when changing from anisotropy to isotropy

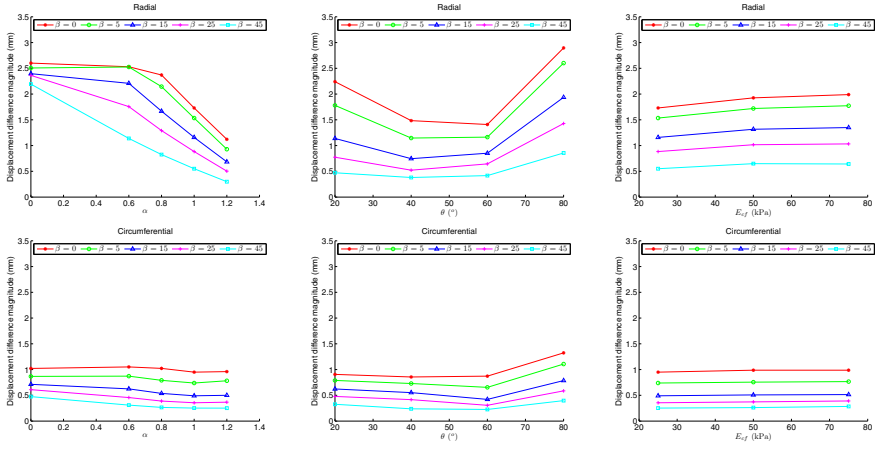

Fig. 3. Synthetic data. Displacement difference magnitude versus the change of model parameters at the end of systole. (a) Active force scaling parameter α. (b) Fiber orientations θ. (c) Cross-fiber Young's modulus E_{cf}. Different colors encode different values of the image force scaling parameter β.

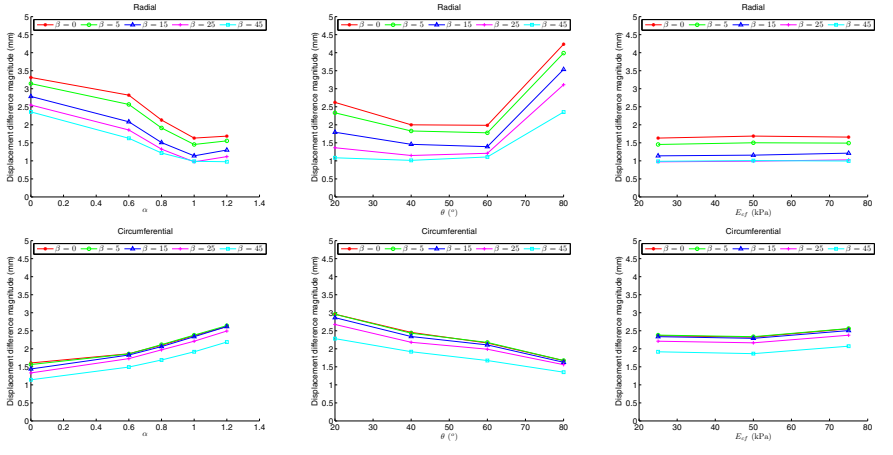

Fig. 4. Patient data set 1. Displacement difference magnitude versus the change of model parameters at the end of systole. (a) Active force scaling parameter α. (b) Fiber orientations θ. (c) Cross-fiber Young's modulus E_{cf}. Different colors encode different values of the image force scaling parameter β.

with fixed fiber distributions described in the literature. On the other hand, the recovery framework is more sensitive to the active forces and the fiber orientations. In fact, the fiber orientations mainly impact two aspects of the model: the

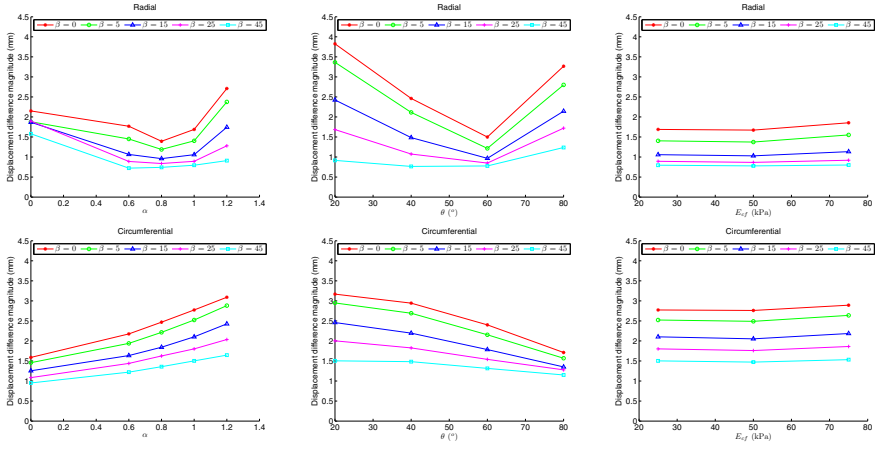

Fig. 5. Patient data set 2. Displacement difference magnitude versus the change of model parameters at the end of systole. (a) Active force scaling parameter α. (b) Fiber orientations θ. (c) Cross-fiber Young's modulus E_{cf}. Different colors encode different values of the image force scaling parameter β.

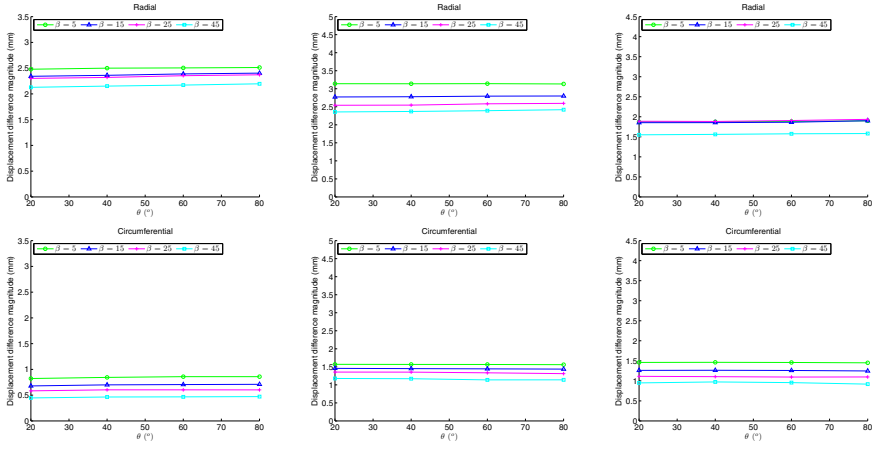

Fig. 6. Displacement difference magnitude versus the change of fiber orientations at the end of systole, with the active force scaling parameter $\alpha = 0$. (a) Synthetic data. (b) Patient data set 1. (c) Patient data set 2. Different colors encode different values of the image force scaling parameter β.

active contraction forces and the passive anisotropic mechanical properties. Although the results already showed that the ProActive Deformable Model is less sensitive to the stiffness anisotropy, we performed additional experiments with

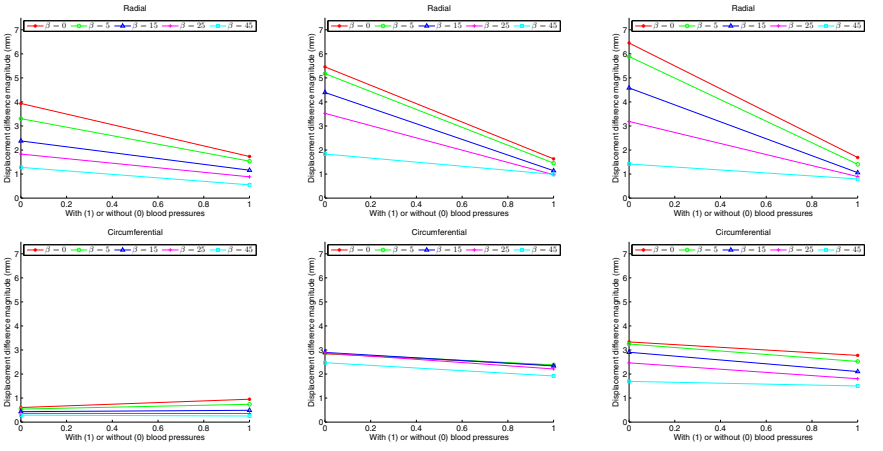

Fig. 7. Displacement difference magnitude versus with or without blood pressures, at the end of systole. (a) Synthetic data. (b) Patient data set 1. (c) Patient data set 2. Different colors encode different values of the image force scaling parameter β.

different fiber orientations without active forces. As it is meaningless to perform tests without both image and active forces, tests with $\beta = 0$ (no image forces) were not performed. Fig. 6 shows that without active forces, the changes of the recovery results versus the changes of fiber orientations are ignorable. Thus if active forces are not used, passive isotropic mechanical models might be enough for motion estimation. Furthermore, the ranges of the displacement difference magnitudes are larger when using active forces, which means that proper active forces are very important for accurate motion recovery.

Fig. 7 shows the test results with or without using blood pressures as boundary conditions. The absence of blood pressures can lead to large deviations in the radial direction, but these deviations decrease with the increase of the image forces. On the other hand, the effects of the blood pressures are less obvious in the circumferential direction. This shows that blood pressure constraints are important when image information is not reliable, but strong image information as boundary conditions can compensate for improper blood pressure specifications.

The red lines in the plots correspond to the absence of image forces, so they provide an objective evaluation of the simulation accuracy of the ProActive Deformable Model through the *in vivo* patient data. As the in-plane resolutions are between 1.42 and 1.56 mm/pixel, the minimum displacement difference magnitudes in the pure simulations are between one and two pixels. This shows that the model can reproduce patient-specific cardiac deformation when the parameters are properly adjusted.

4 Conclusion

From the above discussions, we conclude that the cardiac motion recovery framework is less sensitive to the anisotropy of the passive biomechanical model, and is more sensitive to active forces, fiber orientations, and blood pressures, especially when image information does not provide strong constraints. Therefore, if reliable image information can be extracted, the framework can correctly track cardiac motion up to pixel size even with parameters taken from the literature (cyan lines). On the other hand, if image quality is low, *a priori* information from the electromechanical model is crucial and subject-specific fiber orientations and blood pressures should be estimated from available measurements. Recent progress on *in vivo* diffusion tensor imaging of the heart and pressure estimation from flow data can complement very well such approaches. Furthermore, the cardiac motions recovered from the synthetic images using the ProActive Deformable Model are very close to the simulated ground truth of the nonlinear electromechanical model. This means that even the biomechanical model used is linear, the recovery framework can provide useful patient-specific cardiac motions for parameter estimations of nonlinear models, which can help to predict patient-specific cardiac functions for surgical planning or treatments.

References

1. Sermesant, M., Delingette, H., Ayache, N.: An electromechanical model of the heart for image analysis and simulation. IEEE Transactions on Medical Imaging 25(5), 612–625 (2006)
2. Wong, K.C.L., Zhang, H., Liu, H., Shi, P.: Physiome-model-based state-space framework for cardiac deformation recovery. Academic Radiology 14(11), 1341–1349 (2007)
3. Sundar, H., Davatzikos, C., Biros, G.: Biomechanically-constrained 4D estimation of myocardial motion. In: Yang, G.-Z., Hawkes, D., Rueckert, D., Noble, A., Taylor, C. (eds.) MICCAI 2009. LNCS, vol. 5762, pp. 257–265. Springer, Heidelberg (2009)
4. Nash, M.: Mechanics and Material Properties of the Heart using an Anatomically Accurate Mathematical Model. PhD thesis, The University of Auckland (1998)
5. Niederer, S., Rhode, K., Razavi, R., Smith, N.: The importance of model parameters and boundary conditions in whole organ models of cardiac contraction. In: Ayache, N., Delingette, H., Sermesant, M. (eds.) FIMH 2009. LNCS, vol. 5528, pp. 348–356. Springer, Heidelberg (2009)
6. Sermesant, M., Konukoğlu, E., Delingette, H., Coudière, Y., Chinchapatnam, P., Rhode, K.S., Razavi, R., Ayache, N.: An anisotropic multi-front fast marching method for real-time simulation of cardiac electrophysiology. In: Sachse, F.B., Seemann, G. (eds.) FIHM 2007. LNCS, vol. 4466, pp. 160–169. Springer, Heidelberg (2007)
7. Ourselin, S., Roche, A., Prima, S., Ayache, N.: Block matching: a general framework to improve robustness of rigid registration of medical images. In: Delp, S.L., DiGoia, A.M., Jaramaz, B. (eds.) MICCAI 2000. LNCS, vol. 1935, pp. 557–566. Springer, Heidelberg (2000)

8. Sainte-Marie, J., Chapelle, D., Cimrman, R., Sorine, M.: Modeling and estimation of the cardiac electromechanical activity. Computers and Structures 84, 1743–1759 (2006)
9. Toussaint, N., Mansi, T., Delingette, H., Ayache, N., Sermesant, M.: An integrated platform for dynamic cardiac simulation and image processing: application to personalised tetralogy of fallot simulation. In: Eurographics Workshop on Visual Computing for Biomedicine (VCBM) (2008)
10. Cerqueira, M.D., Weissman, N.J., Dilsizian, V., Jacobs, A.K., Kaul, S., Laskey, W.K., Pennell, D.J., Rumberger, J.A., Ryan, T., Verani, M.S.: Standardized myocardial segmentation and nomenclature for tomographic imaging of the heart: a statement for healthcare professionals from the cardiac imaging committee of the council on clinical cardiology of the American Heart Association. Circulation 105, 539–542 (2002)

Investigating Heart Failure Using Ventricular Imaging and Modelling

Vicky Y. Wang[1], Alistair A. Young[1,2], and Martyn P. Nash[1,3]

[1] Auckland Bioengineering Institute, University of Auckland, New Zealand
{vicky.wang,a.young,martyn.nash}@auckland.ac.nz
[2] Centre for Advanced MRI, University of Auckland, 85 Grafton Road, Auckland, 1142, New Zealand
[3] Department of Engineering Science, University of Auckland, Level3, UniServices House, 70 Symonds Street, Auckland, 1142, New Zealand

Abstract. It is well-established that ventricular hypertrophy is a transitional phase through the development of heart failure. A hypertrophic heart can remodel to compensate the loss of pump function, but it eventually becomes incapable of working efficiently, leading to heart failure. Many heart failure patients have preserved pump function (e.g. normal ejection fraction), but increased LV wall thickness and sometimes increased LV mass, which can mask a decrease in contractility. Alterations in the myofibre structure and myocardial material properties can potentially account for the progression of heart failure. We have developed a canine LV finite element model to investigate the effect of ventricular size, myocardial passive material properties, and cardiac contractility on the LV mechanical performance. By comparing mechanical function of normal and abnormal LVs, due to dilation and/or loss of anisotropy and/or reduced contractility, we found that dilation and compromised muscle contractility decreased most indices of cardiac performance. This modelling framework provides insight into the underlying mechanisms of heart failure.

Keywords: Hypertrophy, Heart failure, Finite Element (FE) Modelling, Left Ventricular (LV) mechanics, tissue remodelling, muscle contractility.

1 Introduction

Impaired diastolic function (e.g. increased LV wall thickness and wall mass) with normal systolic function (i.e. normal ejection fraction) has been found in many heart failure (HF) patients [1], and they have a similar disorder as people with impaired emptying function (systolic HF). Ventricular dilation, characterised by increased ventricular mass and wall thinning, is the primary alteration found in systolic HF patients. Generally, the disturbances in physiological, geometrical and/or haemodynamic loading conditions are considered as a main trigger of changes in wall thickness. This can directly result in a remodelling process in the myocytes to alter both passive stress (diastolic filling) and active stress (systolic contraction), and thus muscle performance during the cardiac cycle.

O. Camara et al. (Eds.): STACOM-CESC 2010, LNCS 6364, pp. 164–173, 2010.

Changes in ventricular chamber size and wall thickness are believed to originate from reorganisation of myocardial structure. The occurrence of structural remodelling through the progression from diastolic HF [2] to decompensated HF has been extensively studied [3]. Detailed morphometric measurements of 3D cardiac tissue architecture showed that the myocytes surrounded by endomysial collagen are arranged in layers or sheets of 3 to 5 cells thick [3]. The branched bundles of myocytes enclosed by perimysial collagen are loosely-coupled to adjacent layers with little direct coupling between cells. The perimysial collagen critically determines the organisation and network of myofibre structure, which affect its electrical and mechanical properties [4], [5], [6].

Discovery of loss of the 3D laminar structure in HF animal studies have brought the understanding of this disease to a new level. Significant growth of endomysial has been reported in [7] and gradual formation of thick sheets from perimysial collagen and the long perimysial cords that connect those layers in rats with hypertensive heart failure has also been revealed [2]. It is concluded that the tissue remodelling process alters the mechanical function of the myocardium by enhancing the transmural coupling, but preventing shearing and sliding of adjacent layers. The consequent myocardial rearrangement leads to LV wall thickening or thinning. Myocardial mechanical properties can also undergo changes [7], leading to compromised pump function.

This study utilised a FE model of a canine LV to simulate ventricular mechanics of the entire cardiac cycle under both normal and HF pathologic conditions. We focused on investigating the effect of altering ventricular size, material properties and muscle contractility on the mechanical function of the LV.

2 Methods

2.1 Anatomical Model

Development of the FE LV model used in this study has been previous described in [8] and this model was treated as the control case. Briefly, a FE LV model was created based on the LV geometry of a healthy canine heart that was imaged using *in vivo* high resolution tagged magnetic resonance imaging (MRI) experiments to obtain detailed non-invasive measurements of cardiac motion. The same heart was also imaged using *ex vivo* diffusion tensor MRI (DTMRI) to reconstruct the local fibre orientations of the entire heart. Imaging parameters and protocols are summarised in [9]. DTMRI provides information on the preferred direction of the local self-diffusion (maximum principle eigenvector of the measured tensor at each voxel) of water molecules, which has been shown to correlate with the local myofibre orientation of biological tissue [10]. However, the possibility of discerning sheet and sheet-normal orientations from the DTMRI still remains unclear. Therefore, only fibre orientations were incorporated into this FE model.

The anatomical FE model consisted of 16-element with surfaces fitted to the endocardial and epicardial contours segmented from the tagged MR images using nonlinear least squares fitting [11]. The nodal parameters were interpolated using cubic-Hermite basis functions. The surface contours of the DTMR images were also identified to extract myofibre orientation information within the LV myocardium. The change in heart

shape between the tagged MRI and DTMRI experiments was accounted for by transforming the fibre orientations derived from the DTMRI to the tagged FE model using a free-form deformation approach [12]. At each voxel, a local fibre angle was defined as the elevation angle with respect to the local circumferential direction in the short-axis plane. Fibre angles were fitted into the FE model using nonlinear optimisation.

2.2 Mechanics Model

The integrative model introduced above provides us with a platform whereby mechanical analysis of cardiac motion can be analysed using finite deformation elasticity and FE methods [11]. To simulate cardiac motion for the entire cycle, we have divided the simulation into two major phases: a passive phase that encompasses diastasis and diastolic inflation during which the LV relaxes from the previous cycle and begins to be filled with oxygenated blood; and an active phase that spans isovolumic contraction, ejection and isovolumic relaxation. Myocardial mechanics is governed by fundamental laws of physics (Newton's laws) with passive and active material relations specific to ventricular muscle.

In our previous study, we used this framework to combine displacement and motion information from *in vivo* MRI tagging with concurrent pressure recordings to estimate passive material properties of myocardium modelled using a transversely-isotropic material relation in Eq. 1[12]. The choice of transversely-isotropic over orthotropic mechanics was made due to lack of sheet orientation data for this study. The material parameters in Eq. 1 were tuned to best match the diastolic LV motion obtained from the tagged MR images and the simultaneously recorded LV cavity pressures.

$$\begin{aligned} W &= C_1 \exp(Q) \\ Q &= C_2 E_{ff}^2 + C_3 (E_{cc}^2 + E_{rr}^2 + E_{cr} E_{rc}) + 2C_4 (E_{fc} E_{cf} + E_{fr} E_{rf}) \end{aligned} \quad . \tag{1}$$

where W is the hyperelastic strain energy function expressed in terms of the components of the Green-Lagrange strain tensor E_{MN}, and $C_1 - C_4$ are the passive material constants estimated in [12].

To drive the muscle contraction through ventricular systole, myofibre shortening was modulated by a time-dependent description of the active contractile stress (T_{Ca}) to represent the isometric tension at resting sarcomere length. The contractile stress T_a generated by the muscle fibres was described using a quasi-static function of the sarcomere extension ratio (λ) and the time-varying T_{Ca} using:

$$T_a(T_{Ca}, \lambda) = T_{Ca} \times \left[1 + \beta(\lambda - 1)\right] \ . \tag{2}$$

with β = 1.45 [13]. This contractile stress component was incorporated into the stress-strain relationship (Eq. 3) that appears in the stress equilibrium equations, which are derived from the equations of continuum mechanics, and were solved using a nonlinear finite element method [11].

$$T^{MN} = \frac{1}{2}\left(\frac{\partial W}{\partial E_{MN}} + \frac{\partial W}{\partial E_{NM}}\right) - p\frac{\partial X_M}{\partial x_k}\frac{\partial X_N}{\partial x_k} + T_a \delta_1^M \delta_1^N \quad . \tag{3}$$

where p is the hydrostatic pressure field arising from the incompressible nature of the myocardial tissue, and $\delta_1^M = 1$ when $M = 1$ is the Kronecker delta.

The tension transient, T_{Ca}, was prescribed based on reported measurements in canine [14]. During isovolumic contraction, T_{Ca} was gradually increased to initiate fibre shortening whilst the cavity volume was kept constant by altering the pressure applied to the LV endocardial surface. Once the LV cavity pressure reached the given afterload (12 kPa, observed from the recorded pressure trace), the LV was allowed to contract indicating the start of ventricular ejection. The end of the ejection phase was determined by the peak contractile stress, which was set at 65 kPa to provide a typical ejection fraction for the normal case. During isovolumic relaxation, the cavity volume was again maintained constant while the pressure was decremented to zero. The elastic energy was released allowing the LV wall to return to its stress-free state before the onset of the next cardiac cycle. Throughout the whole cycle, the basal position of the LV was fixed, whereas the apex was not constrained.

2.3 Mechanical Modelling of Heart Failure

Among the factors that may contribute to the development of HF, we have chosen to investigate the variations in LV geometry and myocardial mechanical properties. The detailed pathological scenarios are summarised as follows:

1) **ventricular dilation**, simulated by increasing the size of the LV cavity by 25%, 50%, 75% and 100% (Fig. 1). The enlarged LV cavity mimicked the wall thinning and the more spherical shape of the LV observed in HF patients. Note that the resting sarcomere length and reference fibre orientation among these enlarged models was held constant.
2) **isotropic passive material properties** by modifying the passive parameters of the control transversely-isotropic material relation. This variation increased the cross-fibre stiffness to reproduce the effect of growth of endomysial collagen, hence tighter coupling between fibres. The overall stiffness of the LV was held constant by reducing the constitutive parameter C_1 to match the diastolic pressure-volume curve of the control case.
3) **reduced contractility** where the maximum isometric tension at resting sarcomere length was decreased by 20% from 65 kPa to 52 kPa, while the rate of change in active tension was similar to the control case.

The combined effect of dilation, material isotropy and reduced contractility were explored in the following case studies:

a) Case 1 : Transversely-isotropic stiffness with normal contractility;
b) Case 2 : Isotropic stiffness with normal contractility;
c) Case 3: Transversely-isotropic stiffness with reduced contractility;
d) Case 4: Isotropic stiffness with reduced contractility.

To assess LV mechanical functions, a series of global cardiac indices (see Table 1) and regional mechanical index were analysed. While the global indices can be readily

compared with studies undertaken using other technologies such as echocardiography and MRI, measurement of regional stress can provide more detailed insight into the underlying mechanisms of this dysfunction at the localised scale.

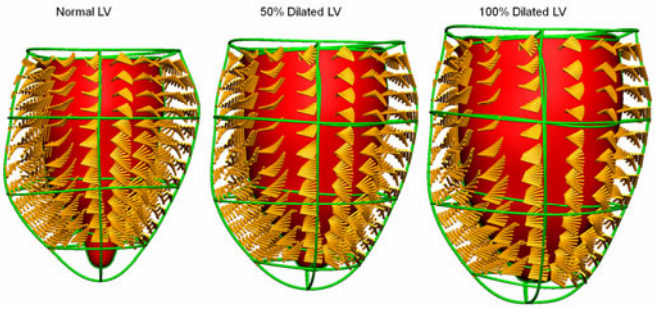

Fig. 1. Anterior view of FE representation of the normal LV (left), the 50% dilated LV (middle) and 100% dilated LV (right). Endocardial surfaces are shaded with the epicardial surfaces delineated with lines. Rotating rods illustrate the transmural rotation of the fibre orientations across the LV wall.

Table 1. Summary of global indices used to compare ventricular mechanics across the case studies

Cardiac Index	Description	Equation
Ejection Fraction (**EF**, [%])	Measures fraction of blood pumped out of the LV ventricle with each heart beat	$EF = \frac{(EDV - ESV)}{EDV}$
Stroke Volume (**SV**, [ml])	Measures amount of blood ejected by the LV with each heart beat	$SV = EDV - ESV$
Average Fractional Shortening in the short-axis plane (**AFSS**, [%])	Measures changes in LV dimension in the short-axis plane at the equator between end-diastolic (ED) and end-systolic (ES) states	$FS = \frac{(LVEDD - LVESD)}{LVEDD}$
Average Wall Thickening (**AWT**, [%])	Measures the changes in wall thickness between the (ED) and (ES) states	$WT = \frac{(ESWT - EDWT)}{EDWT}$

For the calculation of AFSS, the fractional shortening (FS) for each of the short-axes (FSY & FSZ) was calculated (using the equation shown in Table.1 where LVEDD and LVESD are the LV dimensions at ED and ES states respectively), then the average of FSY and FSZ were taken to represent the AFSS. For the calculation of AWT, the Euclidean distances between adjacent endocardial and epicardial nodes at four locations around the LV (anterior, free-wall, posterior and septum) were calculated at ED and ES, then used to calculate the wall thickening (WT) at each region using the equation provided in the table above. The average of the four wall thickening values represented the average wall thickening (AWT). To investigate regional

mechanical behaviours, we examined the total fibre stress developed at the ED and ES states between the normal and 100% dilated LVs.

3 Results

Effect of dilation

The effect of LV dilation at different levels on the global cardiac performances is illustrated in Fig. 2. The influence on each of the global cardiac indices was not uniform. For example, dilating the control LV model resulted in reduction of the ejection fraction (EF) by 25%, 11%, 46% and 34% for Cases 1, 2, 3 and 4 respectively. Moreover, the stroke volume (SV) increased for all Cases with 25% and 50% LV dilation, but decreased as the LV was dilated further for Cases 1, 3 and 4. Trends in AFSS and AWT were similar to that of EF with a steady reduction with LV dilation for Case 1, 3 and 4, whilst the trend was more gradual for Case 2.

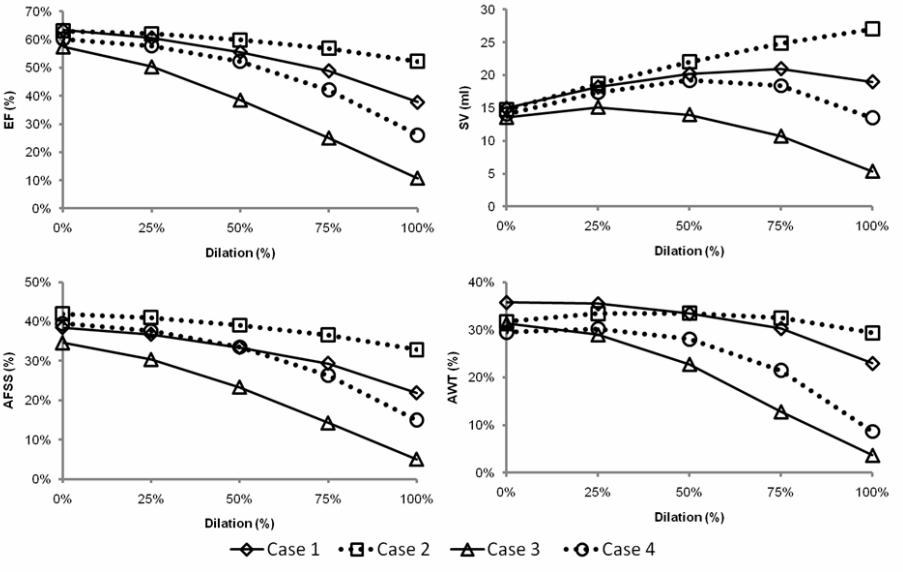

Fig. 2. Changes in cardiac indices: ejection fraction (EF); stroke volume (SV); average fractional shortening in the short-axis plane (AFSS); and average wall thickening (AWT) with changes in LV dilation. Dashed lines correspond to transversely-isotropy cases with 100% contractility (case 1: diamonds) and 80% contractility (case 3: triangles) whereas solid lines represent the isotropic cases with 100% contractility (case 2: squares) and 80% contractility (case 4: circles).

Effect of tissue remodelling (loss of anisotropy)

The effect of loss of tissue anisotropy due to remodelling is demonstrated by Cases 2 and 4 (dashed lines in Fig. 2). For EF and SV, the remodelling in fibre structure had little impact for the control LV. This was primarily due to the fact that the overall stiffness of the LV was similar despite the changes in the relative stiffness between

the fibre and cross-fibre directions. On the other hand, the AFSS and AWT were all altered by +4% and -4% respectively in response to tissue remodelling. At all dilation levels, isotropy resulted in better mechanical behaviour (larger EF, SV and AFSS) compared to the transversely-isotropic models (Case 1 and 3, solid lines in Fig. 2) regardless of muscle contractility. The implication of this observation may be coinciding with the compensated work LV was striving to carry out during the early stage of HF, but eventually leading to more severe microstructural remodelling that occurs during decompensated HF.

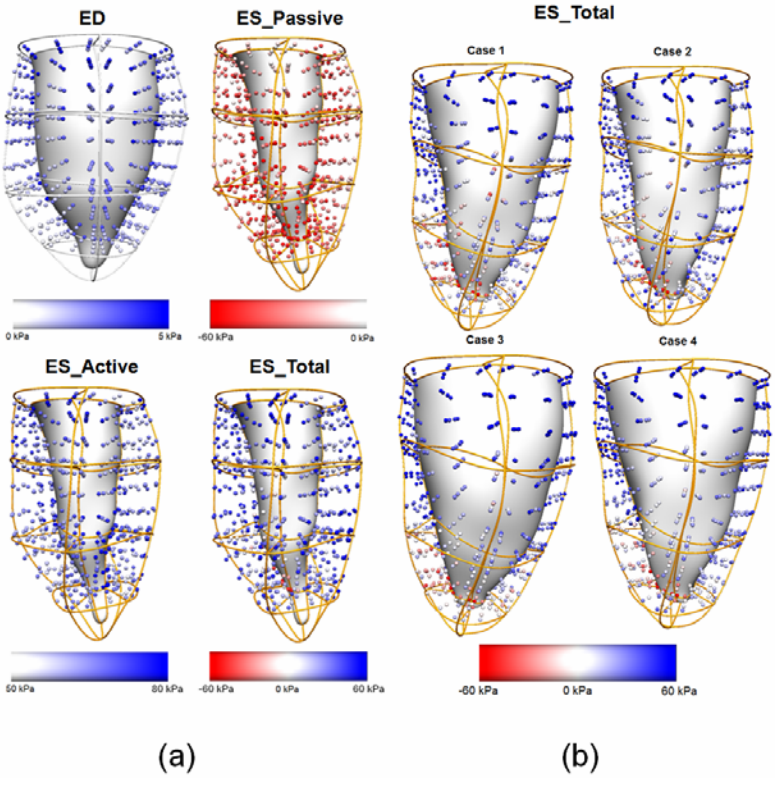

Fig. 3. (a) Anterior views of the spatial distributions of the Cauchy stresses evaluated at each Gauss point of the Control LV. (Top-left) Passive fibre stress at end-diastole. (Top-right) Passive component of fibre stress at end-systole. (Bottom-left) Active component of fibre stress at end-systole. (Bottom-right) Total fibre stress at end-systole. (b) Anterior views of total fibre stress at end-systole evaluated at each Gauss point of the dilated LV for the transversely-isotropic myocardium (top-left), isotropic myocardium (top–right), transversely-isotropic and reduced contractility (bottom-left) and isotropic and reduced contractility (bottom-right).

Effect of reduced contractility

Compromised contractility had significantly reduced the global LV performance for both transversely-isotropic elasticity and isotropic elasticity cases. The decrease in EF, AFSS and AWT for case 3 had the largest gradient with respect to LV dilation.

Therefore, the combined effect of dilation and reduced contractility (case 3) severely affected the mechanical behaviour of the LV with transversely-isotropic elasticity and slight improvements were found for the isotropic elasticity case (case 4) for the same reason described above.

Analysis of myocardial fibre stress

We also evaluated the fibre component of the Cauchy stress tensor at each Gauss point at end-diastole and end-systole for both the control and dilated (100%) LV models. Fig. 3(a) illustrates spatial variations of the fibre stress for a homogeneous activation of T_{Ca}. At end-diastole, there was significant variation with highest fibre stress near the endocardial surface (due to pressure loading), and lowest near the epicardial surface. The stress distribution also varied longitudinally, which is consistent with the heterogeneous fibre orientations within the LV. The total fibre stress at end-systole for the dilated LV under different pathological conditions is illustrated in Fig. 3(b) for comparison. With diminished contractility (case 3 and 4), the end-systolic volume appeared to be larger than that with normal contractility (case 1 and 2).

4 Discussion

A FE model of the LV, combining geometric information from *in vivo* tagged MRI and fibre orientations from *ex vivo* diffusion tensor MRI, was used to investigate LV mechanical behaviour subject to alternations of cardiac structure, such as changes in geometry and material properties initiated by tissue remodelling, ultimately giving rise to decompensated heart failure. This non-invasive approach to study whole ventricular mechanics with accurate geometry and tissue architecture information is essential to address some of the problems we face nowadays regarding the roots of this disease. Whilst we are able to mimick the pathological scenarios suggested by experimental studies and successfully simulate the heart beat, the current model suffers a few limitations summarised as follows:

1. Current analyses focus on the LV only. Lack of right ventricle (RV) means that some of the key boundary conditions exerted by the RV are missing in the current mechanics analysis. And inclusion of the RV is a necessity when we are moving toward to bi-ventricular modelling. RV is not the only anatomical structure that poses substantial boundary conditions for reproducing physiologically realistic mechanical motion. Absence of papillary muscles, pericardium and the ventricular valves explains the longitudinal stretch see in the current simulations which is contrary to clinical observation. To circumvent this, these key structures should be incorporated into this FE model for future study.
2. The fibre structures used for both normal and pathological cases are constant due to lack of data on failed heart. However, with more and more experimental data become available, patient-specific geometry and myofibre structures will definitely be attainable and ideal for this kind of analysis.
3. Characterising subject-specific material properties is also critical to determine the global and regional cardiac functions. The use of appropriate material laws to describe the material responses are of equal importance. In this time-course study, transversely-isotropic constitutive relation was chosen to represent the

material behaviour while it is obvious, based on extensive tissue structure studies, that the myocardium deformed orthotropically. To introduce orthotropy, more material parameters will need to be customised and information on the sheet and sheet-normal orientations are also required. However, given the advances in DTMRI technology and the validation of the correlation between the third eigenvector with sheet-normal direction is already underway, incorporating these orientations to this biophysical model will definitely be feasible.

4. These analyses were carried out assuming there was no change in the active tension that drives contraction and its timing between the healthy and diseased conditions. The rationale behind this assumption is mainly due to insufficient information on *in vivo* measurement of the activation levels for HF case. The next stage of this study will closely look into these assumptions and gradually address them.

5 Conclusions and Future Work

In this paper, we used a FE modelling framework to investigate the contributions of some factors, identified via several imaging studies (i.e. cardiac MRI and confocal microscope), towards causing LV mechanical dysfunction and eventual HF. This model allowed us to simulate three common pathological cases found in patients suffering from HF: 1) LV dilation; 2) loss of anisotropy due to tissue remodelling and 3) reduced contractility. By simulating the cardiac motion over a complete cardiac cycle, the individual effects of the pathologies and their combined influences on LV mechanical performance were explored by comparing the global performance as well as regional fibre stress distributions between the normal and diseased cases. Better customisation of material properties and activation sequence can lead to more accurate 3D motion recovery with this kind of biophysical model. This framework can also be extended to include more factors such as alternations of calcium levels at cellular levels. Further extension of this model to incorporate electrical activation with mechanics will enable us to systematically characterise the other major mechanisms (i.e. electrical dis-synchrony) responsible for this dysfunction.

Acknowledgments. Vicky Y.Wang received funding from the New Zealand Institute of Mathematics & Its Applications (NZIMA) and The University of Auckland. Alistair A. Young is supported by Award Number R01HL087773 from the National Heart, Lung, And Blood Institute, USA. Martyn P. Nash is supported by a James Cook Fellowship administrated by the Royal Society of New Zealand on behalf of the New Zealand Government. We gratefully acknowledge Professor McVeigh, Dr Helm and Assistant Professor Daniel Ennis from National Institutes of Health and Johns Hopkins University for providing the experimental data.

References

1. Wang, J., Nagueh, S.F.: Current perspectives on cardiac function in patients with diastolic heart failure. Circ. 119, 1146–1157 (2009)
2. Pope, A., Sands, G.B., Smaill, B.H., LeGrice, I.J.: Three dimensional transmural organization of perimysial collagen in the rat heart. Am. J. Physiol. Heart Circ. Physiol. 295, H1243–H1252 (2008)

3. Gilbert, S.H., Benson, A.P., Li, P., Holden, A.V.: Regional loacalisation of left ventricular sheet structure: integration with current models of cardiac fibre, sheet and band structure. Eur. J. Cardiothorac. Surg. 32, 231–249 (2007)
4. LeGrice, I.J., Smaill, B.H., Chai, L., Edgar, S., Gavin, J., Hunter, P.J.: Laminar structure of the heart: ventricular myocyte arrangment and connective tissue architecture in the dog. Am. J. Physiol. Heart. Circ. Physiol. 269, H571–H582 (1995)
5. Costa, K., Takayama, Y., McCulloch, A.D., Covell, J.W.: Laminar fiber architecture and three-dimensional systolic mechanics in canine ventricular myocardium. Am. J. Physiol. Heart Circ. Physiol. 283, H2650–H2659 (1999)
6. Nash, M.P., Hunter, P.J.: Computational mechanics of the heart: From tissue structure to ventricular function. J. Elasticity 61, 113–141 (2000)
7. LeGrice, I.J., Pope, A.M., Sands, G.B., Smaill, B.H.: Perimysial collagen remodelling and mechanical dysfunction in hypertensive cardiomyopathy (2010) (under review)
8. Wang, V.Y., Lam, H.I., Ennis, D.B., Young, A.A., Nash, M.P.: Passive ventricular mechanics modelling using MRI of structure and function. In: Metaxas, D., Axel, L., Fichtinger, G., Székely, G. (eds.) MICCAI 2008, Part II. LNCS, vol. 5242, pp. 814–821. Springer, Heidelberg (2008)
9. Ennis, D.B.: Assessment of myocardial structure and function using magnetic resonance imaging. PhD Thesis. John Hopkins University (2004)
10. Le Bihan, D., Mangin, J.F., Poupon, C., Clark, C.A., Pappata, S., Molko, N., Chabriat, H.: Diffusion tensor imaging: concepts and applications. J. Magn. Reson. Imaging 13, 534–546 (2001)
11. Nielsen, P., LeGrice, I.J., Smaill, B.H., Hunter, P.J.: Mathematical model of geometry and fibrous structure of the heart. Am. J. Physiol. Heart Circ. Physiol. 260, H1365–H1378 (1991)
12. Wang, V.Y., Lam, H.I., Ennis, D.B., Young, A.A., Nash, M.P.: Modelling passive diastolic mechanics with quantative MRI of cardiac structure and function. Med. Image Anal. 13, 773–784 (2009)
13. Hunter, P.J., McCulloch, A.D., ter Keurs, H.E.D.J.: Modelling the mechanical properties of cardiac muscle. Prog. Biophys. Mol. Biol. 69, 289–331 (1998)
14. Sipido, K.R., Volders, P.G.A., Marieke de Groot, S.H., Verdonck, F., Van de Werf, F., Wellens, H.J.J., Vos, M.A.: Enhanced Ca2+ Release and Na/CA Exchange Activity in Hypertrophied Canine Ventricular Myocytes: Potential Link between Contractile Adaptation and Arrhythmogenesis. Circ. 102, 2137–2144 (2000)

Incorporating Low-Level Constraints for the Retrieval of Personalised Heart Models from Dynamic MRI

Christopher Casta[1], Patrick Clarysse[1], Jérôme Pousin[2], Joël Schaerer[1], Pierre Croisille[1], and Yue-Min Zhu[1]

[1] Université de Lyon, CREATIS, CNRS UMR5220, INSERM U630, INSA-Lyon
[2] Université de Lyon, ICJ, CNRS UMR5208, INSA-Lyon
Université Lyon 1, 69621 Villeurbanne, France

Abstract. We have recently presented the dynamic deformable elastic template (DET) model for the retrieval of personalised anatomical and functional models of the heart from dynamic cardiac image sequences. The dynamic DET model is a finite element deformable model, for which the minimum of the energy must satisfy a simplified equation of Dynamics. It yielded fairly accurate results during our valuation process on a 45 patients cine MRI database. However, it experienced difficulties when dealing with very large thickening throughout the cardiac cycle, or on highly pathological cases. In this paper, we introduce prescribed displacements as low level constraints to locally drive the model. Non prescribed contour nodes are displaced according to a combination of forces extracted from prescribed points and image gradient. Prescribing a few points in a whole sequence allows us to retrieve much better segmentations on rather difficult cases.

1 Introduction

Retrieving personalized anatomical and functional models from clinical cardiac images remains a challenge. Magnetic resonance imaging (MRI) is a versatile imaging modality, able to provide the required data to reconstruct patient specific models. A few papers have targeted the spatio-temporal analysis of the heart function from dynamic image sequences. Montagnat proposed a dynamic framework based on simplex meshes to analyze 4D SPECT data [1], treating the temporal dimension geometrically. Sermesant proposed a bio-inspired electromechanical model of the heart designed both for the simulation of its electrical and mechanical activity, as well as for the segmentation of time series of medical images [2]. Billet extended this approach to cardiac motion recovery using the adjustment of the previous electromechanical model of the heart to cine MR images [3]. Recently, Lynch proposed a parametric motion model, using a priori knowledge about the temporal deformation of the myocardium that is embedded

O. Camara et al. (Eds.): STACOM-CESC 2010, LNCS 6364, pp. 174–183, 2010.

in a level-set scheme [4]. In a previous paper [5], we introduced the dynamic deformable elastic template model (Dynamic DET) for the automatic segmentation and tracking of the heart in dynamic cine MRI sequences. This spatio-temporal approach imposes temporal smoothness and periodicity constraints to improve the regularity and continuity of the extracted contours throughout the cardiac cycle.

The performance of the Dynamic DET was assessed in the context of the MICCAI 2009 LV Segmentation Challenge (`http://smial.sri.utoronto.ca/LV_Challenge/Home.html`). In the present study, we propose to improve the robustness and accuracy of the obtained models by introducing prescribed displacements to some contour nodes. Attraction of the model by wrong borders can be avoided by introducing a limited number of imposed "passage" points (which are manually designated by the user). Moreover, such point prescription could be provided by a pre-processing step, e.g. extraction of a displacement field from tagged MRI.

First, the principle of the Dynamic DET model is recalled. Then, the proposed methodologies to impose prescribed displacements into Dynamic DET are introduced. In the last section, preliminary results on real pathological human MRI sequences are presented.

2 Dynamic DET Model

In this section, we briefly expose the dynamic DET model which is fully detailed in [5].

2.1 Model Main Equations

We assume the data is available as sequences of N-2D or -3D images, sampling the cardiac cycle. To simplify the mathematical treatment of the problem, we assume that the cardiac cycle is parameterized by $t \in [0, 1[$.

The DET model is a deformable volumetric model submitted to external constraints imposed by the image. The equilibrium of the model is obtained through the minimization of an energy E which is the sum of an elastic deformation energy $E_{Elastic}$ and energy E_{data} due to the action of external image forces f:

$$E_{elastic} = \frac{1}{2} \int_{\Omega} \mathrm{tr}(\sigma \epsilon^T)\, d\Omega, E_{data}(u) = - \int_{\partial\Omega} f(u)\, d\gamma$$

where σ and ϵ are the 3D strain and deformation tensors and Ω is the a priori model domain at rest. The a priori left ventricular (LV) model is an annulus in 2D (a half-ellipsoid in 3D)(Figure 1). The material is considered to be isotropic, homogenous and completely defined by its Young modulus and its Poisson coefficient. $\partial\Omega$ is the border of the object domain Ω.

These energy terms can be approximated by discretizing the displacement u and the force f, using the finite element method (FEM). The displacement is approximated by linear functions on these elements, while the forces are sampled

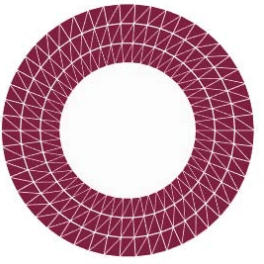

Fig. 1. Sample ring mesh used as initial template for 2D short-axis cardiac MR segmentation tracking

at nodal points. Under this approximation, the minimum of the energy must satisfy the following equation:

$$\mathbf{KU} = \mathbf{F}(\mathbf{U}) \tag{1}$$

where $\mathbf{K}$ is the stiffness matrix corresponding to the response of the elastic material, and $\mathbf{U}$ and $\mathbf{F}$ are respectively the displacement and force vectors on mesh nodes.

The model resulting from equation 1 is purely static. Extending this method to Dynamics [5], the heart dynamics is controlled by the simplified Dynamics equation (where acceleration is neglected):

$$\mathbf{D}\dot{\mathbf{U}} + \mathbf{KU} = \mathbf{F}(\mathbf{U}, t) \tag{2}$$

We consider the matrix $\mathbf{D}$ to be a multiple of identity. It can thus be replaced by a single scalar α.

2.2 Function Basis

Solutions to equation (2) do not neceassarily satisfy the periodicity and smoothness constraints. Hence, we look for solutions in a finite-dimensional subspace $\mathcal{F}$ generated by a set of Fourier harmonics.

The frames represent a collection of uniformly-spaced noisy samples of a smooth and periodic phenomenon. Thus, we can assume the force fields $\mathbf{F}^n$ derived from the images to be samples of an element of $\mathcal{F}$. One and only one element of $\mathcal{F}$ satisfies $\mathbf{F}(\frac{n}{N}) = \mathbf{F}^n$, $\forall n, 0 \leq n < N$. The discrete Fourier Transform of the $\mathbf{F}^n$ samples is defined as [6] (with N even):

$$\mathbf{F}(t) = \sum_{l=-N/2}^{N/2} \mathbf{f}^l e^{2\pi i l t}$$

$$\text{with } \mathbf{f}^l = \begin{cases} \mathbf{dft}[l], & \forall l, 0 \leq l < \frac{N}{2} \\ \mathbf{dft}[l+N], & \forall l, -\frac{N}{2} < l < 0 \\ \frac{1}{2}\mathbf{dft}[\frac{N}{2}], & \forall l, l = \pm\frac{N}{2} \end{cases} \text{ and } \mathbf{dft}[l] = \frac{1}{N}\sum_{n=0}^{N-1} \mathbf{F}^n e^{\frac{-2\pi i l n}{N}}$$

In order to reduce the noise impact and to enforce smoothness of the motion, either data or the computed solution are filtered. In the Fourier basis, filtering

the high frequencies can be achieved by setting $\mathbf{f}^l = \mathbf{f}^{-l} = 0$ for $l > a$, where a is the highest admissible frequency.

2.3 Algorithm Implementation

Solution to equation (2) is achieved through a pseudo-instationary process [7]. Roughly speaking, it consists in introducing a parameter τ, and considering a pseudo-instationary problem with respect to τ derived from the original problem. Let's define the operator $\mathbf{A} = \alpha\frac{d}{d\tau} + \mathbf{K}$ and consider,

$$\begin{cases} \frac{d\mathbf{U}}{d\tau} & = \mathbf{F}(\mathbf{U}) - \mathbf{A}\mathbf{U} \\ \mathbf{U}(0) & = 0. \end{cases} \tag{3}$$

If $\mathbf{U}$ converges when $\tau \to +\infty$, then it tends towards a limit which is a solution of the nonlinear time dependent problem. Discretizing the previous equation with finite differences to solve the temporal equation leads to (see [5] for details):

$$(\frac{1}{\Delta\tau} + \frac{\alpha}{\Delta n} + \mathbf{K})\mathbf{U}_n^\tau = \mathbf{F}(\mathbf{U}_n^{\tau-1}) + \frac{1}{\Delta\tau}\mathbf{U}_n^{\tau-1} + \frac{\alpha}{\Delta n}\mathbf{U}_{n-1}^\tau \tag{4}$$

which is a linear system and thus straightforward to solve.

3 Displacement Constraints Applied to the Model

In the previous section, the model was driven only by image based forces, which are generated with the following sequence of operations:

- Preprocess image with a median filter (5x5 kernel).
- Extract the contours with a Sobel edge detector.
- Compute a Gaussian smoothed gradient of the contours ($\sigma = 0.5$) to obtain a vector field.
- Ensure that forces are null on the contours by applying a Geman-McClure function to the vector norms.

While this approach allows to obtain fairly accurate results in most cases, the method experiences difficulties when dealing with very large thickening throughout the cardiac cycle, or highly pathological cases (ellipsoidal shape on short axis images). Therefore, to obtain better segmentations, we introduce prescribed displacements to locally drive the model with several methods. Prescribed displacements have been used notably in parameter-free elastic deformation for 2D and 3D registrations [8]. With such a method, non prescribed contour nodes are displaced according to a combination of forces extracted from prescribed points and image gradient. In the next subsections, two methods to integrate prescribed displacements as low level constraints to the DET model are described and discussed.

3.1 Peckar's Method

We consider the static case, for which the theory is simpler to apprehend. Let's consider equation 1. The incorporation of prescribed displacements requires a modification of the previous system of equations. Let's suppose that a known subset $\tilde{\mathbf{U}}$ of the solution is prescribed on a fixed number of domain points (the contours of the heart in our case). In the abscence of external image-based forces, the vector $\mathbf{F}$ in the original system is set to zero. We will obtain our solution from the modified system:

$$\tilde{\mathbf{K}}\mathbf{U} = \tilde{\mathbf{F}} \tag{5}$$

where $\tilde{\mathbf{K}}$ is a modified stiffness matrix, and $\tilde{\mathbf{F}}$ contains contributions from the known subset $\tilde{\mathbf{U}}$ of the solution.

For example, to incorporate the prescribed displacement value $\tilde{u}_i$ to the system, we would put $\tilde{u}_i$ to the ith position in $\mathbf{F}$, and leave the other elements of $\mathbf{F}$ to zero. Then, we transform the matrix $\mathbf{K}$ by filling its ith row with 0 and setting the element K_{ii} to 1. Note that if all values of the solution are prescribed, we obtain $\tilde{\mathbf{K}} = \mathbf{I}$ and $\tilde{\mathbf{F}} = \tilde{\mathbf{U}}$, as we would expect.

This process is adapted to the dynamic case, and we can prescribe the value of any subset of the solution, at any given time point. Mainly, it consists in prescribing displacement of some points during initialization. These points are then considered as static points, for which the speed $\dot{u}_i$ is equal to zero.

3.2 Payne's Method

Here again, we consider only the static case for the theoretical explanation. The complete system of equations for equation 1 can be written:

$$\begin{cases} K_{11}u_1 + K_{12}u_2 + ... + K_{1n}u_n = F_n \\ K_{21}u_1 + K_{22}u_2 + ... + K_{2n}u_n = F_n \\ \qquad\qquad etc. \end{cases}$$

If we want to fix the displacement of a node, for example $u_i = \tilde{u}_i$, we can add a large value $\beta\mathbf{I}$ to the coefficient K_{ii} and replace the second member of the equation by $\beta\tilde{u}_i$. If β is much larger than the other coefficients of the stiffness matrix, this modification is equivalent to replacing the initial equation by:

$$\beta u_i = \beta\tilde{u}_i$$

Thus, we have correctly fixed the displacement of the node with the required value. Moreover, the global system is still symmetric, and very few modifications to the program are necessary (see [9] for more details). This process can be extended to the dynamical scheme, and we can fix the displacement of any node at any given time point of the sequence. Mainly, the stiffness matrix $\mathbf{K}$ being a constant and identical at each time of the sequence, adding a large value $\beta\mathbf{I}$ to

the coefficient K_{ii} and replacing the second member of the equation (in equation 2) by our prescribed value at the given time will ensure a correct displacement of the considered node.

3.3 Hybrid Methods

In the above subsection, we presented two methods to prescribe the displacement of points at selected locations. As can be seen, both methods don't take into account external image-based forces. Therefore, the model evolution is only driven by the prescribed point displacements. This is not what we want, since the non prescribed nodes of the model must follow the contours of the myocardium. To this aim, non prescribed nodes are displaced using a combination of forces extracted from both prescribed points and image based forces.

With both methods, we operate as follow:

- Compute prescribed displacements, for end-diastolic (ED) and end-systolic (ES) phases, by selecting a few points.
- Modify the stiffness matrix.
- Interpolate the displacement of the nodes which were prescribed at ED or ES phases to the other phases, by averaging.
- Compute image-based forces.

With Peckar's method, we then substitute image-based force by prescribed-based force for points which were prescribed.

With Payne's method, for points which were prescribed, we then substitute image-based force by a linear combination of image-based force and prescribed-based force.

The way both methods act for dynamic segmentation of the heart will be discussed in Section 6.

4 Method Parameters and User Interaction

The parameters of the algorithms can be divided into the following categories:

- **Initial Template:** In 2D spatial dimension, the initial template is an annulus representing both endocardium and epicardium. It is defined with three geometrical parameters: the center of the annulus, the radius and the thickness. These parameters are manually defined by the user on the ED frame. The template is meshed by dividing the ring into triangles from a regular partition of the LV into sectors and concentric rings (see Figure 1).
- **Mechanical parameters:** The Young modulus represents the rigidity of the model, while the Poisson coefficient characterizes the ability of the material to be compressed.
- **Algorithm parameters:** The stopping criterion defines when the algorithm has converged. We can also choose the number of resolution levels with which the sequence images are processed. The number of harmonics used in Fourier filtering is usually fixed to 5.

A contraction parameter (CP) has also been introduced, to initialize the template correctly at the end-systolic (ES) phase, by making the ring thicker. CP is set automatically during the initialization, based on *a priori* learning to automatically identify endocardial points and fit a circle at ED as well as ES phase.

Finally, at the launching of the algorithm, an interactive window allows the selection of points in the images which will be prescribed using either Peckar's or Payne's method. It consists in choosing some outter and inner contour points of the myocardium, at ED and ES phases, in order to drive the model closer to the solution. When using Payne's method, an additional parameter β allows to balance image-based and prescribed-based forces (see section 6).

5 Results

The experiments were conducted on 17 2D Cine MRI sequences of MICCAI'09 Segmentation Challenge [10] to study the impact on the segmentation results of prescribed displacements with both methods. The Young modulus was set to 0.15 and the Poisson coefficient to 0.2 (this is to cope with the adaptation of the initial template to the data and the myocardial area variation during the cardiac cycle, in 2D). The center of the annulus and its radius were found using a semi-automatic initialization, and CP was automatically set depending on the initialization on both ED and ES phases. The thickness was set to 8 pixels. The annulus was generated with 3 rings and divided into 20 sectors. The number of resolution levels was set to 3, and the stopping criterion to 10^{-5}.

Table 1. Mean Average perpendicular distance for the inner (Avg Dist I) and outer (Avg Dist O) contours. Mean Dice metric for the inner (Avg DM I) and outer (Avg DM O) contours, for HF-NI-15, HF-I-06, HYP-37 and N-05 datasets.

Method	Avg Dist I (mm)	Avg Dist O (mm)	Avg DM I	Avg DM O
No prescription	3.51	3.11	0.84	0.92
Peckar	3.41	2.67	0.84	0.93
Payne	3.10	2.07	0.86	0.95

Figure 2 shows the results of a LV segmentation on a patient affected by heart failure with no ischemia (4th slice level of the HF-NI-15 dataset), at ED, ES and mid-diastolic phases, for segmentation with no prescription, and with prescribed displacements with Peckar's and Payne's methods. Prescription was done using 2 to 5 points for inner and outter contours, at ES and ED phases. Table 1 references Dice metric and average perpendicular distance between estimated and reference contours, for each method, averaged over 4 complicated cases belonging to different classes (heart failure with or without ischemia, hypertrophy, normal). Note that these quantitative results have been evaluated based on ED and ES phases only.

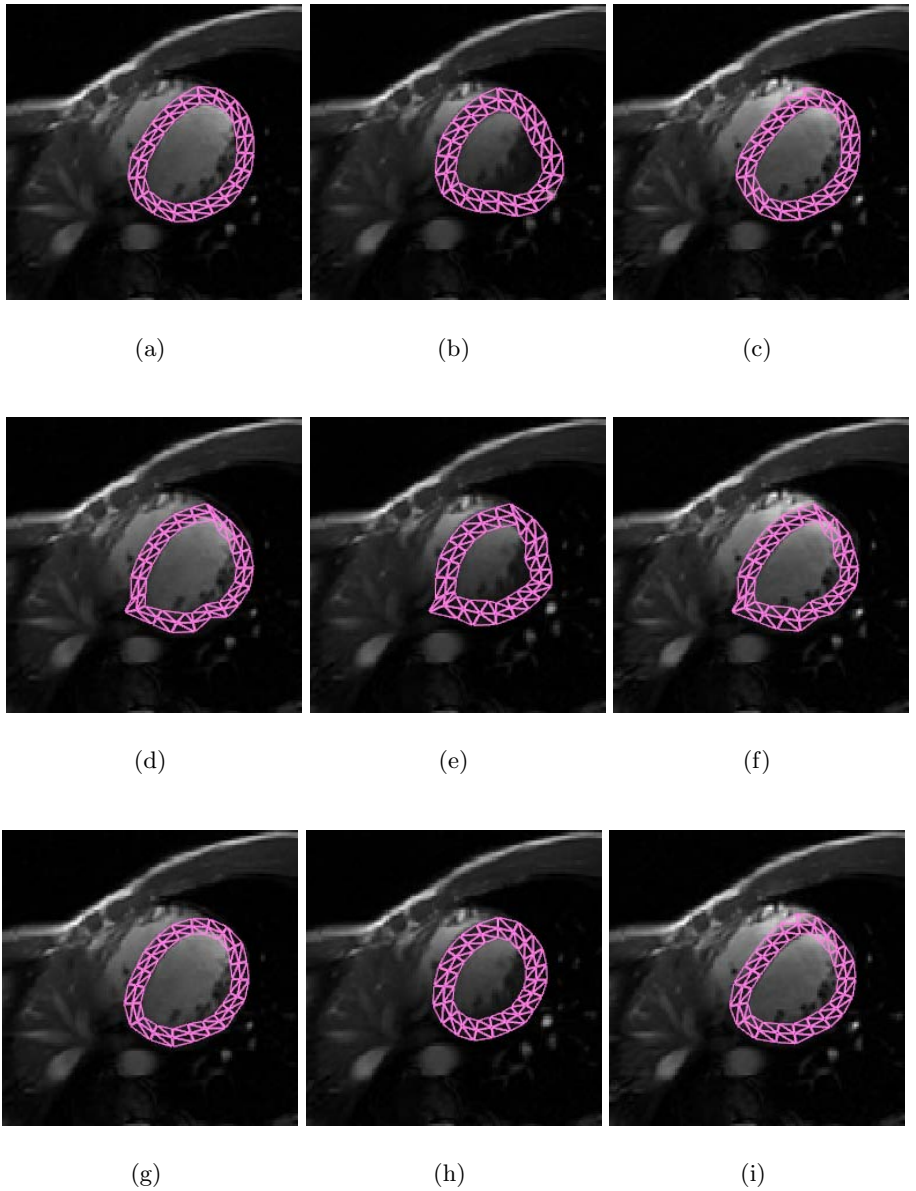

Fig. 2. DET model superimposed onto the images of HF-NI-15 sequence at a median slice of the heart, at ED (left), ES (middle) and mid-diastolic (right) phase. The pink mesh is the model. It is translucent so that correspondance between model and image contours can be appreciated. Figures (a), (b) and (c) correspond to a segmentation with no prescription. Figures (d), (e) and (f) correspond to a segmentation with Peckar's method. Figures (g), (h) and (i) correspond to a segmentation with Payne's method ($\beta = 50$).

6 Discussion

The main advantage of our method is that it allows for the simultaneous segmentation of both endocardium and epicardium over a whole dynamic sequence of images, after the initialization of the templace at the ED phase, and optionally, the prescription of a few points. The results shown in figure 2 demonstrate the advantages of using prescribed displacements. The method experiences difficulties on highly pathological cases, as seen on subfigures (a), (b) and (c). While the segmentation is good at the ED phase, the model cannot correctly follow the epicardium at ES phase, yielding inaccurate results.

Subfigures (d), (e) and (f) show the results obtained using Peckar's method. This method ensures perfect placement of the prescribed points, but at the detriment of regularity (see the lower left part of each images).

Subfigures (g), (h) and (i) give the results obtained using Payne's method. This method leads to the best results among the three. It generates accurate results without sacrificing contour regularity. The value β presented in section 3.2 represents the balance between image-based and prescribed-based forces. If set too low, only the image-based forces will be taken into account. If set too high, prescribed-based forces will be too strong compared to image-based ones, and we will lose regularity. Using an intermediate value allows the model to be attracted correctly towards the prescribed points, while still allowing some slight displacements of prescribed nodes due to image-based forces, which results in better regularity and overall better segmentation. With values of β ranging from 0 to 500, an intermediate value of 50 appeared as a good compromise between image-based and prescribed-based forces. Using an interactive prescription method, we are not sure that the selected points are perfectly placed onto the contours of the myocardium, hence it is necessary to allow prescribed nodes to be slightly displaced. For this reason, Payne's method appears to be the most suited in the case of segmentation of Cine MRI image sequences.

7 Conclusion

We have presented an improved dynamic DET, for the segmentation and tracking of the heart from MRI sequences, and more generally, for the analysis of soft deformable structures in periodic motion. Experiments on rather difficult cases show a very good overall ability of the model to track the heart borders using a few prescribed points to improve accuracy and robustness. Payne's method is the best one to extract accurate contours.

Based on these results, one could use motion information from MRI tagging to drive the deformation.

Finally, extending DET model to track heart borders and motion in 3D, from both Cine and tagged MR image sequences, is very appealing. It should be noted that such extension does not require any further theoretical developments, since the equations remain valid for the 3D case. However, 3D MR image processing poses a number of purely technical problems, such as inter-slice alignement, 3D interpolation and data visualization. This is the purpose of our future work.

Acknowledgements

This work has been supported by the Région Rhônes Alpes through the Simed project of cluster ISLE, as well as the CNRS-GDR STIC-Santé through the support of the MedIEval action (Medical Image Evaluation). It is also part of the French ANR (http://www.agence-nationale-recherche.fr/) projects GWENDIA and VIP.

References

1. Montagnat, J., Delingette, H.: 4D deformable models with temporal constraints: application to 4D cardiac image segmentation. Medical Image Analysis 9(1), 87–100 (2005)
2. Sermesant, M., Delingette, H., Ayache, N.: An Electromechanical Model of the Heart for Image Analysis and Simulation. IEEE Transactions in Medical Imaging 25(5), 612–625 (2006)
3. Billet, F., Sermesant, M., Delingette, H., Ayache, N.: Cardiac Motion Recovery and Boundary Conditions Estimation by Coupling an Electromechanical Model and Cine-MRI Data. In: Ayache, N., Delingette, H., Sermesant, M. (eds.) FIMH 2009. LNCS, vol. 5528, pp. 376–385. Springer, Heidelberg (2009)
4. Lynch, M., Ghita, O., Whelan, P.F.: Segmentation of the Left Ventricle of the Heart in 3D+t MRI Data Using an Optimised Non-Rigid Temporal Model. IEEE Transactions in Medical Imaging 27(2), 195–203 (2008)
5. Schaerer, J., Casta, C., Clarysse, P., Rouchdy, Y., Pousin, J.: A Dynamic Elastic Model for Segmentation and Tracking of the Heart in MR Image Sequences. Medical Image Analysis (in press)
6. Oppenheim, A.V., Schafer, R.W., Buck, J.R.: Discrete-time signal processing, 2nd edn. Prentice-Hall, Inc., Upper Saddle River (1999)
7. Ciarlet, P.G., Lions, J.-L.: Handbook of Numerical Analysis. Finite difference methods, Solution of equations in $\mathbb{Z}^n$, vol. 1. North-Holland, Amsterdam (1990)
8. Peckar, W., Schnorr, C., Rohr, K., Stiehl, H.S.: Parameter-Free Elastic Deformation Approach for 2D and 3D Registration Using Prescribed Displacements. Journal of Mathematical Imaging and Vision 10(2), 143–162 (1999)
9. Zienkiewicz, O.C., Taylor And, R.L., Zhu, J.Z.: The Finite Element Method: Its Basis and Fundamentals. Butterworth-Heinemann, Butterworths (2005)
10. Radau, P., Lu, Y., Connelly, K., Paul, G., Dick, A.J., Wright, G.A.: Evaluation Framework for Algorithms Segmenting Short Axis Cardiac MRI. The MIDAS Journal - Cardiac MR Left Ventricle Segmentation Challenge, `http://hdl.handle.net/10380/3070`

Volumetric Myocardial Mechanics from 3D+t Ultrasound Data with Multi-model Tracking

Yang Wang[1], Bogdan Georgescu[1], Helene Houle[2], and Dorin Comaniciu[1]

[1] Siemens Corporate Research, 755 College Road East, Princeton, NJ 08540
{yang-wang,bogdan.georgescu,dorin.comaniciu}@siemens.com
[2] Siemens Ultrasound, 1230 Shorebird Way, Mountain View, CA 04043
helene.houle@siemens.com

Abstract. Global and regional cardiac deformation provides important information on myocardial (dys-)function in a variety of clinical settings. Recent developments in the field of echocardiography have allowed the cardiologist to quantify cardiac deformation in a non-invasive manner. Unstitched volumetric data can be captured in a high frame rate by real-time ultrasound imaging. However, most existing methods for measuring myocardial mechanics are often limited to measurements in one or two dimensions. Since myocardial tissue is virtually incompressible, the ventricular wall contains the same volume during the cardiac cycle and, thus, deforms in three dimensions. In this paper, we propose an automatic method to estimate the regional 3D myocardial mechanics on ultrasound images by recovering the 3D non-rigid deformation of the myocardium. The key advantage of our method is fusing multiple information, such as speckle patterns, image gradients, boundary detection, and motion prediction, to achieve a robust tracking on 3D+t ultrasound data. Preliminary results in both *in-vitro* and *in-vivo* experiments confirmed these findings in a quantitative manner, as the motion and mechanical parameters, such as displacement and strain, estimated by our method are close to both the ground-truth data and the clinical evaluation. The proposed method is efficient and achieves high speed performance of less than 1 second per frame for volumetric ultrasound data.

1 Introduction

The estimation and analysis of cardiac motion provides important information for the quantification of the elasticity and contractility of the myocardium. Although visual wall motion scoring is the clinically established method for the assessment of regional myocardial function, this methodology has been proven to be highly variable between observers [1]. Tissue Doppler imaging (TDI) is another alternative used in clinical studies to compute strain and strain rate. However, the measurement of regional myocardial velocities is not independent from the overall motion of the heart and suffers from tethering induced by collateral segments [2]. It has been shown that TDI-based dyssynchrony parameters are not reliable enough to predict response to cardiac resynchronization therapy (CRT) when investigated in the PROSPECT trial, a multicenter study [3].

O. Camara et al. (Eds.): STACOM-CESC 2010, LNCS 6364, pp. 184–193, 2010.

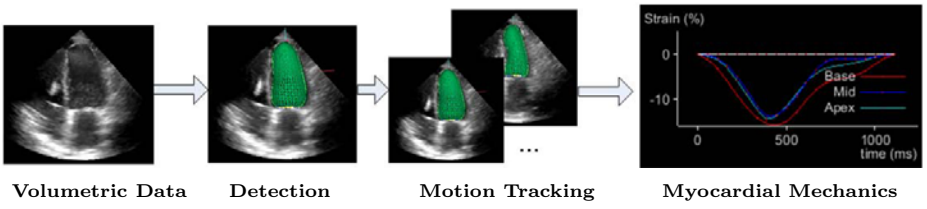

Fig. 1. The outline of our automatic framework

Given the recent progress on real-time ultrasound imaging, unstitched volumetric data can be captured in a high volume rate, which allows to quantify cardiac strain in a non-invasive manner. However, most existing methods for measuring myocardial strain are often limited to measurements in one or two dimensions, including speckle tracking [4,5] and image registration approaches [6]. A few studies have carried out to analyze the change of myocardium mass during a cardiac cycle [7]. The common conclusion is that the mass of the ventricular wall remains relatively consistent during the cardiac cycle and the change is less than 5% [8]. Since myocardial tissue is virtually incompressible, it deforms in all three dimensions simultaneously [9,10,11]. Therefore, it is important to compute the cardiac deformation (strain) in three-dimensional space.

In this paper we propose a new approach to estimate the 3D non-rigid deformation of the ventricular wall and compute myocardial mechanics from 3D+t ultrasound images. Compared to the existing methods, such as image registration [12,13,14] and optical flow [15], our framework has the following advantages:

1. Information from multiple cues, including speckle patterns, image gradients, boundary detection, and motion prediction, are fused into a single Bayesian objective function to improve tracking accuracy and robustness.
2. Efficient optimization is proposed to achieve high speed performance.
3. Image quality measurements based on image intensities and speckleness scores are integrated in a non-orthogonal projection to handle noise and signal dropouts in the ultrasound data.
4. This system provides a fully automatic solution to track and quantify the myocardial deformation and to estimate myocardial mechanics.

To demonstrate the performance, we evaluated the proposed method on *in-vitro* data taken from animals, as well as *in-vivo* data taken from both normal and cardiomyopathy subjects. Preliminary results confirmed these findings in a quantitative manner, as the estimated motion and mechanical values are close to both the ground-truth data and the clinical evaluation.

2 Framework

In this section, we present the new framework to estimate 3D myocardial mechanics. Fig. 1 illustrates the main steps of our system: automatic initialization, dense myocardium tracking, and 3D myocardial mechanics computation.

2.1 Initialization

In the starting frame (typically the end-systole or end-diastole cardiac phase), we initialize the tracking process automatically by detecting the myocardial boundaries of the left ventricle (LV), as shown in Fig. 2, and tessellate the whole myocardium into a 3D mesh. To estimate the pose (i.e., position, orientation, and scale) and shape of the LV, a 3D detector is learned on a pre-annotated database of 668 volumetric ultrasound images using the marginal space learning (MSL) approach [16], and a boundary detector using the steerable features and the probabilistic boosting-tree (PBT) [17]. The training database was manually annotated by clinical experts to provide the ground-truth segmentation. During the testing stage, given an input volume we first align the mean LV shape to the detected pose, and then deform the model to find the best boundary candidate using the trained boundary detector for each point of the model along the normal directions.

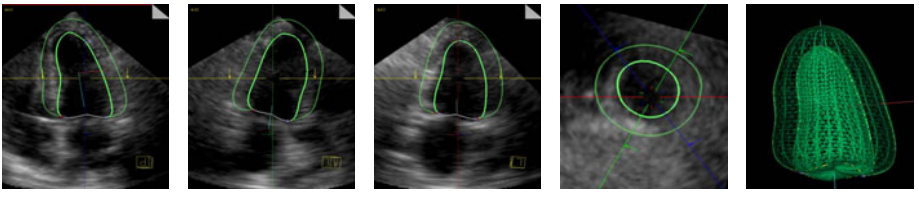

(a)A4C (b)A3C (c)A2C (d)Short Axis (e)3D Mesh

Fig. 2. Example detection results of both the endocardial and epicardial boundaries of the left ventricle (LV). The volumetric ultrasound data is acquired from a cardiomyopathy patient. Automatically detected multi-planar reformatted planes (MPRs): (a) apical four chamber plane, (b) apical three chamber plane, (c) apical two chamber plane, and (d) short axis middle plane. (e) shows the resulting 3D mesh.

2.2 3D Motion Tracking

In order to estimate myocardium strain, dense tracking of the cardiac motion is required to establish the inter-frame correspondences for each point on the 3D mesh initialized in Sec. 2.1. This task is particularly challenging for the ultrasound data because of the noise and missing data [15]. Instead of removing the speckle noise, which might potentially lose discriminative features, we propose to fuse information from multiple cues into a single Bayesian framework as in [18],

$$\arg\max_{\boldsymbol{X}_t} p(\boldsymbol{X}_t|\boldsymbol{Y}_{0:t}) = \arg\max_{\boldsymbol{X}_t} \underbrace{p(\boldsymbol{Y}_t|\boldsymbol{X}_t)}_{likelihood} \int \underbrace{p(\boldsymbol{X}_t|\boldsymbol{X}_{t-1})}_{prediction} p(\boldsymbol{X}_{t-1}|\boldsymbol{Y}_{0:t-1}) \quad (1)$$

where $\boldsymbol{Y}_{0:t} = \boldsymbol{Y}_0, \ldots, \boldsymbol{Y}_t$ are the measurements from the input image sequence $I_{0:t} = I_0, \ldots, I_t$. For clarity, we use $\boldsymbol{X}_t$ to denote a concatenation of the mesh point positions, $\boldsymbol{X}_t = [X_1, \ldots, X_n]$, which need to be estimated at the current time instant t and n is the total number of points in the mesh model.

To maximize the accuracy and robustness of the tracking performance, the ***likelihood*** term $p(\boldsymbol{Y}_t|\boldsymbol{X}_t)$ is computed from both boundary detection and speckle template matching as follows, $p(\boldsymbol{Y}_t|\boldsymbol{X}_t) = (1-\lambda_k)p(y_b|\boldsymbol{X}_t)+\lambda_k p(T_t|\boldsymbol{X}_t)$, where T_t is the speckle pattern template and λ_k is the weighting coefficient of the matching term. In the first term $p(y_b|\boldsymbol{X}_t)$ is the posterior distribution of the myocardial boundaries learned in Sec. 2.1, using the steerable features and the probabilistic boosting-tree (PBT) [17]. The second term $p(T_t|\boldsymbol{X}_t)$ is obtained by a logistic function, $\frac{1}{1+e^{-\|I_t(\boldsymbol{X}_t)-T_t\|^2}}$, based on speckle matching:

$$\|I_t(\boldsymbol{X}_t) - T_t\|^2 = \sum_{i,j,k}(I_t(\boldsymbol{X}_t + (i,j,k)) - T_t(i,j,k))^2 \tag{2}$$

where i, j, and k are the pixel-wise shift in the x, y, and z directions, respectively. λ_k is computed based on the speckleness measure as follows,

$$\lambda_k = \frac{1}{1+e^{-fc(I_t(\boldsymbol{X}_t),T_t)}}, \qquad fc(I_t(\boldsymbol{X}_t), T_t) = \frac{cov(I_t(\boldsymbol{X}_t), T_t)}{\sigma(I_t(\boldsymbol{X}_t))\sigma(T_t)} \tag{3}$$

$cov(I_t(\boldsymbol{X}_t), T_t)$ is the intensity covariance between the image block $I_t(\boldsymbol{X}_t)$ centered at $\boldsymbol{X}_t$ and the speckle template T_t. $\sigma(I_t(\boldsymbol{X}_t))$ and $\sigma(T_t)$ are the intensity variance of the image block $I_t(\boldsymbol{X}_t)$ and the speckle template T_t, respectively. In our experiments, the typical image block size is $11 \times 11 \times 11$, while the typical search range is $7 \times 7 \times 7$. To handle the temporal image variation, the speckle template T_t is also updated online using the image intensities $I_t(\boldsymbol{X}_{t-1})$ from the previous frame $t-1$.

The ***prediction*** term in Eqn. 1, $p(\boldsymbol{X}_t|\boldsymbol{X}_{t-1})$, is the transition probability function $\hat{p}(\boldsymbol{X}_t|\boldsymbol{X}_{t-1})$ augmented by an incompressibility constraint, i.e., $p(\boldsymbol{X}_t|\boldsymbol{X}_{t-1}) = \hat{p}(\boldsymbol{X}_t|\boldsymbol{X}_{t-1})p(f_V(\boldsymbol{X}_t) - f_V(\boldsymbol{X}_{t-1}))$, where $f_V(\boldsymbol{X})$ is the volume enclosed by the mesh $\boldsymbol{X}$ and $\hat{p}(\boldsymbol{X}_t|\boldsymbol{X}_{t-1})$ can be learned directly from the training data set [19]. $p(f_V(\boldsymbol{X}_t) - f_V(\boldsymbol{X}_{t-1}))$ is modeled as a zero mean Gaussian distribution $\mathcal{N}(0, \sigma_V)$ based on the training data.

Computational Efficiency. It has been shown that the 3D correlation in Eqn. 2 is computationally expensive [20]. To achieve a fast processing it is desirable to speed up the estimation of Eqn. 2, i.e.,

$$\|I_t(\boldsymbol{X}_t) - T_t\|^2 = \|I_t(\boldsymbol{X}_{t-1} + \Delta\boldsymbol{X}) - T_t\|^2 \tag{4}$$

where $\Delta\boldsymbol{X}$ is the point displacement between two frames. Let $\boldsymbol{D}_t = I_t(\boldsymbol{X}_{t-1}) - T_t$ be the concatenation of the intensity difference at each point between the current image I_t and the template T_t, and $\boldsymbol{G}_t = \frac{\partial I_t(\boldsymbol{X}_{t-1})}{\partial \boldsymbol{X}}$ be the image gradients of I_t at $\boldsymbol{X}_{t-1}$. We can then rewrite Eqn. 4 using the first order Taylor expansion

$$\|\boldsymbol{D}_t + \boldsymbol{G}_t\Delta\boldsymbol{X}\|^2 = \boldsymbol{D}_t^T\boldsymbol{D}_t + 2\boldsymbol{D}_t^T\boldsymbol{G}_t\Delta\boldsymbol{X} + \Delta\boldsymbol{X}^T\boldsymbol{G}_t^T\boldsymbol{G}_t\Delta\boldsymbol{X} \tag{5}$$

Furthermore, because of the acquisition nature of the ultrasound data, it is important to handle noise and signal dropouts [15,21]. Therefore, we introduce a regularization term based on a non-orthogonal projection as follows,

$$\hat{\boldsymbol{X}} = \bar{\boldsymbol{X}} + \boldsymbol{V}\sqrt{\boldsymbol{C}}\boldsymbol{q}, \quad \boldsymbol{q} = \sqrt{\boldsymbol{C}}\boldsymbol{V}^T(\boldsymbol{X} - \bar{\boldsymbol{X}}) \tag{6}$$

where $\bar{\boldsymbol{X}}$ is the mean shape, $\boldsymbol{V}$ is the matrix of concatenated eigenvectors, and $\boldsymbol{q}$ is a parametric vector describing the non-rigid warp. $\boldsymbol{C}$ is a diagonal weighting matrix whose diagonal entries are defined by a logistic function: $\boldsymbol{C}(i,i) = \frac{1}{1+e^{-\lambda_i I_t(\boldsymbol{X}_t(i))}}$, where each weight λ_i can be learned from the training data. Since each diagonal element in the weighting matrix $\boldsymbol{C}$ has a small value on low intensity values, it gives a small weight on the regions with missing data and signal drop-outs in the volumetric ultrasound images. In our experiments The shape model in Eqn. 6 is computed from 668 manually annotated volumetric ultrasound images, which were acquired by a Siemens SC2000 system.

Consequently, the objective function (1) can be rewritten as,

$$\arg\max_{\boldsymbol{q}_t} p(\boldsymbol{q}_t|\boldsymbol{Y}_{0:t}) = \arg\max_{\boldsymbol{q}_t} p(\boldsymbol{Y}_t|\boldsymbol{q}_t) \int p(\boldsymbol{q}_t|\boldsymbol{q}_{t-1}) p(\boldsymbol{q}_{t-1}|\boldsymbol{Y}_{0:t-1}) \tag{7}$$

which can be solved recursively as in [22]. The 3D correlation in Eqn. 5 can be computed as follows,

$$\|\boldsymbol{D}_t + \boldsymbol{G}_t \Delta\boldsymbol{X}\|^2 = \boldsymbol{D}_t^T \boldsymbol{D}_t + 2\boldsymbol{D}_t^T \mathbb{G}_t \Delta\boldsymbol{q} + \Delta\boldsymbol{q}^T \mathbb{G}_t^T \mathbb{G}_t \Delta\boldsymbol{q} \tag{8}$$

where $\mathbb{G}_t = \boldsymbol{G}_t \boldsymbol{V} \sqrt{\boldsymbol{C}}$. Because $\boldsymbol{D}_t^T \boldsymbol{D}_t$, $\boldsymbol{D}_t^T \mathbb{G}_t$, and $\mathbb{G}_t^T \mathbb{G}_t$ are independent of $\Delta\boldsymbol{q}$, they can be pre-computed to speed up the computation.

In practice the number of warp parameters, $n_{\boldsymbol{q}}$, is much less than the number of mesh points n, e.g., in our experiments a typical value of $n_{\boldsymbol{q}}$ is 150 while n is 771. Thus, the computational cost to solve Eqn. 7 is much less than the original objective function in Eqn. 1. The 3D correlation in Eqn. 2 is an $\mathrm{O}\left(m^3 n\right)$ operation where m (typically 7 in our experiments) is the search range in the x, y, and z directions, while Eqn. 8 has a complexity of $\mathrm{O}\left(n n_{\boldsymbol{q}}\right)$ only. Therefore, our proposed method is computationally efficient and can achieve a high speed performance. In our experiments, the average processing time on a 3.0GHz PC machine is less than 1 second per frame for a 3D+t ultrasound sequence with the volume size of $200 \times 200 \times 140$.

2.3 Mechanical Analysis

Given the tracking result $\boldsymbol{X}$ from Sec. 2.2, various mechanical parameters can be computed, such as displacements, velocities, and strain. In order to describe the 3D deformation of the LV, a local heart coordinate system has been introduced [1]. As illustrated in Figure 3, the three local axes are defined as the longitudinal (meridional) D_L, radial (transmural) D_R, and circumferential D_C directions. Each point position X is then projected from the Cartesian coordinate system to the local cardiac coordinate system, $X' = (X^{(L)}, X^{(R)}, X^{(C)})$. Please note that the LV apex point is excluded from analysis, because of the ambiguity of the longitudinal and circumferential directions at the tip point.

The longitudinal and radial displacements can then be computed as $Z_t^{(L)} = X_t^{(L)} - X_{t-1}^{(L)}$ and $Z_t^{(R)} = X_t^{(R)} - X_{t-1}^{(R)}$, respectively. The circumferential displacement is computed as the rotation angle, $Z_t^{(C)} = \arccos(< D_{R_t}, D_{R_{t-1}} >)$,

where $<,>$ denotes the dot product. $Z_t^{(C)}$ is defined as positive if the rotation is counter-clockwise viewed from the apex, and negative if clockwise. The velocity can be computed as dividing the displacements by the acquisition time step t_f of the input 3D+t ultrasound sequence.

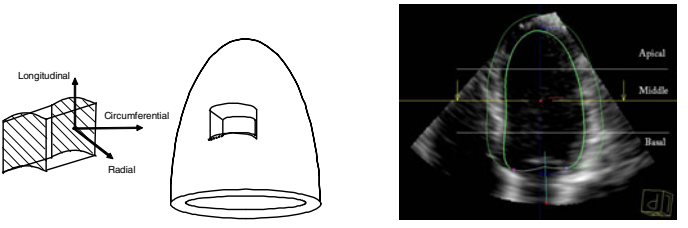

(a) (b)

Fig. 3. Local heart coordinate system. (a) The local coordinate system is defined by the longitudinal (D_L), circumferential (D_C), and radial (D_R) axes. (b) The analysis results are reported on the apical, middle, and basal segments.

To measure the myocardial strain, longitudinal, radial and circumferential tensor values are computed at each mesh point. For each point i and its n_i neighbors in the three-dimensional space, we concatenate the corresponding positions into a $3 \times (n_i + 1)$ matrix, $\boldsymbol{Y'} = \left[X_i'^T, X_1'^T, \ldots, X_{n_i}'^T\right]$. Given the initial positions $\boldsymbol{Y}_0'$ in a sequence, the Lagrangian strain tensor can be computed as

$$F = \frac{1}{2}(\boldsymbol{J}^T\boldsymbol{J} - \boldsymbol{\Lambda}), \quad \boldsymbol{J} = \boldsymbol{Y}_t' \cdot \boldsymbol{Y}_0'^T (\boldsymbol{Y}_t' \cdot \boldsymbol{Y}_0'^T)^{-1} \tag{9}$$

where $\boldsymbol{\Lambda}$ is a 3×3 identity matrix and $\boldsymbol{J}$ is a deformation gradient tensor. The longitudinal, radial, and circumferential strain values are reported as the diagonal elements of F, i.e., $F(0,0)$, $F(1,1)$, and $F(2,2)$, respectively. Example results along with their mapping to the left ventricle surface are shown in Fig. 4.

3 Experimental Results

In this section, we demonstrate the performance of our automatic detection and tracking method as well as the myocardial mechanics estimation. In our experiments, high frame-rate 3D+t ultrasound sequences were acquired by a Siemens SC2000 system with the average volume size of $200 \times 200 \times 140$. The average spatial resolution is 1mm in the x, y, and z directions, and the average temporal resolution is 44 frames per second.

***In-Vitro* Study:** To evaluate the accuracy of our automatic tracking method, we performed an *in-vitro* experiment on animals. The ground-truth motion was generated by a rotation device and a water pump controlling the stroke volume. Two crystals were implanted in the apical and middle regions of the left ventricle, respectively, to measure the myocardial movement. The average distance

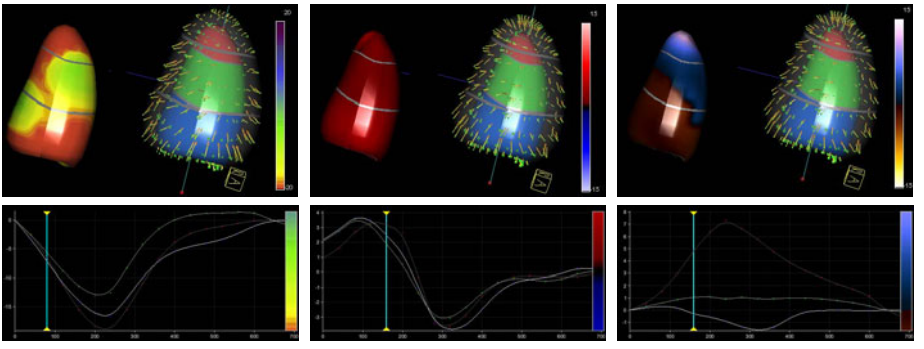

(a) longitudinal strain (b) radial velocity (c) circumferential displacement

Fig. 4. Examples of myocardial mechanics estimation: (a) strain, (b) velocity, and (c) displacement values in the longitudinal, radial, and circumferential direction respectively. In the top row, the left picture in each pair shows the estimated values mapped to the endocardial boundary of the left ventricle, while the right one shows the direction and magnitude of the dense velocity field. The apical, middle, and basal regions are marked in red, green, and blue, respectively. The bottom row shows the plot on each region, where the horizontal axis is time and the vertical axis is the estimated mechanical parameter value. The vertical blue bar indicates the time stamp of the frame displayed in the top row. Please note that in (c) the recovered rotation motion in the apical and basal regions are in opposite directions, which shows that our method can recover the twist motion of the left ventricle.

between two crystals is 30mm. 4 volumetric ultrasound sequences were acquired with 10, 15, 20, and 25 rotation degrees, respectively, and 3 sequences with different stroke volumes. As reported in Table 1, our tracking results are consistent with the ground-truth measurements on both rotation and displacement data.

Furthermore, to evaluate the results of our myocardial strain estimation, we compare them against the crystal measurements for the same subjects in the *in-vitro* study. The ground-truth longitudinal Lagrangian strain can be computed based on the displacement reported in Table 1(b), where the two crystals were implanted in the apical and middle regions of the left ventricle, respectively. Table 2 reports the comparison between our estimated strain values and the ones

Table 1. In-vitro experiments on both (a) rotation and (b) displacement data. The ground-truth motion was generated by a rotation device and a water pump controlling the stroke volume. Two crystals were implanted in the apical and middle regions of the left ventricle respectively to measure the myocardial movement. The displacements in (b) were computed based on a 30mm reference length.

Rotation(degrees)	10	15	20	25
Estimation	9.3	13.5	18.1	21.8
Accuracy	93%	90%	91%	87%

(a) Rotation Data

Displacement(mm)	0.82	1.29	2.02
Estimation	0.9	1.54	2.31
Accuracy	90%	81%	91%

(b) Displacement Data

Table 2. Comparison of the longitudinal strain estimation between our method and the crystal measurements in the *in-vitro* study. The two crystals were implanted in the apical and middle regions of the left ventricle, such that the longitudinal Lagrangian strain can be computed based on the displacement as the ground-truth measurement in the top row. The estimation results in the middle row are computed from the 3D strain tensor using our method. The low difference values in the bottom row show clearly that our estimation is consistent with the clinical measurements.

Longitudinal Strain	2.63%	4.11%	6.68%
Estimation	3.43%	5.19%	8.25%
Difference	0.8%	1.08%	1.57%

Table 3. Performance analysis on a large data set including 503 3D+t ultrasound sequences. In the first experiment, the data set was evenly split into a training set with 239 sequences and a testing set with the remaining 264 sequences, while in the second experiment the training set (434) and the testing set (69) were not balanced. The error measurements were computed as the average point distance between our estimated mesh and the ground-truth annotations by experts on both the end-diastolic and end-systolic frames. The consistent evaluation results demonstrate the robustness of our proposed method.

measure(mm)	training (239)	testing (264)	training (434)	testing (69)
mean/std	2.21/1.57	2.68/2.63	2.26/1.42	2.64/2.23

from crystal measurements. The low difference values in Table 2 show clearly that the results from our method are consistent with the clinical measurements.

***In-Vivo* Study:** To evaluate the robustness of our learning-based detection and tracking method, we tested it on a large data set including 503 volumetric ultrasound sequences from human subjects. The data set was randomly split into a training set and a testing set, where the training set was used to learn the detectors in Sec. 2.1 and the shape model and prior distributions in Sec. 2.2, while the testing set reflected the performance for unseen data. The results on both the training and testing sets are reported in Table 3. The low error values on both the training and testing data demonstrate the high accuracy and robust performance of our learning-based method on both seen and unseen data.

4 Conclusion

In this paper, we proposed an automatic framework to estimate the regional 3D myocardial mechanics on ultrasound images by recovering the 3D non-rigid deformation of the ventricular wall. The advantages of our new method include: **(1)** fusing information from multiple cues into a single Bayesian objective function to achieve accurate and robust tracking, **(2)** providing an efficient optimization approach to achieve high speed performance, **(3)** integrating image quality measurements based on image intensities and speckleness scores in a non-orthogonal

projection to handle noise and missing data, and **(4)** providing a fully automatic solution to track and quantify the myocardial deformation and to estimate myocardial mechanics. Preliminary results on both *in-vitro* and *in-vivo* clinical data demonstrated a strong agreement with the ground-truth values and expert measurements.

Acknowledgement

The authors would like to thank Dr. Sahn and Dr. Ashraf at OHSU for providing the volumetric ultrasound sequences and sonomicrometry data in the *in-vitro* animal study.

References

1. D'hooge, J., Heimdal, A., Jamal, F., Kukulski, T., Bijnens, B., Rademakers, F., Hatle, L., Suetens, P., Sutherland, G.R.: Regional strain and strain rate measurements by cardiac ultrasound: Principles, implementation and limitations. Eur. J. Echocardiogr. 1(3), 154–170 (2000)
2. Hatle, L., Sutherland, G.: Regional myocardial function a new approach. Eur. Heart J. 21, 1337–1357 (2000)
3. Chung, E., Leon, A., Tavazzi, L., Sun, J., Nihoyannopoulos, P., Merlino, J., Abraham, W.T., Ghio, S., Leclercq, C., Bax, J., Yu, C., Gorcsan III, J., St. John Sutton, M., De Sutter, J., Murillo, J.: Results of the predictors of response to crt (PROSPECT) trial. Circulation 117, 2608–2616 (2008)
4. Kaluzynski, K., Chen, X., Emelianov, S., Skovoroda, A., O'Donnell, M.: Strain rate imaging using two-dimensional speckle tracking. Transactions on Ultrasonics, Ferroelectrics and Frequency Control 48(4), 1111–1123 (2001)
5. Suffoletto, M., Dohi, K., Cannesson, M., Saba, S., Gorcsan, J.: Novel speckle-tracking radial strain from routine black-and-white echocardiographic images to quantify dyssynchrony and predict response to cardiac resynchronization therapy. Circulation 113(7), 960–968 (2006)
6. Ledesma-Carbayo, M.J., Kybic, J., Desco, M., Santos, A., Suhling, M., Hunziker, P., Unser, M.: Spatio-temporal nonrigid registration for ultrasound cardiac motion estimation. IEEE Trans. Medical Imaging 24(9), 1113–1126 (2005)
7. Yin, F.C.P., Chan, C.C.H., Judd, R.M.: Compressibility of perfused passive myocardium. American journal of physiology. Heart and circulatory physiology 271(5), 1864–1870 (1996)
8. Zhu, Y., Papademetris, X., Duncan, J.S., Sinusas, A.J.: Cardiac MR image segmentation with incompressibility constraint. In: ISBI, pp. 185–188 (2007)
9. Glass, L., Hunter, P., McCulloch, A.: Theory of Heart: Biomechanics, Biophysics, and Nonlinear Dynamics of Cardiac Function. Springer, New York (1991)
10. Amini, A., Chen, Y., Curwen, R., Manu, V., Sun, J.: Coupled b-snake grides and constrained thin-plate splines for analysis of 2d tissue deformations from tagged mri. TMI 17(3), 344–356 (1998)
11. Leung, K.Y.E., van Stralen, M., van Burken, G., de Jong, N., Bosch, J.G.: Automatic active appearance model segmentation of 3D echocardiograms. In: ISBI, pp. 320–323 (2010)

12. Grau, V., Becher, H., Noble, J.: Registration of multiview real-time 3-D echocardiographic sequences. TMI 26(9), 1154–1165 (2007)
13. Elen, A., Choi, H.F., Loeckx, D., Gao, H., Claus, P., Suetens, P., Maes, F., D'hooge, J.: Three-dimensional cardiac strain estimation using spatio-temporal elastic registration of ultrasound images: A feasibility study. TMI 27(11), 1580–1591 (2008)
14. Craene, M.D., Camara, O., Bijnens, B.H., Frangi, A.F.: Large diffeomorphic FFD registration for motion and strain quantification from 3D-US sequences. In: Ayache, N., Delingette, H., Sermesant, M. (eds.) FIMH 2009. LNCS, vol. 5528, pp. 437–446. Springer, Heidelberg (2009)
15. Duan, Q., Parker, K.M., Lorsakul, A., Angelini, E.D., Hyodo, E., Homma, S., Holmes, J.W., Laine, A.F.: Quantitative validation of optical flow based myocardial strain measures using sonomicrometry. In: ISBI, pp. 454–457 (2009)
16. Zheng, Y., Barbu, A., Georgescu, B., Scheuering, M., Comaniciu, D.: Four-chamber heart modeling and automatic segmentation for 3-D cardiac CT volumes using marginal space learning and steerable features. TMI 27(11), 1668–1681 (2008)
17. Tu, Z.: Probabilistic boosting-tree: Learning discriminative models for classification, recognition, and clustering. In: ICCV, pp. II: 1589–1596 (2005)
18. Zhu, Y., Papademetris, X., Sinusas, A.J., Duncan, J.S.: A dynamical shape prior for LV segmentation from RT3D echocardiography. In: Yang, G.-Z., Hawkes, D., Rueckert, D., Noble, A., Taylor, C. (eds.) MICCAI 2009. LNCS, vol. 5761, pp. 206–213. Springer, Heidelberg (2009)
19. Yang, L., Georgescu, B., Zheng, Y., Foran, D.J., Comaniciu, D.: A fast and accurate tracking algorithm of left ventricles in 3D echocardiography. In: ISBI (2008)
20. Chen, X., Xie, H., Erkamp, R., Kim, K., Jia, C., Rubin, J.M., O'Donnell, M.: 3-D correlation-based speckle tracking. Ultrasonic Imaging 27, 21–36 (2005)
21. Wang, X., Chen, T., Zhang, S., Metaxas, D., Axel, L.: LV motion and strain computation from tMRI based on meshless deformable models. In: Metaxas, D., Axel, L., Fichtinger, G., Székely, G. (eds.) MICCAI 2008, Part I. LNCS, vol. 5241, pp. 636–644. Springer, Heidelberg (2008)
22. Yang, L., Georgescu, B., Zheng, Y., Meer, P., Comaniciu, D.: 3D ultrasound tracking of the left ventricles using one-step forward prediction and data fusion of collaborative trackers. In: CVPR (2008)

Cardiac Active Contraction Parameters Estimated from Magnetic Resonance Imaging

Vicky Y. Wang[1], Hoi I. Lam[1], Daniel B. Ennis[2], Brett R. Cowan[3], Alistair A. Young[1,3], and Martyn P. Nash[1,4]

[1] Auckland Bioengineering Institute, University of Auckland, New Zealand
{vicky.wang,h.lam,a.young,martyn.nash}@auckland.ac.nz
[2] Department of Radiological Sciences Diagnostic Cardiovascular Imaging, University of California, Los Angeles
daniel.ennis@ucla.edu
[3] Centre for Advanced MRI, University of Auckland, 85 Grafton Road, Auckland, 1142, New Zealand
b.cowan@auckland.ac.nz
[4] Department of Engineering Science, University of Auckland, Level3, UniServices House, 70 Symonds Street, Auckland, 1142, New Zealand

Abstract. Impaired systolic ventricular function is common in patients diagnosed with heart failure (HF) or ischaemic heart disease. The diminished contractile performance with impaired contractility (systolic HF) can be induced by impaired filling function (diastolic HF) and the wall stress (both passive and active) may indicate the progression from diastolic HF to systolic HF. In order to better understand the distribution of active stress during ventricular contraction, a left ventricular (LV) finite element (FE) model incorporating LV fibre geometry and function was developed to parameterise a time-varying model of myocardial contraction by simulating LV mechanics. During systole, the isometric active stress monotonically increased to 95 kPa, and rapidly recovered during isovolumic relaxation. We also observed regional variations of the fibre length dependent contractile stress throughout the LV. The time-varying active stress curve thereby obtained enabled quantification of heart muscle performance. This type of integrative modelling enables the investigation of LV mechanics on an individualised basis.

Keywords: Magnetic Resonance Imaging (MRI), Diffusion Tensor MRI (DTMRI), Left Ventricular (LV) mechanics, Finite Element Modelling, Passive Material Parameter estimation, Contractile stress.

1 Introduction

Ventricular hypertrophy is a transitional phase during the development of heart failure (HF). A hypertrophic heart has undergone compensatory remodelling, but eventually becomes incapable of working efficiently. Many HF patients exhibit preserved systolic pump function (e.g. normal ejection fraction), but have increased LV wall thickness and a correspondingly increased LV mass, which masks a decreased contractility. The

O. Camara et al. (Eds.): STACOM-CESC 2010, LNCS 6364, pp. 194–203, 2010.

changes in wall thickness can be triggered by the disturbance in physiological, geometrical and/or haemodynamic loading conditions. A series of remodelling processes occur in the myocytes to alter force/tension relationships, material properties, and hence muscle performance during the whole cardiac cycle. Since diastolic HF occurs at an early stage, the passive material responses have been the centre of cardiac mechanics modelling research. The changes in passive material properties give rise to diastolic dysfunction and can potentially influence the active process of ventricular relaxation. Moreover, the remodelling of the myocardium can be initiated by changes in the contractile force generated by the myofibrils during systole [1].

Heart wall stress, during both diastolic inflation and systolic contraction [2], has been identified as a factor accounting for different patterns of hypertrophy [3]. It has been suggested that patients suffering from either concentric hypertrophy or eccentric hypertrophy exhibit normal peak systolic stress despite elevated end-systolic pressure or elevated end-diastolic stress. To explain the normal wall stress, they proposed that an enlarged chamber leads to increased peak systolic stress, which again leads to an increase in wall thickness, and eventually normalised systolic stress. These observations along with other experimental findings [4] all indicate that systolic wall tension/stress initiates and drives the progression of hypertrophy.

Not only has systolic wall stress been considered as a stimulus to ventricular hypertrophy, but it has also been used by clinicians to assess preoperative and postoperative LV function in patients with mitral valve regurgitation. For patients who have had mitral valve replacement, a rather misleading reduction in EF has been reported. Ejection fraction can also be normalised by hypertrophy. To avoid these problems, the ratio of end-systolic wall stress (ESWS) and end-systolic volume (ESV) has become widely used to better evaluate LV function. Compared to a normal person, an elevated ESWS/ESV ratio indicates a better LV contraction for a given afterload, whereas, worsened LV contractility is defined by a lower ESWS/ESV ratio [5].

Since stress cannot be directly measured *in vivo* like strain and ventricular myocardium has a complicated three-dimensional (3D) structure, which gives rise to anisotropic, nonlinear, time-dependent [6] and hyperelastic material behaviour [7]. This simple one-dimensional stress calculated using theoretical equations is therefore not physiologically realistic for making clinically relevant observations. Moreover, the stress generated by the myofibres is largely dependent on the material properties of the underlying myocardium. Finite element (FE) modelling enables direct computation of the stress field based on the realistic geometry and strain field together with knowledge of the mechanical properties of the myocardium. With the development of cardiac MRI, we can also validate the stress calculation and estimate myocardial mechanical properties by matching myocardial deformation (strains) measured non-invasively using tagged MRI. In our previous study [8], we established a FE model incorporating *in vivo* tagging and concurrent pressure recordings with *ex vivo* DTMRI in a normal canine heart. This biophysical model was then used to simulate the diastolic inflation using a transversely-isotropic constitutive relation. Passive constitutive parameters were tuned by matching the predicted localised motion of a large set of embedded material points with those derived from tagged MRI [9].

In this study, we have extended the estimation process to model the systolic mechanics and optimise the activation parameters by matching the pressure-volume

relation established from the pressure recordings during ventricular contraction and relaxation. This integrative FE model-based framework enables us to assess the stress development throughout the systole which can facilitate investigating the effect of changing passive material properties on active contraction and effect of changing wall stress on wall thickening – the critical point for the start of remodelling.

2 Methods

2.1 Model Creation

The anatomical model used in this study based the geometric information on *in vivo* tagged magnetic resonance imaging (MRI) of a canine left ventricle (LV) and myocardial fibre structure information on *ex vivo* diffusion tensor MRI of the same LV. The imaging and data acquisition was performed at the NIH Laboratory of Cardiac Energetics. A summary of imaging protocols and parameters are presented in [9].

From the short-axis tagged MRI images, surface contours of the LV were segmented at the end of isovolumic relaxation (assumed to be the unloaded, zero pressure reference state) using Zinc Digitiser[1]. The surface contours of the DTMRI images were also digitised in the 2D imaging coordinate system using same digitisation software. The segmented surface contour for each short-axis slice was used to create a mask to exclude the pixels outside of the LV myocardium. Concurrent pressure recordings were achieved by inserting a MR compatible Millar transducer into the left ventricular cavity before tagged MRI data were acquired. Illustration of the synchronisation of pressure recording with imaging trigger and right atrial pacing can be found in [9].

The *in vivo* geometric information (tagged MRI) and *ex vivo* microstructural information (DTMRI) of the same heart were combined using a mathematical model. We created a LV FE model using nonlinear geometric fitting to match segmented contours of the MR tagged images. The geometric model consisted of 16 smoothly continuous tri-cubic Hermite hexahedral elements, arranged with 4 circumferential elements, 4 longitudinal elements and 1 transmural element (Fig. 1a). The endocardial and epicardial surfaces of FE model were fitted to the corresponding segmented surface data using a nonlinear least squares approach [10] implemented in CMISS[2].

Directions of maximum diffusion (principle eigenvectors) obtained from the DTMRI data were transformed into the above LV FE model using free-form deformation techniques (host mesh fitting) as described previously in [9]. To incorporate the fibre orientations to the FE model, the fibre angle (defined as positive for an elevation angle above the short-axis plane) was calculated for each vector prior to fitting. It was assumed that fibre vectors lay parallel to the epi/endo wall planes. Imbrication (transverse) angles and sheet angles were neglected in this study. Myofibre orientations were incorporated into the geometric model as a fibre angle field (interpolated using tricubic Hermite basis functions), which was fitted using nonlinear least squares. Fig. 1b illustrates the LV model with the fitted fibre orientation field and demonstrates the transmural variation throughout the LV wall.

[1] http://www.cmiss.org/cmgui/zinc.
[2] http://www.cmiss.org/.

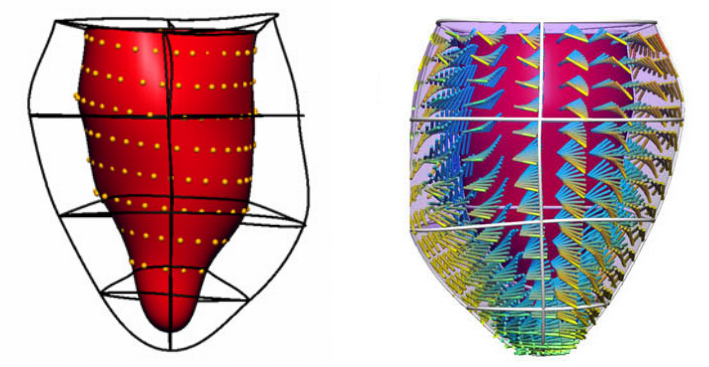

(a) (b)

Fig. 1. Endocardial surface of the model fitted to the segmented epicardial and endocardial data from tagged MRI (endo RMSE = 0.31mm; epi RMSE = 0.33mm); (b) Anterior view of the LV model superimposed with the fibre orientation field fitted to the transformed DTMRI data.

2.2 Mechanics Model

The stress-strain relationship characterises the material properties of individual materials that play major roles in determining the mechanical function. The following equation expresses the second Piola-Kirchhoff stress tensor (T) in terms of the Lagrangian Green strain tensor (E) (which defines the kinematic relationship between the reference coordinates X, and the deformed coordinates x of a material point) via the strain energy density function (W) which defines the passive material properties.

$$T^{MN} = \frac{1}{2}\left(\frac{\partial W}{\partial E_{MN}} + \frac{\partial W}{\partial E_{NM}}\right) - p\frac{\partial X_M}{\partial x_k}\frac{\partial X_N}{\partial x_k} + T_a \delta_1^M \delta_1^N \quad . \tag{1}$$

The variable p is a reaction stress (also known as the hydrostatic pressure), which arises due to the incompressible nature of the tissue, and was interpolated using a trilinear Lagrange scheme; δ_1^M is the Kronecker delta and T_a is the active stress generated by myocytes. In the absence of body forces and rigid body acceleration, the stress equilibrium equation (Eq. 1) can be expressed in terms of the microstructural material coordinates [11] and solved using nonlinear Galerkin finite element techniques to determine the deformed state of the body under specified boundary conditions.

In this study, two sets of two-state quasi-static analyses were considered: 1) deformation from the reference LV state (zero-pressure / unloaded state) to the passively inflated (end-diastolic) state due to LV endocardial pressure loading; 2) deformation from the end-diastolic state to the fully contracted (end-systolic) state. In each case, the equations of motion formed a set of nonlinear residuals that were solved using Newton's method to linearise the equations. This resulting linear system was solved using LU decomposition. The initial solution for the finite elasticity equations was chosen to be the reference geometry modified by any kinematic constraints.

To reproduce the experimental LV deformation, physiologically realistic loading constraints must be defined. The *in vivo* LV cavity pressure recordings, which were

temporally synchronised with the tagged MRI data, allowed us to apply the appropriate endocardial surface constraints required to inflate the LV during diastole, resist systolic contraction during isovolumic contraction until the afterload was reached and guide the LV contraction during ejection phase by matching the pressure recordings. By analysing the long-axis tagged MRI images, we derived the kinematic constraints for the base of the LV model throughout the cardiac cycle. To simulate the passive ventricular mechanics, the end-diastolic LV pressure load of 0.5 kPa was applied to the endocardial surface of the model in incremental steps of 0.1 kPa. The long-axis (x) positions of the basal plane were prescribed to match the tag plane movements tracked from the long-axis images. The passive stress-strain behaviour of the ventricular myocardium in this study was modelled using the transversely-isotropic exponential constitutive [12] relation in Eq. 2.

$$\begin{aligned} &W = C_1 \exp(Q) \\ &\text{where } Q = C_2 E_{ff}^2 + C_3(E_{cc}^2 + E_{rr}^2 + E_{cr}E_{rc}) + 2C_4(E_{fc}E_{cf} + E_{fr}E_{rf}) \end{aligned} . \tag{2}$$

where $E_{\alpha\beta}$ are the components of Green's (Lagrange) strain tensor referred to fibre (f), cross-fibre (c) and radial (r) coordinates. C_1 - C_4 are the myocardial constitutive parameters and have been tuned to match the model predicted motions of the set of 3D material points derived from MRI tagging, as described in [9]. At the reference state, the material points were embedded in the reference FE model. As the model was passively inflated, the motions of the embedded material points were tracked to predict their positions at end-diastole. A detailed description of the constitutive parameter estimation technique is provided in [9]. The passive parameters used for this study are summarised in Table 1.

The contraction of the LV myocardium is driven by activation of myocytes initiated by an electrical wave propagating through the heart. The contractile stress generated by the myocytes is combined with the passive stress-strain relation to simulate the isovolumic contraction and ejection phases of the cardiac cycle. We assume that contractile tension is only generated along the axes of the myocytes. In this study, we have used a steady-state active tension model:

$$T_a(T_{Ca}, \lambda) = T_{Ca} \times \left[1 + \beta(\lambda - 1)\right] . \tag{3}$$

where T_{Ca} the time-varying isometric tension at resting sarcomere length, which is modified by a linear function of the sarcomere extension ratio (λ), where the constant $\beta = 1.45$ [13].

We estimated the T_{Ca} using the pressure-volume relationship customised to data from this particular animal (Fig. 2). This was achieved using the following approach: 1) all short-axis tagged MR images between the end-diastolic frame and the end-systolic frame and 4 frames during isovolumic relaxation were segmented using the Zinc Digitiser; 2) an anatomical FE model was created for each frame using the segmented surface contours; 3) a cavity mesh was created for each of the FE models to evaluate the cavity volume at each frame; 4) a pressure-volume loop was created by combining these data together with the concurrent in vivo pressure measurement at each frame.

Table 1. Passive myocardial constitutive parameters [11]

Passive Parameters	C_1(kPa)	C_2	C_3	C_4
Values	0.831	14.3	4.49	0.762

Following the end of passive inflation, the value of T_{Ca} was gradually increased from zero to simulate the onset of isovolumic contraction. The cavity volume during this phase was kept constant by altering the pressure applied to the LV endocardial surface for each tension increment. The end of isovolumic contraction was determined when the endocardial pressure first exceeded the LV afterload (obtained from the concurrent pressure recordings). This marked the onset of ejection, during which the basal plane motion of the ventricular base was prescribed (as recorded from the long axis images) whilst the position of the apex was fixed. For each time point during ejection, the LV cavity pressure was set to the recorded value, and T_{Ca} was iteratively altered until the cavity volume matched (to within 0.5%) the volume of the associated fitted cavity mesh. Closing of the mitral valve marked the onset of the isovolumic relaxation phase, during which the endocardial pressure was decremented (according to the recorded value) and T_{Ca} was iteratively reduced in order to maintain a constant cavity volume as the LV relaxed.

3 Results

Figure 2 illustrates the relationship between LV cavity pressure and volume for the entire cardiac cycle with values derived from the tagged MRI data and concurrent pressure recordings. We have also analysed a selection of image frames during relaxation, diastasis and passive inflation to complete the cardiac cycle. The temporal step between

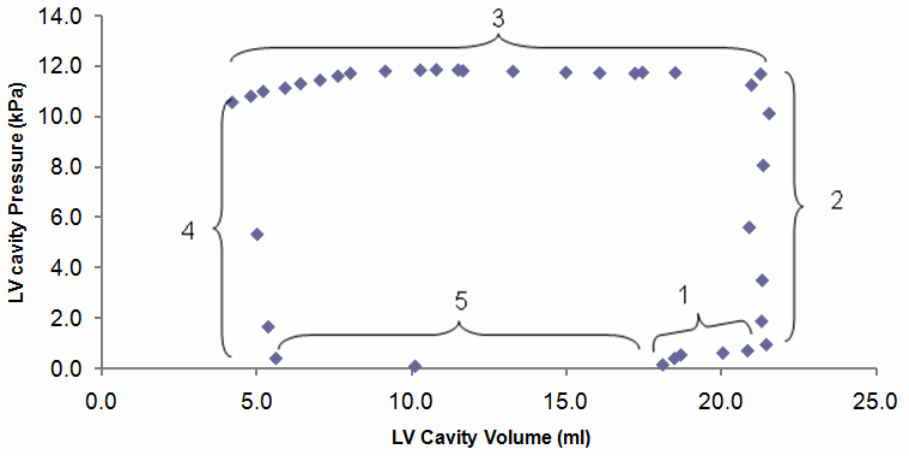

Fig. 2. LV pressure-volume loop derived from the concurrent *in vivo* pressure recording and tagged MR images. Labels 1-5 indicate the different phases of the cardiac cycle (see text for details) as determined from the mitral valve activity in the long-axis MRI.

each recording was 8 ms and the afterload was approximately 78 mmHg (12 kPa). The end-diastolic and end-systolic cavity volumes were 22 ml and 4.5 ml, respectively. As illustrated, the LV cavity volume during phase 2 remained relatively constant (isovolumic contraction), while the cavity pressure increased dramatically. During ejection (phase 3), the LV cavity pressure remained relatively constant until end-systole, but the cavity volume decreased as blood was pumped out of the LV. During phase 4, the endocardial pressure rapidly decreased whilst cavity volume slightly increased - this slight discrepancy during the so-called isovolumic relaxation phase was possibly due to surface contour segmentation error. The recoil phase (phase 5) restored the cavity to its reference state before the onset of passive filling (phase 1).

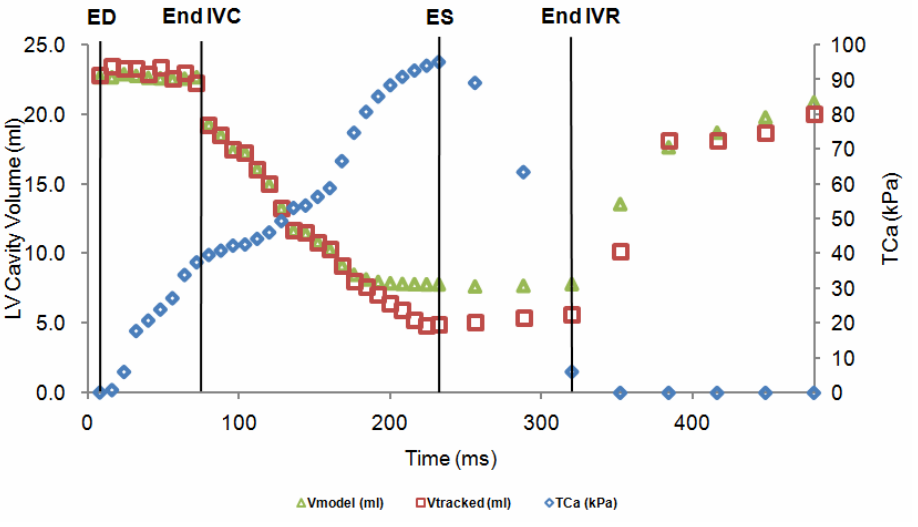

Fig. 3. Estimated value of T_{Ca} and the model predicted cavity volume versus tracked cavity volume during the heart cycle. ED: end-diastole; IVC: isovolumic contraction; ES: end-systole; IVR: isovolumic relaxation.

As illustrated in Fig. 3, T_{Ca} was initially set to zero at end-diastole but steadily increased throughout isovolumic contraction and ejection to a maximum of 95 kPa at end-systole. This was followed by a decrease back to zero by the end of isovolumic relaxation. The comparison between the LV cavity volume determined from MRI ($V_{tracked}$: triangles) and that predicted using the FE model (V_{model}: squares) is also shown in Fig. 3. With the rise in active tension, the LV cavity volume remained relatively constant during isovolumic contraction, then decreased rapidly as the LV emptied during ejection. The simulated end-systolic cavity volume was approximately 7.8 ml, which was slightly greater than that calculated from the tagged MRI data (4.8 ml). This slight discrepancy was possibly due to an assumption(s) of the model breaking down near end-systole. During the subsequent isovolumic relaxation phase, the predicted cavity volume remained relatively constant, but rose when the active tension reduced to zero signifying the start of filling.

We have also evaluated the active contractile stress at end-systole throughout the LV. Even though a homogeneous activation T_{Ca}, was determined, the stresses evaluated at each of the Gauss points varies due to the linear length dependence term in Eq. 3. The models at end-diastole and ejection are illustrated in Fig. 4a and Fig. 4b&c respectively. As illustrated, fibres in most of regions of the LV are under compression at end-systole.

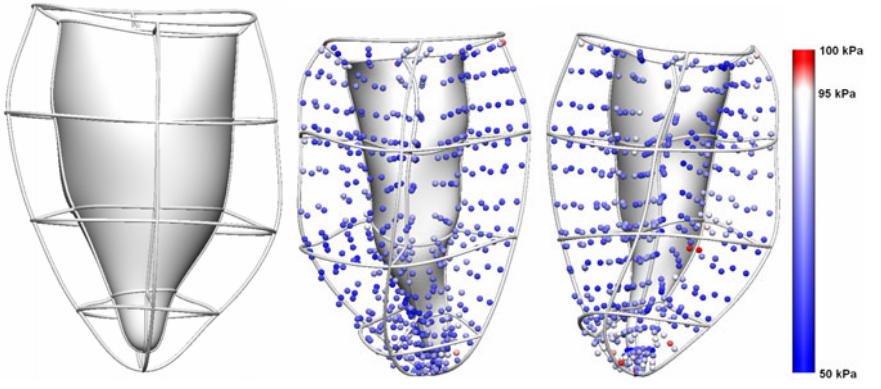

Fig. 4. (a) Anterior view of the end-diastolic model; (b) Anterior and (c) posterior views of the maximum active fibre stress evaluated at each Gauss point

4 Discussion

In this study, we have extended the integrative FE model analysis developed in [9] to analyse the systolic mechanics of a healthy canine LV. This is the first study to estimate *in vivo* myocytes contractile stress based on concurrent measures of LV motion from MRI and endocardial pressure. We have previously estimated the parameters of a passive transversely-isotropic constitutive relation to match the recorded LV kinematics. Here, we have investigated the mechanical behaviour of the LV during systolic contraction (isovolumic contraction, ejection) and the isovolumic relaxation phase of the heart cycle. We prescribed the basal motion observed from long-axis tagged MR images, and the LV endocardial pressure as boundary constraints to realistically reproduce the ventricular mechanics. Using this integrative modelling approach, we show the time-varying active stresses generated by the myocytes, which cannot be measured directly *in vivo*. To achieve this, we iteratively estimated the level of active stress to match the LV cavity volume. This differs from other researchers who have investigated systolic mechanical properties of sheep hearts [14] using strains and a time-varying elastance model, combined with pressure recordings taken at a different point in time.

There are several limitations of this LV model: 1) lack of a right ventricle and other structural features, such as the pericardium, valves and papillary muscles; 2) only short-axis tagged MR images were used to create FE models for volume

calculations (the inclusion of long-axis tagged MR images may provide a more accurate volume evaluation); 3) the isometric tension at resting length (T_{Ca}) was constrained to be spatially homogeneous, but it is likely to vary throughout the LV due, for example, to the spreading wave of excitation leading to spatially heterogeneous calcium transients. This limitation may explain the small discrepancy in the cavity volume predicted by the FE model near end-systole and through IVR (Fig. 4). Another limitation relates to the quasi-static assumption of the contraction model. The timing of the peak in the tension trace (Fig. 4) coincided with end-systole; however this may not be the case if the dynamics of calcium binding were taken into account using a more detailed time-dependent description of contractile stress [15]. This simplification may also affect the estimated rate of rise and decay of contractile stress. We are presently working on estimating the active tension based on matching the regional LV deformation using the same set of 3D material points as were used for the estimation of passive material properties in [9]. To be able to reliably match the localised motion, a heterogeneous distribution of material properties may be required. Sensitivity and convergence analyses will also be necessary to investigate the uniqueness of the estimated active parameter.

5 Conclusions

We have developed and demonstrated a FE modelling technique to determine the first *in vivo* estimates of myocardial contractile stress throughout the heart cycle using time-varying LV cavity volume changes derived from cardiac MRI with concurrent LV endocardial pressure recordings to parameterise a contraction model. Isometric tension monotonically increased to 95 kPa during systole, and rapidly recovered during isovolumic relaxation, and we observed regional variations of the length dependent contractile stress throughout the LV. The long-term goals of this research are to gain a better understanding of the underlying pathophysiological basis of ventricular mechanics, and to apply these techniques to medical images in order to assist clinicians with the diagnosis and treatment of patients suffering from heart failure.

Acknowledgments. Vicky Y. Wang received funding from the New Zealand Institute of Mathematics & Its Applications (NZIMA) and The University of Auckland. Alistair A. Young is supported by Award Number R01HL087773 from the National Heart, Lung, And Blood Institute, USA. Martyn P. Nash is supported by a James Cook Fellowship administrated by the Royal Society of New Zealand on behalf of the New Zealand Government. We gratefully acknowledge Professor McVeigh and Dr Helm from National Institutes of Health and Johns Hopkins University for providing the experimental data.

References

1. Moulton, M.J., Creswell, L.L., Downing, S.W., Actis, R.L., Szabo, B.A., Pasque, M.K.: Myocardial material property determination in the in vivo heart using magnetic resonance imaging. Int. J. Card. Imaging 12, 153–167 (1996)

2. Linzbach, A.J.: Heart failure from the point of view of quantitative anatomy. Am. J. Cardiol. 5, 370–382 (1960)
3. Grossman, W., Jones, D., McLaurin, L.P.: Wall Stress and Patterns of Hypertrophy in the Human Left Ventricle. J. Clin. Invest. 56, 56–64 (1975)
4. Meerson, F.Z.: The myocardium in Hyperfunction and Heart Failure. Circ. Res. 25 (1969)
5. Carabello, B.A., Nolan, S.P., McGuire, L.B.: Assessment of Preoperative Left Ventricular Function in Patients with Mitral Regurgitation: Value of the End-systolic Wall Stress-End-Systolic Volume Ratio. Circulation 64, 1212–1217 (1981)
6. Costa, K.D., Holmes, J.W., McCulloch, A.D.: Modelling cardiac mechanical properties in three dimensions. Phil. Trans. Royal. Soc. Lond. 359, 1233–1250 (2001)
7. Demer, L.L., Yin, F.C.: Passive biaxial mechanical properties of isolated canine myocardium. J. Physiol. 339, 615–630 (1983)
8. Wang, V.Y., Lam, H.I., Ennis, D.B., Young, A.A., Nash, M.P.: Passive Ventricular Mechanics Modelling Using MRI of Structure and Function. In: Metaxas, D., Axel, L., Fichtinger, G., Székely, G. (eds.) MICCAI 2008, Part II. LNCS, vol. 5242, pp. 814–821. Springer, Heidelberg (2008)
9. Wang, V.Y., Lam, H.I., Ennis, D.B., Cowan, B.R., Young, A.A., Nash, M.P.: Modelling Passive Diastolic Mechanics with Quantative MRI of Cardiac Structure and Function. Med. Image. Anal. 13, 773–784 (2009)
10. Nielsen, P.M.F.: The anatomy of the heart: A finite element model. PhD Thesis, Vol. PhD. The University of Auckland (1987)
11. Nash, M.P., Hunter, P.J.: Computational Mechanics of the heart. J. Elast. 61, 113–141 (2000)
12. Guccione, J.M., McCulloch, A.D., Waldman, L.K.: Passive material properties of intact ventricular myocardium determined from a cylindrical model. J. Biomech. Eng. 113, 43–55 (1991)
13. Hunter, P.J., McCulloch, A.D., ter Keurs, H.E.D.J.: Modelling the mechanical properties of cardiac muscle. Prog. Biophys. Mol. Biol. 69, 289–331 (1998)
14. Walker, J.C., Ratcliffe, M.B., Zhang, P., Wallace, A.W., Edward, B.F., Hsu, W., Saloner, D.A., Guccione, J.M.: Magnetic resonance imaging-based finite element stress analysis after linear repair of left ventricular aneurysm. Am. J. Physio. Heart Circ. Physiol. 289, H692–H700 (2004)
15. Niederer, S.A., Hunter, P.J., Smith, N.P.: A quantitative analysis of cardiac myocyte relaxation: a simulation study. Biophys. J. 90(5), 1697–1722 (2006)

Recovering Cardiac Electrical Activity from Medical Image Sequence: A Model-Based Approach

Heye Zhang[1,2], Bo Li[3], Pengcheng Shi[4], Hu Qingmao[1,2], and Pheng Ann Heng[2]

[1] Shenzhen Institutes of Advanced Technology, Chinese Academy of Sciences, China
[2] The Chinese University of Hong Kong, Hong Kong
[3] NextWindow Ltd., New Zealand
[4] Computational Biomedicine Laboratory, Rochester Institute of Technology, USA

Abstract. Because of the intrinsic physiological coupling between the motion and the electrical activity of human heart and available higher resolution imaging sequences, we believe that image-derived cardiac kinematic measurement should be able to reflect patient-specific propagation of cardiac transmembrane potential (TMP). Therefore, in this paper we developed a model-based filter framework, which can recover cardiac electrical activity from MR image sequences. In this particular implementation, the cardiac electro-mechanical coupling process will be properly modelled over a meshfree particle representation of cardiac volume and its fiber structure, and then a model-based unscented Kalman filter (UKF) will be created to incorporate an electro-mechanical coupling model into the state space equation to estimate cardiac electrical activity from MR image sequences. At the end, we not only investigate the performance of our algorithm through two synthetic motion data sets, which are generated by healthy and diseased propagation patterns in an authentical cardiac geometry respectively, but also show the potential usage of our algorithm in clinical diagnosis through a test of one clinical MR image sequence.

1 Introduction

Current non-invasive functional imaging of cardiac electrical activity is aimed to compute cardiac TMP on the epicardium or inside myocardium from body surface potentials (BSPs), or even electrocardiograms (ECGs). Such non-invasive functional imaging problems are ill-posed, so that a regularization term or a model constraint will be introduced to overcame the illness [1,2,3]. Though a recent effort has demonstrated its promising results [4], current non-invasive functional imaging techniques are still in the infancy. In the same time, a different approach has been gradually developed in medical image community to provide a novel angle of view to understand cardiac electrical activity using available dense cardiac motion descriptions (displacement, stress or strain) extracted from cardiac images, through inverting the electro-mechanical coupling process. In this paper, we can call this approach as inverse electro-mechanical coupling

O. Camara et al. (Eds.): STACOM-CESC 2010, LNCS 6364, pp. 204–211, 2010.

approach/problem. A probabilistic measure of the onset of regional myocardial activation, derived from 3D motion field obtained by tracking tagged MR image sequence with non-rigid registration [5], and regularized optimization using the law of force equilibrium [6] are two recent efforts to solve this inverse approach. Though these two approaches of non-invasive functional imaging and inverse electro-mechanical coupling are developed separately in different scientific communities, we believe that a framework to integrate these two approaches will become the trend to compute cardiac electrical activities.

Our work in this paper is inspired by the encouraging performance of physiological models in recent cardiac image analysis works [7,8]. In our implementation, a simple electro-mechanical coupling model [7,8] is first adopted into the stochastic state space, and the active stress then becomes the state variables. Since the active stress is only driven by cardiac TMP, we just need to compute the active stress to obtain the propagation pattern of cardiac TMP. Because of non-linear coupling process between the active stress and cardiac movement, we apply UKF algorithm [9] to inverse this coupling process. So the inverse approach from medical images to cardiac electrical activity is finally interpreted into a multi-frame model-based filter framework. This framework is verified in Auckland Heart Model [1] under different physiological conditions with favorable results, and its potential usage is also shown in one set of clinical data.

2 Meshfree Particle Representation

In our framework, we adopt the meshfree particle representation, which has been well explored in medical image community [6,2,8], to represent the heart by a set of unstructured sample nodes inside and in its boundaries. In Fig. 1, meshfree particle representation is illustrated in Auckland Heart Model. Let $u(x)$, $\dot{u}(x)$ and $\ddot{u}(x)$ be the displacement, velocity and acceleration of the myocardial tissue at point x. The approximated displacement, velocity and acceleration $u_h(x)$, $\dot{u}_h(x)$ and $\ddot{u}_h(x)$ are then given: $u_h(x) = \sum_{I=1}^{N} \phi(x) u_I$, $\dot{u}_h(x) = \sum_{I=1}^{N} \phi(x) \dot{u}_I$ and $\ddot{u}_h(x) = \sum_{I=1}^{N} \phi(x) \ddot{u}_I$ where $\phi(x)$ is the meshfree shape function [10] of node I, N is the total number of sample nodes used for local support, u_I is the nodal displacement value, $\dot{u}_I$ is the nodal velocity value and $\ddot{u}_I$ is the nodal acceleration value.

3 Stochastic State Space Equation

In our framework, the electro-mechanical coupling model in Equation (1),

$$\dot{\sigma_c} + \sigma_c = u_e \sigma_0 \tag{1}$$

describes the relation between cardiac TMP, u_e, and the active stress, σ_c, which is an one-dimensional variable along the local fiber orientation and only determined

[1] http://www.bioeng.auckland.ac.nz/cmiss/cmiss.php

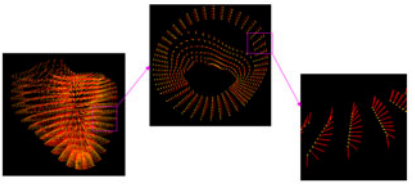

Fig. 1. Anisotropic cardiac fiber structure

by u_e [7]. The reasons to choose this simple model are: the performance of this electro-mechanical model have been tested in cardiac image analysis [7,8], and fewer parameters can help to reduce the complexity of inverse approach. Our proposed algorithm will combine electro-mechanical coupling model and patient-specific loading (external loading) through UKF to recover the waveform of active stress in the heart. After the waveform of active stress is available, the temporal changing of cardiac TMP can be obtained, too (Equation (1)).

However the coupling process is continuous, and mapping between external loading and active stress is nonlinear. Though the extended Kalman filter (EKF) has been applied extensively to nonlinear estimation [11], but the inherent flaws of the EKF are due to its linearization approach for calculating the mean and covariance of a random variable which undergoes a nonlinear transformation. UKF addresses these flaws by utilizing a deterministic "sampling" approach to calculate the mean and covariance terms [9]. Essentially, $2L + 1$, sigma points (L is the state dimension), are chosen based on a square-root decomposition of the prior covariance. These sigma points are propagated through the true nonlinearity, without approximation, and then a weighted mean and covariance is taken. UKF approaches results in approximations that are accurate to the third order (Taylor series expansion) for Gaussian inputs for all nonlinearities. For non-Gaussian inputs, approximations are accurate to at least the second-order [9]. In contrast, the linearization approach of the EKF results only in first order accuracy.

3.1 State Space Model

The electro-mechanical coupling model in Equation (1) is transformed into a continuous stochastic equation with deterministic input:

$$\dot{\sigma_c}(t) = -\sigma_c(t) + u_e(t)\sigma_0 + n^p(t) \tag{2}$$

where $\sigma_c(t)$ is the active stress and $n^p(t)$ the additive, zero-mean, white noise ($E[n^p(t)] = 0$; $E[n^p(t)n^p(s)'] = \boldsymbol{Q}_v(t)\delta_{ts}$). The deterministic input, $u_e(t)$, is cardiac TMP, which can be estimated from BSPs [1,2,3] or calculated from a computational model [12]. The Equations (2) has continuous dynamics, thus further temporal discretization is demanded because the sigma points of UKF have to propagate through the electro-mechanical model numerically. A Runge-Kutta method [13] that can automatically and adaptively select the size of time

step is embedded in our implementation to fulfil the discretization implicitly for the sake of reasonable accuracy and numeric stability.

An associated measurement equation, which describes the mapping between external loading and active stress, can be expressed in this form:

$$\boldsymbol{R}(t) = \boldsymbol{H}\boldsymbol{\Sigma} + n^o(t) \tag{3}$$

where $\boldsymbol{R}(t)$ external loading, $\boldsymbol{H}$ the measurement matrix and $\boldsymbol{\Sigma}$ active stress vector. $n^o(t)$ is the measurement noise which is additive, zero mean, and white $(E[n^o(t)] = 0; E[n^o(t)n^o(s)'] = \boldsymbol{Q}_n(t)\delta_{ts})$, independent of $n^p(t)$. The main component of external loading, active force, is always considered as body force, which is the only force inside myocardium. This is closed to reality since other forces, such as blood pressures and fixed boundaries, always exist in the cardiac surface. Hence $\boldsymbol{R}(t)$ could be modelled as a noisy active force loading inside myocardium. The active force can be calculated from active stress [7,8]:

$$\begin{aligned}\boldsymbol{R} &= \int_V div(\sigma_c \boldsymbol{f}_{fiber} \otimes \boldsymbol{f} fiber) dV \\ &= \int_V \begin{bmatrix} \frac{d(\sigma_c f_x f_x)}{dx} + \frac{d(\sigma_c f_x f_y)}{dy} + \frac{d(\sigma_c f_x f_z)}{dz} \\ \frac{d(\sigma_c f_y f_x)}{dx} + \frac{d(\sigma_c f_y f_y)}{dy} + \frac{d(\sigma_c f_z f_z)}{dz} \\ \frac{d(\sigma_c f_z f_x)}{dx} + \frac{d(\sigma_c f_z f_y)}{dy} + \frac{d(\sigma_c f_z f_z)}{dz} \end{bmatrix} dV\end{aligned} \tag{4}$$

with $\boldsymbol{f}_{fiber} = [f_x, f_y, f_y]^T$ a fiber vector, V volume of the heart and σ_c active stress.

After discretizing Equation (4), the meshfree shape function is applied here again to construct the $\boldsymbol{H}$ in Equation (3):

$$\boldsymbol{R} = \int_V div(\sigma_c \boldsymbol{f}_{fiber} \otimes \boldsymbol{f}_{fiber}) dv = C_R(\int \Phi_R^T B_R dV) A_R \boldsymbol{\Sigma} = \boldsymbol{H}\boldsymbol{\Sigma} \tag{5}$$

The state vector $\boldsymbol{\Sigma}$ is built from the active stress:

$$\boldsymbol{\Sigma} = \begin{bmatrix} \sigma_{c1} \cdots \sigma_{cn} \end{bmatrix}^T \tag{6}$$

where $\sigma_{ci}, i = 1, \ldots, n$ is the active stress in the each sample node.

C_R is used to remove effect of boundary nodes in measurement vector and constructed in a very simple way by deleting corresponding rows according the index of boundary nodes. We also can get:

$$A_R = \begin{bmatrix} 1\,1\,1\,0\,0\,0\,0\,0\,0 \cdots 0\,0\,0\,0\,0\,0\,0\,0\,0 \\ 0\,0\,0\,1\,1\,1\,0\,0\,0 \cdots 0\,0\,0\,0\,0\,0\,0\,0\,0 \\ 0\,0\,0\,0\,0\,0\,1\,1\,1 \cdots 0\,0\,0\,0\,0\,0\,0\,0\,0 \\ \vdots\,\vdots\,\vdots\,\vdots\,\vdots\,\vdots\,\vdots\,\vdots\,\vdots \ddots \vdots\,\vdots\,\vdots\,\vdots\,\vdots\,\vdots\,\vdots\,\vdots\,\vdots \\ 0\,0\,0\,0\,0\,0\,0\,0\,0 \cdots 1\,1\,1\,0\,0\,0\,0\,0\,0 \\ 0\,0\,0\,0\,0\,0\,0\,0\,0 \cdots 0\,0\,0\,1\,1\,1\,0\,0\,0 \\ 0\,0\,0\,0\,0\,0\,0\,0\,0 \cdots 0\,0\,0\,0\,0\,0\,1\,1\,1 \end{bmatrix} \tag{7}$$

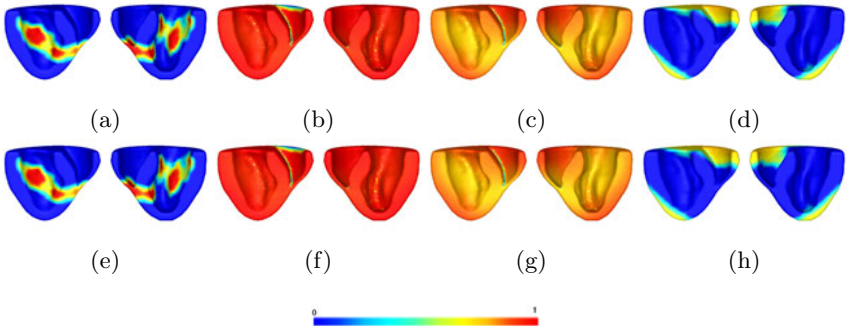

Fig. 2. From (a) to (d) the ground truth of normal propagation in frame 2, 12, 22, 32; From (e) to (h) the estimated results of normal propagation in frame 2, 12, 22, 32; The color bar is scale mapping of transmembrane potentials

$$\Phi_R = \begin{bmatrix} \phi_1 & 0 & 0 & \cdots & \phi_n & 0 & 0 \\ 0 & \phi_1 & 0 & \cdots & 0 & \phi_n & 0 \\ 0 & 0 & \phi_1 & \cdots & 0 & 0 & \phi_n \end{bmatrix}; B_R = \begin{bmatrix} b_{1,1} & 0 & 0 & \cdots & b_{n,1} & 0 & 0 \\ 0 & b_{1,2} & 0 & \cdots & 0 & b_{n,2} & 0 \\ 0 & 0 & b_{1,3} & \cdots & 0 & 0 & b_{n,3} \end{bmatrix} \quad (8)$$

$$b_{i,1} = \phi_{i,x} f_x f_x + \phi_{i,y} f_x f_y + \phi_{i,z} f_x f_z + \phi_i \left(\frac{d(f_x f_x)}{dx} + \frac{d(f_x f_y)}{dy} + \frac{d(f_x f_z)}{dz}\right)$$

$$b_{i,2} = \phi_{i,x} f_y f_x + \phi_{i,y} f_y f_y + \phi_{i,z} f_y f_z + \phi_i \left(\frac{d(f_y f_x)}{dx} + \frac{d(f_y f_y)}{dy} + \frac{d(f_y f_z)}{dz}\right)$$

$$b_{i,3} = \phi_{i,x} f_z f_x + \phi_{i,y} f_z f_y + \phi_{i,z} f_z f_z + \phi_i \left(\frac{d(f_z f_x)}{dx} + \frac{d(f_z f_y)}{dy} + \frac{d(f_z f_z)}{dz}\right)$$

where ϕ_i meshfree shape functions, $\phi_{i,x}$, $\phi_{i,y}$ and $\phi_{i,z}$ the derivatives of the meshfree shape function with respect to x, y and z, and B_R the differential matrix. A_R is used to extend the 1D active stress vector into 3D space vector. Φ_R and B_R are transferred matrices, which build a mapping between active stress and external loading.

3.2 Measurements

Another major challenge in our approach is how to obtain meaningful measurements, $\boldsymbol{R}(t)$, from noisy image data. Assuming the cardiac motion field has been estimated from medical image sequences (quite a lot works in medical image community could accomplish [7,8,14,15]), and the material property of heart is *a prior* knowledge, we can calculate $\boldsymbol{R}(t)$ through the law of force equilibrium [16]:

$$\boldsymbol{M}_m \ddot{\boldsymbol{U}}_m(t) + \boldsymbol{C}_m \dot{\boldsymbol{U}}_m(t) + \boldsymbol{K}_m \boldsymbol{U}_m(t) = \boldsymbol{R}(t) \quad (9)$$

with $\boldsymbol{M}_m$, $\boldsymbol{C}_m$ and $\boldsymbol{K}_m$ the mass, damping and stiffness matrices where $\boldsymbol{R}$ the load vector, and $\boldsymbol{U}_m$ the displacement vector. $\boldsymbol{M}_m$ is a known function of

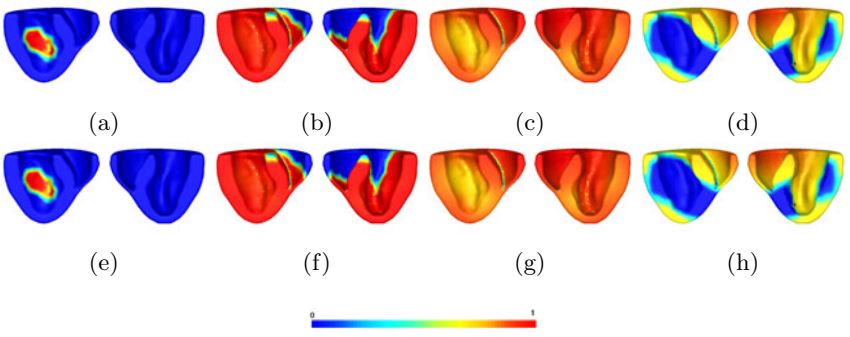

Fig. 3. From (a) to (d) the ground truth of RBBB propagation in frame 2, 12, 22, 32; From (e) to (h) the estimated results of RBBB propagation in frame 2, 12, 22, 32; The color bar is scale mapping of transmembrane potentials

material density and is assumed temporally constant for incompressible material. $\boldsymbol{K}_m$ is a function of material constitutive law, and is related to the Young's modulus and Poisson's ratio which are again assumed constant. $\boldsymbol{C}_m$ is frequency dependent, and Rayleigh damping with $\boldsymbol{C}_m = \alpha \boldsymbol{M}_m + \beta \boldsymbol{K}_m$ is assumed here [16]. However, there is not information of the external loadings in the boundary, which means that they could contain potentially larger error. Those poential error resulted from unknown boundary conditions will increase unknown factors into our UKF framework, so the effect of the boundary nodes are removed from measurement vector in our current approach, which is accomplished by C_R in section 3.1.

4 Experiments

Our approach is first tested under two different cardiac conditions: normal case and right bundle branch block (RBBB)[2]. In each case with 2081 sample nodes, 40 frames are generated respectively, and used as the ground truth. Then noisy external loadings are generated in this way: A) calculate the active stress from cardiac TMP using Equation (1); B) calculate the external loading using Equation (4); C) add $10dB$ gaussian noise into the external loading, $\boldsymbol{R}$. As we discussed above, the external loading in the boundary nodes are corrupted by the other forces. Therefore, we remove those boundary nodes from measurement vector in both cases. After two kinds of noisy measurements are ready, they are put into our model-based filter frame by frame. The initial covariance matrix are set to large enough to guarantee fast convergence. Estimated results in both cases are compared to the ground truths in Fig. 2(normal case) and Fig. 3 (RBBB case) respectively.

[2] RBBB is the right bundle branch of cardiac conduction system no longer conducts electricity. Therefore, as the electrical impulse leaves the His bundle, it enters left bundle branch only, and is carried to the left ventricle.

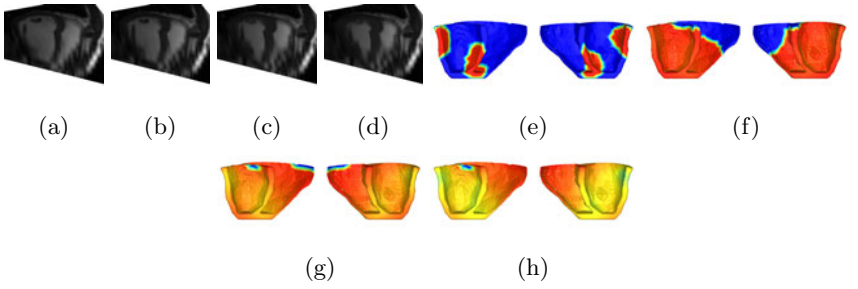

Fig. 4. From (a) to (d), MR image sequence of a normal human heart during systole (frame 1, 3, 5 and 6); From (e) to (h) the estimated propagation results of human data (frame 1, 3, 5 and 6, again); The color bar is scale mapping of transmembrane potentials

One experiment on a cardiac MR image sequence of normal human has been conducted to show the practical potentials of our framework. The image sequence contains 20 frames of a cardiac cycle. Each 3D image frame contains 8 image slices (Fig. 4), with 10mm inter-slice spacing, in-plane resolution of 1.56mm/pixel, and temporal resolution of 43ms/frame. The initial geometry of the heart is obtained by segmentation of the first image frame, and fibers are mapped from the fiber architecture of the Auckland heart model. Since the BSPs are not available yet, simulation of cardiac TMP propagation in this human geometry is currently applied as deterministic input to our framework again. The external loading is calculated using image-derived motion field, which has been described in section 3.2. Experiment is conducted in the first 7 frames using our framework, and the results are shown in Fig. 4. Further experiments on diseased human and animal hearts are ongoing for further verifications.

5 Discussion

In this work, cardiac electrical activity is estimated through a recursive model-based filter from image data. It is first done in our approach to adopt the electro-mechanical coupling model to recover patient-specific cardiac electrical activity from medical image data. The available higher resolution image data and more powerful motion tracking algorithm will be able to provide much better input data for us, and help to understand cardiac electrical activity from a different way. However, the inverse approach from the medical image data to cardiac TMP is still very difficult due to complicated coupling process between cardiac electrical activities and cardiac mechanical behaviors, which introduce great difficulties in establishing the inverse approach and running computation. Therefore, a model with more physiological meanings should be sought to guide the recovery work more efficiently. However, the computational load resulted from adopting complicated model into UFK is still quite heavy (large state vector and large covariance matrix). Hence, a sub-optimal algorithm, which can achieve similar accuracy in a fast convergence speed, should be considered in the future

works. Furthermore, real BSPs should be applied to provide better input into our framework.

References

1. MacLeod, R., Brooks, D.: Recent progress in inverse problems in electrocardiology. IEEE Eng. Med. Biol. Mag. 17(1), 73–83 (1998)
2. Wang, L.W., Zhang, H.Y., Shi, P.C., Liu, H.F.: Imaging of 3D cardiac electrical activity: A model-based recovery framework. In: Larsen, R., Nielsen, M., Sporring, J. (eds.) MICCAI 2006. LNCS, vol. 4190, pp. 792–799. Springer, Heidelberg (2006)
3. Liu, Z., Liu, C., He, B.: Noninvasive reconstruction of three-dimensional ventricular activation sequence from the inverse solution of distributed equivalent current density. IEEE Trans. Med. Img. 25(10), 1307–1318 (2006)
4. Wang, L., Zhang, H., Wong, K., Liu, H., Shi, P.: Noninvasive volumetric imaging of cardiac electrophysiology. In: CVPR, pp. 2176–2183 (2009)
5. Sanchez-Ortiz, G., Sermesant, M., Rhode, K., Chandrashekara, R., Razavi, R., Hill, D., Rueckert, D.: Localization of abnormal conduction pathways for tachyarrhythmia treatment using tagged MRI. In: Duncan, J.S., Gerig, G. (eds.) MICCAI 2005. LNCS, vol. 3749, pp. 425–433. Springer, Heidelberg (2005)
6. Zhang, H.Y., Wong, K.C.L., Shi, P.C.: Estimation of cardiac electrical propagation from medical image sequence. In: Larsen, R., Nielsen, M., Sporring, J. (eds.) MICCAI 2006. LNCS, vol. 4191, pp. 528–535. Springer, Heidelberg (2006)
7. Sermesant, M., Delingette, H., Ayache, N.: An electromechanical model of the heart for image analysis and simulation. IEEE Trans. Med. Img. 25(5), 612–625 (2006)
8. Wong, K.C.L., Wang, L.W., Zhang, H.Y., Shi, P.C.: Integrating functional and structural images for simultaneous cardiac segmentation and deformation recovery. In: Ayache, N., Ourselin, S., Maeder, A. (eds.) MICCAI 2007, Part I. LNCS, vol. 4791, pp. 270–277. Springer, Heidelberg (2007)
9. Julier, S.J., Uhlmann, J.K.: Unscented filtering and nonlinear estimation. Proc. of the IEEE 92(3), 401–422 (2004)
10. Belystchkoand, T., Lu, Y., Gu, L.: Element-free Galerkin methods. Int. J. Numer. Methods. Engrg. 37(2), 229–256 (1994)
11. Glad, T., Ljung, L.: Control Theory. Taylor & Francis, London (1977)
12. Rogers, J., McCulloch, A.: A collation-Galerkin finite element model of cardiac action potential propagation. IEEE Trans. Biomed. Eng. 41(8), 743–756 (1994)
13. Press, W.H.: Numerical Recipes in C: the Art of Scientific Computing. Cambridge University Press, Cambridge (1988)
14. Frangl, A., Rueckert, D., Duncan, J.: Three-dimensional cardiovascular image analysis. IEEE Transctions on Medical Imaging 21(9), 1005–1010 (2002)
15. Chandrashekara, R., Mohiaddin, R., Rueckert, D.: Analysis of 3D myocardial motion in tagged MR images using nonrigid image registration. IEEE Trans. Med. Img. 23(10), 1245–1250 (2004)
16. Bathe, K.: Finite Element Procedures. Prentice Hall, Englewood Cliffs (1996)

Non-invasive Activation Times Estimation Using 3D Echocardiography

Adityo Prakosa[1], Maxime Sermesant[1], Hervé Delingette[1], Eric Saloux[2], Pascal Allain[3], Pascal Cathier[3], Patrick Etyngier[3], Nicolas Villain[3], and Nicholas Ayache[1]

[1] Asclepios Research Project, INRIA Sophia-Antipolis, France
[2] Service de Cardiologie CHU Caen, France
[3] Medisys, Philips Healthcare Suresnes, France

Abstract. Despite advances in both medical image analysis and intracardiac electrophysiological mapping technology, the understanding of cardiac mechano-electrical coupling is still incomplete. This knowledge is of high interest since it would help estimating the cardiac electrophysiology function from the analysis of widely available cardiac images, such as 3D echocardiography. This is important, for example, in the evaluation of the cardiac resynchronization therapy (CRT) where the placement and tuning of the pacemaker leads plays a crucial role in the outcome of the therapy. This paper proposes a method to estimate activation times of myocardium using a cardiac electromechanical model. We use Kernel Ridge Regression to find the relationship between the kinematic descriptors (strain and displacement) and the contraction force caused by the action potential propagation. This regression model is then applied to two 3D echocardiographic sequences from a patient, one in sinus rhythm and the other one with left ventricle pacing, for which strains and displacements have been estimated using incompressible diffeomorphic demons for non-rigid registration.

Keywords: cardiac electrical mapping, Kernel Ridge Regression, 3D echocardiography.

1 Introduction

The wide availability of cardiac imaging modalities especially 3D echocardiography allows clinicians to estimate some geometrical characteristics of the myocardium motion such as displacement, strain or strain rate. However, these quantities are only related to the kinematics of the heart whereas in many cases it is important to also obtain information about the patient's cardiac electrical propagation. Indeed contact or non-contact intracardiac electrical mappings are invasive procedures which are not classically used for diagnosis but rather for applying a therapy. Electrocardiographic imaging[1] (*a.k.a.* body surface potential mapping) is a non-invasive technique for imaging activation times of the myocardium but still remains to be validated thoroughly and is not widely available in clinical centers. Therefore there is a strong need to quantitatively assess a

O. Camara et al. (Eds.): STACOM-CESC 2010, LNCS 6364, pp. 212–221, 2010.

patient electrophysiological condition from non-invasive imaging modalities such as 3D echocardiography. This is especially valid in the context of cardiac resynchronization therapy (CRT) for which up to 30% of the patients with pacemaker leads show no benefit[2]. Providing activation maps from a 3D echocardiography for instance, would be of great interest to select patients responding to the therapy and to optimize the lead placements and delays during and after therapy. More fundamentally, understanding the relationship between cardiac mechanics and electrophysiology is essential to improve the diagnosis and therapy of patients suffering from heart failure.

A study on the relation between cardiac magnetic resonance (MR) motion tracking and the electrical activation pattern has been published by Sanchez-Ortiz *et al.*[3] which combines some cardiac motion descriptors in order to obtain the electrical activation time. However, in this study, the weights were assigned manually to get an estimation of the activation. McVeigh *et al.*[4] also consider only the circumferential strain estimated from tagged MR images as the mechanical activation measure. Very high frame rate ultrasound in electromechanical imaging (EWI), which could map the electromechanical wave (EMW) correlated with cardiac electrical activation in 2D echocardiography, has been published by Provost *et al.*[5]. However, understanding the 3D cardiac electrical propagation is still very important for clinicians.

In this paper, our main objective is to find a relationship between the different kinematic parameters obtained from cardiac image analysis and the activation times of the myocardium using a machine learning method. The activation times are defined as moments at which the activation forces at a given point sharply increase. Activation times are strongly correlated with the action potential signal through the mechano-electrical coupling.

The training stage is based on motion and contraction forces estimated from an electromechanical model of the heart. This *in silico* cardiac model serves as a reference model in the absence of reliable intracardiac mapping information. Several pathologies and pacing scenarios are considered in this training phase. Based on this learning process, we can predict the cardiac electrical propagation from kinematic parameters estimated from cardiac image analysis. This approach has been evaluated on synthetic cases as well as on one patient. The results are thoroughly discussed and perspectives of this work are provided in a final section.

2 3D Echocardiography Image Registration and Motion Estimation

We use 3D echocardiography images provided by the University Hospital of Caen, Normandy - France. This data was acquired from patients under CRT with two implanted electrodes, one in the left ventricle and the other in the right ventricle. Two different pacemaker stimulation modes were imaged and analysed. The first mode corresponds to the sinus rhythm mode when no pacemaker lead is activated. In the second mode, the left ventricle is stimulated. Left ventricle segmentation along whole cardiac sequence was provided by the Medisys Group

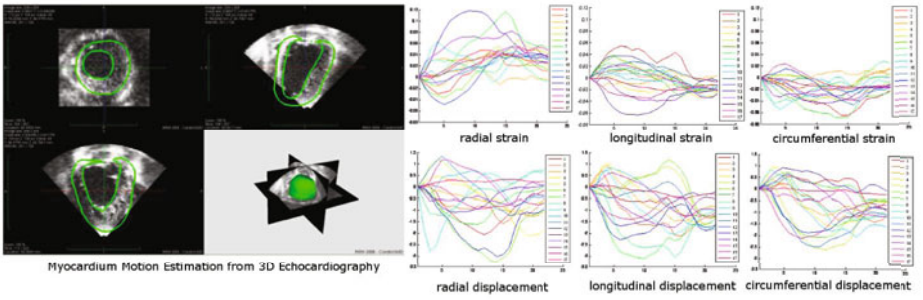

Fig. 1. 3D echocardiography myocardium motion estimation. Myocardium motion is tracked and then strains and displacements with respect to the first reference image in the cardiac cycle are computed and projected in a local frame representing the radial, longitudinal and circumferential directions. The different colors in the curves show the 17 different AHA zones. The strain and displacement curves shown are from a patient with LBBB and without any pacemaker stimulation. The strain vertical axis is dimensionless while the displacement vertical axis is in millimeters. The horizontal axis shows the image frame number in the cardiac cycle.

of Philips Healthcare, Suresnes - France. The 3D echocardiography sequence begins at the end-diastolic phase of the cardiac cycle.

2.1 Incompressible Diffeomorphic Demons

Cardiac motion is estimated through a non-linear image registration algorithm applied between consecutive frames of the same cardiac cycle. The purpose of applying this non-linear image registration is to find the displacement vector field $\mathbf{u(x)}$ associated with the transformation $\phi(\mathbf{x}) = \mathbf{x} + \mathbf{u(x)}$ which aligns a template image $\mathrm{T}(\mathbf{x})$ to a reference image $\mathrm{R}(\mathbf{x})$, where $\mathbf{x} \in \mathbb{R}^3$ is the space coordinate (voxel (x,y,z)). This displacement vector field $\mathbf{u(x)}$ is considered as the cardiac displacement field. All images in the cardiac sequence are registered to the same reference image which is the first image of the 3D echocardiography sequence, corresponding to the end-diastolic phase.

We take into account the myocardium near-incompressibility assumption (maximum 5 to 7% of volume variation during the cardiac cycle) by relying on the incompressible demons algorithm proposed by Mansi *et al.*[6] to estimate cardiac motion. This algorithm improves the diffeomorphic demons algorithm[7] by adding 2 constraints: the myocardium near-incompressibility and linear elastic regularization of velocity fields. This method has been developed and evaluated for cardiac motion estimation on cine MRI images [6].

A 3D myocardium segmentation for the first frame of the sequence is used as the incompressible region. The 3D echocardiography sequence starts at the end-diastolic phase of a cardiac cycle. All image frames in the 3D echocardiography sequence are being registered to this end-diastolic frame.

The recovered displacement vector field is projected in the radial, circumferential and longitudinal directions using the heart local coordinate system.

2.2 Strain Estimation

The displacement vector field $\mathbf{u(x)}$ which recovers the cardiac motion $\phi(\mathbf{x}) = \mathbf{x}+\mathbf{u(x)}$ is then used to compute the Lagrangian finite strain tensor $E = \frac{1}{2}(\nabla\mathbf{u}+\nabla\mathbf{u}^T+\nabla\mathbf{u}^T\nabla\mathbf{u})$. The strain is calculated by using the end-diastolic frame as the reference image $\mathrm{R}(\mathbf{x})$. Similarly for the displacement vector field, the obtained strain is projected in the radial, circumferential and longitudinal directions (cf. Fig. 1).

3 Inverse Mechano-Electrical Coupling

3.1 Electromechanical Model

In order to learn how the cardiac kinematics are related to the cardiac electrophysiology it is necessary to get for the same patient descriptors of the cardiac motion and electrical wave propagation. This could be provided by 3D echocardiography and intracardiac electrophysiological mapping acquired on the same patient. To merge both information, the patient must be in the same stimulation mode and endocardial surfaces reconstructed from intracardiac mappings must match those segmented in 3D US. However, such joint acquisition was not available in our study. Therefore, we proposed to use an electromechanical model of the heart [8] to simulate patient cases. From those simulated cases, we could obtain both electrophysiological and kinematic measurements. To be realistic, this model uses the cardiac anatomy extracted from echocardiography images as a priori information about the shape of the left ventricle (LV). We simulated four cardiac cases using the electromechanical model to create a training database. First, we simulate the cardiac propagation and contraction in normal sinus rhythm where the electrical simulation is coming from the left and right ventricle endocardium. In the second simulation, we simulate a left bundle branch block (LBBB) where the stimulation is coming only from the right ventricle endocardium while the third simulation is the right bundle branch block (RBBB) case where stimulation is coming only from the left ventricle endocardium. The last case is the bi-ventricular pacing case where we initiate the electrical propagation from a zone in the lateral freewall and a zone in the right ventricle apex in order to simulate the pacemaker bi-ventricular pacing (cf. Fig. 2).

The simulation gives the deformation of the cardiac mesh along with the contraction value and the potential value for each point in the mesh. We perform a thresholding in order to obtain the time at which the contraction value increases. We also compute the displacement vector field which maps the myocardium at a given time point to the end-diastolic image of the sequence. Kinematic descriptors extracted from the obtained displacement vector field are the displacement and the strain projected in the radial, longitudinal and circumferential directions.

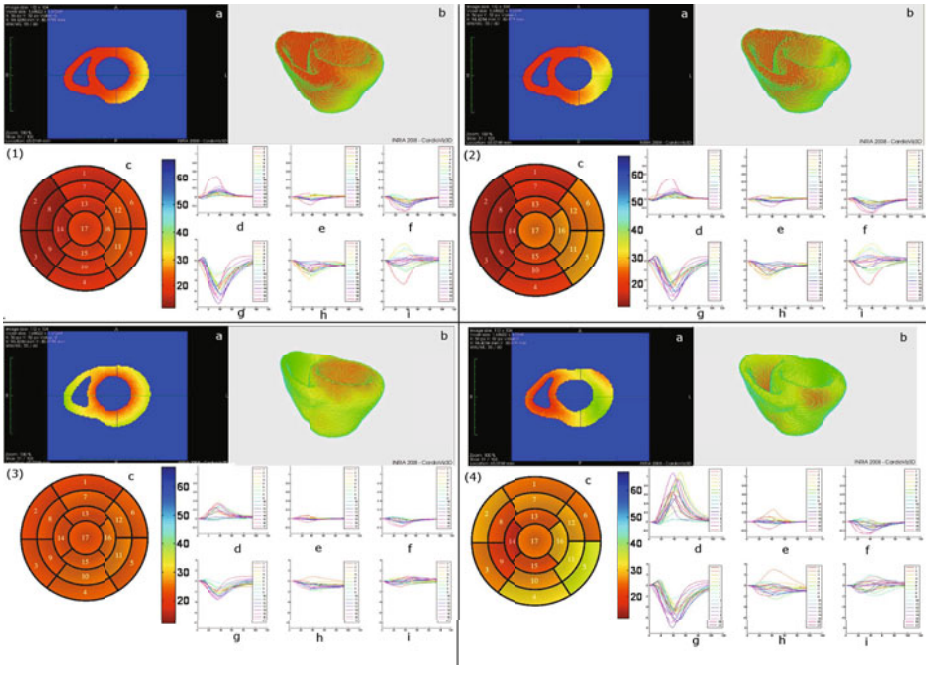

Fig. 2. Electromechanical simulation. 4 cardiac cases simulated using the electromechanical model. (1) normal case, (2) LBBB case, (3) RBBB case and (4) biventricular pacing case. (a), (b) and (c) are the contraction force isochrone. (c) is the isochrone for the LV divided to 17 AHA zones. (d), (e), (f) are the radial, longitudinal and circumferential strains respectively and (g), (h), (i) are the radial, longitudinal and circumferential displacements. Axis units are as explained in Fig. 1. These strains and displacements are extracted from the deformation of the mesh simulated by the electromechanical model.

3.2 Kernel Ridge Regression as a Learning Method

Using an electromechanical model of the heart, we learn the relationship between the kinematic descriptors and the electrical activation. We use Kernel Ridge Regression to find a relationship between these 2 quantities.

Ridge Regression searches a linear function $\mathbf{y} = \mathbf{w}^T\mathbf{x}$ that models the dependencies between the descriptor vectors $\mathbf{x}_i \in \mathbb{R}^d$ and the response vectors $\mathbf{y}_i \in \mathbb{R}^r$ (all vectors are column vectors) from a set of T examples $(\mathbf{x}_1, \mathbf{y}_1), (\mathbf{x}_2, \mathbf{y}_2), ..., (\mathbf{x}_T, \mathbf{y}_T)$. Classically, we need to minimize the quadratic cost $C(\mathbf{w}) = \frac{1}{2}\sum_i^T (\mathbf{y}_i - \mathbf{w}^T\mathbf{x}_i)^2$, where $\mathbf{w}$ is a $d \times r$ matrix. Regularizing this equation, the total cost function which needs to be minimized hence becomes $C(\mathbf{w}) = \frac{1}{2}\sum_i^T (\mathbf{y}_i - \mathbf{w}^T\mathbf{x}_i)^2 + \frac{1}{2}\lambda \|\mathbf{w}\|^2$, where $\lambda > 0$ is the regularization parameter. Introducing a $T \times d$ matrix $X = (\mathbf{x}_1, \mathbf{x}_2, ..., \mathbf{x}_T)^T$ which contains the vectors $\mathbf{x}_i$ in its row and a $T \times r$ matrix $Y = (y_1, y_2, ..., y_T)^T$ which contains the vectors $\mathbf{y}_i$ in its row, the equation can be written as $C(\mathbf{w}) = \frac{1}{2}\|Y - X\mathbf{w}\|^2 + \frac{1}{2}\lambda\|\mathbf{w}\|^2$.

Minimizing this function by taking its derivative with respect to $\mathbf{w}$ and setting it equal to zero gives $-X^TY + X^TX\mathbf{w} + \lambda\mathbf{w} = 0 \Rightarrow \mathbf{w} = \left(\lambda\mathbf{I} + X^TX\right)^{-1} X^TY$.

Ridge Regression can be extended to Kernel Ridge Regression by rewriting the solution $\mathbf{y} = \mathbf{w}^T\mathbf{x} = \left(\left(\lambda\mathbf{I} + X^TX\right)^{-1} X^TY\right)^T \mathbf{x} = Y^T\left(\lambda\mathbf{I} + XX^T\right)^{-1} X\mathbf{x} = Y^T\left(\lambda\mathbf{I} + K\right)^{-1}\mathbf{k}$ with $K = XX^T$ and $\mathbf{k} = X\mathbf{x}$. We choose to use Radial Basis Function as a Kernel function $K(x_i, x_j) = e^{-\frac{|x_i - x_j|}{\sigma^2}}$ with $i, j = \{1, ..., T\}$.

Parameter Optimization. The chosen λ and σ parameters are optimized by using leave-one-out estimates which train the model with all members of the training set but one and test the performance on the singleton. The process is repeated for all the singletons in the training set. We use Allen's PRESS (predicted residual sum of squares) statistic for this process, $PRESS = \sum_i^T \mathbf{e}_{(i)}^2$ [9], where $\mathbf{e}_{(i)} = \mathbf{y}_i - \hat{\mathbf{y}}_{(i)}$ is the residual for the ith example with the ith example excluded from the training process and $\hat{\mathbf{y}}_{(i)}$ is the predicted response for the ith example based on the training process. Fortunately, we have $e_{(i)} = \frac{e_i}{1-h_{ii}}$ where $e_i = \mathbf{y}_i - \hat{\mathbf{y}}_i$ is the residual for the ith example in the training process which includes all examples and $\hat{\mathbf{y}}_i$ is the fitted response based on this training. h_{ii} is the ith element of the leading diagonal of the hat matrix $H = X(\lambda\mathbf{I} + X^TX)^{-1}X^T = XX^T(\lambda\mathbf{I} + XX^T) = K(\lambda\mathbf{I} + K)^{-1}$. Therefore, in the end, we can have the PRESS for the chosen parameters λ and σ in one iteration. We use the downhill simplex search method in MATLAB in order to optimize these parameters to have the smallest PRESS.

With this approach, we learn a non-linear relationship (due to the choice of Radial Basis Function as the Kernel function) between the kinematic descriptors and the activation force caused by the action potential. We take the radial, longitudinal and circumferential strains ($\mathbf{E}_r, \mathbf{E}_l, \mathbf{E}_c \in \mathbb{R}^{t_d}$) and also the radial, longitudinal and circumferential displacements ($\mathbf{u}_r, \mathbf{u}_l, \mathbf{u}_c \in \mathbb{R}^{t_d}$) from points in the myocardium as the components of the kinematic descriptor vector $\mathbf{x}_i \in \mathbb{R}^{d=6\times t_d}$, where t_d is the number of each descriptor sampling time in a cardiac sequence. The contraction force along a cardiac cycle t_r is set as the response vector $\mathbf{y}_i \in \mathbb{R}^{r=t_r}$. The descriptor sampling time t_d is taken for 20 time instances in order to follow the temporal resolution of the real patient data. However, the response vector sampling time t_r is chosen as 100 time instances in order to have high temporal resolution of the contraction force along a cardiac cycle, starting before the beginning of the P wave of the ECG. The examples in the training set consist of the different points in the myocardium. We take 30 points from each of the American Heart Association (AHA) 17 zones so we have 510 learning points along a cardiac cycle. We separate the value σ for the displacement and the strain used in the Kernel $K(x_i, x_j) = e^{-\frac{|u_i - u_j|}{\sigma_u^2} - \frac{|E_i - E_j|}{\sigma_E^2}}$. Once the learning process is done, we obtain the optimal values for λ, σ_u and σ_E. We use these parameters to predict the other points in the myocardium in order to obtain the cardiac contraction force mapping caused by the potential.

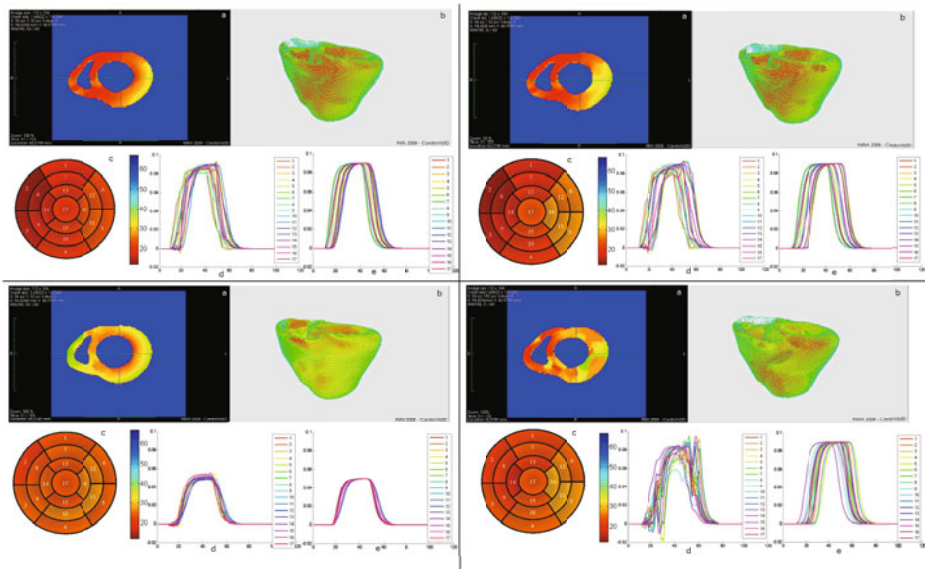

Fig. 3. Prediction of contraction forces from synthetic data. (a), (b) are the whole contraction force isochrones (activation times) obtained after applying the learning method on the whole points in the myocardium for case (1) (sinus rhythm), (2) (LBBB), (3) (RBBB) and (4) (bi-ventricular pacing) whereas (c) is the whole contraction force isochrone only for the left ventricle. (d) is the contraction force curve along a cardiac cycle which predicted by the learning method whereas (e) is the ground truth contraction force curve as produced by the electromechanical model. The vertical axis unit is in MPa. The horizontal axis shows the frame number in the cardiac cycle.

4 Results

4.1 Evaluation on Simulated Data

First, we tested our machine learning method using the simulated motion from the electromechanical model for which we have a ground truth to compare to. The first 3 cases which have been described in section 3.1 are included in our training set, whereas the fourth case has not been included. The optimal parameters of the regression have been found as $\lambda = 0.0004$, $\sigma_u = 107.1030$ and $\sigma_E = 9.0276$ which yield the root mean squared error (RMSE) value between the predicted and the ground truth value 0.0016 MPa. This seems to imply that strains are more correlated with activation times than displacements since their variances are smaller (for a similar range of values). We applied the regression method to all points of the first, second and third cases producing quite smooth predicted contraction force curves (see Fig. 3). Note that the training stage only included a very small subset of those points thus showing that the kernel ridge regression is able to generalize the correlations between strains and forces to the whole myocardium.

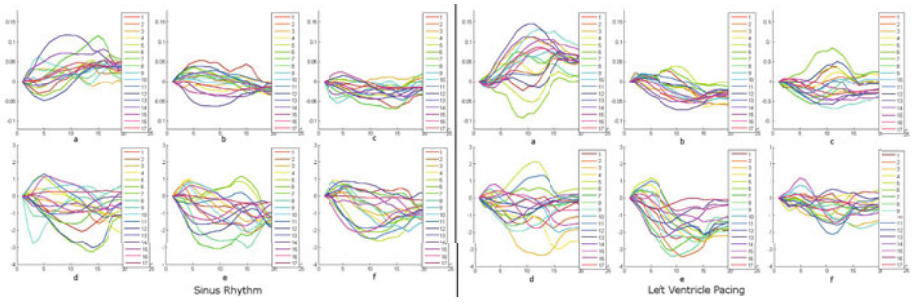

Fig. 4. Kinematic descriptors extracted from patient's 3D echocardiography. (a) (b) and (c) are the radial, circumferential and longitudinal strains whereas (d), (e) and (f) are the radial, circumferential and longitudinal displacements. Axis units are as explained in Fig. 1.

In the fourth case, the predicted force values are not as smooth as expected. However the predicted and the ground truth value of the fourth case have the same global bell shape where up and down slopes can be detected using thresholding. The bull's eyes plot computed from the estimated activation times also correspond to their expected value. In the second case (LBBB) we clearly have an early activation from the septal wall whereas in the third case (RBBB) the early activation originated from the endocardial wall of the left ventricle. In the fourth case (bi-ventricular pacing), not included in the training set, the delays between right and left ventricles are slightly decreased. The left ventricle RMSE value between the predicted and the ground truth activation time is 7 ms for the first 3 cases and 37 ms for the fourth case.

4.2 Application to Clinical Data

From the time series of 3D echocardiography images, we segmented the myocardium and then estimated the cardiac motion using the incompressible demons algorithm. The myocardium segmentation is used to specify the region where the incompressibility constraint must be satisfied. From the knowledge of the left ventricle axis, we can define the 3 local directions and then project strain tensors and displacements along those three directions (cf. Fig. 4). These values are then used as input descriptors in the regression method.

5 Discussion

The estimation of contraction forces for each AHA segment and for the two simulation modes are shown in Fig. 5. The estimated curves of contraction forces are noisy as in the case of simulated data but also no longer have a bell shape. In particular, those curves have negative parts at the beginning of systole whereas

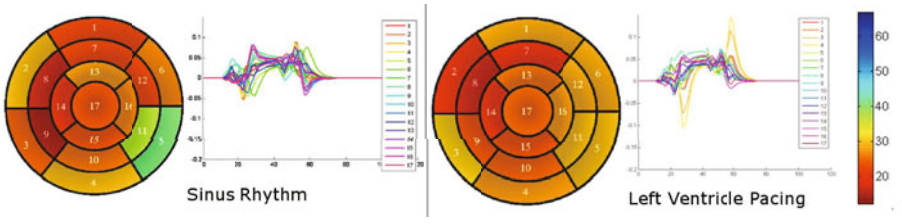

Fig. 5. Patient contraction force prediction. Predicted contraction force time and activation time isochrone (bull's eyes) for two different pacemaker stimulation mode from the same patient. Axis units are as explained in Fig. 3.

they have been trained to be positive. Those curves have been thresholded (value chosen as 0.03) to obtain two bull's eyes plot of activation times for the sinus rhythm and left ventricular pacing. It should be noticed that the late activation in green on the lateral wall of the left ventricle at sinus rhythm has been activated much earlier after pacing in the left ventricle which is expected.

From the preliminary results obtained on one patient with 2 stimulation modes, the estimation of activation times seems to correspond to the expected values. However, the shape and negative values of the estimated contraction forces indicate that the regression model does not capture well the observations. This may originate from several factors. First of all, there may be a difference of patterns between the simulated strains and displacement and the ones estimated by the non-linear registration. Second, there is a slight error when choosing the reference end diastolic image which produces significant errors in the estimation of strains. One could cope with those errors by having several regression methods corresponding to several choices of reference images. Finally, it should be noted that the electromechanical model involved for training the method used the anatomy of the left ventricle of the patient (see section 3.1) on which it was evaluated. Further evaluation on more patient images should indicate whether the learning method is sensitive to the patient anatomy.

6 Conclusion

We presented in this paper a method to estimate contraction forces and activation times from echocardiographic images. A supervised learning method has been proposed which relies on synthetic measurements from an electromechanical model of the heart for the training stage. The method has been evaluated on synthetic data and a patient case. Further work will test the proposed method on a larger sets of patients with various stimulation protocols. Sensitivity of our approach to the estimation of strains and the choice of the reference image will be studied. Learning from intracardiac electrophysiological mapping and 3D echocardiography of the same patient should improve the result and will be done as soon as the data is acquired.

References

1. Ghanem, R.N., Jia, P., Ramanathan, C., Ryu, K., Markowitz, A., Rudy, Y.: Noninvasive electrocardiographic imaging (ECGI): comparison to intraoperative mapping in patients. Heart Rhythm 2, 339–354 (2005)
2. Helm, R.H., Byrne, M., Helm, P.A., Daya, S.K., Osman, N.F., Tunin, R., Halperin, H.R., Berger, R.D., Kass, D.A., Lardo, A.C.: Three-dimensional mapping of optimal left ventricular pacing site for cardiac resynchronization. Circulation 115, 953–961 (2007)
3. Sanchez-Ortiz, G., Sermesant, M., Chandrashekara, R., Rhode, K., Razavi, R., Hill, D., Rueckert, D.: Detecting the onset of myocardial contraction for establishing inverse electro-mechanical coupling in xmr guided rf ablation. In: Proceedings of IEEE International Symposium on Biomedical Imaging, Arlington, USA, pp. 1055–1058 (2004)
4. McVeigh, E.R., Prinzen, F.W., Wyman, B.T., Tsitlik, J.E., Halperin, H.R., Hunter, W.C.: Imaging asynchronous mechanical activation of the paced heart with tagged MRI. Magn. Reson. Med. 39, 507–513 (1998)
5. Provost, J., Lee, W.N., Fujikura, K., Konofagou, E.E.: Electromechanical wave imaging of normal and ischemic hearts in vivo. IEEE Trans. Med. Imaging 29, 625–635 (2010)
6. Mansi, T., Peyrat, J.M., Sermesant, M., Delingette, H., Blanc, J., Boudjemline, Y., Ayache, N.: Physically-constrained diffeomorphic demons for the estimation of 3d myocardium strain from cine-MRI. In: Ayache, N., Delingette, H., Sermesant, M. (eds.) FIMH 2009. LNCS, vol. 5528, pp. 201–210. Springer, Heidelberg (2009)
7. Vercauteren, T., Pennec, X., Perchant, A., Ayache, N.: Non-parametric diffeomorphic image registration with the demons algorithm. In: Ayache, N., Ourselin, S., Maeder, A.J. (eds.) MICCAI 2007, Part II. LNCS, vol. 4792, pp. 319–326. Springer, Heidelberg (2007); PMID: 18044584
8. Sermesant, M., Moireau, P., Camara, O., Sainte-Marie, J., Andriantsimiavona, R., Cimrman, R., Hill, D.L., Chapelle, D., Razavi, R.: Cardiac function estimation from MRI using a heart model and data assimilation: Advances and difficulties. Medical Image Analysis 10(4), 642–656 (2006)
9. Cawley, G.C., Talbot, N.L.C.: Fast exact leave-one-out cross-validation of sparse least-squares support vector machines. Neural Networks 17(10), 1467–1475 (2004)

Modeling Drug Effects on Personalized 3D Models of the Heart: A Simulation Study

Rafael Sebastian[1,⋆], Elvio Heidenreich[2], Lydia Dux-Santoy[3], Jose F. Rodriguez[4], Jose Maria Ferrero[3], and Javier Saiz[3]

[1] Department of Computer Science, Universitat de Valencia, Valencia, Spain
[2] Instituto de Investigaciones Cientificas y Tecnicas para la Defensa, Buenos Aires, Argentina
[3] Grupo de Bioelectronica (GBIO), I3BH, Universitat Politecnica de Valencia, Valencia, Spain
[4] Grupo de Estructuras y Modelado de Materiales (GEMM),Universidad de Zaragoza, Zaragoza, Spain

Abstract. The use of anti-arrhythmic drugs is common to treat heart rhythm disorders. Computational modeling and simulation are powerful tools that can be used to investigate the effects of specific drugs on cardiac electrophysiology. In this work a patient-specific anatomical heart model is built to study the effects of dofetilide, a drug that affects IKr current in cardiac cells. We study the multi-scale effects of the drug, from cellular to organ level, by simulating electrical propagation on tissue coupled cellular ion kinetics for several heart beats. Different cell populations configurations namely endocardial, midmyocardial and epicardial are used to test the effect of tissue heterogeneity. Results confirmed the expected effects of dofetilide at cellular level, increasing the action potential duration. Pseudo-ECGs obtained for each heart beat correlated well with cellular results showing prolongation of QT segment. These techniques can be applied over the development of more complex drugs that affect multiple cellular currents.

Keywords: Cardiac electrophysiology, multi-scale modeling, simulation, drug modeling, therapy planning, drug cardio-toxicity.

1 Introduction

The use of anti-arrhythmic drugs is common to treat heart rhythm disorders. Compounds of those drugs are known to interact with cell ionic channels altering their physiological properties, e.g., prolonging action potential duration (APD), which has a global electrophysiological effect at organ level. Prolonged repolarization might be beneficial during ventricular tachycardia because of the subsequent increase in the refractory period, which also prevents the formation of potentially fatal re-entrant circuits. However, the same drugs can induce certain

⋆ rafael.sebastian@uv.es

O. Camara et al. (Eds.): STACOM-CESC 2010, LNCS 6364, pp. 222–231, 2010.

arrhythmias, increasing the risk of mortality under specific conditions[1]. Drug-induced increase of action potential repolarization and QT interval prolongation and its proarrhythmic effect are major concerns for the pharmaceutical industry. The QT interval prolongation is associated with a form of acquired long QT syndrome (LQTS) which can induce a polymorphic ventricular arrhythmia called *Torsades de Pointes* (TdP). There are a number of experimental models (in vivo and in vitro) for assessing the QT prolongation and proarrhythmic potential effects[2,3], but in most cases these are inadequate ECG biomarkers of drug-induced arrhythmias in human.

The repolarization phase in cardiac cells is a complex physiological process which depends on many membrane currents, including potassium and calcium currents. Among them, the rapid component of the delayed rectifier potassium current (I_{Kr}) plays a determinant role. The pore protein of the (I_{Kr}) current (encoded by the human Ether-a-go-go-Related Gene or hERG) is a target for compounds that prolongs ventricular repolarization. I_{Kr} is considered to be the most widely targeted K^+ channel linked to potential arrythmogenesis. Currently, the potential risk of a drug is estimated by testing the ability of the drug to reduce hERG current, and the calculation of the IC_{50} value, i.e. the concentration of the drug that blocks hERG current to 50%, which implies a significant impact on cellular repolarization. Although the IC_{50} can be used as a proxy indicator in the early stages of the drug development, it is not sufficient to clearly predict the proarrhythmic potential of a compound. For some drugs involved in TdP in humans, there is a poor correlation between IC_{50} values obtained using hERG assay and the results obtained using tissue preparations and in clinical routine.

The identification of accurate and robust biomarkers is complex since there are many possible complex scenarios, such as multiple ion channel block exerted by many compounds, different expression between tissues and species of several currents, different electrical activity in isolated cells as opposed to multicellular preparations or the influence of patient risk factors, among others. Due to the multiscale and highly coupled nature of the problem, computer models could bring new insights into the interaction of compounds with multiple ionic channels. Furthermore, computational cardiac electrophysiology is today a mature discipline that allows the study of heart rhythm mechanisms.

The main objective of this paper is to present a computational study of in silico modeling and assessing of specific drug compounds in a realistic 3D human heart. The effect of dofetilide, a specific and potent blocker of the rapid component of the delayed rectifier K^+ current (I_{Kr}), is studied on a personalized 3D human heart model. The geometrical model and its main characteristics such as fiber orientation are extracted from a clinical imaging dataset and included in complete anatomical model. A complex human biophysical model [4] that includes a large number ionic currents is used to simulate the cell ion kinetics and the effects of dofetilide for different concentrations. Electrical propagation on tissue is simulated considering different cell populations, endocardial, M and epicardial and two different heterogeneity configurations for those populations throughout the wall. This is important since ion channel properties varies between cell

populations and might affect the ECG complex. Study of 3D simulations allows us to characterize activation and repolarization dispersion in a large number of locations. Pseudo-ECGs are also calculated to analyze the global effect of the drug and correlate it to cell level results.

2 Material and Methods

2.1 Ventricular Model

A 3D volumetric human heart model was used to study the electrical sequences of activation. The geometry was segmented from a MRI data set acquired at John Hopkins University [5]. The MRI volume stack has a resolution of $0,4297 \times 0,4297 \times 1,0mm^3$ and was segmented by using a simple threshold. From the segmented volume, a regular hexahedral mesh was constructed with a resolution of $0,5 \times 0,5 \times 0,5mm^3$, which gave rise to 1.43 million nodes and 1.29 million hexahedra [6] (Fig.1(a)). In order to improve the numerical accuracy of the model, enriched finite elements with second order bubble functions were used for the simulations. This formulation greatly improves the numerical efficiency of the algorithm while keeping numerical accuracy [6]. The model was labeled to differentiate regions with different electrical properties, and included endocardium, midmyocardium and epicardial regions. The percentage of the wall given to each regions was varied to take into account the effect of the channel heterogeneity.

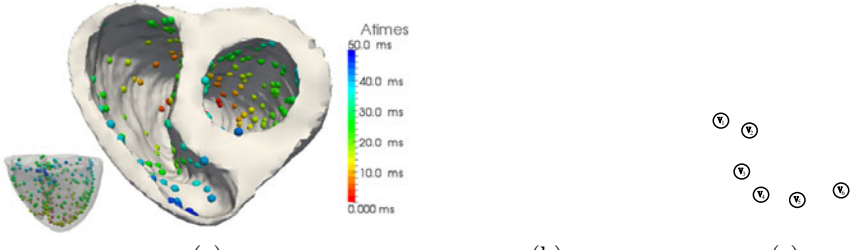

(a) (b) (c)

Fig. 1. Anatomo-functional human heart model built from a DTMRI stack. (a) Right and left ventricles were segmented and meshed with hexahedral elements. Endocardial, midmyocardial and epicardial layers were identified and labeled for each model taking into account different transmural heterogeneity configurations. Stimulation points used to initiate the tissue activation are displayed as small spheres on the endocardium. Color indicates time of activation, which ranged from 0ms to 50ms. (b) the myocardial fiber orientation was obtained from DTMRI [5]. Orientation is represented by small vectors which rotate transmurally from endocardium to epicardium. (c) Ventricular model inserted in a human torso to calculate the approximate location of precordial points V1-V6 for the pseudo-ECG.

Fiber Orientation. The fiber orientation was integrated in the model by using DTMRI (Diffusion Tensor Magnetic Resonance Imaging), which allowed to quantify the anisotropy of the different tissues throughout the ventricular wall [5]. That is a relevant part of heart microstructure since the electrical activation depends on the spatial distribution of fibers. Fiber direction was given by the three eigenvectors associated with eigenvalues of the diffusion tensor. This information was incorporated into the finite element model by defining an averaged fiber direction for element.

The heart was considered transversely isotropic. Transmural variation of the angle in fibers direction ranged from $-60°$ on the epicardial surface to $[+40°, +60°]$ on the endocardium. Fig. 1(b) shows fiber orientation in the epicardial layer of the heart.

Heterogeneity. Several studies have shown that ventricular myocardium is formed by three types of cells: epicardial, midmyocardial and endocardial [7,8,9]. However, it is not clear the real volume percentages of the different types of cells that cannot be differentiated in-vivo. These cells differ in the morphology of the action potential, especially in the spike-and-dome action potentials of midmyocardial and epicardial cells due to the transient outward current, I_{to}. Midmyocardial cells can be distinguished from other types of cells because they have a short and slow delayed rectifier current, I_{ks}, a strong I_{to} current and a relatively large Na-Ca exchange current, I_{NaCa}. These differences result in a longer APD relative to epicardial and endocardial cells ($336ms$ in midmyocardial cells v. $276ms$ and $282ms$ in epicardial and endocardial cells respectively) for BCL=$1000ms$ [10]. We modeled two different heterogeneity cases with the following distributions for each cell population, (1) 0% endocardium, 67.5% midmyocardium and 32.5% epicardium; and (2) 17% endocardium, 41% midmyocardium and 42% epicardium. The scenario with 0 percentage endo was considered in order to compensate for the lack of Purkinje fibers which should elongate the APD of subendocardial cells rendering a more realistic pseudo-ecg from the simulations.

2.2 Electrophysiology Simulation

Cardiac electrophysiology was modeled and simulated with the finite element solver ELVIRA [11]. The ten Tusscher model [10] was chosen to represent ion kinetics at cellular level. This model allowed us to alter specific currents that can be affected by drugs, such as I_{Kr} and still obtain physiological responses for the activation and repolarization of the different cells. Electrical activation throughout the ventricular tissue was simulated using the reaction-diffusion monodomain equation [12,13]. The monodomain equation is formulated as,

$$\nabla \cdot (D \nabla V) = C_m \frac{\partial V}{\partial t} + I_{ion} \tag{1}$$

The ODEs from the ionic model were solved using a forward method with an adaptive time step from $20\mu s$ to $100\mu s$. Using a homogeneous discretization of

$500\mu m$ with enriched finite elements [6] and longitudinal conductivity of 0.0016 cm^2/s and transverse conductivity of 0.0006 cm^2/s. The resulting conduction velocities along the fibers and in the direction perpendicular to the fibers were $0.7m/s$ and $0.4m/s$ respectively.

Drug modeling. The effect of dofetilide was modeled by introducing the factor $(1-b)$ in the I_{Kr} formulation (where b is the fraction of channels blocked by the drug). Thus, the new formulation of the rapid component of the delayed rectifier K^+ current taking into account the effect of dofetilide is:

$$I_{kr}(D) = I_{kr}(1-b) \tag{2}$$

$$\frac{I_{kr}(D)}{I_{kr}} = \frac{1}{1+\frac{[D]}{IC_{50}}} = 1-b \tag{3}$$

with $IC_{50} = 7nmol/l$.

Calculation of pseudo-ECG. Electrical potentials obtained from the solution of monodomain equation can be used to approximate the extracellular potential. Equation (4) is used to calculate the extracellular potential at a given position r,

$$V_e(r) = -\frac{\gamma}{4\pi}\frac{\sigma_i}{\sigma_e}\int_\Omega \nabla V(r')\cdot\nabla\left[\frac{1}{|r'-r|}\right]d\Omega \tag{4}$$

where σ_i and σ_e are the intracellular and extracellular conductivities, V is the membrane potential and r is the position at which we are calculating the extracellular potential. Fig. 1 (c) shows the points at which the extracellular potential (pseudo-ECG) is calculated. In order to approximate the position of those points, the heart was inserted into a segmented human torso and properly oriented.

3 Results

A simulation study was carried out on the computational hexahedral mesh built from the segmented human DTMRI sequence. Axisymmetric anisotropy was extracted from the DTMRI sequence and included for each element. In order to obtain meaningful simulations and due to the lack of a Purkinje system in our model we defined the following protocol to stimulate the ventricles. Firstly, the isochronal maps and descriptions for right (RV) and left ventricle (LV) given by Durrer [14] were analyzed. Secondly, we randomly choose 100 locations from the RV endocardium and 150 locations from the LV endocardium. The activation time for each stimulation point is dictated by a variable that depends on the distance of each point to the apex, and was bounded to $40ms$ for the furthest stimulus. Activation time followed an apex-to-base, and endo-to-epicardium sequence. Fig. 1 (a) shows the disposition of the activation points on the endocardial regions. Colors correspond to the time in milliseconds at which each stimulus was given. Five consecutive pulses of $2ms$ were given to all stimuli with a frequency of $1Hz$ (BCL = 1000 ms) to stabilize the ionic channels and reach an

steady state. Action potentials (APs) and pseudo-ECG during the last pacing beat were analyzed.

In order to examine differences in response to changes in I_{Kr} several simulations were conducted with different drug doses. In particular 6 scenarios were tested combining normal and different dofetilide concentrations, 10 nM and 100 nM (complete I_{Kr} block), together with two different tissue configurations in which percentage of endocardial, midmyocardial and epicardial cells through the wall were changed.

For each simulated scenario we analyzed the activation sequence, extracted the local activation time isochronal maps (LATs) and action potential duration (APD) isochronal maps. Fig. 2 (a) shows the isochronal maps of a normal sequence (without any drug) and tissue configuration type (1). No significative changes in the activation sequence were observed between simulations with and without I_{Kr} block as expected, since it does not contributes to the activation phase. Subtle differences were noticed in the the activation wavefront orientation between tissue configurations at the epicardial region. Total activation time was around $90ms$ where activation of the endocardial region took around $50ms$, producing and endocardial to epicardial activation, which was considered physiological. The analysis of the repolarization sequences showed a big difference between cell populations. Fig. 2 (b) shows the isochronal map of local APDs where the APD heterogeneity is visible through the wall. Fig. 3 (a) shows the intrinsic differences between APD cell durations for the fifth stimulus on each cell type.

In all the scenarios in which I_{Kr} was blocked the APDs were greatly increased for all cell populations (see Fig. 3 and table 1 (b)). Table 2 summarizes the average APD_{90} obtained for each cell type and a given dofetilide dose, together with the APD_{90} increment compared with the physiological case. It is remarkable the effect that cell-to-cell electrotonic interactions produced in the APD distribution. APD prolongation was almost double for configuration type (1)

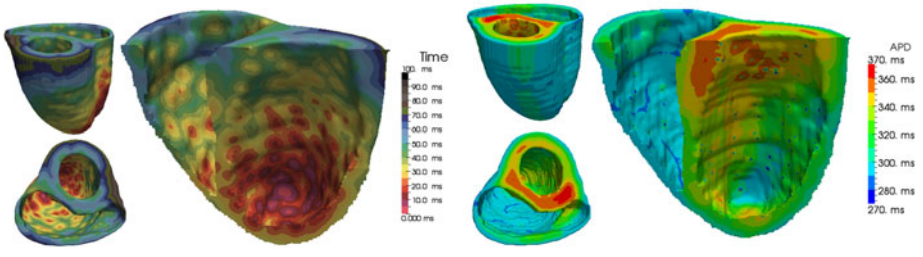

(a) (b)

Fig. 2. Activation and repolarization sequence without dofetilide and heterogeneous scenario (1). The local activation times and local action potential durations are obtained at each element of the model. Colormap shows in millisecond (a) the activation time and (b) the time to repolarization.

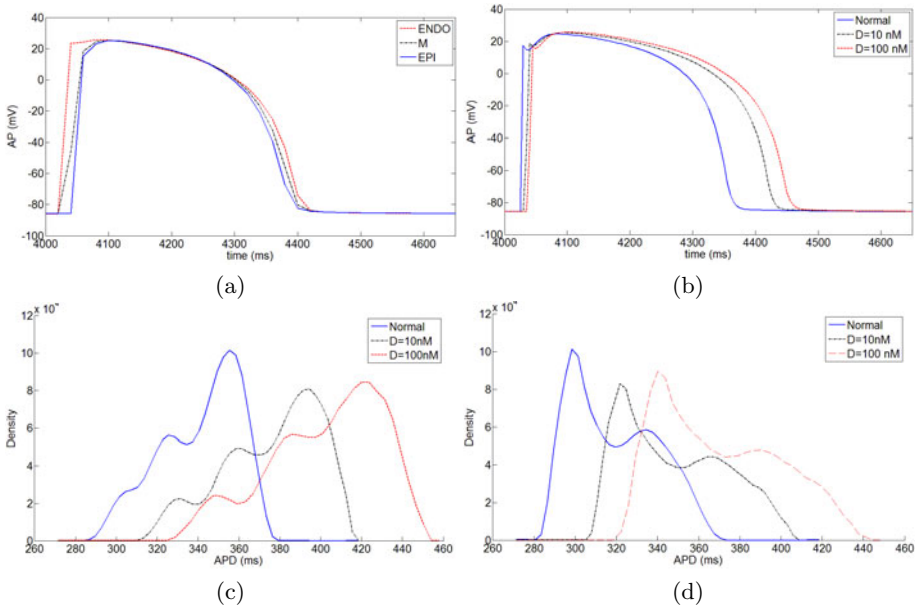

Fig. 3. Different behavior of epicardial, endocardial, and midmyocardial cell types. (a) Steady-state action potentials for BCL of 1000 for endocardial, midmyocardial and epicardial cells in normal conditions. (b) prolongation of the APD for midmyocardial cells as a function of the dofetilide dose. Equivalent increments were obtained for all three cell populations. (c) and (d) show the dispersion in APD as a function of the dofetilide concentration for heterogeneity types (1) and (2), respectively.

than type (2) for both midmyocardial and epicardial cells. The lack of endocardial cells in configuration type (1) only left one border for interaction between epicardial and midmyocardial (which accounted for 66% of the wall). Figs. 3 (c) and (d) present changes in dispersion of APD for different I_{Kr} block degrees and wall heterogeneity. Again cell heterogeneity played an important role and changed the dispersion of APD shifting the average and tail of the distribution. Dofetilide prolonged the APD for all cell types, although it had a greater global effect for configuration (1), since midmyocardial cells were more abundant in case (1) and showed the most affected by dofetilide.

Table 1. Differences in activation and repolarization times

Dofetilide	Heterogeneity	Activation (ms)	Repolarization (ms)	QT (ms)
0 nM	(1)/(2)	90/88	460/460	450/439
10 nM	(1)/(2)	89/88	500/480	500/505
100 nM	(1)/(2)	89/88	540/520	544/537

Table 2. Average APD_{90} and APD_{90} prolongation for different cell types and dofetilide doses for heterogeneity (1)/(2)

Dofetilide	ENDO (ms)	M (ms)	EPI (ms)
0 nM	-/320	330/300	320/300
10 nM	-/340 (-/6.3%)	385/320 (16.7%/6.7%)	355/320 (10.9%/6.7%)
100 nM	-/380 (-/18.8%)	410/340 (24.2%/13.3%)	380/340 (18.8%/13.3%)

Pseudo-ECGs were calculate at the six precordial points (see Fig. 1 (c)), and were consistent with results obtained at cellular level. A QT interval of $440ms$ was measured under normal conditions which was longer than expected, probably due to a slow activation time. Prolongation of QT for total I_{Kr} block ($D = 100nM$) increased the QT interval up to $100ms$ in lead V5 for both scenarios. Second scenario was consistent with results obtained by ten Tusscher [15] at cellular level. Different experimental studiers have demonstrated the key importance of spatial dispersion of repolarization in LQTS arrhythmia [16]. The increase of QT interval (22%) is in agreement to the clinical recorded degree of QT prolongation induced by the effect of dofetilide (15%) [17].

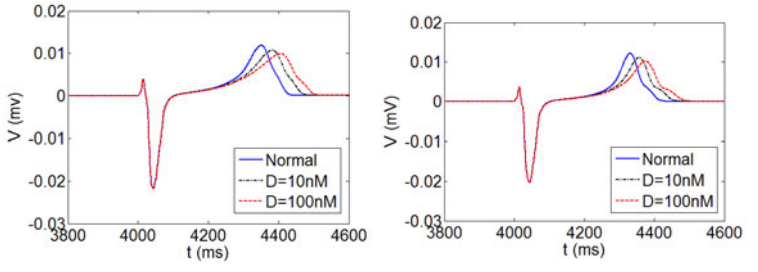

(a) (b)

Fig. 4. Pseudo-ECGs for lead V3. Effect of dofetilide in pseudo-ECG for (a) heterogeneity type (1) and (b) type (2). Prolongation of the QT interval is clearly visible and coherent with APD prolongation.

4 Conclusions

We have built a 3D model of a human subject and included the main anatomical and functional components required to perform in-silico electrophysiology studies. We designed a simulation study to simulate the multi-scale effects of drug-induced ion channel block in ventricular electrophysiology at the cellular, tissue and whole ventricular levels for different ventricular cell heterogeneity scenarios. A well known drug called dofetilide which affects specifically I_{Kr} channels was chosen to study the effect of current block in a 3D heart model. Results showed the effect of dofetilide in cardiac cells, a prolongation of APD and QT. Average APD and APD distributions were obtained for each drug concentration and each scenario. The scenario that included endocardial, midmyocardial

and epicardial cells produced the more realistic results. Pseudo-ECG confirmed the results observed at cellular level regarding the prolongation of repolarization phase. Results confirmed the importance of structural personalization since the response to the drug block varies as a function of the cell type. The overall geometry should not have a great impact on the results or the overall effects of the drug beyond subtle changes in the ECG. Nonetheless, differentiated models for dilated, normal or hypertrophied hearts might have an impact. Computational modelling and simulation tools might help in the understanding of complex drug to cell and organ interactions, as well as help for the assessment of drug safety pharmacology.

Acknowledgments

This work has been partially funded by the Ministerio de Ciencia e Innovacion, TEC-2008-02090.

References

1. Yap, Y.G., Camm, A.J.: Drug induced qt prolongation and torsades de pointes. Heart 89(11), 1363–1372 (2003)
2. Recanatini, M., Poluzzi, E., Masetti, M., Cavalli, A., Ponti, F.D.: Qt prolongation through herg k(+) channel blockade: current knowledge and strategies for the early prediction during drug development. Med. Res. Rev. 25(2), 133–166 (2005)
3. Gintant, G.A., Su, Z., Martin, R.L., Cox, B.F.: Utility of herg assays as surrogate markers of delayed cardiac repolarization and qt safety. Toxicol. Pathol. 34(1), 81–90 (2006)
4. Tusscherten, K.H.W.J., Panfilov, A.V.: Eikonal formulation of the minimal principle for scroll wave filaments. Phys. Rev. Lett. 93(10), 108106 (2004)
5. Helm, P.: A novel technique for quantifying variability of cardiac anatomy application to the dyssynchronous failing heart, Ph.D. thesis, Johns Hopkins University (2005)
6. Heidenreich, E., Ferrero, J.M., Doblare, M., Rodriguez Jose, F.: Adaptive macro finite elements for the numerical solution of monodomain equation in cardiac electrophysiology. Annals of Biomedical Engineering 38, 2331–2345 (2010)
7. Drouin, E., Charpentier, F., Gauthier, C., Laurent, K., Marec, H.L.: Electrophysiologic characteristics of cells spanning the left ventricular wall of human heart: evidence for presence of m cells. J. Am. Coll. Cardiol. 26(1), 185–192 (1995)
8. Antzelevitch, C., Sicouri, S., Litovsky, S.H., Lukas, A., Krishnan, S.C., Diego, J.M.D., Gintant, G.A., Liu, D.W.: Heterogeneity within the ventricular wall. electrophysiology and pharmacology of epicardial, endocardial, and m cells. Circ. Res. 69(6), 1427–1449 (1991)
9. Sicouri, S., Fish, J., Antzelevitch, C.: Distribution of m cells in the canine ventricle. J. Cardiovasc. Electrophysiol. 5(10), 824–837 (1994)
10. ten Tusscher, K.H.W.J., Noble, D., Noble, P.J., Panfilov, A.V.: A model for human ventricular tissue. Am. J. Physiol. Heart Circ. Physiol. 286(4), 1573–1589 (2004)
11. Heidenreich, E.A.: Algoritmos para ecuaciones de reaccion difusion aplicados a electrofisiologia, Ph.D. thesis, Departamento de Ingenieria Mecanica, Universidad de Zaragoza (2009)

12. Plonsey, R.: Bioelectric sources arising in excitable fibers (alza lecture). Ann. Biomed. Eng. 16(6), 519–546 (1988)
13. Potse, M., Dub, B., Richer, J., Vinet, A., Gulrajani, R.M.: A comparison of monodomain and bidomain reaction-diffusion models for action potential propagation in the human heart. IEEE Trans. Biomed. Eng. 53(12 Pt 1), 2425–2435 (2006)
14. Durrer, D., van Dam, R.T., Freud, G.E., Janse, M.J., Meijler, F.L., Arzbaecher, R.C.: Total excitation of the isolated human heart. Circulation 41(6), 899–912 (1970)
15. Tusscher, K.H.W.J.T., Panfilov, A.V.: Cell model for efficient simulation of wave propagation in human ventricular tissue under normal and pathological conditions. Phys. Med. Biol. 51(23), 6141–6156 (2006)
16. Yan, G.X., Wu, Y., Liu, T., Wang, J., Marinchak, R.A., Kowey, P.R.: Phase 2 early afterdepolarization as a trigger of polymorphic ventricular tachycardia in acquired long-qt syndrome: direct evidence from intracellular recordings in the intact left ventricular wall. Circulation 103(23), 2851–2856 (2001)
17. Okada, Y., Ogawa, S., Sadanaga, T., Mitamura, H.: Assessment of reverse use-dependent blocking actions of class iii antiarrhythmic drugs by 24-hour holter electrocardiography. J. Am. Coll. Cardiol. 27(1), 84–89 (1996)

How Much Geometrical Detail Do We Need in Cardiac Electrophysiological Imaging? A Generic Heart-Torso Representation for Fast Subject-Specific Customization

Linwei Wang[1], Ken C.L. Wong[2], Heye Zhang[3], Huafeng Liu[4], and Pengcheng Shi[1]

[1] Computational Biomedicine Laboratory
Rochester Institute of Technology, Rochester, New York, USA
[2] Asclepios Research Project, INRIA Sophia-Antipolis, France
[3] Bioengineering Institute, University of Auckland, Auckland, New Zealand
[4] State Key Laboratory of Modern Optical Instrumentation
Zhejiang University, Hangzhou, China

Abstract. Noninvasive cardiac electrophysiological imaging (IECG), the effort to use body surface potential measurement to estimate subject-specific electrophysiological activity of the heart, traditionally is performed on detailed heart-torso models that are completely reconstructed from a large amount of images. This geometrical modeling brings high demands of operational time and data acquisition, rendering current IECG techniques clinically impractical. In this study, we investigate the feasibility to use an alternative geometrical model that excludes local details but captures subject-specific global geometrical parameters that have been regarded essential for reliable IECG solutions. This is done by using limited images and image metadata to customize a pre-defined, generic ventricle and electrode-array representation to subject-specific ventricle size, position, orientation and electrode position on the body surface. We apply this simplified geometrical modeling in IECG studies of post myocardial infarction patients; the results of transmembrane potential imaging and infarct quantitation are compared with the gold standard and results from the same IECG approach using traditional, detailed heart-torso model. This study shows that local geometrical details do not have significant impact on IECG solutions and excluding them from geometrical modeling might be of potential to drive cardiac electrophysiological imaging closer towards clinical practicability.

Keywords: Cardiac electrophysiological imaging, Geometrical modeling, Myocardial infarction.

1 Introduction

Noninvasive cardiac electrophysiological imaging, also known as the inverse problem of electrocardiography (IECG), seeks to computationally reconstruct electrophysiological activity of the heart from electrical potential measurements on the body surface. It has been a common practice to solve this problem on a

O. Camara et al. (Eds.): STACOM-CESC 2010, LNCS 6364, pp. 232–241, 2010.

realistic heart-torso geometrical model that is built, as in detail as possible, from tomographic images of individual subjects [1,2]. This, however, renders the current IECG techniques clinically impracticable and unfavorable: on one hand, it requires a serial operations such as image registration, segmentation, and surface-/volume-mesh generation to construct a detailed geometrical model entirely from images; each step *per se* often involves a non-automatic task that is nontrivial, labor-intensive, time-consuming and associated with intricate, ambiguous errors; on the other hand, while advanced algorithms might expedite the modeling procedure [3], large amount of heart and whole-body images always have to be collected for each subject of interest. This inconveniently high demand on operational time and data acquisition is one of the major obstacles to the clinical practicability of cardiac electrophysiological imaging.

Impact of geometrical modeling on IECG solutions has long been studied, including geometrical errors caused during modeling [4,5,6], heart motion [7] and respiratory [8]. The consensus is that, for reliable IECG solutions, a fixed, standard geometrical model is insufficient [4] and important global geometrical parameters, including heart orientation, position, size and electrode positioning on the body surface [4,5,6], have to be accurately captured. Nevertheless, no study has examined the role of local heart-torso geometrical details in IECG problem. This raises the question that, in order to improve the efficiency and practicability of current IECG techniques, is it feasible to replace the traditional fully-detailed geometrical model with a simplified one that accurately incorporates global geometrical parameters known to be crucial to IECG solutions, but neglects local complex geometrical details of individual subjects?

In this paper, we develop and apply a customizable, generic representation of ventricle-torso geometry in the reconstruction of subject-specific volumetric transmembrane potential (TMP) dynamics from body surface potential (BSP) data, an IECG approach developed in [1]. This generic ventricular representation takes shape from four standard concentric ellipsoids, while the torso representation defines a schematic description of electrode array setup in any given BSP mapping system. In IECG study of individual subjects, instead of gradually reconstructing a fully-detailed ventricle-torso model from large amounts of images, we use limited images and image metadata to quickly customize the pre-defined abstract ventricle-torso representation to subject-specific ventricular size, position, orientation and electrode positions. This is tested in IECG studies of post myocardial infarction (MI) patients. Results of 3D TMP imaging and infarct quantitation are validated with the gold standard provided by cardiologists, and are compared to the results obtained from the same IECG approach using traditional fully-detailed heart-torso model [1].

2 Methodology

2.1 Generic Representation of Ventricle-Torso Geometry

Ventricular Representation. Instead of describing in detail the intricate ventricular shape for individual subjects, the generic ventricular representation

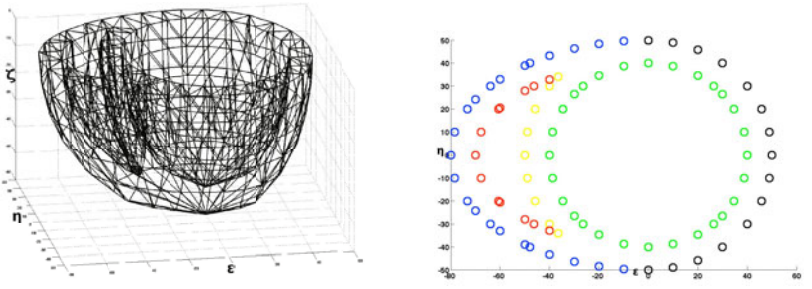

(a) (b)

Fig. 1. (a) Surface mesh of the generic ventricular representation in $\{\varepsilon, \eta, \zeta\}$ coordinate system. (b) Example of a short-axis view of the generic ventricular representation (base); color implies which ellipsoid each part of the contour belongs to.

offers a standard, abstract description of ventricular shape. As shown in Fig 1, in a Cartesian coordinate system $\{\varepsilon, \eta, \zeta\}$, the generic description of ventricular geometry is mathematically defined by the surfaces (in negative-ζ space) of four concentric, intersecting ellipsoids, of which the center locates at the origin and the semi-principal axes corresponds to the ε, η and ζ axes:

$$(\frac{\varepsilon}{a_i})^2 + (\frac{\eta}{b_i})^2 + (\frac{\zeta}{c_i})^2 = 1 \qquad i \in \{li, lo, ri, ro\} \tag{1}$$

where $\{a_i, b_i, c_i\}$ represent equatorial and polar radii of the four ellipsoids labeled by subscript i. Ellipsoids li and lo are prolate spheroids with equal equatorial radii smaller than polar radius ($a_i = b_i < c_i, i \in \{li, lo\}$): li surface represents LV endocardium (green in Fig 1 (b)); lo surface on $+\varepsilon$ direction to $lo{-}ro$ intersection represents part of epicardium (black), and lo surface on $-\varepsilon$ direction to $lo - ri$ intersection represents the septal part of RV endocardium (yellow). Ellipsoids ri and ro have equatorial radius b_i and polar radius c_i equal to those of li and lo, respectively, but equatorial radius a_i larger than a_{lo} ($a_j > a_{lo}; b_j = b_i; c_j = c_i.(j, i) \in \{(ro, lo), (ri, li)\}$) so that they both intersect with lo: ro surface on $-\varepsilon$ direction to $lo - ro$ intersection represents part of the epicardium (blue); ri surface on $-\varepsilon$ direction to $lo - ri$ intersection represents the free-wall part of RV endocardium (red). This ventricular representation is rendered in surface mesh with $a_{lo} = 50, c_{lo} = 60, a_{li} = 40, c_{li} = 50, a_{ro} = 70$ and $a_{ri} = 80$, with fiber orientation mapped from the mathematical ventricular fibrous model in [9].

Torso Representation. Because the relative position between heart and recording electrodes is the major determinant of IECG solutions [4,6], the torso representation is designed to describe the electrode positioning instead of complete torso geometry. Since when a given BSP mapping system is applied to individual subjects, only a few electrodes are located to landmarks while the remaining ones are arranged in keeping with the pre-specified setup of electrode array, it is sensible to construct a schematic representation of the electrode array

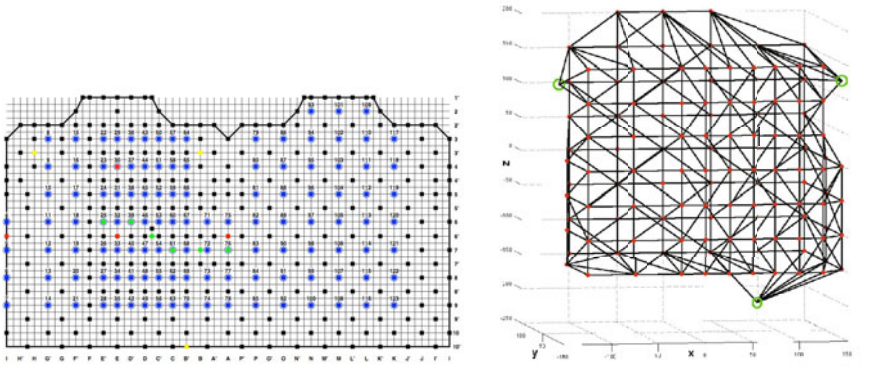

(a) (b)

Fig. 2. (a) Dalhousie 123-lead body surface potential mapping system, with 120 torso leads (blue) and 3 limb leads (green); the 6 chest electrodes used in standard 12-lead electrocardiograms are marked as green. (b) The schematic representation of Dalhousie 123-lead mapping system; 120 torso leads are marked as red, and 3 limb leads are marked as green. The view direction is from the front to the back of the body.

for each given BSP mapping system, which can be customized to each subject according to subject-specific landmarks located in images.

As an example, this paper elaborates on the *Dalhousie* 123-lead mapping system [10] used in our real data experiments. Fig 2 (a) shows the standard arrangement of electrode sites in this mapping system, including 120 torso leads (blue) and 3 limb leads (yellow); Fig 2 (b) shows the schematic representation (surface mesh) of the electrode array, taking into account the following rules: the electrodes are mounted $5cm$ apart in flexible rubber strips; columns B' to G' are structurally-spaced array (spaced as in Fig 2 (a)) on the front of the torso with column E to be located over the sternum, and column I and column A to be located in the right and left axillary line (sides of the body), respectively; column B and P are to be located in the anterior and posterior axillary lines on the left side of the body; columns K to O are evenly-spaced electrode array on the back of the torso, with column O, N and M are to be located directly posterior to column C, D and E on torso front, respectively. Absolute position of the electrodes are not relevant in this schematic representation because it is the mesh and relative positioning among electrodes that is of interest.

2.2 Fast Subject-Specific Geometry Customization from Images

In application to individual IECG studies, the predefined ventricle and electrode-array representation are quickly customized to the electrode positioning and ventricular orientation, position and size of individual subjects using limited images and image metadata. The customized ventricle-torso models are described in the patient-based Cartesian coordinate system (x, y, z) that is used as standards in medical images, where the x-axis increases from the right to the left hand side

of the patient, the y-axis increases from the anterior to the posterior part of the patient, and the z-axis increases from the feet toward the head of the patient.

In the generic ventricular representation in local $\{\varepsilon, \eta, \zeta\}$ coordinate system, ventricular size is reflected in ellipsoidal radii: four equatorial radii a_i characterize the left- and right-ventricular cavity radii as well as wall thickness; polar radii c_{lo} and c_{li} define ventricular long-axis length. The origin corresponds to the center of LV base, and the ε-, η-, and ζ- axes correspond to the vertical long axis (vLA), horizontal long axis (hLA) and short axis (SA) views of standard cardiac imaging, respectively. As a result, customization of ventricular model is simplified into the straightforward practice of coordinate transformation: **1) Scaling:** approximate LV and RV endocardial radii (a_{li}, a_{ri}) and epicardial radii (a_{lo}, a_{ro}) from base-slice SA cardiac image; calculate LV long-axis epicardial and endocardial length (c_{li}, c_{lo}) from the position of base- and apex-slice SA cardiac images with respect to the patient-based coordinate system (defined by *Image Position (Patient)* in image metadata); scale the four standard ellipsoids by these six parameters. **2) Translation:** locate the center of LV base O_c in base-slice SA cardiac image; translate the origin of the $\{\varepsilon, \eta, \zeta\}$ coordinate to O_c. **3) Rotation:** calculate the SA, hLA, and/or vLA view direction from the orientation of SA-, hLA-, and/or vLA-view images with respect to the patient-based coordinate system (defined in *Image Orientation (Patient)* in image metadata); rotate the $\{\varepsilon, \eta, \zeta\}$ coordinate system to the (vLA, hLA, SA) view directions.

With the above transformation between the local $\{\varepsilon, \eta, \zeta\}$ and global (x, y, z) coordinate system, the generic ventricular representation is customized to the correct position inside individual subject's torso with orientation and size as indicated by images; the associated surface fiber orientation is rotated accordingly. A cloud of meshfree points, with flexible spatial resolution suitable for different applications, is then generated inside the subject-specific ventricular surfaces for the volume representation of ventricular wall; to account for myocardial anisotropy, fiber structure associated with the three-dimensionally distributed points is interpolated from surface fiber orientation based on the knowledge that ventricular fibers are spirally arranged and fiber orientations change from epi- to endo-cardium in a counterclockwise manner [11].

Customization of torso model involves locating the schematic electrode array to the following landmarks: from whole body sagittal plane (SAG) image, the forth row of electrodes from the bottom is determined by the fourth intercostal space parasternally as the reference for the z-direction positioning for the entire electrode array and for the y-direction positioning of the front electrodes; from whole body coronal plane (COR) image, columns E, E' and D' are located by the sternum, $V1$ position and $V2$ position[1], respectively, as the reference for x-direction positioning of the entire array except on the body sides; from whole body transversal plane (TRA) image, column M is located from the dorsal spine to determine the y-position of all back electrodes, and x- and y-positions of columns I, A, B and P (sides of the body) are located by the right mid-, left mid-, left anterior and left posterior axiliary lines, respectively. The remaining

[1] $V1$, $V2$ are chest leads in standard electrocardiograms.

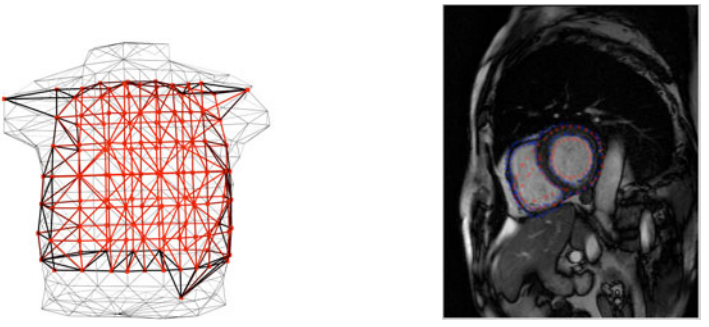

(a) (b)

Fig. 3. (a) Simplified torso model customized from 123-electrode array mesh (Fig 2 (b)) to the electrode positioning on the body surface of patient 3 (the mesh is highlighted with thicker edge and the electrodes are marked as red), superimposed with the detailed, complete torso model. (b) Example slice of the generic ventricular model in Fig 1 (red contour) customized to the ventricle position, orientation and size of patient 3, superimposed with the detailed ventricular model (blue contour) and MRI.

electrodes fall into place in keeping with the prespecified array setup. By using the same landmarks used in locating the electrode strips during mapping practice [10], this customization process *replicates* the electrode positioning process and thus offers an accurate description of subject-specific electrode positions on the body surface. Note that y-direction (anterior to posterior) customization of electrodes on body front and back is less certain because of the lack of landmarks and the following simplification is made based on the characteristic of torso shape: for body back, we assume the same y position for all the electrodes as the dorsal spine located from TRA plane image; for body front, we further locate the first and last rows of electrodes from whole body SAG image and interpolate y-positions of the remaining electrodes in between.

In summary, by examining four images (cardiac base-slice SA image, whole-body COR-, SAG-, and TRA-plane images), and using image metadata to obtain the position and orientation of four images (cardiac base-slice and apex-slice SA image, hLA and/or vLA image), we efficiently obtain a ventricle-torso representation that ignores local geometrical details of the ventricles or the torso, but accurately captures subject-specific electrode positions, ventricular orientation, position and size, which are global geometrical parameters regarded most crucial to cardiac electrophysiological imaging.

3 Experiments

We apply the proposed geometrical modeling in the IECG approach presented in [1], where *a priori* knowledge of normal cardiac electrophysiology is incorporated through monodomain FitzHugh-Nagumo models to constrain the IECG solution, and a rigorous statistical framework of state-space filtering is formulated to

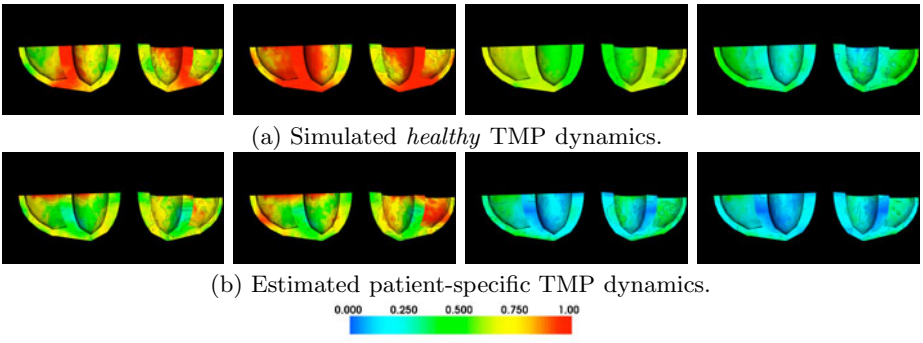

(a) Simulated *healthy* TMP dynamics.

(b) Estimated patient-specific TMP dynamics.

Fig. 4. Time sequence of volumetric TMP dynamics for patient 3 on simplified geometry. Color encodes normalized TMP magnitude $(0-1)$; black contour represents TMP isochrones. Left to right: $9.1ms$, $12.2ms$, $121.7ms$, 128.3ms after QRS onset. During depolarization (left two figures), patient-specific TMP conduction delay appears around mid-basal LV and lateral part of mid-apical LV that coincides with *true* infarct location; during repolarization (right two figures), shorter activation duration and lower resting potential appears around the same location.

obtain the *maximum a posteriori* estimation of volumetric TMP dynamics from subject-specific BSP data. Experiments are performed on MRI and BSP data of three post-MI patients provided in *2007 PhysioNet / CinC Challenge* [12]. Cardiac SA, hLA and vLA MRI of patients are provided with 1.33mm/pixel in-plane resolution; whole body SAG, COR, and TRA plane MRI are provided with 1.41mm/pixel in-plane resolution. BSP is recorded at 2k Hz by the *Dalhousie* 123-lead system introduced in section 2.1. From Gd-enhanced MRI, cardiologists identified the center (CE), extent (EP) and segments of infarct for each patient (based on AHA 17-segment LV division [13]); Tab 1 and Fig 5 (a) lists this *gold standard* of infarct quantitation and the corresponding visualization.

As an example, Fig 3 shows a superimposed comparison of the ventricle (a) and torso model (b) between that is customized from the generic representation and that is fully reconstructed from images, respectively, for patient 3. Fig 4 compares the results of volumetric TMP dynamics obtained on the simplified geometrical model (b) to the simulated *healthy* TMP dynamics on the same geometry (a): it is evident that the estimated patient-specific TMP dynamics exhibits distinct conduction delay during ventricular depolarization, and shorter activation duration and lower resting potential during repolarization; these irregular behaviors collect around the inferior mid-basal LV and lateral mid-apical LV that coincides with *true* infarct location of the patient (Fig 5 (a)).

Using the method described in [1], infarct quantitation is performed based on two prominent features, activation time and action potential duration, of patient-specific TMP dynamics. Fig 5 shows the 3D infarct imaging as a result of MI quantitation on the simplified geometry (c), compared to those obtained with traditional detailed geometry [1] (b) and *gold standard* (a); Table 1 lists the corresponding quantitative comparison. As shown, the overall accuracy of

Table 1. MI quantitation results obtained with simplified geometry (SG), compared to the *gold standard* (GS) and results with detailed geometry (DG) [1]. Infarct center and location are labelled by segment number as defined by AHA 17-segment LV division. False-positive identification is highlighted by color blue. Infarct extent measures the percentage of infarct in the ventricular mass. Segment overlap measures the percentage of true positive identification in estimation results.

		Extent (EP)	Center (CE)	Location	Segment Overlap (SO)
Case 1	GS	31%	8	1,2,3,8,9,13,14,15	NA
	DG	28%	8	1, 2,9, 13, 14, 15, 17	76%
	SG	41%	8	1, 2, 3, 6, 8, 9, 13, 14, 16	84%
Case 2	GS	30%	3/4/9/10	3, 4, 9, 10	NA
	DG	24%	9	3, 8, 9, 10, 14, 15	56%
	SG	27%	9	2, 3, 4, 8, 9, 10	76%
Case 3	GS	52%	10/11	3,4,5,9,10,11,12,15,16	NA
	DG	43%	9	2,3,4,5, 8, 11,12,16, 17	56%
	SG	43%	9	2, 3,5, 8,9,10,11,15,16	61%

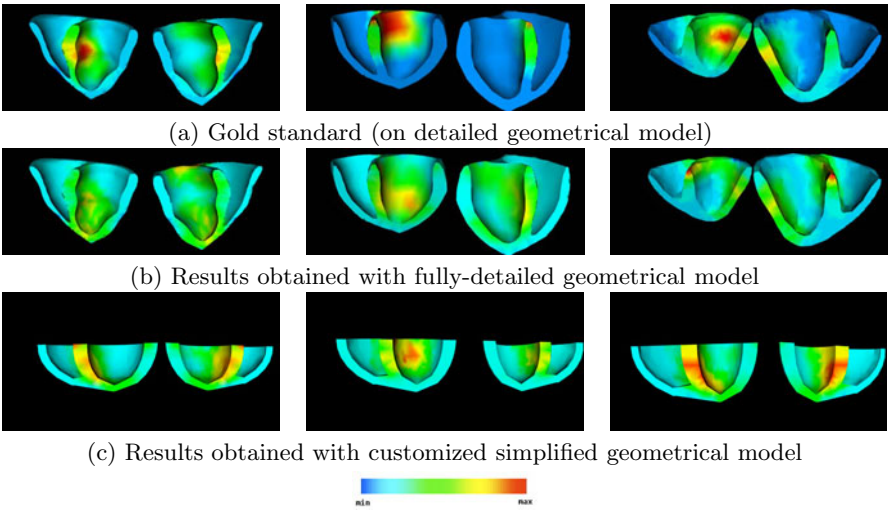

(a) Gold standard (on detailed geometrical model)

(b) Results obtained with fully-detailed geometrical model

(c) Results obtained with customized simplified geometrical model

Fig. 5. 3D Infarct Imaging. (a): Infarct segments are highlighted as green with the center as red. (b) and (c): Color encodes the value of infarct metric as defined in [1], where larger value corresponds to larger difference from normal TMP activity. Because of the difference in geometry, identical visual appearance is not expected. For quantitative comparison refer to Table 1.

MI quantitation is not negatively impacted by replacing the fully-detailed geometrical model with the simplified one: the localization of infarct center in not affected in any case; slightly different false-positive and true-positive identification of infarct location are given with the simplified geometry but the overall performance is similar; more interestingly, the same or better accuracy is

obtained on the percentage of true-positive identification (SO) with the simplified geometry. This could be explained by the fact that, because the simplified ventricular model is of more regular shape, it gives rise to less uncertainty in the 17-segment LV division and, as a result, leads to improvement in the accuracy of 17-segment based MI quantitation. Nevertheless experiments on a larger datasets are needed for any conclusive remark.

4 Discussion and Conclusion

As the first step in investigating the role of local heart-torso geometrical details in IECG solutions, this feasibility study shows that, as long as global geometrical parameters are accurately captured, local geometrical details do not have significant impact on IECG solutions. Therefore, in place of the traditional fully-detailed geometrical models, an alternative, which excludes local shape details but allows fast, accurate customization of global geometrical parameters, might be of the potential to drive cardiac electrophysiological imaging closer towards clinical practicability. In comparison, a fully-detailed geometrical model requires complete SA scans from apex to the base of the heart ($\sim$10 images), and COR-, SAG-, TRA-plane scans of whole body at different depths ($\sim$ 30-50 images for each plane); the simplified model needs only 6 images (base- and apex-slice SA, hLA/vLA image, COR-, SAG-, TRA-plane image). Furthermore, detailed heart and body modeling often involves non-automatic task that requires expertise at image processing; customization of the presented geometrical model, while still requires user interaction with the images, does not require image-proessing expertise and can be quickly performed in clinical practice. This could largely ease one of the major challenges to the clinical practicability of cardiac electrophysiological imaging. Because these manual interaction steps determine the global geometrical parameters that are crucial to IECG solutions, it is important to assure their accuracy as well as to further develop the simplified geometrical model to employ minimum manual interaction.

Experiments in this study only consider myocardial infarction in left ventricle. As shown in Fig 3 (b), compared to LV, the simplified RV model shows relatively larger discrepancy from the realistic RV shape, the impact of which should be investigated in a larger variety of cardiac conditions in future study. While this paper demonstrates that local geometrical details do not have significant impact on the specific IECG approach presented in [1], conclusion regarding general IECG methodologies can only be given with a more comprehensive study in the future. Furthermore, at this initial stage, the presented simplified geometrical model could expedite and therefore improve the applicability of noninvasive TMP imaging in guiding diagnosing, detecting and approximately localizing electrophysiologically-altered tissue in the 3D myocardium; future development of this geometrical model should extend its applicability to scenarios where detailed heart surface or transmural geometry are needed, for example, through the addition of post-processing step that interpolates or deforms the ellipsoid surface to patient's cardiac images [14].

It is a difficult problem to estimate electrophysiological information inside the 3D myocardium from electrode recordings on the body surface: while the results of MI quantitation presented in [1] appear to noticeably differ from the gold standard provided by cardiologists, they showed evident improvement over other existing IECG results on the same data sets. Though further methodological development is much needed for IECG approaches, it is out of the scope of this study which focus on how to reduce the cost of operational time and image acquisition of IECG approaches.

References

1. Wang, L., Zhang, H., Wong, K., Liu, H., Shi, P.: Physiological-model-constrained noninvasive reconstruction of volumetric myocardial transmembrane potentials. IEEE Trans. Biomed. Eng. 5(2), 296–315 (2010)
2. Rudy, Y., Messinger-Rapport, B.: Inverse problem of electrocardiography: solutions in terms of epicardial potentials. Criti. Rev. Biomed. Eng. 16, 215–268 (1988)
3. Cheng, L.: Non-invasive Electrical Imaging of the Heartl. PhD thesis, Univ. of Auckland, New Zealand (2001)
4. Huiskamp, G., van Oosterom, A.: Tailored versus realistic geometry in the inverse problem of electrocardiography. IEEE Trans. Biomed. Eng. 36, 827–835 (1989)
5. Rapport, B.J., Rudy, Y.: The inverse problem in electrocardiography: a model study of the effects of geometry and conductivity parameters on the reconstruction of epicardial pontetials. IEEE Trans. Biomed. Eng. 33(7), 667–675 (1986)
6. Cheng, L.K., Bodley, J.M., Pullan, A.J.: The effect of experimental and modeling errors on the electrocardiographic inverse problem. IEEE Trans. Biomed. Eng. 50(1), 23–32 (2003)
7. Jiang, Y., Farina, D., Doessel, O.: Effect of heart motion on the solution of forward and inverse electrocardiographic problem - a simulation study. In: Proc. Computers in Cardiology, pp. 365–368 (2008)
8. Jiang, Y., Meng, Y., Farina, D., Doessel, O.: Effect of respiration on the solution of forward and inverse electrocardiographic problem - a simulation study. In: Proc. Computers in Cardiology (2009)
9. Nash, M.: Mechanics and Material Properties of the Heart using an Anatomically Accurate Mathematical Model. PhD thesis, Univ. of Auckland, New Zealand (May 1998)
10. Dawoud, F., Wagner, G., Moody, G., Horacek, B.M.: Using inverse electrocardiography to image myocardial infarction - reflection on the 2007 physionet/computers in cardiology challenge. Eur. J. Cardiovasc. Prev. Rehabil. 41(6), 630–635 (2008)
11. Nielsen, P.M.F., Grice, I.J.L., Smaill, B.H., Hunter, P.J.: Mathematical model of geometry and fibrous structure of the heart. Am. J. Cardiol. 260, H1365–H1378 (1991)
12. Goldberger, A.L., et al.: Physiobank, physiotoolkit, and physionet components of a new research resource for complex physiological signals. Cric. 101, e215–e220 (2000)
13. Cerqueira, M.D., Weissman, N.J., Dilsizian, V., Jacobs, A.K., Kaul, S., Laskey, W.K., Pennell, D.J., Rumberger, J.A., Ryan, T., Verani, M.S.: Standardized myocardial segmentation and nomenclature for tomographic imaging of the heart. Circ. 105, 539–542 (2002)
14. Sung, D., Omens, J.H., McCulloch, A.D.: Model-based analysis of optically mapped epicardial activation patterns and conduction velocity. Ann. Biomed. Eng. 28, 1085–1092 (2000)

Influence of Geometric Variations on LV Activation Times: A Study on an Atlas-Based Virtual Population

Corné Hoogendoorn[1,2], Ali Pashaei[1,2], Rafael Sebastián[3], Federico M. Sukno[2,1], Oscar Cámara[1,2], and Alejandro F. Frangi[1,2,4]

[1] Center for Computational Imaging and Simulation Technologies in Biomedicine (CISTIB), Universitat Pompeu Fabra, Barcelona, Spain
[2] Networking Center on Biomedical Research - CIBER-BBN, Barcelona, Spain
[3] Computational Multi-Scale Physiology Lab, Universitat de València, Valencia, Spain
[4] Institució Catalana de Recerca i Estudis Avançats (ICREA)

Abstract. We present the fully automated pipeline we have developed to obtain electrophysiological simulations of the heart on a large atlas-based virtual population. This virtual population was generated from a statistical model of left ventricular geometry, represented by a surface model. Correspondence between tetrahedralized volumetric meshes was obtained using Thin Plate Spline warps. Simulations are based on the fast solving of Eikonal equations, and stimulation sites correspond to physiological activation. We report variations of total activation time introduced by geometry, as well as variations in the location of last activation. The obtained results suggest that the total activation time has a strong dependence on LV geometrical variation such as dilation-to-hypertrophy.

1 Introduction

In order to improve the understanding of the physiological phenomena underlying the clinical observations relating to particular pathologies, it is imperative that large amounts of multimodal data are collected and analyzed. Challenges to achieve this goal lie mainly in the processing of this data in a consistent way, with feasible processing times and levels of interaction.

Regarding the heart, *in silico* models are used to study electrophysiology. Electrical activation patterns obtained through simulations show the impact of pathology on cardiac function, and should consequently shed light on the open issues surrounding therapy options. One example of a treatment option with strong potential but with an as of yet poorly defined responder profile is Cardiac Resynchronization Therapy (CRT) [1,2]. A better understanding of what compromises CRT efficacy is expected to lead to improvement of the current response rate of 70%.

In this work, we use a large virtual population derived from a surface Point Distribution Model (PDM) of the left ventricle (LV) to demonstrate our pipeline

O. Camara et al. (Eds.): STACOM-CESC 2010, LNCS 6364, pp. 242–251, 2010.

for large scale personalized cardiac electrophysiological simulations. This corresponds to using the output of an automated image segmentation algorithm, after which the steps of volumetric meshing, definition of fiber orientation and Purkinje terminals, execution of electrophysiological simulation, and analysis of the activation pattern are fully automated. The total running time of these five steps is on the order of minutes, although mesh resolutions –both surface and volumetric– have a strong influence on this.

2 Atlas-Based Virtual Population

We create a virtual population of left ventricular geometries based on the principal modes of variation observed in a sample of 80 subjects, both healthy and pathological.

2.1 Point Distribution Model

Our statistical model of the geometry is a PDM as used in Active Shape Model (ASM) based segmentation [3]. Each shape in the training set is represented by a number of corresponding points –landmarks– which in our case are all located on the LV epi- and endocardial surface.

Represented by n_l landmarks, Procrustes alignment [4] is used to remove pose and size variations from the set of surfaces. Then, each of the n_s aligned shapes is represented by a single $3n_l$-dimensional shape vector $\mathbf{s}_i, 0 \leq i < n_s$, by concatenating the coordinates of the landmarks. From these, we compute the mean shape vector:

$$\bar{\mathbf{s}} = \frac{1}{n_s} \sum_i \mathbf{s}_i, \tag{1}$$

and we compose the data matrix $\mathbf{S}$:

$$\mathbf{S} = \begin{pmatrix} \mathbf{s}_0 - \bar{\mathbf{s}} \\ \mathbf{s}_1 - \bar{\mathbf{s}} \\ \vdots \\ \mathbf{s}_{n_s-1} - \bar{\mathbf{s}} \end{pmatrix} \tag{2}$$

By applying Principal Component Analysis (PCA) [5] to the sample covariance matrix $\mathbf{C} = \frac{1}{n_s}\mathbf{S}^T\mathbf{S}$, we obtain the reoriented coordinate system $\mathbf{\Phi}$ which is best aligned to the principal modes of variation of the shape set in a least squares sense, as well as the observed variances $\lambda_i, 0 \leq i < n_s$ along each of these components. It is within this reoriented coordinate system that we sample our virtual population.

The coefficient vector corresponding to a shape is denoted $\mathbf{b}$; new shapes are generated using the equation $\mathbf{s}_{\text{new}} = \bar{\mathbf{s}} + \mathbf{b}\mathbf{\Phi}$, and scaled using the mean scaling factor obtained at the Procrustes alignment step. Note that our use of PCA does not imply that the segmentation has to be done using a PCA-based model.

The left panel of Fig. 1 illustrates the distribution of our input shapes.

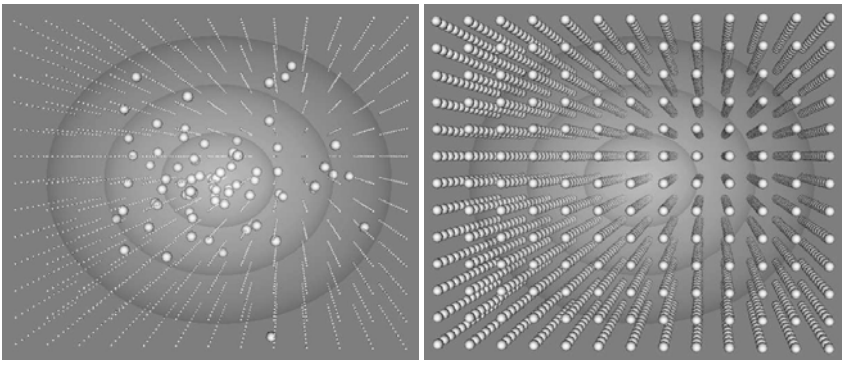

Fig. 1. Left: Input shapes in 3-dimensional shape space; right: Shapes sampled on the grid in 3-dimensional shape space (also overlaid left as small glyphs). The large transparent ellipsoids illustrate isoprobability associated with 1, 2 and 3 standard deviations from the mean, under the assumption that the input shapes follow a multivariate Gaussian distribution.

2.2 Sampling Strategy

As we assume a Gaussian distribution underlying our shapes, the λ_i we obtain correspond to the variances of this multivariate Gaussian distribution [6]. Using this information, we sample up to 3 standard deviations from the mean in each of the first three principal directions, to study the extremes we should expect based on our input shape set. Three standard deviations is the amount of variation usually allowed in ASM-based segmentation tasks, although the number of components used is typically greater than our three [7].

Our sampling frequency is 0.5 standard deviations, leading to a virtual population of $n_m = 13^3 = 2197$ meshes, as illustrated in the right panel of Fig. 1. This number can be increased with more modes of variation and finer sampling, but we chose this for ease of visualization. The mean shape and shapes on the main axes are shown in Fig. 2 in the left panel, illustrating the main modes of variation. Combinations of these modes lead to the 'extreme' shapes shown in Fig. 2 in the right panel, corresponding to the corners of our sampling grid.

3 Volumetric Population

The meshes produced by the sampling in PCA coefficient space are surfaces only; to obtain correspondence between tetrahedron-based volumetric meshes, only the mean shape surface is tetrahedralized. This is done using Tetgen[1]. While the accuracy of the solver used is not sensitive to mesh coarseness, we needed a sufficiently fine mesh to define transmural variations in fiber orientation. On the

[1] Weierstrass Institute for Applied Analysis and Stochastics, Berlin, Germany. Website: http://tetgen.berlios.de

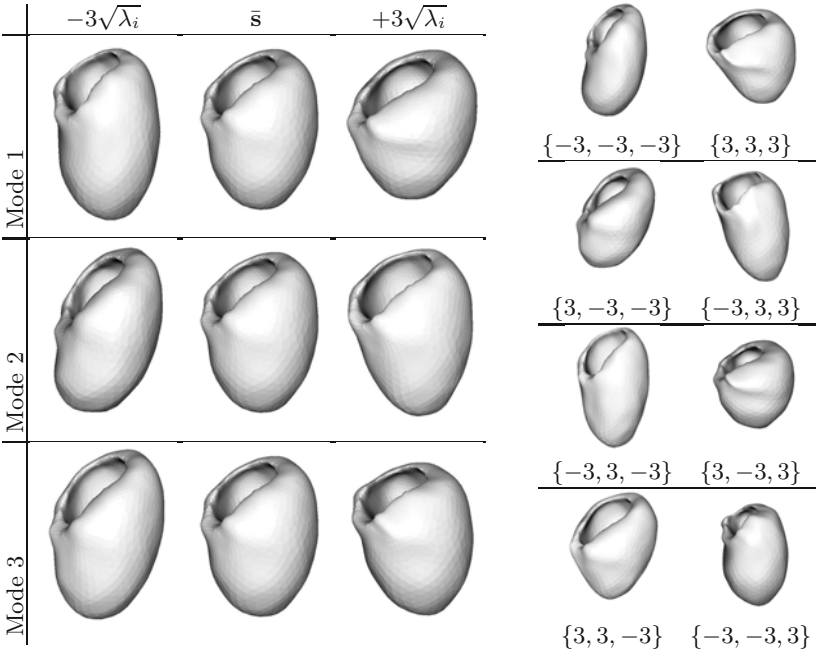

Fig. 2. Left: The first three modes of variation; left to right: $\bar{\mathbf{s}} - 3\sqrt{\lambda_i}$, $\bar{\mathbf{s}}$, $\bar{\mathbf{s}} + 3\sqrt{\lambda_i}$. These correspond to the center points of the faces in the sampling grid. Right: Shapes corresponding to the corner points of the sampling grid, rows corresponding to space diagonals. Element-wise multiplication with $\{\sqrt{\lambda_0}, \sqrt{\lambda_1}, \sqrt{\lambda_2}\}$ returns their coefficient vectors $\mathbf{b}$.

other hand the simulation time increases with the number of nodes, therefore we increased the resolution until the simulation result on the mean geometry stabilized, which occurred at a target tetrahedron volume of 1.5 mm^3, while the target aspect ratio ($H_{\max}/(2r_{\text{in}}\sqrt{6})$: $H_{\max}$ is the length of the longest edge, r_{in} is the radius of the insphere; the optimum value is 1) was fixed throughout at 1.2. The resulting mesh contained 20300 nodes and 112815 tetrahedrals. The actual mean tetrahedron volume was 1.14 mm^3, respectively.

3.1 TPS Registration of Point Sets

To generate the volumetric meshes corresponding to the other 2196 meshes, we use the correspondence between surface points to derive a Thin Plate Spline (TPS) warp [8]. To reduce the load of computing the warp, which involves the inversion of a $(n_k+3)\times(n_k+3)$-sized matrix, with n_k the number of landmarks used to define it, the mean surface was first decimated to a subset of the original landmarks, vectorized into $\bar{\mathbf{s}}'$. Then, the displacements $\bar{\mathbf{s}}' - \mathbf{s}'_i$ are used to obtain the TPS warps.

The correspondence that already existed on the surface meshes is then transferred to the volumetric meshes by applying the TPS warp to each of the nodes

of the mean volumetric mesh. This strategy degrades the quality of the volumetric mesh, measured by the maximum aspect ratio and mean tetra volume we report in Fig. 3. However, we placed more importance on node correspondence to be able to compare results throughout our population.

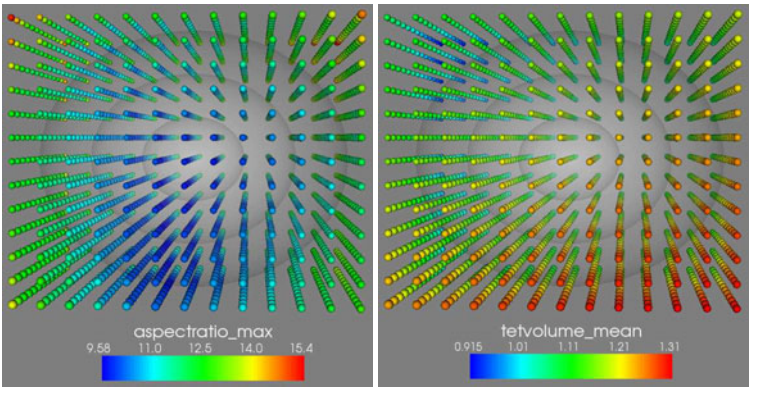

Fig. 3. Quality measures of the volumetric meshes generated through Thin Plate Spline warping of a mean volumetric mesh. Left: maximum tetrahedron aspect ratio; right: mean tetrahedron volume (mm^3).

4 Electrophysiological Simulation

4.1 Substructure Modeling

Histological studies have been instrumental in better understanding the geometrical microstructure of cardiac tissue [9]. However, obtaining information on patient specific arrangement of myocytes is still challenging. It requires specific imaging techniques such as diffusion tensor magnetic resonance imaging (DT-MRI), which currently can only be used on ex-vivo hearts. Therefore, since no patient-specific data are available, a simpler approach to include the myocardial fiber orientation is used. It consists in calculating the myofiber orientation at every node on the deformed volumetric mesh, according to the histological results obtained by Streeter [10]. The left panel of Fig. 4 shows the change in fiber orientation from endocardium to epicardium.

We have set conduction velocities in cardiac tissue according to the values obtained by Caldwell et al. [11] on recent experimental models. Along the fiber direction it is set to 0.67 m/s; however, perpendicular to these, Caldwell found velocities of 0.30 m/s parallel to the myocyte layers and 0.17 m/s in the transmural direction. Since we do not have these two perpendicular directions defined with the fiber direction, we set the conduction velocity perpendicular to the fiber direction to the mean of the parallel and transmural velocities, at 0.24 m/s.

To palliate the absence of a complete conduction system yet still produce realistic activation sequences of the ventricle, we defined a simple stimulation

protocol. We randomly chose n_p points in the LV wall. The activation time for those stimuli were set by measuring their distances to the apex, and bounding the maximum activation time of the endocardium. Absolute numbers where bounded by studying endocardial activation maps given by Durrer et al. in human hearts [12], producing apex-to-base and endo-to-epicardial activations as reported in literature. The stimuli network was consistent between different hearts, as illustrated in Fig. 4's right panel, yet absolute activation times were recomputed for each case. In the figure, the activation times are for the mean geometry.

Fig. 4. Left: transmural variation of fiber orientation. Right: Purkinje terminals and their activation delays, up to 39 ms (in red, at the basal level).

4.2 Propagation Model

There exist several models with different degree of complexity to simulate cardiac electrical activation. The complexity is usually selected as a function of the final application and has a great impact on computation times. In this work, we use a simplified electrical propagation model that uses a Purkinje terminal model as described in the previous section. It is a simple wave propagation model [13,14] that takes into account the myocardial fiber orientation, and is based on the assumption that propagation speed varies more slowly and over larger spatial scales than the transmembrane potential. The model used here is based on the Hamilton-Jacobi Equation (HJE), a formulation of mechanics in which the motion of a particle can be represented as a wave. The static HJE equation is of the form

$$\forall x_i \in \Omega : \mathcal{H}(x_i, \frac{\partial \phi}{\partial x_i}) = 0, \quad \text{with} \quad \forall x_i \in \partial\Omega : \phi(x_i) = \phi_0(x_i). \tag{3}$$

Here ϕ is the seed value, x_i is the coordinate component, and Ω and $\partial\Omega$ the domain and domain boundary, respectively. The Eikonal equation is an important member of the family of HJEs, which can be described in anisotropic format as

$$\forall x_i \in \Omega : a_{ij} \frac{\partial \phi}{\partial x_i} \frac{\partial \phi}{\partial x_j} - f^2(x_i) = 0, \quad \text{with} \quad \forall x_i \in \partial\Omega : \phi(x_i) = \phi_0(x_i). \tag{4}$$

where a_{ij} is the anisotropy coefficient, and $f(x)$ a positive function. To solve Eq. (4), we used the Fast Marching Method (FMM) introduced by Sethian [15].

5 Experiments and Results

We simulated physiological activation by using a stimulation point at the location where the insulating sheath around the His bundles is expected to end. This corresponds to one node of the volumetric mesh, and it is this same node that is used in all simulations. Similarly, the set of nodes at which we define Purkinje terminals is kept equal throughout the population.

The outcome of the simulations that are analyzed are the Local Activation Times (LAT); Fig. 5 illustrates how the total activation time and varies throughout the population, as well as the variability in last activated nodes (the nodes whose LATs define the total activation times). A more spherical geometry leads to a longer total activation time. Figure 6 shows the LAT pattern observed; together with Fig. 7 it shows that this pattern is much the same throughout the population, with only absolute values varying. This would be according to expectation, as no other variation but geometry is introduced. Further investigation is required to study how the location of the last activated node varies.

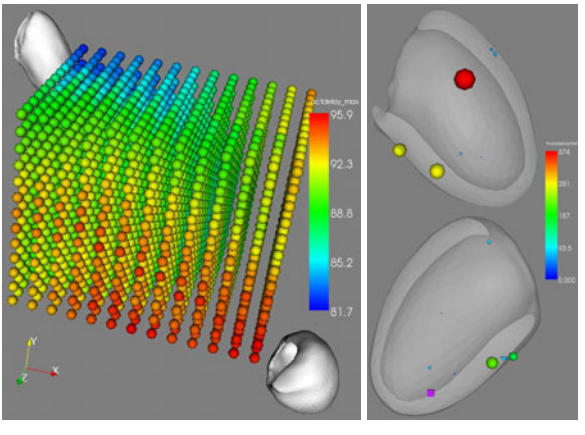

Fig. 5. Left: The sample grid with total activation times. Each sphere corresponds to a shape, as in Fig. 1, and its total activation time is color-coded from 81.7 ms (blue) to 95.9 ms (red). The greatest difference is observed between the spheres in the third row of Fig. 2's right panel, which are depicted near their respective corners. Right: Epicardial views, on which sphere size and color indicate in how many of the 2197 simulations the last activated node was there (max: 374); the box indicates the stimulation point, the geometry is that of the mean shape.

Running times per generated shape are on the order of minutes; the simulation takes up the vast majority of this time. On a high-end desktop PC (Intel Core i7 at 2.67 GHz, 6 Gb of RAM), the TPS warping takes about 2 seconds, which includes the decimation of the mean mesh. Subsequently the generation of the fiber orientation and computation of Purkinje terminal activation delays take up another second. Finally, the simulation takes up around 50 seconds.

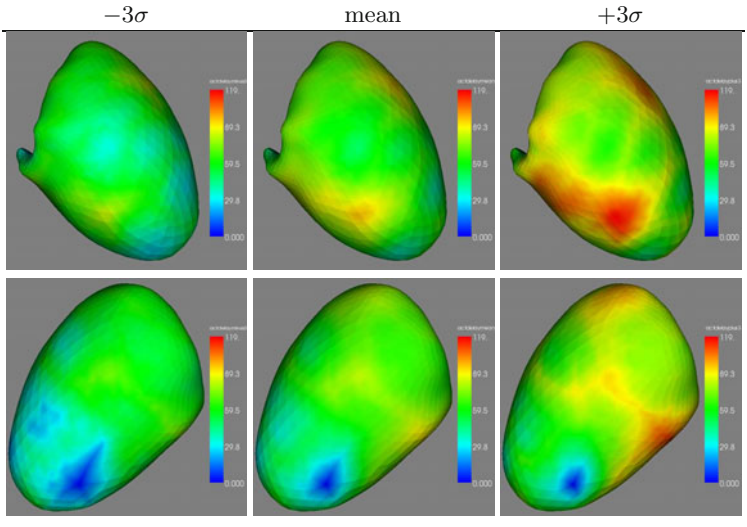

Fig. 6. Local Activation Time maps, mean and plus and minus three standard deviations on each node, shown on the mean shape. The color map ranges from 0 to 119 ms (blue to red).

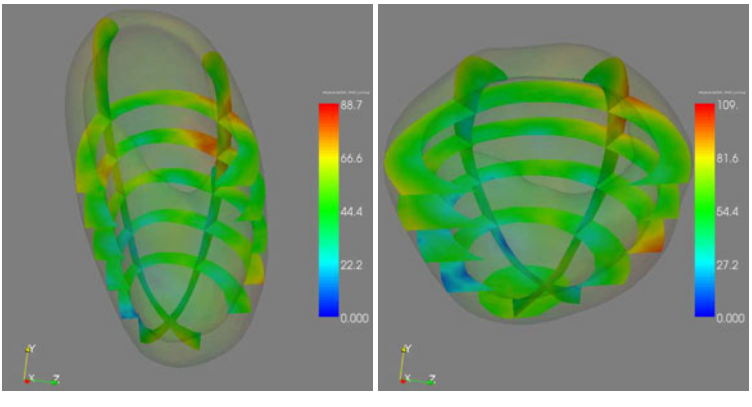

Fig. 7. Local Activation Time maps, depicting intramural activation for the two most extreme shapes, with the septal wall removed. As the cuts are equal with respect to the coordinate system, they do not coincide anatomically. However, there is evidence of equality in the activation patterns.

6 Conclusions and Discussion

We have presented an implementation of the pipeline from image segmentation to electrophysiological simulation, and used it to demonstrate high-throughput simulation studies on a large virtual population. This shows the feasibility of

doing simular studies on large real populations, to ensure sufficient statistical power of the simulation results, whose variations may not be correctly observed in small studies.

The greatest variation was observed along a space diagonal of our sampling grid, corresponding to a variation of the LV's elongation, together with a wall thickening. We would argue, however, that the normalization of the LV size in the set of training surfaces has a damping effect on this variation; an isotropic scaling of the more spherical ventricle to more closely match the length of the more elongated ventricle would only serve to increase internodal distances, and consequently the activation times.

The strategy of deforming a volumetric atlas mesh seems to have little influence on the simulation quality, yet when more complex propagation models are employed this could become an issue. Such propagation models would also call for a mean volumetric mesh of one order of magnitude higher resolution.

Extension of this work would involve the generation of a larger population with biventricular or full heart models as well as exploring different pacing strategies such as CRT, LV epicardial or endocardial pacing under particular conditions such as the presence of scar. For the latter condition, automated identification and delineation of scar tissue will be required; this step will probably be placed in the pipeline during or immediately after segmentation of the cardiac geometry. Subsequently different propagation speeds are to be asigned to the associated nodes. Different pacing strategies would amount to the selection of different nodes or pairs of nodes to serve as stimulation points.

Acknowledgments

This work was funded by the Integrated Project euHeart (FP7/ICT-2007-224495) in the European Commission's 7th Framework Programme, and by the Spanish Ministry of Innovation and Science through grant TIN2009-14536-C02-01, Plan E and FEDER, and through the cvREMOD project (CEN-20091044) under the CENIT programme of the Industrial and Technological Development Center (CDTI).

References

1. Abraham, W.T., Fisher, W.G., Smith, A.L., DeLurgio, D.B., Leon, A.R., Loh, E., Kocovic, D.Z., Packer, M., Clavell, A.L., Hayes, D.L., Ellestad, M., Messenger, J.: Cardiac resynchronization in chronic heart failure. N. Engl. J. Med. 346, 1845–1853 (2002)
2. Chung, E.S., Leon, A.R., Tavazzi, L., Sun, J.P., Nihoyannopoulos, P., Merlino, J., Abraham, W.T., Ghio, S., Leclercq, C., Bax, J.J., Yu, C.M., Gorcsan III, J., St. John Sutton, M., De Sutter, J., Murillo, J.: Results of the predictors of response to CRT (PROSPECT) trial. Circulation 117, 2608–2616 (2008)
3. Cootes, T.F., Cooper, D.H., Taylor, C.J., Graham, J.: Trainable method of parametric shape description. Image Vis. Comput. 10, 289–294 (1992)
4. Goodall, C.: Procrustes methods in shape analysis. J. R. Stat. Soc. Ser. B-Stat. Meth. 53, 285–339 (1991)

5. Pearson, K.: On lines and planes of closest fit to systems of points in space. Philos. Mag. S6(2), 559–572 (1901)
6. Hotelling, H.: Analysis of a complex of statistical variables into principal components. J. Educ. Psychol. 24, 417–441, 498–520 (1933)
7. Heimann, T., Meinzer, H.P.: Statistical shape models for 3D medical image segmentation: A review. Med. Image Anal. 13, 543–563 (2009)
8. Bookstein, F.L.: Principal warps: Thin-plate splines and the decomposition of deformations. IEEE Trans. Pattern Anal. Mach. Intell. 11, 567–585 (1989)
9. Jouk, P.S., Mourad, A., Milisic, V., Michalowicz, G., Raoult, A., Caillerie, D., Usson, Y.: Analysis of the fiber architecture of the heart by quantitative polarized light microscopy.: Accuracy, limitations and contribution to the study of the fiber architecture of the ventricles during fetal and neonatal life. Eur. J. Cardio-Thorac. Surg. 31, 915–921 (2007)
10. Streeter Jr., D.D.: Gross morphology and fiber geometry of the heart. In: Berne, R.M., Sperelakis, N., Geigert, S.R. (eds.) Handbook of Physiology: The Cardiovascular System. The Heart, vol. I, pp. 61–112. American Physiology Society, Hyattsville (1979)
11. Caldwell, B.J., Trew, M.L., Sands, G.B., Hooks, D.A., LeGrice, I.J., Smaill, B.H.: Three distinct directions of intramural activation reveal nonuniform side-to-side electrical coupling of ventricular myocytes. Circ. Arrhythm. Electrophysiol. 2, 433–440 (2009)
12. Durrer, D., van Dam, R.T., Freud, G.E., Janse, M.J., Meijler, F.L., Arzbaecher, R.C.: Total excitation of the isolated human heart. Circulation 41, 899–912 (1970)
13. Tomlinson, K.A., Hunter, P.J., Pullan, A.J.: A finite element method for an Eikonal equation model of myocardial excitation wavefront propagation. SIAM J. Appl. Math. 63, 324–350 (2002)
14. Chinchapatnam, P., Rhode, K.S., Ginks, M., Rinaldi, C.A., Lambiase, P., Razavi, R., Arridge, S., Sermesant, M.: Model-based imaging of cardiac apparent conductivity and local conduction velocity for diagnosis and planning of therapy. IEEE Trans. Med. Imag. 27, 1631–1642 (2008)
15. Sethian, J.A.: A fast marching level set method for monotonically advancing fronts. Proc. Natl. Acad. Sci. USA 93, 1591–1595 (1996)

Generic Conduction Parameters for Predicting Activation Waves in Customised Cardiac Electrophysiology Models

Pablo Lamata[1,*], Steven Niederer[1,*], Gernot Plank[1,2], and Nic Smith[1]

[1] Computing Laboratory, University of Oxford, Wolfson Building, Parks Road
Oxford, OX1 3QD, UK
{Pablo.Lamata,Steven.Niederer,Nic.Smith}@comlab.ox.ac.uk
[2] Institute of Biophysics, Medical University of Graz, Auenbruggerplatz 2/4,
A-8036 Graz, Austria
Gernot.Plank@meduni-graz.at

Abstract. Model customisation to represent specific experimental or clinical cases is becoming increasingly important as simulations aim to characterise individual variability under physiological and pathological conditions. This study presents a new methodology to customise and regularise heart shape and fibres using imaging data (MRI and DT-MRI). The effect of using generic conductivity tensor values in electrophysiology simulations on these customised meshes is investigated. Simulation results demonstrate the ability of generic parameters to approximate epicardial activation patterns in healthy porcine hearts. Results also show a limited sensitivity of electrical activation times to the anisotropy of these parameters.

Keywords: model customization, cubic Hermite mesh, electrophysiological simulation.

1 Introduction

Simulations of cardiac activation offer the ability to integrate multimodal data enabling the characterization and prediction of cardiac electophysiological function. Central to the effective application of cardiac electophysiology models in a clinical context is their ability to capture an individual patient's cardiac function. The need for such personalisation is motivated by both the wide spectrum of physiological variability in individual cardiac patients and the sensitivity of electrical activity, and heart function in general, to this variability.

To simulate patient specific electrical activation requires multiple elements that constitute the model that are available, either directly or via inference, from specific diagnostic modalities. These model elements include the cardiac geometry, cardiac microstructural orientation, material heterogeneities, fast conducting Purkinje network, cellular homeostasis and material conductivity. The anatomical geometry of the

[*] Both authors share the main authorship of the work.

O. Camara et al. (Eds.): STACOM-CESC 2010, LNCS 6364, pp. 252–260, 2010.

heart is readily provided in patients through the use of MRI, CT or 3D electrocardiography. The use of late enhancement imaging complements these anatomical descriptions by identifying volumes of scar within the myocardium. Finally, while currently mapped from animal or cadaveric studies, continuing advances in DT-MRI suggest that patient specific fibre orientations will also be obtainable in cardiac patients in the near future.

The assimilation of the data from these imaging modalities means that many of the necessary components required to develop patient specific models of cardiac electrophysiology will soon be available through non-invasive methods. However, at present obtaining detailed spatial information on the spread of electrical activation across the heart requires an invasive procedure.

If cardiac models are to be developed based solely on non-invasive diagnostic modalities then a method for defining the myocardial conductivities is required. It is possible that aspects of cardiac physiology are either consistent within a pathology or, while significantly altered by disease, only have a limited impact on the sensitivity of model predictions of clinical relevant indices. Specifically if myocardial conductivity does not change significantly across a specific class of cardiac disease, compared with, for example, heart geometry scaring or failure of the Purkinje network, then it is possible that using generic conductivity tensors derived from animal or human measurements may enable a sufficient representation of cardiac conductance to allow for the simulation of realistic activation patterns.

This study describes the application of a new automated method to create personalised geometric and microstructure orientation models. Using anatomically personalised meshes we investigate the repercussions of using generic conductivity tensor values from the literature in a model of ex-vivo porcine hearts. Simulations are then performed in two porcine geometries for three different pacing configurations using the mono domain equations with three generic conduction tensors [1]. The differences between the measured and simulated activation times are then compared.

2 Material and Methods

The model geometry was created through personalisation of a template cubic Hermite mesh in order to efficiently represent the cardiac ventricular anatomy. A second high resolution linear tetrahedral mesh was embedded in the domain described by the cubic Hermite geometry mesh. The high resolution mesh was used for the simulation of cardiac electrophysiology, where a smaller spatial scale is necessary to capture the high spatial gradients in the membrane potential. Each of these steps is summarized in further detail in the following sections.

2.1 Data

The models are based on DT-MRI, MRI and epicardial activation times from two porcine datasets [2]. Model construction uses a binary segmentation of the anatomy derived from MRI, and three images, one for each of the fibre vector components, from DT-MRI. Epicardial activation times are only used to be compared to model simulations, and not to fit any conductivity property.

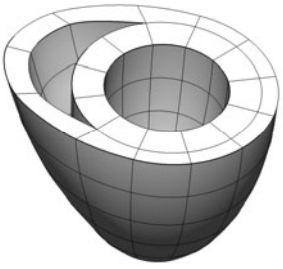

Fig. 1. Cubic Hermite idealized biventricular template

Fig. 2. Geometrical personalisation results. The idealised biventricular cubic Hermite template was customized to both porcine anatomies. Segmented voxelised anatomy from medical images was represented by its isosurface, and the resulting mesh as a smooth surface.

2.2 Geometrical Fitting

Cubic Hermite meshes are a useful and popular choice for the representation of cardiac anatomy [3-5]. A new automated personalisation strategy was applied here, which uses medical image registration techniques to warp an idealized cubic Hermite template mesh onto the desired geometry [6]. This method provides a fast and robust option when compared to existing alternatives, including the "host mesh fitting" technique or mesh generation by fitting Hermite surfaces from a linear scaffold [7].

The binary representation of each heart anatomy after segmentation was used as the target shape for the cubic Hermite personalisation process. An idealized template of a biventricular model was generated by the union of two ellipsoids with a total of 168 elements and 264 nodes, see Fig. 1. The number of elements in this mesh was chosen to achieve an accurate and efficient representation of the geometry. The template has second versions of derivatives in nodes at the joint between right and left ventricles, allowing C^1 discontinuities across these joints.

The mesh warping process involves two major computation steps, a fast binary image registration [8], and the fitting of the warping field into the cubic Hermite mesh by solving three linear systems of equations. This process took approximately 15 minutes in a desktop machine (processor AMD5200 at 2.69GHz) with images consisting of 0.75 million voxels and meshes with 6,000 degrees of freedom. The final result is illustrated in Fig. 2. The average error in the fitting was 0.95 mm RMS.

No further registration is needed between this cubic Hermite mesh, built from the anatomical MRI study, and the DT-MRI datasets as described for in-vivo conditions [9].

2.3 Fibre Anatomical Fitting

Fibre orientation obtained from DT-MRI images was fitted within the material space of the geometric domain defined by the cubic Hermite geometry mesh. The same variational formulation used in the anatomical fitting was applied to find the fit the three fields (one for each of the fibre vector components) using cubic Hermite basis functions.

The representation of fibres as vectors necessitates the introduction of a preprocessing step to align the polarity of adjacent fibres, see Fig. 3. While DT-MRI images provide information about fibre direction, this direction has no vector sense

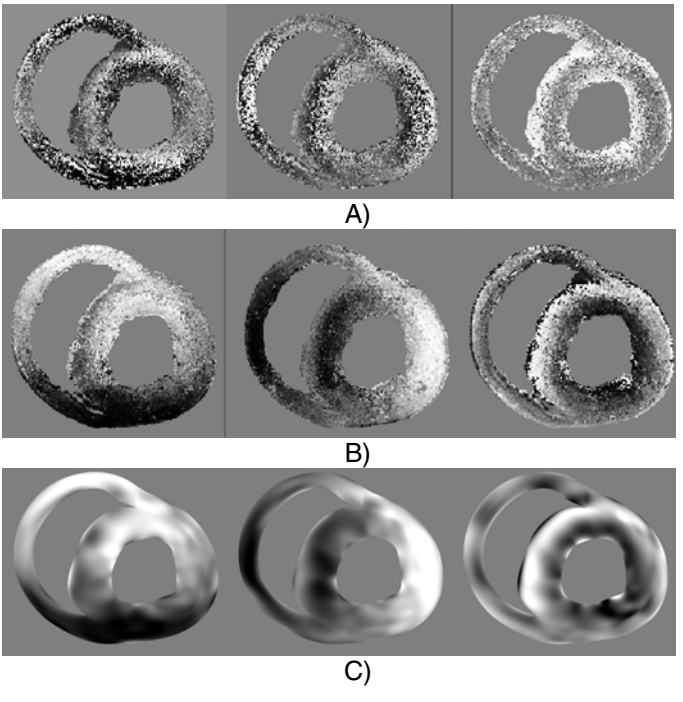

Fig. 3. Reorientation of fibre vector sense in case 1 and cubic Hermite fitting. (a) Original fibre x, y, z component images, showing abrupt and apparently random changes. (b) Fibre component images after reorientation. (c) Cross section of fitted model fibre components. Grayscale black – white is -1 to 1.

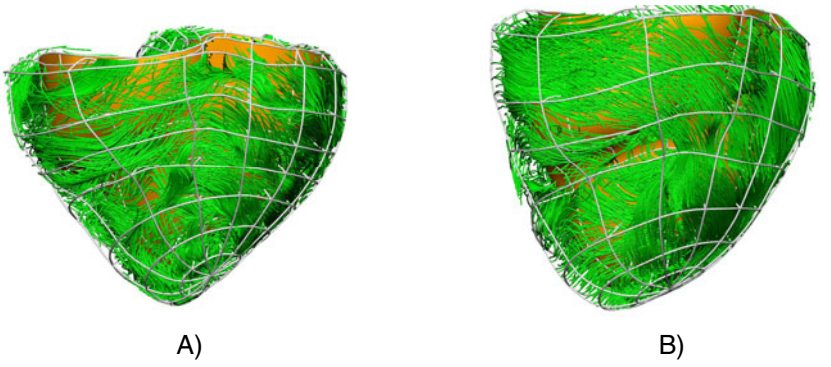

Fig. 4. Cubic Hermite description of fibres personalised to case 1 (a) and case 2 (b). Models are oriented in the same position where electrical activation fluorescence images were acquired, and show the outer layer of elements in the left ventricle.

(polarity), producing 180 degree discontinuities in extracted fibre vector fields. This causes an apparent noisy distribution of fibre vector components, because adjacent voxels have the opposite sense. On the other hand, any field fitted using a finite element with cubic basis functions is constrained to have a smooth variation. A vector realignment step was therefore introduced to swap the sense of each fibre vector pointing in the opposite direction (negative dot product) with respect to a predefined reference vector. This reference vector is defined at each point as the unitary vector in the material circumferential direction, which is obtained directly from the cubic Hermite representation of the shape. The final result of fibre anatomical fitting in both cases is illustrated in Fig. 4.

2.4 Electrophysiological Mesh

An equivalent description of the geometry domain with a high resolution linear tetrahedral mesh was generated using Tarantula (CAE Software Solutions, Eggenburg, Austria) from a binary image of the cubic Hermite geometry model (0.18mm isotropic voxel size). The meshes have a mean edge length of ~0.24mm, ~11million nodes and ~65million elements each. Fibres are defined by a unit vector for each element that was evaluated from the fitted fibre field described above.

2.5 Electrophysiological Simulations

All simulations were performed using the CARP implementation of the monodomain equations [10] run on 128 processors on SAL or REDQUEEN at the Oxford Supercomputing Centre. All models had homogenous material parameters. Results were visualised in a down sampled hexahedral mesh in cmGUI (www.cmiss.org/cmgui). Due to the scarcity of porcine cardiac electrophysiology models a human cell model was used in all simulations [11]. This is expected to have a nominal impact on activation times as both pigs and human have comparable conduction velocities [12] and maximum action potential upstroke rates [13].

3 Results

Generic bi-domain conductivity parameters from [1] were converted to mono-domain conductivities (see Table 1) as described by Keener and Sneyd [14].

Figure 5 compares the predicted activation times against the measured activation times for epicardial pacing at 1.1Hz in case 1. The model results are significantly different from the recorded activation times. Two characteristics in the experimental data of this case suggest that this is not a healthy subject. It shows two cases of electrical block at physiological pacing frequencies (1.1Hz), as indicated by the bunching of isochrones (see Fig.5A), and an extremely long electrical activation time of 280ms from apex to base. Despite significant differences in the conduction parameters and anisotropy in the model parameters the three sets of parameters tested resulted in similar predictions (Fig.5B-D). A decrease in the conductivity of parameter set 1 by a factor of 3 slowed the activation times resulting in Fig. 5E. This result shows that the model was capable of replicating the bulk activation pattern, although failing to capture the activation blocks, through a simple scaling of the conductivities.

Table 1. Mono-domain conductivity parameter sets

Parameter Set	Fibre Conductivity (S/m)	Transverse Conductivity (S/m)	Anisotropy
1	0.1334	0.0176	7.58
2	0.1232	0.0217	5.69
3	0.0887	0.0343	2.59

Fig. 5. A) Recorded epicardial activation pattern at 1Hz pacing for case 1. Note that not coloured regions illustrate the lack of data due to limitations during acquisition [2]. B) –D) simulated activation patterns using generic conductivity parameter sets1-3, respectively, from Table 1. E) Simulated activation times using generic conduction parameter set 1 from Table 1 divided by 3. Colour scale shows activation times with red – blue as 0 to 300ms in 50ms bands.

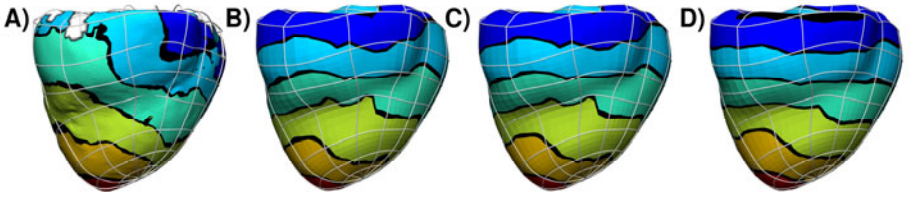

Fig. 6. A) Recorded activation pattern in case 2 with left ventricle endocardium apex pacing. B) –D) simulated activation patterns using generic conductivity parameters 1-3, respectively, from Table 1. Colour scale shows activation times with red – blue as 0 to 180ms in 30ms bands.

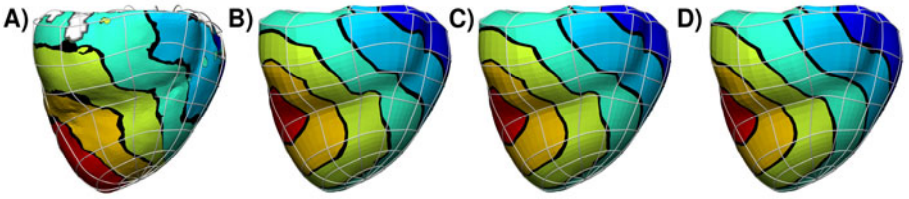

Fig. 7. A) Recorded activation pattern in case 2 with right ventricle epicardium apex pacing. B) –D) simulated activation patterns using generic conductivity parameters 1-3, respectively, from Table 1. Colour scale shows activation times with red – blue as 0 to 180ms in 30ms bands.

Activation times in case 2 (Fig.6 and Fig.7) again show limited variation between the three generic conduction parameter sets. However, unlike case 1 the generic parameters were able to reproduce a reasonable approximation of the recorded activation pattern without the need for rescaling. Isochrones from the left ventricle (LV) apical endocardial pacing site (Figure 6) show activation reaching the heart base during the same 30ms time band in simulations, whereas in the experimental data propagation is faster in the RV free wall. The model results are consistent with the fibre orientations, showing slower conduction on the RV free wall, where fibres are primarily circumferential and perpendicular to the direction of propagation (Fig.4B). A similar inconsistency between model and experimental results is found at the isochrones from the right ventricle (RV) apical epicardial activation pacing site (Fig.7), this time in the region of the apex. Again simulation results, not experimental recordings, are consistent with fibre orientation.

4 Discussion

The quality of the computational mesh has a significant impact in the convergence and accuracy of simulation results. Smoothing the DT-MRI data in order to obtain a continuous representation of fibres can potentially lead to a better fit of isochronal maps [2]. A cubic Hermite description of shape and fibre orientation, as proposed in this work, enables the smoothing of the information provided by medical images resulting in better posed models.

The mesh development process proposed here results in two meshes, a hexahedral cubic Hermite and a linear tetrahedral mesh. These two meshes have two different spatial resolutions but represent the same geometric domain and fibre fields. While the high resolution tetrahedral mesh is well suited for simulating electrical activation the cubic Hermite mesh is well posed for the simulation of deformation. Describing mapping functions between these two meshes enables the simulation of the coupled electrical and mechanical function of the heart. Capturing both of these physical systems is essential to provide a realistic and relevant representation of many cardiac pathologies and clinical treatments, and to link electrophysiology activation patterns to pump function.

Electrophysiology simulations using a personalised anatomy and generic conduction parameters have been able to qualitatively reproduce two of the three experimental conditions investigated. The model was unable to represent the regions of block

observed in case 1 (Fig.5), and to a lesser degree the model was unable to capture apparent regions of high conduction in case 2 (Fig.6 and Fig.7). These differences can be attributed to the model assumptions. Specifically the model assumes that the heart was healthy and has homogenous conductivity and ion channel densities, and neglects the Purkinje fibre network, fibroblasts and deformation, which are known to contribute to electrophysiological function.

The simulated activation patterns were not sensitive to either the anisotropy or the magnitude of the conduction parameters with nominal changes in the activation patterns with 50% and 3 fold variation in the magnitude and anisotropy ratio, respectively (Table 1). This insensitivity of the epicardial activation times to conduction parameters will impede identifying a unique homogenous conduction tensor. However, these initial simulation results do show that the use of generic species non-specific mono-domain conduction parameters could potentially offer a viable approximation for healthy heart simulations.

5 Conclusion

Generic species non-specific mono-domain conduction parameters, combined with a customised anatomy of the model, are, in specific cases, able to approximate the epicardial activation patterns of healthy hearts. Results also suggest the insensitivity of model simulations to the anisotropy of conduction parameters.

Acknowledgments

Financial support for this project was provided by the UK Engineering and Physical Sciences Research Council through grants EP/F043929/1 and EP/F059361/1, and by European Commission through euHeart project (FP7/2007-2016/224495). Technical support was provided by the Oxford Supercomputing Centre.

References

1. Roth, B.J.: Electrical conductivity values used with the bidomain model of cardiac tissue. IEEE Transactions on Biomedical Engineering 44, 326–328 (1997)
2. Pop, M., Sermesant, M., Lepiller, D., Truong, M.V., McVeigh, E.R., Crystal, E., Dick, A., Delingette, H., Ayache, N., Wright, G.A.: Fusion of optical imaging and MRI for the evaluation and adjustment of macroscopic models of cardiac electrophysiology: A feasibility study. Medical Image Analysis 13, 370–380 (2009)
3. Nielsen, P.M., Le Grice, I.J., Smaill, B.H., Hunter, P.J.: Mathematical model of geometry and fibrous structure of the heart. Am. J. Physiol. Heart Circ. Physiol. 260, H1365–H1378 (1991)
4. Stevens, C., Remme, E., LeGrice, I., Hunter, P.: Ventricular mechanics in diastole: material parameter sensitivity. Journal of Biomechanics 36, 737–748 (2003)
5. Vetter, F.J., McCulloch, A.D.: Three-dimensional analysis of regional cardiac function: a model of rabbit ventricular anatomy. Progress in Biophysics and Molecular Biology 69, 157–183 (1998)

6. Lamata, P., Niederer, S., Barber, D., Nordsletten, D., Lee, J., Hose, R., Smith, N.: Personalization of cubic hermite meshes for efficient biomechanical simulations. In: Proc. MICCAI (2010)
7. Fernandez, J.W., Mithraratne, P., Thrupp, S.F., Tawhai, M.H., Hunter, P.J.: Anatomically based geometric modelling of the musculo-skeletal system and other organs. Biomech. Model Mechanobiol. 2, 139–155 (2004)
8. Barber, D.C., Oubel, E., Frangi, A.F., Hose, D.R.: Efficient computational fluid dynamics mesh generation by image registration. Med. Image Anal. 11, 648–662 (2007)
9. Wang, V.Y., Lam, H.I., Ennis, D.B., Cowan, B.R., Young, A.A., Nash, M.P.: Modelling passive diastolic mechanics with quantitative MRI of cardiac structure and function. Medical Image Analysis 13, 773–784 (2009)
10. Vigmond, E.J., Hughes, M., Plank, G., Leon, L.J.: Computational tools for modeling electrical activity in cardiac tissue. Journal of Electrocardiology 36, 69–74 (2003)
11. ten Tusscher, K.H.W.J., Panfilov, A.V.: Alternans and spiral breakup in a human ventricular tissue model. Am. J. Physiol. Heart Circ. Physiol. 291, H1088–H1100 (2006)
12. Caldwell, B.J., Trew, M.L., Sands, G.B., Hooks, D.A., LeGrice, I.J., Smaill, B.H.: Three Distinct Directions of Intramural Activation Reveal Nonuniform Side-to-Side Electrical Coupling of Ventricular Myocytes. Circ. Arrhythm Electrophysiol. 2, 433–440 (2009)
13. Pereon, Y., Demolombe, S., Baro, I., Drouin, E., Charpentier, F., Escande, D.: Differential expression of KvLQT1 isoforms across the human ventricular wall. Am J. Physiol. Heart Circ. Physiol. 278, H1908–H1915 (2000)
14. Keener, J., Sneyd, J.: Mathematical Physiology (1998)

A Statistical Physiological-Model-Constrained Framework for Computational Imaging of Subject-Specific Volumetric Cardiac Electrophysiology Using Optical Imaging and MRI Data

Linwei Wang[1], Ken C.L. Wong[2], Heye Zhang[3], Huafeng Liu[4], and Pengcheng Shi[1]

[1] Computational Biomedicine Laboratory
Rochester Institute of Technology, Rochester, New York, USA
[2] Asclepios Research Project, INRIA Sophia-Antipolis, France
[3] Bioengineering Institute, University of Auckland, Auckland, New Zealand
[4] State Key Laboratory of Modern Optical Instrumentation
Zhejiang University, Hangzhou, China

Abstract. Computational *imaging* of personalized cardiac electrophysiology has attracted increasing research interest because of its clinical relevance in aiding in the diagnosis and prediction of cardiac electrical malfunctions of individual subjects. We have developed a statistical physiological-model-constrained framework that, rather than delivering a personalized cardiac electrophysiological model with customized parameters, uses simple standard electrophysiological models as constraints and produces *maximum a posteriori* estimation of three-dimensionally distributed transmembrane potential (TMP) dynamics inside the ventricular myocardium of individual subjects [1]. Taking part in 2010 Cardiac Electrophysiological Simulation Challenge (CESC'10), we modify this framework to use epicardial optical mapping data to estimate subject-specific TMP dynamics inside the 3D myocardium. Results of estimated dynamics are compared to the simulations by the same electrophysiological model with standard or adjusted parameters. As shown, while it is rather challenging to personalize the parameters of a cardiac electrophysiological model for the entire 3D myocardium, because of the drastically simplified model structure and limited subject's data, the presented approach of TMP estimation is able to computationally reproduce subject-specific electrical functions inside the 3D myocardium with simple standard model as constraints.

Keywords: Cardiac electrophysiological imaging, transmembrane potential, tissue excitability, optical imaging, MRI.

1 Introduction

Much interest has been put in computational *imaging* of subject-specific cardiac electrophysiology, of which the fundamental goal is to use individual subject's

O. Camara et al. (Eds.): STACOM-CESC 2010, LNCS 6364, pp. 261–269, 2010.

electrical mapping and imaging data to personalize a cardiac electrophysiological model that can be used to aid in diagnosis, treatment planning and prediction of cardiac electrical malfunctions of that subject. This is commonly done by adjusting model parameters to minimize the difference between model output and subject's electrical mapping data [2,3].

As an inverse problem that involves using a partial (such as the optical mapping data on a local region of epicardium) or indirect (such as electrode recording on the body surface) observation to conjecture the underlying quantity of interest, the level of details to be estimated, in this case the model parameters to be adjusted, is restricted by its identifiability given the limited quantity and quality of observation. As a result, in solving this problem, simplified macroscopic electrophysiological models are often favored because they offer 1) identifiability given limited data; and 2) computational feasibility. However, this leads to modeling error not only in model parameters but also in model structures that are substantially simplified compared to the underlying electrophysiology. Furthermore, unknown initial-condition in practice, such as the pacing location and frequency, adds to another source of model uncertainty. Therefore it is challenging to pursue a personalized cardiac electrophysiological model for the entire 3D myocardium by attributing all these uncertainties to model parameters, particularly when the available data is limited to a local area of the heart.

We present a different approach that, instead of delivering a personalized cardiac electrophysiological model with customized parameters, produces Bayesian *maximum a posteriori* estimation of subject-specific electrical activity: a simple electrophysiological model is used as constraints and can be standardly parameterized; the estimation is performed in a statistical formulation to allow for modeling error caused by parameters, structures and initial conditions; given electrical mapping data of an individual subject, the output is the corresponding transmembrane potential (TMP) dynamics inside the 3D myocardium. We have developed this statistical physiological-model-constrained framework that uses noninvasive body surface potential data and tomographic images to estimate subject-specific TMP dynamics inside the 3D myocardium [1].

In this challenge, we modify the framework to use local epicardial, optical mapping data to reconstruct TMP dynamics that is three-dimensionally distributed inside the ventricular myocardium. To test the impact of the constraining model in this approach, we perform and compare TMP estimation under three type of constraints: 1), standardly-parameterized models with known pacing locations; 2), standardly-parameterized models with unknown pacing locations, where first-excited ventricular sites are determined according to [4]; and 3), models with unknown parameters, where TMP dynamics and model parameter are simultaneously estimated. While TMP dynamics simulated with the same conditions are nothing similar to subject-specific conditions, the estimation results are positively validated by the optical mapping data on epicardium. It shows that, with constraints from simple, standard model, the presented

approach of TMP estimation is able to computationally reproduce subject-specific electrical functions inside the 3D myocardium given any set of electrical measurements from the subject. This approach is particularly of clinical relevance when the input is *noninvasive* electrode recording on the body surface.

To explore the possibility of parameter personalization with this type of simplified model, we also investigate simulation with parameters adjusted from subject's data (via dual TMP-parameter estimation, respectively); while the simulated TMP dynamics are significantly closer to subject's epicardial mapping data compared to simulations with standard parameters, it is substantially less accurate than the results of TMP estimation. This confirms our earlier analysis that, at the current stage, it is rather challenging to produce a personalized cardiac electrophysiological model through parameter adjustment because of the drastically simplified model structure. Issues on model personalization is worthy of much future investigation.

2 Methodology

2.1 Review and Revision of the Framework

As illustrated in Fig 1, in this framework we introduced *a priori* physiological models of normal cardiac electrical activity to constrain TMP solution, and developed a rigorous statistical scheme that obtains Bayesian *maximum a posteriori* estimation of subject-specific TMP dynamics by coupling prior model and personal data with respect to their uncertainties.

In the context of a dynamic system, TMP activity is the underlying system dynamics three-dimensionally distributed inside the heart wall, and optical mapping on epicardium is the partial measurement of system dynamics. This physiological system is modeled on personalized 3D ventricular model represented by unconnected, mesh-free points with anisotropic electrical conduction. To balance between physiological plausibility of the models and algorithmic / computational feasibility of TMP estimation, we select the monodomain two-variable *Aliev-Panfilov* model (1) [5] to describe myocardial TMP dynamics and develop it into the volumetric TMP activity model (2) on the personalized heart structure with meshfree method [6]. In the original framework [1], the available observations are in terms of noninvasive electrode recordings on the body surface. In this challenge, we are provided with a more direct type of observations: mapping of TMP dynamics on a local subregion of epicardium. The observation process, therefore, is a straightforward, partial mapping from the *state space* of 3D ventricular mass to the *data space* of a fraction of epicardial surface (the data space is a small subset of the state space) as formulated in (3) in Fig 1.

As explained earlier, a general cardiac electrophysiological model like (2) involves modeling errors from parameters, structures and initial conditions when applied to subject-specific conditions. On the other hand, data error is always present in optical mapping. Existence of all these uncertainties makes it challenging to use deterministic optimization of model parameters to fit model output to subject's observations. Therefore, we take a statistical approach to combine

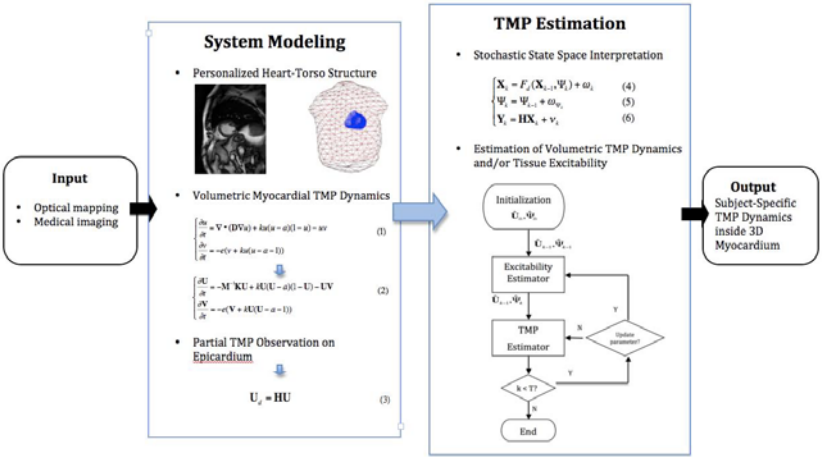

Fig. 1. Overview of the physiological-model-constrained statistical framework for personalized cardiac electrophysiology. This diagram outlines the input, output and the major components of the framework: *system modeling* and *TMP estimation*. Notations: (1): u stands for TMP; v stands for recovery current; $\mathbf{D}$ is the diffusion tensor related to myocardial electrical conductivity; $\nabla \cdot (\mathbf{D}\nabla u)$ accounts for intercellular electrical propagation; parameters e, k and a determine individual TMP shapes; particularly, a represents myocardial tissue excitability. (2): vectors $\mathbf{U}$ and $\mathbf{V}$ consist of u and v from all meshfree points; matrices $\mathbf{M}$ and $\mathbf{K}$ encode the 3D structure and conductive anisotropy of heart wall. (3): $\mathbf{U}_d$ stands for epicardial optical mapping data; $\mathbf{H}$ represents the partial mapping from 3D ventricular myocardium to local epicardium with valid optical mapping data. $(4)-(6)$: state vector $\mathbf{X} = \left(\mathbf{U}^T \mathbf{V}^T\right)^T$; measurement vector $\mathbf{Y} = \mathbf{U}_d$; $\mathbf{\Psi}$ includes unknown parameter a from all meshfree nodes, if necessary. ω, ν represent modeling and data errors.

prior models and subject's data for Bayesian *maximum a posteriori* estimation of subject-specific TMP dynamics. To explicitly account for model and data uncertainty, the original physiological system $(2, 3)$ is transformed and discretized into a stochastic state space representation $(4, 6)$ with fixed parameters or $(4, 5, 6)$ when parameter estimation is activated (Fig 1); at current stage, model and data uncertainty are assumed to be zero-mean Gaussian noises with predefined covariance matrices. To accommodate the nonlinear dynamics and large-scale, high dimensionality of the system $(4, 6)$, we develop the TMP and parameter estimator based on the unscented Kalman filter (UKF) [7]. Because of space limit, algorithmic details are omitted and can be found in [8].

2.2 Experimental Setup and Procedure

From the dataset provided by CESC'10, we perform the following processing to prepare input for the framework:

1. Using the provided FEM model of the ventricle mass, we distribute evenly-spaced points inside the volume mesh to generate meshfree representation of the same ventricles. As explained in [1], spatial resolution of the meshfree points is restricted by the algorithmic and computational feasibility of the estimation problem. Specifically, ventricles for case 1 are represented with 1555 points; ventricles for case 2 are represented with 1045 points. Fiber orientation associated with each point is interpolated from its nearest neighbor in the FEM mesh. Unknown TMP or tissue excitability associated with each point in the ventricles constitutes the *state space* in the estimation problem.
2. From the filtered optical mapping data on the reconstructed stereoscopic surface, we identify locations with valid TMP signals and project them onto the meshfree representation of the ventricles. Meshfree points with projected TMP signals constitute the *data space* in the estimation problem.
3. Because of computational issue, we only consider one action potential (AP) cycle; as a result, we do not consider pacing with different frequencies. For case 1, we consider the 2rd AP cycle from the $0.7Hz$ pacing data; for case 2, we consider the 2rd AP cycle for both the left-side and right-side LV apex pacing. Furthermore, because of the coarse spatial resolution of the ventricular model, high temporal resolution is needed for solving the TMP activity model (1). Specifically, Runge-Kutta method is used to implicitly discretize (2) in time with fine and adaptive temporal resolution, to which the input optical mapping data is temporally scaled and interpolated.
4. From the provided 26-segment division of the FEM model, the corresponding segment indices of all meshfree points are identified according to which tetrahedron they belong to in the FEM mesh. These segment indices are used to locate regular first-excited endocardial sites as determined in [4]. In addition, ventricular pacing sites are determined as the meshfree points that are the closest neighbors to the given pacing locations in the FEM mesh.

To investigate the effect of constraining model (2) on TMP estimation, we perform the following experiments for each case: 1), TMP estimation with standard model (2) and known pacing locations; 2) TMP estimation with standard model (2) and pacing locations unknown; electrical stimuli are applied on regular first-excited ventricular sites; and 3) TMP estimation with simultaneous parameter estimation. Results of TMP estimation are compared to simulations with 1) standard models and known pacing locations; 2) standard models and pacing at regular first-excited sites; 3), models with adjusted parameters obtained in dual TMP-parameter estimation. In all experiments, the longitudinal and transverse component of $\mathbf{D}$ is equal to 4.0 and 1.0, respectively [9]; e and k are fixed at 0.01 and 8[5]; a is fixed at 0.15 except in dual TMP-parameter estimation. We carry out each TMP estimation, unless otherwise stated, with $\mathbf{U} = \mathbf{0}$ and $\mathbf{P}_u = 0.01\mathbf{I}_n$ where $\mathbf{I}_n$ is an $n \times n$ identity matrix; $\mathbf{Q}_\omega$ is set to be a constant diagonal matrix $0.01\mathbf{I}_n$ and $\mathbf{R}_\nu$ is set to be time-invariant but spatially inhomogeneous, each diagonal component of which equal to the noise power calculated from 20dB SNR and time-averaged power of optical mapping TMP signal at the corresponding

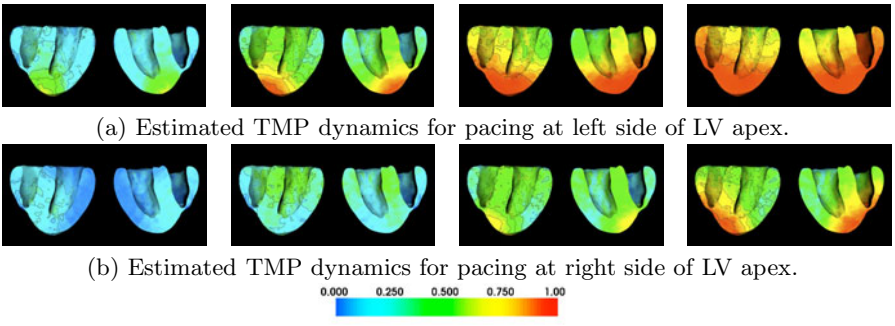

(a) Estimated TMP dynamics for pacing at left side of LV apex.

(b) Estimated TMP dynamics for pacing at right side of LV apex.

Fig. 2. Time sequence of TMP dynamics inside the 3D myocardium. Color encodes normalized TMP magnitude $(0-1)$; black contour represents TMP isochrones. Left to right: $13.9ms$, $23.2ms$, $32.5ms$, $41.8ms$, $51.2ms$, and $60.7ms$ with pacing starting at $0ms$ and the complete AP sequence scaled between $0-150ms$.

meshfree point. When parameter estimation is involved, we initialize homogeneous $a = 0.15$ for all meshfree points and $\mathbf{P}_u = 1\text{e-}004\mathbf{I}_n$; $\mathbf{Q}_{\omega_k^\Psi}$ is set to be a constant diagonal matrix $0.01\mathbf{I}_n$ and $\mathbf{R}_\nu$ is the same as described in TMP estimation. Electrical stimuli are applied with $5ms$ duration. All the estimations and simulations are compared to the optical mapping data for evaluating the accuracy of TMP dynamics and activation time, where activation time is calculated as the time instant with maximum first derivative of the AP upstroke; we implemented our own method for extracting activation time and apply it to both the optical mapping data and our results.

3 Results

Because of the high computational requirement, so far we only have results for case 2, including pacing at left side and right side of LV apex epicardium. Table 1 lists the accuracy of the aforementioned 3 types of TMP estimations and 3 types of TMP simulations compared to the optical mapping data, including the absolute error of activation time, relative root mean squared error and correlation coefficient of TMP sequence, respectively. As shown, because of the simplicity of the model (2), simulations with standard parameters (known or unknown pacing locations) are far away from subject-specific TMP mapping data; in comparison, while these models are used as constraints in our framework, the results of TMP estimation are in good accordance with the subject's measurement. Furthermore, estimations with the 3 type of constraints deliver similar accuracy, with dual TMP-parameter estimation in general showing the highest accuracy. Fig 2 shows the results of TMP dynamics inside the 3D myocardium for left and right side pacing in case 2, obtained with simultaneous parameter estimation. Fig 3 shows the corresponding activation isochrones on the epicardium compared to that extracted from optical mapping.

As to the possibility of parameter personalization for a predictive cardiac electrophysiological model, as shown in Table 1, compared to simulations with

Table 1. Difference of TMP estimations and simulations from optical mapping. EP: Estimation with standard parameters and known pacing locations; EE: Estimation with standard parameters and regular first-excited sites; ED: Estimation with simultaneous parameter estimation. SP: Simulation with standard parameters and known pacing locations; SE: Simulation with standard parameters and regular first-excited sites; SD: Simulation with parameter estimated from ED. Err(AT): absolute error of activation time in ms; RRMSE(TMP) and CC(TMP): relative root mean squared error and correlation coefficient of TMP signals. Best results highlighted with blue among estimations and simulations, respectively.

Left Side	EP	EE	ED	SP	SE	SD
Err(AT)	9.84 ± 10.04	9.44 ± 8.80	9.68 ± 9.56	64.44 ± 32.59	84.13 ± 39.10	53.04 ± 31.89
RRMSE(TMP)	0.10 ± 0.03	0.09 ± 0.02	0.08 ± 0.03	0.7 ± 0.18	0.74 ± 0.18	0.54 ± 0.18
CC(TMP)	0.55 ± 0.07	0.56 ± 0.07	0.57 ± 0.08	0.24 ± 0.05	0.21 ± 0.07	0.38 ± 0.13
Right Side	EP	EE	ED	SP	SE	SD
Err(AT)	6.72 ± 17.71	7.66 ± 20.11	7.38 ± 20.11	125.18 ± 37.27	131.18 ± 41.46	109.30 ± 40.52
RRMSE(TMP)	0.11 ± 0.04	0.09 ± 0.03	0.08 ± 0.03	1.01 ± 0.23	1.03 ± 0.24	0.94 ± 0.21
CC(TMP)	0.62 ± 0.08	0.62 ± 0.08	0.63 ± 0.08	0.16 ± 0.05	0.15 ± 0.06	0.19 ± 0.14

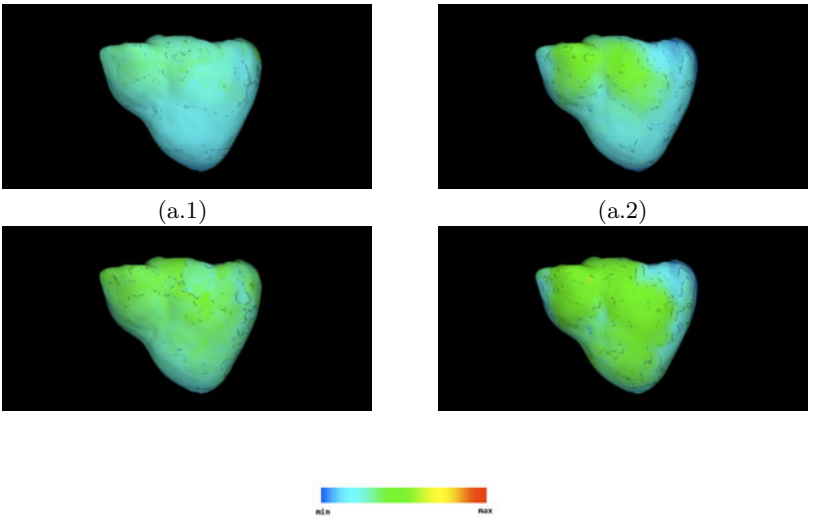

Fig. 3. Estimated activation isochrone (a.1, b.1) compared to that extracted from (a.2, b.2). Color encodes scaled activation time ($0 - 150$ms); black contour represents activation time isochrones. (a) Pacing at left side of LV apex. (b) Pacing at right side of LV apex.

standard parameters, simulations with parameters adjusted from optical mapping data do show substantially smaller difference from subject's data. However, they are still much further away from real subject-specific conditions compared to the results of TMP estimation. This agrees with our earlier analysis that it is challenging to produce a personalized cardiac electrophysiological model through

parameter adjustment, because of the existence of other modeling errors such as the simplified structure and unknown initial conditions.

4 Conclusion and Discussion

In this paper, we present an approach to estimate subject-specific TMP dynamics inside the 3D myocardium using optical mapping data on local epicardium. Rather than pursuing a personalized cardiac electrophysiological model by parameter adjustment, this approach uses simple, standard models as constraints to estimate three-dimensionally distributed TMP dynamics for individual subjects from a partial observation. While these simplified models *per se* produce TMP dynamics that are drastically different from subject-specific conditions, under their constraints, our approach is able to reconstruct valid TMP dynamics for individual subjects under different conditions. We also investigate the possibility of parameter estimation for the cardiac electrophysiological model: while simulations with the estimated parameter show evident improvement over the standardly-parameterized model, future investigation is needed in order to achieve accuracy as high as those obtained in TMP estimation.

As the electrophysiological model (1) in use is simplified from the original model presented in [5], it involves not only parameter errors but also, maybe more importantly, errors from simplified structure and unknown initial conditions. As a result, as explained earlier, it would be rather challenging to personalize the electrophysiological model by attributing all the uncertainties to model parameters. Instead, the current approach uses this type of simplified models as a tool, to guide the extraction of subject-specific information from data. Using only partial observation, in this case the optical mapping on a local region of epicardium, this approach is able to reconstruct the TMP dynamics not only on the epicardium but also inside the 3D myocardium. With a more advanced and sophisticated model, parameter estimation might produce a better personalized model. Given limited data, however, the identifiability of model parameters remains a critical issue, particularly for details inside the 3D myocardium where measurement is not usually available.

In the provided datasets, optical mapping data is provided at 3.7ms sampling rate with 1023 sampling points. As explained earlier, because of the relatively coarse spatial resolution of the meshfree model of the ventricles, temporal resolution needed for discretizing (1) is often one or two orders smaller (t_d^s at the order of $10^{-1} - 10^{-3}$). Therefore, on average 10^3 steps of filtering steps need to be executed for one AP cycle. This leads to a high cost of computational time for the current experiment: on a MacPro desktop with 2×3GHz Quad-Core Intel Xeon processor, each complete filtering step requires ~ 2 minutes to execute and therefore each TMP estimation experiment requires ~ 60 hours. As a result, it is computational impractical for us to consider the complete sequence of optical mapping data with three or four AP cycles. At the current stage we only consider one AP cycle for estimation. In consequence, if the pacing is applied at the same location for the same subject, we are not able to utilize the extra information

from different pacing frequencies. For case 1, because the optical mapping is provided with the same pacing locations at three different frequencies, we only consider the dataset obtained at 0.7Hz pacing. For case 2, we consider data from the two different pacing locations.

On additional factor contributing to the error of TMP estimations and simulations might come from the value of parameter a, which is set to be 0.15 in the current study. We are currently performing a new set of experiments with $a = 0.1$ according to [10]. These experiments as well as those for case 1 are still in computation. The feasibility of applying high performance computing to the current approach is one major direction of ongoing research, the fulfillment of which could largely improve the clinical applicability of the presented framework.

References

1. Wang, L., Zhang, H., Wong, K., Liu, H., Shi, P.: Physiological-model-constrained noninvasive reconstruction of volumetric myocardial transmembrane potentials. IEEE Transactions on Biomedical Engineering 5(2), 296–315 (2010)
2. Chinchapatnam, P., Rhode, K.S., Ginks, M., Rinaldi, C.A., Lambiase, P., Razavi, R., Arridge, S., Sermesant, M.: Model-based imaging of cardiac apparent conductivity and local conduction velocity for diagnose and planning of theropy. IEEE Transactions on Medical Imaging 27(11), 1631–1641 (2008)
3. Pop, M., et al.: Fusion of optical imaging and mri for the evaluation and adjustment of macroscopic models of cardiac electrophysiology: A feasibility study. Medical Image Analysis 13, 370–380 (2009)
4. Durrer, D., Dam, R., Freud, G., Janse, M., Meijler, F., Arzbaecher, R.: Total excitation of the isolated human heart. Circulation 41, 899–912 (1970)
5. Aliev, R.R., Panfilov, A.V.: A simple two-variable model of cardiac excitation. Chaos, Solitions & Fractals 7(3), 293–301 (1996)
6. Liu, G.: Meshfree Methods. CRC Press, Boca Raton (2003)
7. Julier, S.J., Uhlmann, J.K.: A new extension of the kalman filter to nonlinear systems. In: International Symposium on Aerospace/Defense Sensing, Simulation, and Controls, pp. 182–193 (1997)
8. Wang, L.: Personalized Noninvasive Imaging of Volumetric Cardiac Electrophysiology. PhD thesis, Rochester Institute of Technology (May 2009)
9. Rogers, J.M., McCulloch, A.D.: A collocation-galerkin finite element model of cardiac action potential propagation. IEEE Transactions on Biomedical Engineering 41(8), 743–757 (1994)
10. Nash, M.P., Panfilov, A.V.: Electromechanical model of excitable tissue to study reentrant cardiac arrhythmias. Progress in Biophysics and Moledular Biology 85, 501–522 (2004)

Estimation of Reaction, Diffusion and Restitution Parameters for a 3D Myocardial Model Using Optical Mapping and MRI

J. Relan[1], M. Pop[2], H. Delingette[1],
G.A. Wright[2], N. Ayache[1], and M. Sermesant[1,3]

[1] INRIA, Asclepios Project, Sophia Antipolis, France
[2] University of Toronto, Sunnybrook Health Sciences Centre, Canada
[3] King's College London, Division of Imaging Sciences, St. Thomas Hospital, UK

Abstract. Personalisation, i.e. parameter estimation of a cardiac ElectroPhysiology (EP) model is needed to build patient-specific models, which could then be used to understand the true complex dynamics involved in patient's pathology. In this paper, we present a personalisation method for a simplified ionic 3D EP model, the Mitchell-Schaeffer model. The personalisation is performed by optimising the 3D model parameters, which represent the tissue conductivity, Action Potential Duration (APD) and restitution for APD and conduction velocity, using only 2D epicardial surface data obtained *ex-vivo* from optical imaging of large porcine healthy hearts. We are also able to estimate all of the model parameters, thus resulting in a total heart-specific 3D EP model. Finally, we also test the sensitivity of the described personalisation results with respect to different pacing locations.

1 Introduction

Modelling of the cardiac electrophysiology has been an important research interest for the last decades, but in order to translate this work into clinical applications, there is an important need for personalisation of such models, i.e. estimation of the model parameters which best fit the simulation to the clinical data. Cardiac model personalisation is required to develop predictive models that can be used to improve therapy planning and guidance. For instance, RadioFrequency (RF) ablation therapy on patients suffering from Ventricular Tachycardia (VT) has a success rate of only 50% due to non availability of a clinical consensus on the optimum RF ablation patterns [1]. Thus the procedure is a trial and error process and highly dependent on cardiologist's experience. Personalised cardiac models can provide a way to test *in silico* different RF ablation patterns, consecutively increasing the success rate of RF therapy.

A variety of mathematical models describing the cardiac electrophysiology have been developed and simulated at various scales. These models can be broadly categorised into three main categories: Ionic Models (IM), Phenomenological Models (PM) and Eikonal Models (EM). IM [2] characterise ionic currents flowing through the cardiac cell membrane and have a lot of parameters

O. Camara et al. (Eds.): STACOM-CESC 2010, LNCS 6364, pp. 270–280, 2010.

and variables, thus are not well suited to solve the inverse problem. EM [3] are very simple, describing only the time at which a depolarisation wave reaches a given point without precisely modelling the action potential. At the intermediate level are PM [4], which describe the action potential generation and propagation along the cell membrane. Here, we personalise a simplified generic ionic model, the Mitchell-Schaeffer (MS) model [5], modelling the action potential as a combination of sodium (Na^+), calcium (Ca^{2+}) and potassium (K^+) phenomenological ionic currents.

In the past years, authors have focused on the parameter estimation of the PM and MS model on 3D volumes [6,7,8,9] using optical and MR data. In these works, the tissue conductivity parameter was estimated only on 17 American Heart Association (AHA) subdivisions of the bi-ventricular myocardium. Also not all model parameters were estimated. The two main contributions of this paper are: 1) Estimation of the tissue conductivity parameter using a multi-resolution technique, and 2) Estimation of all model parameters, simulating tissue features such as local Conduction Velocity (CV), Action Potential Duration (APD) and APD and CV restitutions. Thus resulting in a total heart-specific 3D electrophysiology model.

2 3D Electrophysiology Model Simulation

The MS model [5] is a generic simplified ionic model and is described by the following system of Partial Differential Equations (PDE):

$$\begin{cases} \partial_t u = div(D\nabla u) + \dfrac{zu^2(1-u)}{\tau_{in}} - \dfrac{u}{\tau_{out}} + J_{stim}(t) \\ \partial_t z = \begin{cases} \dfrac{(1-z)}{\tau_{open}} \; if \; z < z_{gate} \\ \dfrac{-z}{\tau_{close}} \quad if \; z > z_{gate} \end{cases} \end{cases} \tag{1}$$

where u is the normalised action potential variable, and z is the gating variable for Na^+ influx, which depicts the repolarisation phase. $J_{in} = (zu^2(1-u))/\tau_{in}$ represents the combination of inward Na^+ & Ca^{2+} phenomenological ionic currents and $J_{out} = -u/\tau_{out}$ represents the outward K^+ phenomenological ionic current. J_{stim} is the stimulation current at the pacing location. The parameter τ_{in} mostly depicts the cardiac tissue conductivity for the model reaction part. τ_{in} and τ_{out} jointly controls the shape of CV and APD restitutions. The parameter τ_{open} mainly controls the slope of the APD restitution curves and τ_{close} is directly related to the asymptotic value of the APD restitution curves.

The diffusion term in the model is controlled by the diffusion tensor D. This spatial diffusion can be related to a pseudo-conductivity of the cardiac tissue. In the longitudinal direction of the fiber, this pseudo-conductivity is set to a parameter d and to $d/2.5^2$ in the transverse directions [4]. The MS model is spatially integrated using a linear tetrahedral mesh of the bi-ventricular myocardium, taking into account the fiber orientation as well, and is temporally

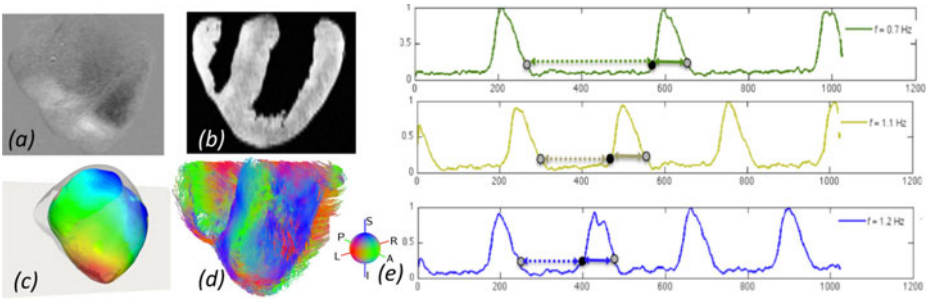

Fig. 1. (a) A snapshot from 2D+t optical mapping data recorded for the electrical activity (antero-lateral view), (b) A slice from DT-MRI volume acquired for geometry and fiber orientations, (c) The optical and MR fusion showing the stereoscopic surface (transparent) fused with the volumetric mesh along with projection of the extracted features (here depolarisation time isochrones) from the optical data to the volumetric mesh, (d) Tracking of fibers from DT-MRI, (e) The filtered optical signals for a pixel of dataset 1 showing the $APD - DI$ pairs for various pacing frequencies.

integrated using an optimum time integration scheme (MCNAB), which was tested in details in [10,7]. The electrical time-step used here is $\delta t = 0.1ms$ on a mesh with a mean edge length of $h = 1.5mm$.

3 Optical and MR Dataset Processing

In this paper, we performed the adjustments on a healthy porcine heart model. The experimental set-up is described in details in [11]. The acquired data consists of Diffusion Tensor MRI (DT-MRI) representing geometry and fiber orientation (Fig 1(b & d)), and epicardial optical recordings (Fig 1(a & e)), from which we compute features (such as the Depolarisation Time (DT) isochrones, the APD maps and the CV and APD restitution). The features are then projected on the volumetric myocardial mesh derived from the DT-MRI (Fig 1(c)) as explained in [6]. This results in features on the epicardial surface of the 3D bi-ventricular model. Here, we used 2 *ex-vivo* hearts, which were MR and optically imaged for steady state cycles. The datasets were prepared as follows: one heart was optically imaged to produce 3 different optical datasets, all paced at one location (at the apex of the LV epicardium), but for 3 different pacing frequencies (Fig 1(e) & Fig 2):

– *Dataset 1*: 0.7 Hz, 1.1 Hz and 1.2 Hz

Second heart was optically imaged to produce 2 different optical datasets, paced at a frequency of 1.1 Hz, but obtained using 2 different pacing locations (Fig 2) Near the apex of:

– *Dataset 2*: Right Ventricle Epicardium (RV-Epi) and Left Ventricle Endocardium (LV-Endo).

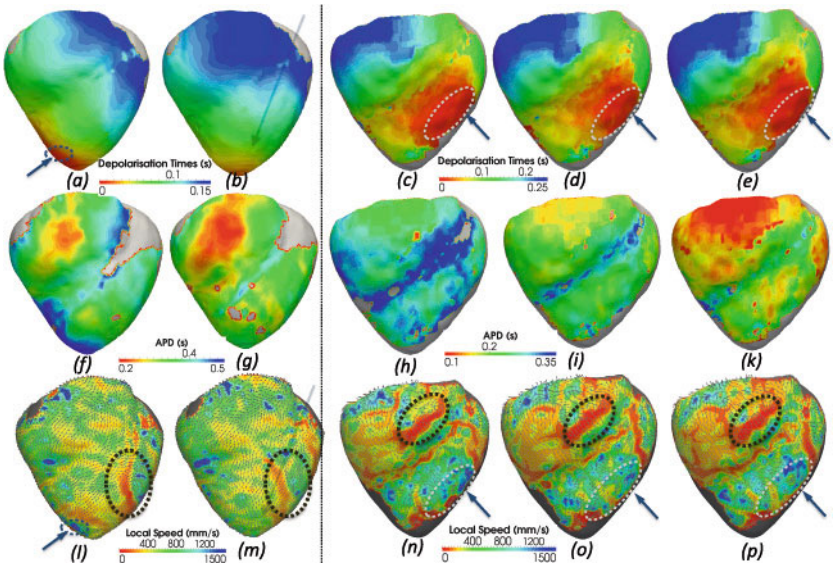

Fig. 2. The first row shows epicardial DT isochrones, second row shows the APD maps and third row shows the estimated local conduction velocity depicting the tissue conductivity. First two columns are for dataset 2 and remaining three columns are for dataset 1. Arrows and white dotted contours highlight the pacing locations and black dashed contours highlight areas of low tissue conductivity.

Although these were healthy hearts, we could identify discrete areas of low conductivity (see black dashed contour in Fig 2). This was most likely due to tissue becoming ischemic around a small collateral blood vessel, partially occluded by an air bubble accidentally trapped into the perfusion line, resulting in oxygen deprivation of the tissue and further installation of acute ischemia and cellular uncoupling.

4 Personalisation Method

Estimation of the model parameters that result in a simulation which is similar to the measured data is defined as personalisation. Here, we perform model personalisation by matching features such as the DT isochrones, the APD maps and the CV and APD restitution all derived from the optical data. Dataset 2 was used for personalisation using DT isochrones and APD maps only, whereas the dataset 1 was used for personalisation using additional features such as APD and CV restitutions.

4.1 Feature: Depolarisation Times

The epicardial DT isochrones show variations in CV of the propagating action potential wave over the epicardial surface.The local conduction velocity CV^{msd}

is estimated from the spatial gradient of these measured DT isochrones T on the epicardial surface as, $1/CV^{msd} = \|\nabla T_x\|$ [4]. Due to the imaging and registration errors, the DT isochrones could present local variations. To avoid the amplification of this noise by the spatial derivatives of the DT, we smooth CV^{msd} by averaging it over a neighbouring area, weighted by the Euclidean distance between the vertices and the point where the speed is computed. This feature is used for estimation of parameter d, which is achieved in the following two successive phases:

Calibration: This step is used to initialise the model parameter values using analytical relationships between the measures and the parameters. The calibration function used here is similar to [7] and is given as $c(d) = \alpha\sqrt{d}+\beta$, where c is the CV and the constants α and β are determined by performing several model simulations for a range of d values and computing the corresponding c, and then fitting the function in a non-linear least squares sense to the measures c. Once the relationship is estimated, it is used to determine the initial parameter value d for the median value of c computed for the actual reference data.

Iterative Adjustment: This step is used to optimise the parameter d locally in space, using a multi-resolution technique, with calibration result as an initial guess. In order to start the domain decomposition, we divide the left ventricle into 17 zones as defined by AHA and a similar division of 9 zones for the right ventricle is performed. The algorithm used here is a trust region method [12] and is implemented using the Trilinos solver package[1]. Here we use an objective function that minimises the sum of squared differences (SSD) between the simulated and the measured depolarisation times by iteratively adjusting the d parameter value for each zone. Thereafter, when the SSD error remains stagnant, we perform another domain decomposition level where zones of higher error are divided into 4 (Fig 4)and so on. In order to have smoother connectivity between zone parameters and to avoid piecewise parameter functions, we estimate parameter d on the zonal barycenter and perform a diffusive parameter regularisation as explained in the next subsection.

4.2 Feature: Action Potential Duration

For τ_{close}, the maximum APD for a single cardiac cycle is directly given by the model [5] as follows: $APD = \tau_{close} ln(1/h_{min})$ where $h_{min} = 4\tau_{in}/\tau_{out}$. For dataset 2, we only have one measured APD available from the data, we chose to adjust τ_{close}, while keeping the other parameter values from the literature [5]. It is defined by the model that c has no relationship with τ_{close}, which provides no coupling between the APD and the CV. Thus we can simultaneously adjust parameter d and τ_{close}. The defined relationship between τ_{close} and APD remains valid also in 3D thus allowing us to directly estimate it locally at each vertex. The parameter τ_{close} is estimated on the epicardial surface having measures. To propagate the τ_{close} values from the epi to endocardium, we diffuse the τ_{close}

[1] http://trilinos.sandia.gov/

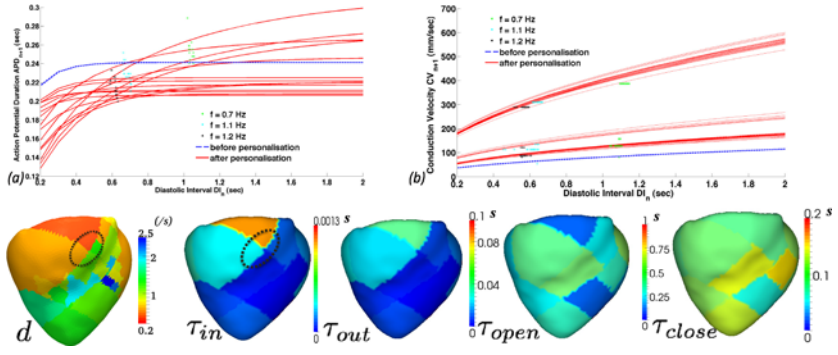

Fig. 3. For dataset 1, (a) shows the fitting of the model restitution to the extracted APD restitution points from different pacing frequency data for a few number of pixels. (b) is the same but for CV restitution. Lower row shows the estimated parameter vector θ, with parameter d estimated using multi-resolution.

spatially in the myocardium using $div(\nabla P) = 0$ in myocardium with $P = \tau_{close}$ estimated on epicardium. The same is done to diffuse parameter d with $P = d$ estimated at the zonal barycenter as explained before.

4.3 Feature: CV and APD Restitution

Restitution defines the dependency of the next cycle APD (resp. CV) on the previous cycle Diastolic Interval (DI). For a constant pacing frequency f, a steady state Basic Cycle Length (BCL) remains constant : $BCL = 1/f = APD + DI$ and thus $APD - DI$ relationship remains constant. In order to extract the observed macroscopic restitution, we need to have the heart optically imaged for multiple pacing frequencies, thus resulting in multiple BCL (Fig 1(e)) and multiple $APD - DI$ pairs for a spatial point (pixel). Thus this personalisation step was performed only on Dataset 1. APD restitution curve for MS model is explicitly formulated [5] as

$$f(DI) = APD = \tau_{close} \ln\left(\frac{h(DI)}{h_{min}}\right) \tag{2}$$

where $h(DI) = 1 - (1 - h_{min})\, e^{-DI/\tau_{open}}$, with $f(DI) = APD$ is the succeeding APD and DI is the preceding DI. Similarly also CV restitution curve is derived [5] as

$$g(DI) = \left(\frac{1}{4}\left(1 + \sqrt{1 - \frac{h_{min}}{h(DI)}}\right) - \frac{1}{2}\left(1 - \sqrt{1 - \frac{h_{min}}{h(DI)}}\right)\right)\sqrt{\frac{2dh(DI)}{\tau_{in}}} \tag{3}$$

with $g(DI) = CV$ as the succeeding CV. From Eq 2 & Eq 3, we can observe parameter ratio ($h(DI)$) controlling both APD & CV restitution. This shows a coupling between both restitutions. Thus we chose to estimate the parameters

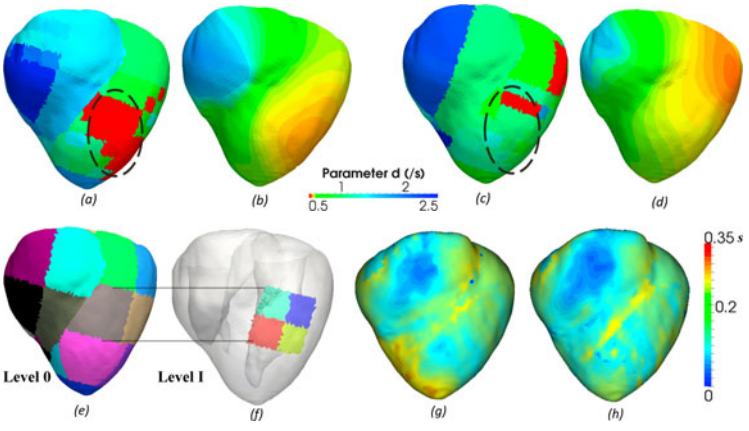

Fig. 4. For dataset 2, (a) is the final domain decomposition for parameter d after personalisation for RV-Epi and (b) parameter d after diffusive regularisation, whereas (c) & (d) are the same but for LV-Endo, (e) & (f) levels for the multi-resolution method (Level 0 represents the AHA subdivision, Level I is the subdivision of a zone into 4), (g) & (h) are the parameter τ_{close} maps for RV-Epi and LV-Endo (respectively).

for CV restitution (h_{min}, τ_{in}, d) and APD restitution (h_{min}, τ_{open}, τ_{close}) in a joint manner, by having a cost function C_r which minimises the error on both restitution curves. C_r is given as

$$C_r = \min_{\theta} \sum_{j=1}^{N} ((f(DI^j, \theta) - APD^j)^2 + (g(DI^j, \theta) - CV^j)^2) \tag{4}$$

where N is the total number of frequency data, APD^j (resp. CV^j) is the measured APD (resp. CV) for the preceding measured DI at the optical data pixel, and $\theta = [\tau_{close}, h_{min}, \tau_{open}, \tau_{in}]$ is the estimated parameter vector. θ is estimated locally at each pixel of the optical data and then a mean value for each AHA zone is computed and set to the zonal barycenter in the mesh. The parameter optimisation used here is a constrained Active-Set Algorithm, which uses a sequential quadratic programming method. The parameter d is then adjusted using iterative adjustment for a single cycle at the lowest pacing frequency ($f = 0.7$ Hz), since it represents the asymptotic value of the CV restitution curve. This is done in order to have the parameter d take into account the CV due to the wave front curvature on the volumetric mesh.

5 Results

5.1 Application to Dataset 1

The model is personalised to dataset 1 by estimating the parameter vector θ (explained in section 4.3), using restitution defined with steady state cycles from

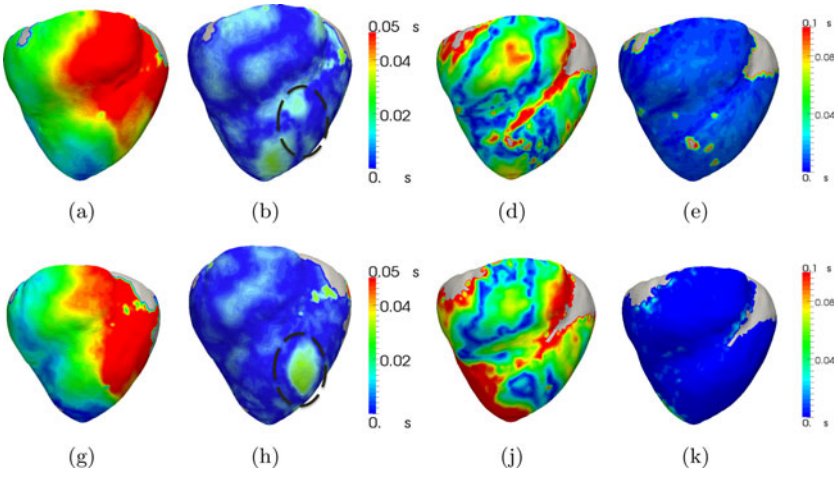

Fig. 5. For dataset 2, first row stands for LV-Endo and the second row for RV-Epi. DT error maps before (a,g) and after (b,h) personalisation. APD error maps before (d,j) and after (e,k) personalisation.

different pacing frequencies. Before personalisation, the model is simulated using standard parameter values [5]. The absolute mean square error C_r (Eq 4), before personalisation is 20.35 reduced to 0.54 after personalisation, which implies a good fit of the both APD and CV restitution curves to the data, as shown in Fig 3(a & b). The zonal parameters estimated show clear differences in values of τ_{in} & τ_{out} for LV and RV. τ_{close} shows lower values at the pacing location and RV zones, thus showing APD heterogeneity between the LV and RV. τ_{open}, a parameter controlling the APD restitution slope, shows lower values (flat slope) near the pacing and basal regions compared to the remaining epicardium. The parameters depicting the tissue conductivity from the diffusion term (d) and reaction term (τ_{in}), are also able to locate the low conductivity area observed in the dataset 1 (see black dashed contour in Fig 2 & 3). Also parameter d shows an overall map of low conductivity over the heart, compared to dataset 2 (see Fig. 3 & 4), which is confirmed by higher total activation time ($\approx$ 250 ms) for this dataset.

5.2 Application to Dataset 2

The model is personalised to dataset 2 using DT isochrones and APD maps for two different pacing locations as explained before. A comparison of the estimated parameter values and APD and DT errors after personalisation for both pacing locations, helps us also evaluate the sensitivity of the described personalisation method. As the electrophysiology personalisation is performed on the same heart but under different pacing scenarios, we should expect the personalisation results to be similar, showing low sensitivity of the personalisation method to different pacing locations.

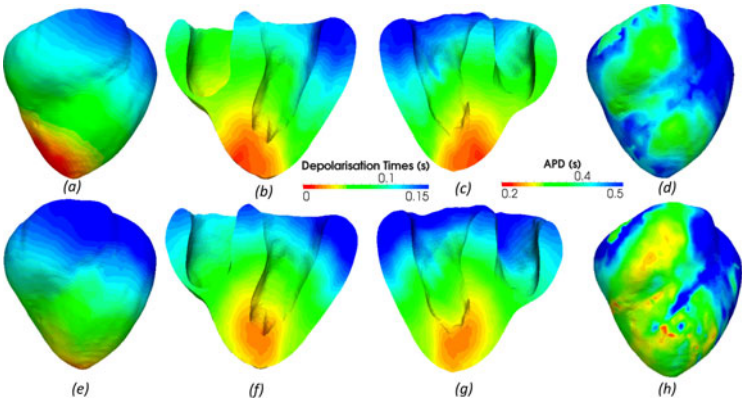

Fig. 6. For dataset 2, simulated volumetric DT isochrones (a,b,c) and APD maps (d) for LV-Endo, after personalisation. Similarly for RV-Epi (e,f,g & h) after personalisation. (For true experimental DT & APD values refer Fig 2)

Comparison of the Estimated Parameter Values and Errors: From DT error maps of two different pacing locations (Fig.5(b) and 5(h)), we can observe that the personalisation method does reduce the overall error with both pacing locations. It is also able to locate the areas of low CV irrespective of the pacing location (black dashed contour in Fig 2 & 5). APD error maps also show less error with both pacing locations (Fig.5(e) and 5(k)). This demonstrates low sensitivity of the personalisation method application to different pacing locations. Fig.4 and Table.1 show a qualitative and quantitative comparison of the estimated parameter d for both pacing locations. Here we can observe that the parameter values are mostly similar for both pacing locations, except for pacing location LV endocardium, where the low conductivity area is moved more towards the base as probably the purkinje system is recruited (activated) using the endocardial pacing location thus increasing the conduction velocity. On the other hand, the locally estimated parameter τ_{close} for both pacing locations is very similar as shown in Fig.4 and Table.1. This analysis does confirms the low sensitivity of the estimated parameter values to various pacing locations.

Table 1. Comparison of the estimated parameter values and the mean errors for personalisation using dataset 2. (Mean-Δ, Standard Deviation-σ)

Pacing Location	Parameter $d \pm \sigma$ (s^{-1})		DT Error $\Delta \pm \sigma$ (ms)	Parameter $\tau_{close} \pm \sigma \times 10^{-4}$ (ms)		APD Error $\Delta \pm \sigma$ (ms)
	LV	RV		LV	RV	
LV-Endo	0.95 ± 0.03	1.36 ± 0.16	4.22 ± 6.75	0.22 ± 1.25	0.20 ± 4.90	4.98 ± 8.89
RV-Epi	0.96 ± 0.03	1.38 ± 0.11	2.54 ± 5.12	0.22 ± 3.04	0.21 ± 6.81	4.73 ± 5.57

6 Discussion and Conclusion

In this work, we described a personalisation method for a simplified ionic MS model in 3D, using epicardial activation maps obtained with optical imaging. The model personalisation is done using the measured CV, APD and their restitution properties. The estimated pseudo-conductivity parameter d map is able to locate low conductivity areas for both datasets, using a multi-resolution technique. All the model parameters can be estimated when data is acquired at multiple frequencies and thus exhibits the restitution properties. Next, we evaluated the sensitivity of our personalisation method to different pacing scenarios and observed the reproduction of the same estimated parameter values irrespective of the pacing location. Such fairly robust cardiac electrophysiology personalisation with different pacing locations from epi- or endocardium opens up possibilities for clinical applications, where typically only the endocardial surface can be mapped and with often an ambiguity on the pacing location. Nevertheless, we also need to validate the model predictions, at different heart rates and pacing locations, which is important in arrhythmias. This is the topic which will be addressed in the next step.

Acknowledgements

The research leading to these results was partially funded by the the euHeart project (FP7/2007-2013 under grant agreement n 224495).

References

1. Aliot, E., Stevenson, W., Almendral-Garrote, J.: Ehra/hrs expert consensus on catheter ablation of ventricular arrhythmias. Europace 11, 771–817 (2009)
2. Noble, D.: A modification of the Hodgkin-Huxley equations applicable to Purkinje fibre action and pace-maker potentials. Physiology 160, 317–352 (1962)
3. Sermesant, M., Konukoglu, E., Delingette, H., Coudiere, Y., Chinchaptanam, P., Rhode, K., Razavi, R., Ayache, N.: An anisotropic multi-front fast marching method for real-time simulation of cardiac electrophysiology. In: Sachse, F.B., Seemann, G. (eds.) FIHM 2007. LNCS, vol. 4466, pp. 160–169. Springer, Heidelberg (2007)
4. Keener, J., Sneyd, J.: Mathematical Physiology. Springer, Heidelberg (1998)
5. Mitchell, C.C., Schaeffer, D.G.: A two current model for the dynamics of cardiac membrane. B. of Mathematical Biology 65, 767–793 (2003)
6. Lepiller, D., Sermesant, M., Pop, M., Delingette, H., Wright, G.A., Ayache, N.: Cardiac electrophysiology model adjustment using fusion of mr and optical imaging. In: Metaxas, D., Axel, L., Fichtinger, G., Székely, G. (eds.) MICCAI 2008, Part I. LNCS, vol. 5241, pp. 678–685. Springer, Heidelberg (2008)
7. Relan, J., Sermesant, M., Delingette, H., Pop, M., Wright, G.A., Ayache, N.: Quantitative comparison of two cardiac electrophysiology models using personalisation to optical and mr data. In: ISBI, pp. 1027–1030 (2009)

8. Relan, J., Sermesant, M., Pop, M., Delingette, H., Sorine, M., Wright, G., Ayache, N.: Parameter estimation of a 3d cardiac electrophysiology model including the restitution curve using optical and mr data. In: IFMBE Proceedings of World Congress on Medical Physics and Biomedical Engineering, pp. 1716–1719 (2009)
9. Relan, J., Sermesant, M., Pop, M., Delingette, H., Sorine, M., Wright, G., Ayache, N.: Volumetric prediction of cardiac electrophysiology using a heart model personalised to surface data. In: MICCAI Workshop on Cardiovascular Interventional Imaging and Biophysical Modelling - CI2BM 2009, pp. 19–27 (2009)
10. Ethier, M., Bourgault, Y.: Semi-implicit time discretization schemes for the bidomain model. Siam J. Numer. Anal. 46(5), 2443–2468 (2008)
11. Pop, M., Sermesant, M., Lepiller, D., Truong, M.V., McVeigh, E.R., Crystal, E., Dick, A., Delingette, H., Ayache, N., Wright, G.A.: Fusion of optical imaging and mri for the evaluation and adjustment of macroscopic models of cardiac electrophysiology: A feasibility study. Med. Image Anal. (July 2008)
12. Conn, A.R., Gould, N.I.M., Toint, P.: Trust Region Methods. SIAM, Philadelphia (2000)

Personalization of Fast Conduction Purkinje System in Eikonal-Based Electrophysiological Models with Optical Mapping Data

Oscar Camara[1,2], Ali Pashaei[1,2], Rafael Sebastian[3], and Alejandro F. Frangi[1,2,4]

[1] Center for Computational Imaging and Simulation Technologies in Biomedicine (CISTIB), Universitat Pompeu Fabra, Barcelona, Spain
oscar.camara@upf.edu
[2] Networking Biomedical Research Center on Bioengineering, Biomaterials and Nanomedicine (CIBER-BBN), Barcelona, Spain
[3] Computational Multi-Scale Physiology Lab, Universitat de València, València, Spain
[4] Institució Catalana de Recerca i Estudis Avançats (ICREA), Barcelona, Spain

Abstract. We present a pipeline for the personalization of model-based Purkinje fast conduction system using fast electrophysiological models and optical mapping data acquired from ex-vivo porcine hearts. The regional density of the Purkinje terminals as well as the latest endocardial activation time were the parameters personalized in an iterative procedure maximizing the similarity between the outcome of the electrophysiological simulations and measurements obtained from optical mapping data. We used a fast wave-front Eikonal-based electrophysiological model that generated the depolarization time maps that were subsequently compared with measurements at each iteration of the optimization stage. The pacing site given by the experimental data and the optimized Purkinje system were introduced into the electrophysiological model. We obtained a regional distribution of Purkinje end-terminals in agreement with findings in the literature. Nevertheless, remaining differences between simulations and measurements after personalization suggest that epicardial data obtained from optical mapping data might not be sufficient to optimize the Purkinje system, which is basically located at the endocardium. On the other hand, the developed pipeline could also be used with endocardial data on electrical activation provided by non-contact or contact mapping system.

Keywords: Purkinje fast conduction system, personalization, electrophysiological models, optical mapping.

1 Introduction

Advances in computational physiology of the heart in recent years have improved our understanding of the patho-physiological mechanisms underlying

O. Camara et al. (Eds.): STACOM-CESC 2010, LNCS 6364, pp. 281–290, 2010.

heart failure, advancing towards a more patient-specific diagnosis as well as pre-operative *in silico* interventional planning [1].

The personalization of these computational models with patient data such as ventricular geometries derived from images, it substantially improves the realism of the resulting electromechanical simulations [2,3]. However, there are some parameters that cannot currently be measured *in vivo* such as myocardial fibre orientation or Purkinje fibres, which have strong influence on the electromechanical behaviour of the heart. In general, this type of non-observable data is incorporated into computational models in the form of analytical models that are tuned to better fit measurements obtained from experimental models. For instance, Streeter [4] performed some experiments with canine hearts to model myocardial fibre distribution, represented by the helix and transversal fibre angles, varying from the epicardium to the endocardium. The Streeter model is currently the most popular strategy to incorporate fibre orientation into the electromechanical models, although some improvements have also been suggested [5,6,7].

In addition to fibre orientation, other sub-structural information which is very critical for the outcome of the electrophysiological simulations include the presence of the fast conduction system involving Purkinje fibres. In Romero et al. [8], a consistent overestimation of the degree of electrical dyssynchrony was found when assessing Cardiac Resynchronization Therapy (CRT) scenarios when omitting the Purkinje system (PS). In a recent work [9], we developed a methodology to generate Purkinje trees specific to a given biventricular geometry and following some rules to visually reproduce the activation sequence reported experimentally by Durrer et al. [10]. However, several parameters of the Purkinje tree generation such as the density of end terminals were not personalized and were chosen according to literature.

In this work, we present a pipeline for the personalization of model-based Purkinje fast conduction systems using fast electrophysiological models and optical mapping data acquired from ex-vivo porcine hearts. The regional density of the Purkinje terminals as well as the latest endocardial activation time were the parameters personalized in an iterative procedure maximizing the similarity between the outcome of the electrophysiological simulations and measurements obtained from optical mapping data.

2 Experimental Data

Pop et al. [11] designed an experimental model on healthy ex-vivo porcine hearts, containing cardiac geometry and fibre orientations from MRI as well as epicardial transmembrane potential from optical mapping. The available electrophysiological data comprised depolarization/repolarization times and isochrones as well as action potential duration maps for different pacing locations and different pacing frequencies, defined at the epicardium of some regions in two different biventricular geometries, as illustrated in Fig. 1. This data was provided to the participants of the MICCAI STACOM-CESC'10 challenge (`http://cilab2.upf.edu\stacom_cesc10`) for personalization purposes. The interested reader is

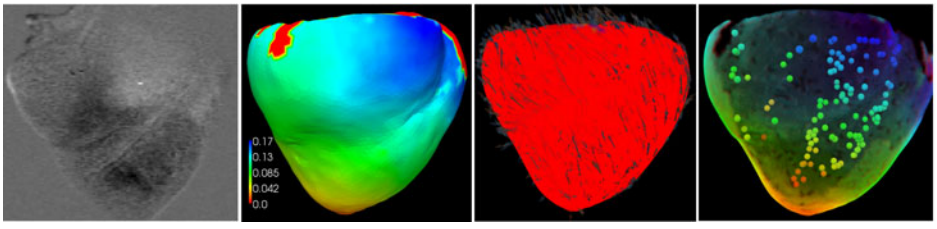

Fig. 1. Experimental data and sub-structural information. From left to right: optical mapping data (left) showing the action potential wave (black); depolarization times computed from the optical mapping data; fibre orientation extracted from DT-MRI; end-terminals of Purkinje showing the fast conduction system.

referred to Pop et al. [11] for a complete description of the data. In addition, binary segmentations and geometrical meshes as well as processed optical mapping and fibre orientation data was provided by INRIA researchers, who previously worked with this data [12].

We selected one of the two available datasets in the challenge, corresponding to two different ex-vivo porcine hearts, and used the available tetrahedral mesh with a *coarse* resolution, having 37923 nodes and 204841 elements rather than the fine mesh (460693 nodes and 2597710 elements). This choice was justified by the need of running a considerable number of simulations in the iterative procedure to optimize the Purkinje tree parameters. Measurements obtained with the left ventricular endocardial pacing location and with a pacing frequency of $1.1Hz$ was used in this work.

3 Methods

3.1 Generation of Purkinje Fast Conduction System

Due to the lack of patient-specific data on the Purkinje system of the subjects we defined a strategy to activate the heart in a realistic fashion. There are several ways to model the fast conduction system in electrophysiological simulations, varying the degree of model complexity and going from the most complete cellular-to-cellular interaction and cable models with Purkinje tree-like geometrical models [8] to just simulate the macroscopic effect in electrical wave propagation by selecting a set of endocardium points with earlier activation points and faster conduction velocities [13]. The most appropriate model will be different for different applications. In this work, we were interested on developing a personalization framework to assess the possibility of personalizing some of the most relevant parameters of the fast conduction system with optical mapping data. This means that we focused on simple and fast models that allowed us to embed the parameter optimization in an iterative procedure. Hence, in this work, the most important parameters to personalize were the number of end-terminals of the Purkinje system in different heart regions as well as the latest endocardial activation time.

Anatomical surface models for each subject were labeled to differentiate, endocardium and epicardium of LV and RV. In addition, the LV was divided into 17 zones as defined by American Heart Association and a similar division of 9 zones for the right ventricle was used. Subsequently, for a given number of Purkinje end-terminals per each of these 26 heart regions, they were spatially distributed within these regions using a random algorithm. Therefore, the density of end-terminals for the LV and RV regions were parameters introduced into the optimization procedure.

Since the activation times of the nodes would be imposed by the Purkinje structure, we choose not to optimize them. Instead we considered an apex to base, and endocardial to epicardial activation similar to the one observed by Durrer [10]. Following Durrer's observations, the last activated endocardial stimulus should be set to around 40ms and from this, the activation for the remaining stimuli could be computed as a function to the distance to the apex. Nevertheless, we introduced into the personalization procedure the last activated endocardial stimulus since the available experimental data had a very long total activation time ($170ms$) compared to Durrer's experiments. Finally, we took into account that measurements were acquired on pacing conditions by setting to $0ms$ the activation time of the nodes corresponding to pacing locations. Then, the activation time of the Purkinje terminal closest to the pacing nodes was estimated from their distance and the tissue conduction velocity. Fig. 2 shows two exemplary stimuli map generated for the biventricular geometry from the experimental data in a pacing scenario (left) and in normal sinus rhythm (right). We can observe in the figure that the earlier activated points are located in pacing site (the RV epicardium) in the pacing scenario (left) while they are found in the LV endocardium in normal sinus rhythm. The total activation time is substantially longer ($124ms$) in the pacing scenario compared to the non-pacing configuration ($39ms$) due to the large amount of "slow" tissue between the pacing site and the RV endocardium.

Finally, the conduction velocities along and transverse to the myocardial fibres were set to values found in the literature, in particular based on findings recently reported by Caldwell et al. [14] . Hence, a value of $0.67m/s$ was taken as conduction velocity along the myofibre axis and $0.24m/s$ transverse to this, which was an average between the maximum conduction velocities parallel to the myocyte layers, $0.30m/s$, and normal to them, $0.17m/s$. Finally, the conduction velocity of the Purkinje system was set to $1.59m/s$, according to Rawling et al. [15].

3.2 Fast Eikonal-Based Electrophysiological Models

There exist several models with different degree of complexity to simulate cardiac electrical activation. The complexity is usually selected as a function of the final application and has a great impact in computational times. In this work, we used a simplified electrical propagation model that is solved on the ex-vivo porcine anatomical model, including the myocardial fibre orientation provided by the available Diffusion Tensor Imaging (DTI) data and the Purkinje

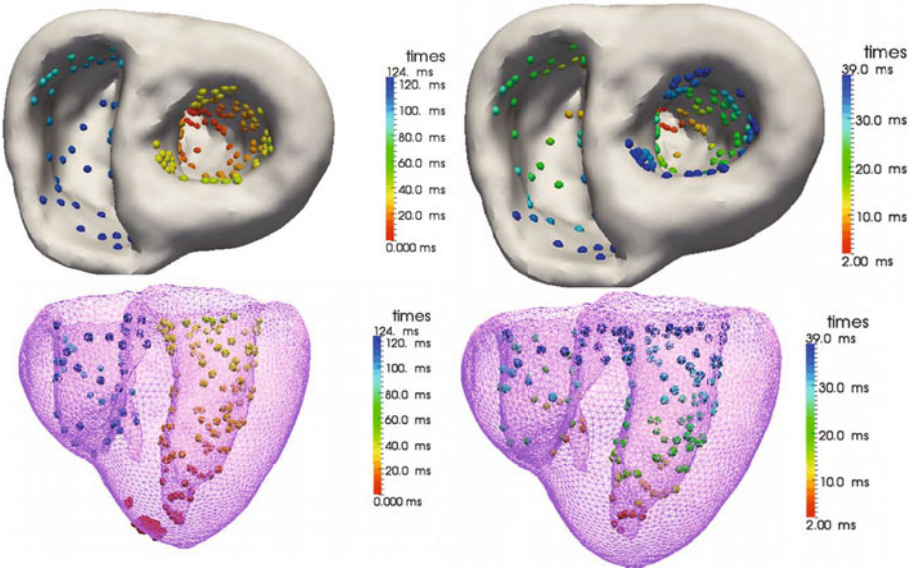

Fig. 2. Purkinje terminal maps with (left) and without (right) pacing. Spheres correspond to the Purkinje terminals and are color-coded with respect to their activation times

terminals given by the algorithm described above. These simple wave propagation models [16,17,18] are based on the assumption that the speed of propagation varies more slowly and over much larger spatial scales than the transmembrane potential. The model that is used in this study is based on the Hamilton-Jacobi Equation (HJE) that is a formulation of mechanics in which the motion of a particle can be represented as a wave. This equation can be represented in its static form as the following:

$$\begin{cases} \mathcal{H}(x_i, \frac{\partial \phi}{\partial x_i}) = 0 \text{ for } x_i \in \Omega \\ \phi(x_i) = \phi_0(x_i) \text{ for } x_i \in \partial\Omega \end{cases} \tag{1}$$

Here ϕ is the seed value and x_i is the coordinate components. The Eikonal equation is an important member of the Hamilton-Jacobi equations, which can be described in anisotropic format as:

$$\begin{cases} a_{ij} \frac{\partial \phi}{\partial x_i} \frac{\partial \phi}{\partial x_j} - f^2(x_i) = 0 \text{ for } x_i \in \Omega \\ \phi(x_i) = \phi_0(x_i) \qquad\qquad\quad \text{for } x_i \in \partial\Omega \end{cases} \tag{2}$$

where a_{ij} is the anisotropy coefficient which is related to the conduction velocity in the tissue, being $f(x)$ a positive function. In order to solve Equation (2), we used the Fast Marching Method (FMM), introduced by Sethian [19], to Hamilton-Jacobi equations of Eikonal type by a finite difference discretization

up-wind scheme. This method allows speeding up the convergence of the classical iterative finite difference scheme for electrophysiological simulations for the heart [20]. It computes the approximate solution in a finite number of steps and the complexity behaves as $O(N \ln N)$ where N is the total number of nodes [21].

3.3 Optimization Procedure

The main objective of the optimization procedure was to find the parameters (number of Purkinje end-terminals per region and the latest endocardial time) that minimized the difference between simulation results and measurements. The cost function guiding the optimization step used in this work was the absolute mean error, integrated over all heart regions with available measurements, between the depolarization time maps provided by the fast electrophysiological models and by the optical mapping data.

Due to the discrete nature of the parameters to optimize and the randomness of the location of a particular Purkinje end-terminal within a region, the estimation of reliable enough and computationally reasonable Jacobians with the proposed cost function was difficult. For this reason, we choose to use a classical genetic algorithm for the personalization of regional density of Purkinje end-terminals and for the latest endocardial time. In a genetic algorithm, a population of strings (genotype of the genome), which encode candidate solutions (called individuals) to an optimization problem, evolves toward better solutions. Different steps in the procedure need to be defined for each particular problem: initialization; selection; reproduction including crossover and mutation; and termination.

In this work, each individual is basically a string composed of the number of Purkinje end-terminals per region and the latest endocardial activation time (27 parameters). Furthermore, according to observations by Durrer et al. [10], we did not allow the presence of Purkinje end-terminals in some regions (mainly basal regions) and we forced the presence of at least one end-terminal in the remaining regions, as can be deduced from Fig. 3 . In order to be more robust with respect to the randomness of terminal locations given by the Purkinje tree generation, we run 50 simulations per each individual in order to compute the corresponding latest endocardial activation time (average of the 50 simulations) and the value of the cost function (error given by the average of the 50 simulations).

In the initialization step, we choose 45 individuals per each iteration of the procedure, having 10 individuals surviving at each iteration according to a probability function depending on the corresponding error. At the following iteration, the missing 35 individuals were generated at the reproduction phase. First, for couple of individuals, we randomly recombine (crossover) each of the parameters (50% for each individual). then for each individual, we mutate each parameter according to a Gaussian probability centered at the parameter value obtained in the previous iteration. Finally, the algorithm is manually stopped when there is no substantial improvement in the error cost function for several iterations.

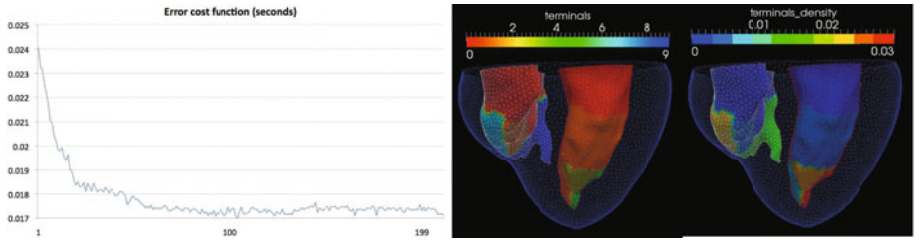

Fig. 3. Convergence of the optimization procedure (left) and the obtained total number (centre) and density (right) Purkinje end-terminal maps.

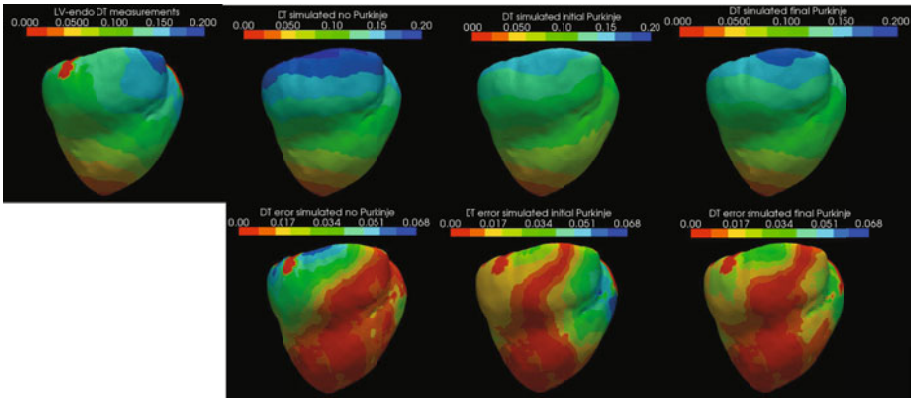

Fig. 4. Depolarization time measurements and simulated. Top (from left to right): depolarization time measurements from optical mapping data; simulated depolarization times without Purkinje; simulated depolarization times with Purkinje and initial parameters; simulated depolarization times with Purkinje and personalized parameters. Bottom (from left to right): depolarization time error maps for simulations without Purkinje; depolarization time error maps for simulations with Purkinje and initial parameters; depolarization time error maps for simulations with Purkinje and personalized parameters.

4 Results

Fig. 3 shows the convergence obtained with the personalization of the parameters of the Purkinje structural model, as well as the resulting number of terminal and terminal density maps. We can easily observe that the convergence is reached after around 50 iterations, having an initial absolute mean error of 24ms (1 terminal in 14 regions) and a final value of 17ms. The set of parameters providing lower error values included a total number of 58 Purkinje end-terminals (with a maximum of 9 terminals, found in 1 region, and a minimum of 1 terminal, found in 6 regions) in the whole heart and a latest endocardial activation time of 72ms. From a visual inspection of Fig. 3, the distribution of the Purkinje end-terminals

agrees with findings in the literature [10], having more terminals in the apical heart and less in the basal part.

Fig. 4 illustrates the depolarization times given by the analysis of the experimental data as well as the ones obtained with the electrophysiological models in three different parameter scenarios: without Purkinje conduction system; with a Purkinje model with non-personalized parameters; with a Purkinje model with personalized parameters. Error maps of the measured and simulated depolarization maps are also included in the figure. Several aspects need to be pointed out from the visual inspection of this figure. First, the absolute mean error of the simulation result without Purkinje was larger ($21ms$) than with the personalized Purkinje model. We can observe large errors in the basal part without Purkinje that are minimized when including Purkinje, in particular at the right ventricle. In fact, the total activation time was closer to the ground truth ($170ms$) when personalizing Purkinje ($172ms$) than without Purkinje ($190ms$). It also looks like the incorporation of Purkinje is beneficial mostly for the RV, while it does not improve or even slightly increase errors in the LV, in particular if the Purkinje model is not personalized.

5 Discussion and Conclusions

We presented a pipeline for the optimization of some relevant parameters in the modelling of the Purkinje system in electrophysiological simulations. Even though simulations with personalized parameters provided lower depolarization time errors with respect to baseline parameters, there were still substantial differences between simulation results and measurements. The optimization of these Purkinje model parameters was achieved using the optical mapping data obtained from experiments on ex-vivo porcine hearts, which were available just in some regions of the epicardium. The modelled fast conduction system was located at the endocardial wall as it is found in humans, even if it is known that in some species Purkinje terminals such as pigs can be found transmurally. After analyzing the obtained results, we reckon that endocardial electrophysiological measurements, that could be acquired *in vivo* either with contact or non-contact mapping systems, might be more appropriate than epicardial optical mapping data for the study of the fast conduction system. Once personalized, these Purkinje models optimized with fast electrophysiological simulations could be subsequently used as initialization of more detailed models.

Acknowledgments

The authors would like to thank Martin Steghofer, a developer from the CISTIB, whose contribution was fundamental for the execution of this work. This research has been partially funded by the Industrial and Technological Development Centre (CDTI) under the CENIT Programme (cvRemod project) and the European Community's Seventh Framework Programme (FP7/2007-2013) under grant agreement n. 224495 (euHeart project). OC and RS acknowledge grant

support from the Spanish Ministry of Research and Innovation, under a Ramon y Cajal and Juan de la Cierva Research Fellowship respectively.

References

1. Ecabert, O., Smith, N.: euheart: integrated cardiac care using patient-specific cardiovascular modeling. In: SPIE Newsroom, Biomedical Optics and Medical Imaging (2008)
2. Sermesant, M., Moireau, P., Camara, O., Sainte-Marie, J., Andriantsimiavona, R., Cimrman, R., Hill, D., Chapelle, D., Razavi, R.: Cardiac function estimation from mri using a heart model and data assimilation: advances and difficulties. Medical Image Analysis 10(4), 642–656 (2006)
3. Kerckhoffs, R., Healy, S., Usyk, T., McCulloch, A.: Computational methods for cardiac electromechanics. Proceedings of the IEEE 94(6), 769–783 (2006)
4. Streeter, D.: Gross morphology and fibrous structure of the heart. In: Handbook of Physiology: The Cardiovascular System, vol. 1, pp. 61–112. Oxford University Press, Oxford (1979)
5. Peyrat, J.M., Sermesant, M., Pennec, X., Delingette, H., Xu, C., McVeigh, E.R., Ayache, N.: A computational framework for the statistical analysis of cardiac diffusion tensors: application to a small database of canine hearts. IEEE Trans. Med Imaging 26(11), 1500–1514 (2007)
6. Kroon, W., Delhaas, T., Bovendeerd, P., Arts, T.: Adaptive reorientation of cardiac myofibers: Comparison of left ventricular shear in model and experiment. In: Ayache, N., Delingette, H., Sermesant, M. (eds.) FIMH 2009. LNCS, vol. 5528, pp. 58–67. Springer, Heidelberg (2009)
7. Muñoz-Moreno, E., Frangi, A.: Spatial normalization of cardiac diffusion tensor imaging for modeling the muscular structure of the myocardium. In: Proceedings of the IEEE International Conference on Image Processing (ICIP 2010) (2010) (in Press)
8. Romero, D., Sebastian, R., Bijnens, B.H., Zimmerman, V., Boyle, P.M., Vigmond, E.J., Frangi, A.F.: Effects of the purkinje system and cardiac geometry on biventricular pacing: a model study. Ann. Biomed. Eng. 38(4), 1388–1398 (2010)
9. Zimmerman, V., Sebastian, R., Bijnens, B., Frangi, A.: Modeling the purkinje conduction system with a non deterministic rule based iterative method. Computer in Cardiology 36, 461–464 (2009)
10. Durrer, D., van Dam, R.T., Freud, G.E., Janse, M.J., Meijler, F.L., Arzbaecher, R.C.: Total excitation of the isolated human heart. Circulation 41(6), 899–912 (1970)
11. Pop, M., Sermesant, M., Lepiller, D., Truong, M., McVeigh, E., Crystal, E., Dick, A., Delingette, H., Ayache, N., Wright, G.: Fusion of optical imaging and mri for the evaluation and adjustment of macroscopic models of cardiac electrophysiology: a feasibility study. Medical Image Analysis 13(2), 370–380 (2009)
12. Relan, J., Sermesant, M., Delingette, H., Pop, M., Wright, G., Ayache, N.: Quantitative comparison of two cardiac electrophysiology models using personalisation to optical and mr data. In: Proc. IEEE International Symposium on Biomedical Imaging: From Nano to Macro (ISBI 2009), pp. 1027–1030 (2009)
13. Kerckhoffs, R.C.P., Faris, O.P., Bovendeerd, P.H.M., Prinzen, F.W., Smits, K., McVeigh, E.R., Arts, T.: Timing of depolarization and contraction in the paced canine left ventricle: model and experiment. J. Cardiovasc. Electrophysiol. 14(10 suppl.), 188–195 (2003)

14. Caldwell, B., Trew, M., Sands, G., Hooks, D., LeGrice, I., Smaill, B.: Three distinct directions of intramural activation reveal nonuniform side-to-side electrical coupling of ventricular myocytes. Circulation: Arrhythmia and Electrophysiology 2(4), 433–440 (2009)
15. Rawling, D.A., Joyner, R.W., Overholt, E.D.: Variations in the functional electrical coupling between the subendocardial purkinje and ventricular layers of the canine left ventricle. Circ. Res. 57(2), 252–261 (1985)
16. Franzone, P., Guerri, L., Pennacchio, M.M., Taccardi, B.: Spread of excitation in 3-d models of the anisotropic cardiac tissue. ii. effects of fiber architecture and ventricular geometry. Math Biosci. 147(2), 131–171 (1998)
17. Tomlinson, K.A., Hunter, P.J., Pullan, A.J.: A finite element method for an eikonal equation model of myocardial excitation wavefront propagation. SIAM Journal on Applied Mathematics 63, 324–350 (2002)
18. Chinchapatnam, P., Rhode, K.S., Ginks, M., Rinaldi, C.A., Lambiase, P., Razavi, R., Arridge, S., Sermesant, M.: Model-based imaging of cardiac apparent conductivity and local conduction velocity for diagnosis and planning of therapy. IEEE Trans. Med. Imaging 27(11), 1631–1642 (2008)
19. Sethian, J.A.: A fast marching level set method for monotonically advancing fronts, vol. 93, pp. 891–906 (1991)
20. Sermesant, M., Coudière, Y., Moreau-Villéger, V., Rhode, K., Hill, D., Razavi, R.: A fast-marching approach to cardiac electrophysiology simulation for XMR interventional imaging, vol. 8, pp. 607–615 (2005)
21. Mauch, S.: Efficient algorithms for solving static hamilton-jacobi equations, PhD thesis California Institute of Technology (2003)

Author Index